ARMY RESEARCH OFFICE
AND
AIR FORCE OFFICE OF SCIENTIFIC RESEARCH

2000

CONTRACTORS' MEETING
IN
CHEMICAL PROPULSION

20000703 017

REPORT DOCUMENTATION PAGE

AFRL-SR-BL-TR-00-

0243

1. REPORT DATE (DD-MM-YYYY)	2. REPORT TYPE	3. DATES COVERED (From - To)
21 June 2000	Technical	1 June 1999 – 31 May 2000

4. TITLE AND SUBTITLE	5a. CONTRACT NUMBER
(U) ARO and AFOSR Contractors Meeting in Chemical Propulsion	5b. GRANT NUMBER
	5c. PROGRAM ELEMENT NUMBER 61102A, 61102F

6. AUTHOR(S)	5d. PROJECT NUMBER
David M. Mann and Julian M. Tishkoff	5e. TASK NUMBER
	5f. WORK UNIT NUMBER

7. PERFORMING ORGANIZATION NAME(S) AND ADDRESS(ES)	8. PERFORMING ORGANIZATION REPORT NUMBER
Army Research Office Research Triangle Park NC 27709-2211 Air Force Office of Scientific Research Arlington VA 22203-1977	

9. SPONSORING / MONITORING AGENCY NAME(S) AND ADDRESS(ES)	10. SPONSOR/MONITOR'S ACRONYM(S)
AFOSR/NA 801 North Randolph Street Room 732 Arlington VA 22203-1977	11. SPONSOR/MONITOR'S REPORT NUMBER(S)

12. DISTRIBUTION / AVAILABILITY STATEMENT

Approved for public release; distribution is unlimited

13. SUPPLEMENTARY NOTES

14. ABSTRACT

Abstracts are given for 6.1 basic research in chemical propulsion supported by the Army
Research Office and the Air Force Office of Scientific Research

15. SUBJECT TERMS

Flames, Propulsion, Gas Turbines, Diesel Engines, Scramjets, Hydrocarbon Fuels, Chemistry, Sprays, Droplets, Supercritical Fluids, Diagnostics

16. SECURITY CLASSIFICATION OF:			17. LIMITATION OF ABSTRACT	18. NUMBER OF PAGES	19a. NAME OF RESPONSIBLE PERSON Julian M. Tishkoff
a. REPORT Unclassified	b. ABSTRACT Unclassified	c. THIS PAGE Unclassified	UL	197	19b. TELEPHONE NUMBER (include area code) (703) 696-8478

Standard Form 298 (Rev. 8-98)
Prescribed by ANSI Std. Z39.18

ARMY RESEARCH OFFICE
AND
AIR FORCE OFFICE OF SCIENTIFIC RESEARCH

2000

CONTRACTORS' MEETING
IN
CHEMICAL PROPULSION

DTIC QUALITY INSPECTED 4

Layout & Design by DTI Associates, Inc

ARO/AFOSR Contractors' Meeting in Chemical Propulsion
TABLE OF CONTENTS

Abstracts of Work Units Not Presented at the Meeting

ARO/AFOSR CONTRACTORS' MEETING

IN

CHEMICAL PROPULSION

Fort Marcy Hotel and Suites
Santa Fe, NM
12-14 June 2000

MONDAY, 12 JUNE

8:00 - 8:15	AFOSR Combustion and Diagnostics Program – Julian Tishkoff
8:15 - 8:30	Air Force Office of Scientific Research Overview – Dr. Joseph Janni, AFOSR Director
8:30 - 8:45	Army Research Office Overview - David Mann

Topic: Atomization and Sprays

8:45 - 9:15	Transient Spray Experiments and Modeling at the Engine Research Center Patrick V. Farrell, University of Wisconsin-Madison
9:15 - 9:45	Improved Modeling of Drop Vaporization and Combustion In Diesel Sprays John Abraham, Purdue University
9:45 - 10:15	Modeling Diesel Engine Injector Flows Stephen Heister, Purdue University
10:15 - 10:45	BREAK
10:45 - 11:15	Internally Mixed Injectors and Two-Phase Flow Modeling Jerry Seitzman, Georgia Institute of Technology
11:15 - 11:45	Fluorescent Diagnostics and Fundamental Approaches to Droplet, Spray, Engine, and Aerodynamic Behavior Lynn Melton, University of Texas at Dallas
11:45 - 1:00	LUNCH
1:00 - 1:30	Ramjet Research Thomas A. Jackson, AFRL/PRSS

1:30 - 2:00	Sub- and Supercritical Evaporation and Combustion of a Moving Droplet George Gogos, University of Nebraska
2:00 - 2:30	Study of the Sub- and Supercritical Behavior of Fuel Droplets and Jets Yaw Yeboah, Clark Atlanta University
2:30 - 3:00	BREAK
3:00 - 3:30	Drop-Gas Interactions in Dense Sprays G. M. Faeth, University of Michigan
3:30 - 4:00	Nonlinear Distortion and Disintegration of Conical Liquid Sheets at High Pressures William A. Sirignano, University of California, Irvine
4:00 - 4:30	Large-Eddy Simulations of Supercritical Multicomponent Mixing Layers Josette Bellan and Kenneth Harstad, Jet Propulsion Laboratory
4:30 - 5:00	NSF Information Technology Research Initiative Stefan Thynell, Pennsylvania State University
5:00 - 7:30	DINNER BREAK
7:30 - 9:30	EVENING DISCUSSION – Weakly Ionized Flows – Coordinating With Russian Research Dr. David Van Wie, Johns Hopkins University Applied Physics Lab Dr. Mark Gruber, AFRL/PRSS

TUESDAY, 13 JUNE

8:15 - 8:30	Announcements

TOPIC: Diagnostics

8:30 - 9:00	In-Cylinder Two-Dimensional Two-Color Optical Pyrometry as an Indicator of Engine Out Emissions: Experiment and Simulation David E. Foster, University of Wisconsin-Madison

9:00 - 9:45	Advanced Diagnostics for Reacting Flows R. K. Hanson, Stanford University
9:45 - 10:15	Diode Laser Spectroscopy and MEMS Pressure Sensors Jerry Seitzman, Georgia Institute of Technology
10:15 - 10:45	BREAK
10:45 - 11:15	Crossed-Plane Laser Imaging of Premixed Turbulent Combustion Processes Frederick C. Gouldin, Cornell University
11:15 - 11:45	Planar Image Particle Analyzer for Whole Field Spray Applications Cecil Hess, MetroLaser
11:45 - 1:00	LUNCH
1:00 - 1:30	Planar Thermometry in Sooting, Transient Diffusion Flames William Roberts, North Carolina State University
1:30 - 2:00	Simultaneous Measurements of Species Concentrations, Temperature, and Flow Velocity in a Flame Rajendra Gupta, University of Arkansas
2:00 - 2:30	Statistical Interpretation of Power Spectral Densities Measured by Picosecond Time-Resolved Laser-Induced Fluorescence in Turbulent Nonpremixed Flames Normand Laurendeau and Galen King, Purdue University
2:30 - 3:00	Supercritical Fuels/Combustion Research James Gord, AFRL/PRSF
3:00 - 3:30	BREAK
3:30 - 3:50	BUSINESS SESSION - Contractors in Dr. Mann's Program Only
3:50 - 4:30	BUSINESS SESSION - Contractors in Dr. Tishkoff's Program Only
4:30 - 7:30	DINNER BREAK

7:30 - 9:30   PANEL DISCUSSION — Future Directions for Chemistry In
                 Combustion System Design

                 PANELISTS: W. M. Roquemore, AFRL/PRSC
                            Robert Ryder, Flow Parametrics, LLC
                            Andrew Brankovic, Flow Parametrics, LLC
                            Stephen B. Pope, Cornell University
                            Suresh Menon, Georgia Institute of Technology
                            Kalyanasundaram Seshadri, University of California-
                                                          San Diego

WEDNESDAY, 14 JUNE

8:15 - 8:30   Announcements

Topic: Combustion Chemistry

8:30 - 9:00   Effect of Nitric Oxide and Other Diluents on Cold Starting,
                 Combustion Instability, and White Smoke Emissions in
                 Diesel Engines
                 Naeim Henein, Wayne State University

9:00 - 9:30   Investigation of Preflame Reactions and Flame Propagation In
                 Direct-Injection Diesel Engines
                 Kyung T. Rhee, Rutgers, the State University of New Jersey

9:30 - 10:00   BREAK

10:00 - 10:30   Chemical Kinetic Characterization of Autoignition and Combustion
                 of Diesel and JP-8
                 Kalyanasundaram Seshadri, University of California-San Diego

10:30 - 11:00   Mechanisms Controlling Soot Formation in Diffusion Flames
                 Meredith B. Colket III, United Technologies Research Center

11:00 - 11:30   Catalytic Ignition as a Tool for Converting Small Engines to
                 Efficient JP-8 Operation
                 Judi Steciak, University of Idaho

11:30 - 1:00   LUNCH

1:00 - 1:30   Chemical Reactions in Turbulent Mixing Flows
                 Paul E. Dimotakis, California Institute of technology and
                 Fokion Egolfopoulos, University of Southern California

1:30 - 2:00   Chemical Kinetics and Aerodynamics of Ignition
                 C. K. Law, Princeton University

| 2:00 - 2:30 | Physical and Chemical Processes in Flames
C. K. Law, Princeton University and Hai Wang, University of Delaware |
| 2:30 - 3:00 | BREAK |

Topic: High Pressure Behavior

3:00 - 3:30	The Chemistry Controlling Ignition of Hydrocarbons and Their Mixtures at High Pressures Nicholas Cernansky, Drexel University
3:30 - 4:00	Advanced Supercritical Fuels/Supercritical Combustion Tim Edwards, AFRL/PRSF
4:00 - 4:30	Fuels Combustion Research: Supercritical Fuel Pyrolysis Mary Wornat, Princeton University
4:30	ADJOURN

AFOSR SPONSORED RESEARCH IN COMBUSTION AND DIAGNOSTICS

PROGRAM MANAGER: JULIAN M. TISHKOFF

AFOSR/NA
801 North Randolph Street, Room 732
Arlington VA 22203-1977

SUMMARY/OVERVIEW: The Air Force Office of Scientific Research (AFOSR) program in combustion and diagnostics currently is focused on five areas of study: high-speed propulsion, turbulent combustion, atomization and sprays, diagnostics, and super-critical fuel behavior. An assessment of major research needs in each of these areas is presented.

TECHNICAL DISCUSSION

AFOSR is the single manager for Air Force basic research, including efforts based on external proposals and in-house work at the Air Force Research Laboratory (AFRL). Combustion and Diagnostics is assigned to the AFOSR Directorate of Aerospace and Materials Sciences along with programs in rocket and space propulsion, fluid and solid mechanics, and structural materials.

Interests of the AFOSR Combustion and Diagnostics subarea are given in the SUMMARY section above. Many achievements can be cited for these interests, yet imposing fundamental research challenges remain. The objective of the program is publications in the refereed scientific literature describing significant new understanding of multiphase turbulent reacting flow. Incremental improvements to existing scientific approaches, hardware development, and computer codes fall outside the scope of this objective.

The Combustion and Diagnostics subarea reflects a new Air Force commitment to support space science and technology. Accordingly, the research in this subarea will address research issues related to chemical propulsion for all Air Force aerospace missions, including combined cycle propulsion for access to space. This program will complement related research activities in space propulsion and energetic materials.

Future airbreathing propulsion systems will require fuels to absorb substantial thermal energy, raising fuel temperatures to supercritical thermodynamic conditions. Understanding and controlling fuel properties at these conditions will be crucial for avoiding thermal degradation and for optimizing subsequent processes within the combustor. Environ-

mental concerns and the availability of petroleum supplies also will contribute to future propulsion system design and operational needs.

One programmatic change relative to previous research interests is a discontinuation of activities to understand soot formation and growth. Although this research area has been, and continues to be, of primary importance to Air Force airbreathing propulsion technology, Air Force basic research is being eliminated in favor of new programs being initiated by the Department of Defense (DOD) Strategic Environmental Research and Development Program (SERDP). Interested researchers should visit the DOD web site for further information.

Decisions on support for research proposals are based on scientific opportunities and technology needs. Researchers interested in submitting proposals should contact Dr. Tishkoff for information on time constraints associated with proposal evaluations. Further information on research interests and proposal preparation can be found on the AFOSR web site, http://www.afosr.af.mil. The availability of funds places a major constraint on program redirection and growth. Figure 1 shows the recent trend of funding for basic research in combustion and diagnostics from Air Force and DOD sources. Funding in the next fiscal year (FY 2001) is expected to be roughly the same as that for FY 2000. Informal inquiries for new research are encouraged throughout the year. Formal proposals should be submitted by 1 April for peer review by the National Research Council.

The purpose of this abstract has been to communicate AFOSR perceptions of research trends to the university and industrial research communities. However, communication from those communities back to AFOSR also is desirable and essential for creating new research opportunities. Therefore, all proposals and inquiries for fundamental research are encouraged even if the content does not fall within the areas of emphasis described herein. Comments and criticisms of current AFOSR programs also are welcome.
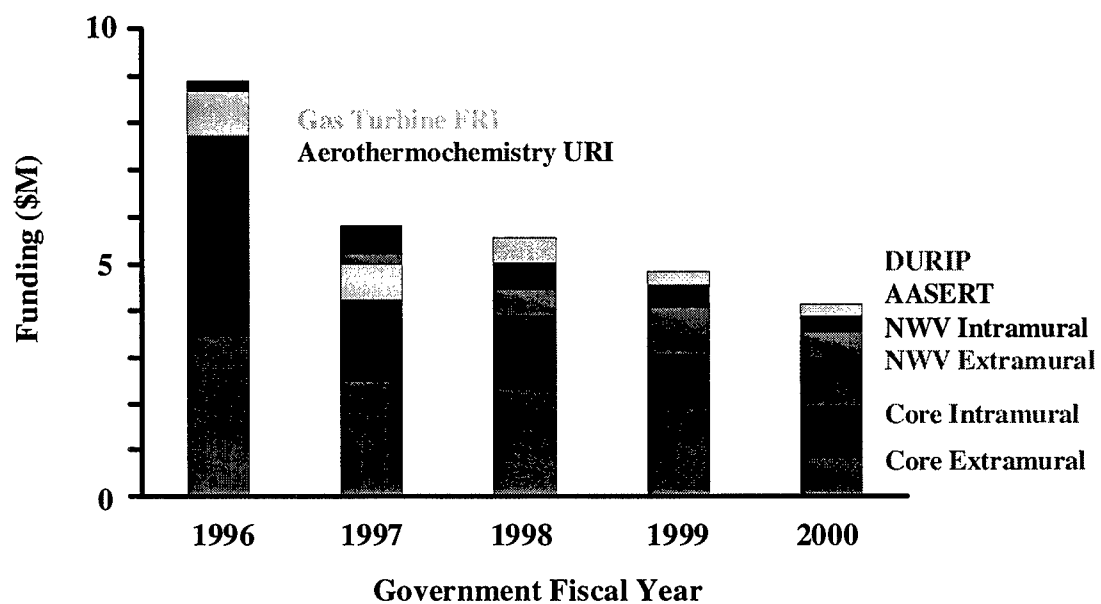
Figure 1. Research Funding History

US Army Research Office
Propulsion and Energetics Research

David M. Mann
Associate Director, Engineering Sciences Directorate
Mechanics and Environmental Sciences Division

The Chief of Staff of the Army, General Eric Shinseki, has issued a new vision for future Army capability, a vision that is shaping the Army's science and technology (S&T) efforts. It is the intent that, "Heavy forces must be more strategically deployable and more agile with a smaller logistical footprint, and light forces must be more lethal, survivable and tactically mobile. Achieving this paradigm will require innovative thinking about structure, modernization efforts and spending." He further stated that, "The S&T community is the key to the long term transformation of the Army." Many Army in-house research and development programs have been refocused on the development of technologies for a new, lighter, faster, more effective force. Through investing in long-term, basic research, the Army Research Office program is providing the fundamental understanding that will enable even greater advances in systems' capability. In the areas of propulsion and energetics, the focus remains on the development of high efficiency, high power density vehicle propulsion and innovative approaches to achieve improved performance in gun and missile propulsion systems.

The presentation will provide a background on the new Army emphasis and its implications for the Army Research Office and Army Research Laboratory programs in propulsion and energetics.

TRANSIENT SPRAY MODELING AND EXPERIMENTS AT THE ENGINE RESEARCH CENTER

Grant No: DAAH04-94-G-0328 and TACOM DAAE07-99-3-005

Principal Investigators: Profs. Corradini, Farrell, Foster, Ghandhi, Martin, Moskwa, Reitz and Rutland

Engine Research Center
University of Wisconsin-Madison
Madison Wisconsin 53706

SUMMARY/OVERVIEW:

This presentation describes some of the work on transient sprays supported under these grants as well as under grants from industry (the TACOM DUAP grant requires 100% industrial match). The goals of this work include:

- Identify critical spray characteristics for the range of spray applications of interest (DI Diesel, HSDI Diesel, GDI) which are likely to have a large influence on engine characteristics of interest (air utilization/power density, BSFC, BSHC, BSNOx, particulates, vaporization of multicomponent fuels,...)
- Measure critical characteristics of realistic injector systems (penetration, cone angle, SMD, vapor distribution,...)
- Develop appropriate models of these injector systems, suitable for incorporation into large-scale engine modeling codes including these effects.
- Evaluate injector systems in engine combustion systems; this provides data for code validation, a direct measure of the sensitivity of combustion to spray characteristics, and an avenue for system optimization.

In general, the results of this work to-date include:

- Detailed studies of commercial and experimental injector systems operating as unit injector systems and common rail injector systems under a wide range of conditions (varying injection rates, cylinder densities and temperatures, injector geometries, injection strategies,...)
- Special case studies: e.g. direct impingement sprays for low-temperature atomization
- Detailed spray sub-models have been added or improved; these are all incorporated into KIVA (and other commercial codes) which is the primary large-scale engine combustion code used at the ERC.
- Engine experiments have demonstrated the effects of different spray characteristics on engine performance (BSFC, BSNOx, particulates)
- The combination of these results has pushed the model (KIVA) closer to being a predictive design tool

TECHNICAL DISCUSSION:

The presentation described by this abstract represents a portion of the work conducted at the ERC in recent years on transient sprays. This work has included fundamental work aimed at improving understanding of atomization and distribution of liquid fuel sprays for a variety of engine applications, and specific examples that provide results of immediate use (such as the direct wall impingement studies for enhanced cold-start atomization). In this presentation, I will show a sample of these results to illustrate the scope and depth of the work at the ERC.

Fuel sprays are known to have a significant, if not dominant, effect on engine performance and emissions for direct injection (DI) Diesel engines. The impact of different spray characteristics changes somewhat depending on engine size, fuel injection system, and injection pressure. For example, for medium size diesel engines (~150 mm bore), injection pressures are often as high as 160 MPa providing very high-speed fuel jets (~ 300 m/s) into a high temperature, high pressure, but relatively quiescent chamber. For smaller bore HSDI engines (90 mm bore, typical of a V8 diesel for small truck or utility vehicle use) injection pressures must be much lower to avoid spraying fuel on the piston bowl, resulting in much more modest and consequently less dominant fuel velocities.

In the following paragraphs some specific examples of the spray work at the ERC will be shown. This work involves several of the PI's listed above, and many of their graduate students.

Example 1: Spray penetration in a firing engine

Spray penetration (liquid and vapor fuel location relative to the injector as a function of time) seems to be an important parameter in the coupling between the spray and chamber gas, and impacts the fuel-air mixing and subsequent combustion. Under some conditions, small injector holes producing small spray droplets with modest penetration have been shown to be advantageous, but under other engine operating conditions, larger holes and larger initial droplet sizes allowed better penetration and air utilization, resulting in lower emissions and BSFC values.

Previous studies at various laboratories have shown relatively short penetration lengths (c.a. 20 mm) for high temperature spray environments [c.f. 1,2]. The specific experiment discussed here attempts to evaluate those characteristics under conditions of a minimally modified modern diesel engine with a high-pressure unit injection system (HEUI). A sample sequence of Mie backscatter images (slightly processed for enhanced contrast) is shown in fig. 1. Figure 2 shows a summary result of spray impingement in this set of experiments with in-cylinder density. Varying the level of supercharging (intake pressure) and intake temperature (to simulate charge heating due to turbocharging) varied TDC pressure and density. As expected, higher cylinder densities produced lower penetration values due to different droplet drag effects and differences in the vaporization thermodynamics. Detailed results are available in [3].

Example 2: Wall impingement studies

Spray impingement on the piston or cylinder wall is often viewed as a feature to be avoided as it apparently leads to much higher particulate emissions as well as being a limiting factor in developing higher power density engines. Under some conditions, wall impingement may be advantageous, because there is some evidence that wall impingement leads to increased atomization and mixing of fuel. This set of experiments investigates the conditions under which enhanced atomization occurs, and to what degree. A parallel activity developed models of this behavior. Some details of the experimental work are available in [4].
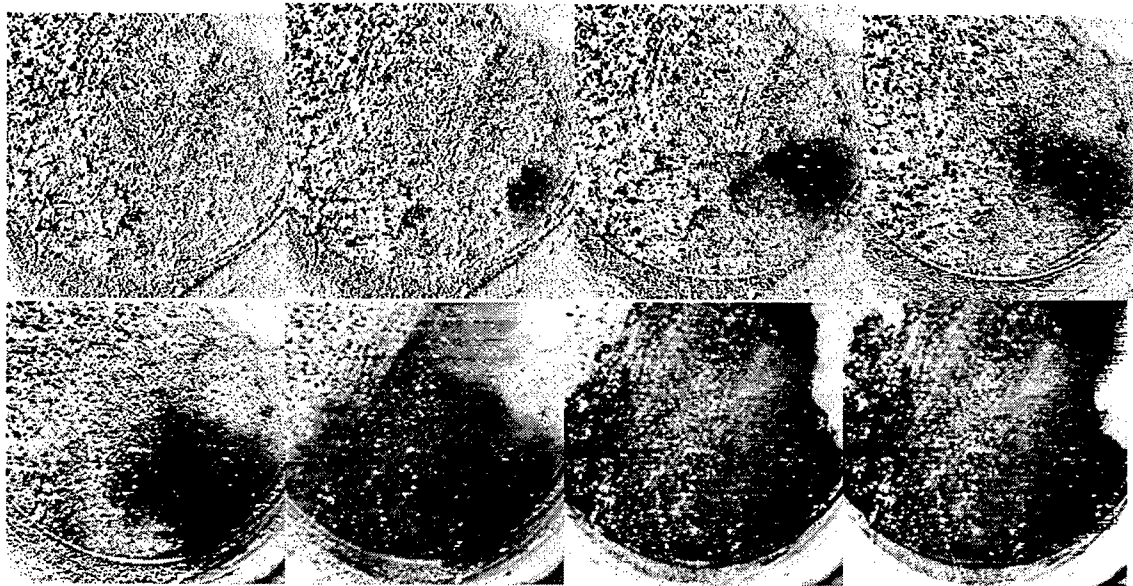
Figure 1: Spray images for 120 MPa injection pressure (HEUI Injector); SOI 8° BTDC (T_{amb} ~ 680°C, ρ_{amb} ~ 16.9 kg/m3). Images at 4500 fps (δt = 222 μs) starting at 1.55 ms ASOI (L to R across top row, then L to R across bottom row). Ignition appears a bright cloud in 5th image; piston bowl edge is easily seen in 6th image.
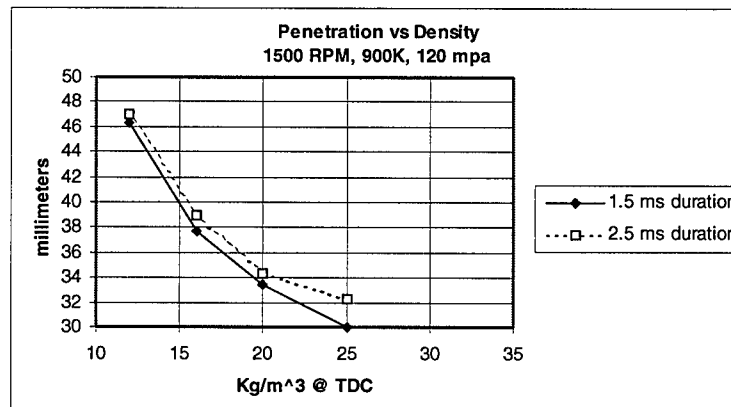
Figure 2: Liquid spray penetration vs TDC cylinder density

Initially, the model used for wall impingement in KIVA was successful in modeling wall impingement at relatively low speed at small impingement angles. For the current case, impingement distances are small (~10 mm for the case pictured in fig. 3) so velocities are high (~60 m/s or more) at the target; additionally the impingement angle is nearly 90°. A modified model accounting for wall-induced breakup, rebound, and the subsequent film formation and stripping at the edge of the target was developed. Results for the conditions of the photo in fig. 3a are shown in figs. 3b and 3c, where fig. 3b shows the spray distribution at the time of the photo using the earlier KIVA model, and fig. 3c shows the improved model.

Example 3: Multi-pulse injection for HSDI engines

One method for increasing air utilization in diesel engines, and hence the possibility of higher energy density (higher output/volume for constrained BSFC or emissions or…) is to take advantage of newer common rail injection systems which can provide more than one injection per cycle. This idea has been shown to be successful under some conditions with one en-

15

gine [5] and work is currently underway to investigate the same effect on a very different size engine and injection system.
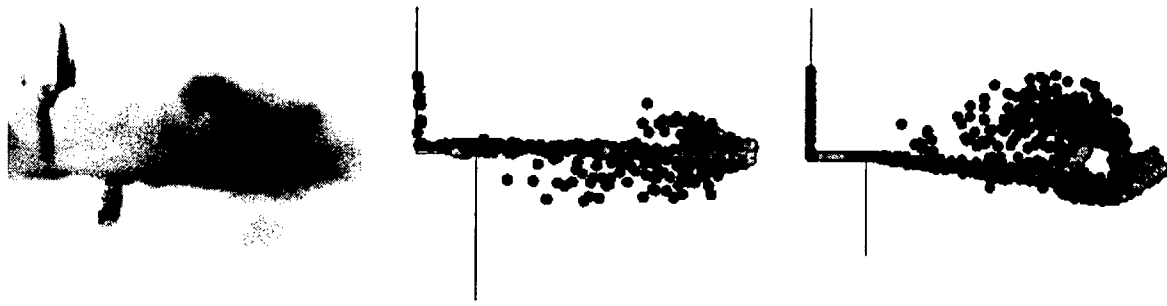
Figure 3: a) Spray impingement on near-field target; b) 'old' spray wall impingement model; c) 'new' spray-wall impingement model.
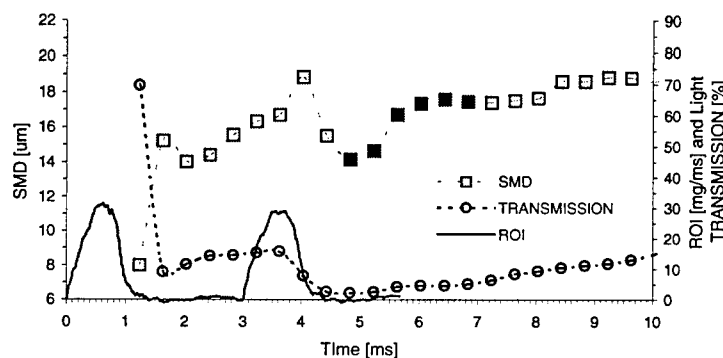
Figure 4: SMD, ROI, and transmission for a 50(1.83 ms) 50 split for a Bosch common rail injector in a room temperature spray chamber

A sample of the experimental results for this work is shown in fig. 4. This figure shows the results of a 50 (1.83) 50 split (50% of mass, 1.83 ms 'dwell', 50 % of mass), including SMD measured in the center of the spray plume with a diffraction sizing method, rate of injection (ROI) vs. time, and the transmission through the plume from a series of back-lit high speed images taken in a spray chamber. The rise of the SMD values after the end of injection is different from results acquired in prior work with higher flow injectors using a different measurement method (light extinction) and is still under investigation.

REFERENCES:

1. J. Dec, " A Conceptual Model of DI Diesel Combustion Based on Laser-Sheet Imaging", *Trans. SAE 106*, pp. 1319-1348 (1997).
2. D. Siebers, "Liquid-Phase Fuel Penetration in Diesel Sprays", SAE Paper 980809.
3. P. Borthwick, "Fuel Penetration and Wall Impingement in a Firing DI Diesel Engine", Ph.D. Thesis, Department of Mechanical Engineering, University of Wisconsin-Madison (2000).
4. S. Mislevy and P. V. Farrell, "Secondary Atomization from Diesel Fuel Spray Impingement", accepted for publication in Proceedings, ICLASS 2000.
5. C. T. Chang, T. F. Su, D. A. Pierpont, P. V. Farrell, and R. D. Reitz Effects of Injection Pressure and Nozzle Geometry on Spray SMD and DI Diesel Emissions", SAE Paper 952360.

IMPROVED MODELING OF DROP VAPORIZATION AND COMBUSTION IN DIESEL SPRAYS

Principal Investigator: John Abraham

Maurice J. Zucrow Laboratories
School of Mechanical Engineering
Purdue University
West Lafayette, IN 47907

SUMMARY/OVERVIEW

The objective of this effort is to study the vaporization of liquid drops and the penetration of the liquid phase in Diesel sprays under cold start conditions. During the reporting period, progress has been made in both aspects of this program as discussed below. It is shown that the simplified vaporization models that are employed for droplet vaporization in Diesel sprays reproduce the vaporization time estimated from detailed studies within 30%. It is also shown that the liquid penetration in vaporizing sprays appears to be mixing-controlled under all operating conditions.

TECHNICAL DISCUSSION

Under typical cold-start conditions in a Diesel engine, the compression temperature may be as low as 600-700 K with the peak pressure of 30-50 bar. This may be compared to a warm operating engine where the compression temperature may be about 1000 K with the peak pressure over 100 bar. Under cold start conditions, the vaporization rate of the droplet will be noticeably lower than that under warm operating conditions and the liquid penetration will be longer which increases the probability of liquid impingement on the piston and cylinder walls. The complexity of carrying out experiments in real engines to study these processes and the cost associated with optimizing engine designs and operating parameters have been a strong motivation for employing multidimensional models for the engine processes to study the processes and optimize engine designs. The accuracy of the model would depend on the accuracy of the submodels that are employed and that of the numerics. In this work, specific attention is focused on the droplet vaporization model. We address two questions: How do the simplified droplet vaporization models employed in multidimensional models compare with results from detailed numerical studies of droplet vaporization? How relevant is individual droplet vaporization in controlling liquid penetration in Diesel sprays?

In the case of the simplified droplet vaporization model, two equations are solved for droplet mass transfer and energy transfer. In the case of the detailed numerical model, the following assumptions are made and a one-dimensional set of equations solved: droplet vaporization is spherically symmetric; all non-radial velocities and fluxes are zero; Fick's and Fourier's laws for mass and energy diffusion are used; energy terms arising from viscous dissipation, radiation, interdiffusion, and flow work are neglected; negligible Soret and Dufour effects; pressure is uni-

form and constant throughout; thermal, mechanical, and chemical equilibrium at the vapor/liquid interface; and, Lewis and Raoult assumptions are valid at the vapor/liquid interface. Additional details may be found in Reference [1] and droplet vaporization studies by a large number of authors have been reviewed in the literature [2-4].

Results are presented below comparing the vaporization characteristics of n-hexadecane droplets. Figure 1 shows the computational grid employed in the detailed numerical study and in the multidimensional computation. Results are presented for a droplet of 20 μm diameter vaporizing in a 1 mm x 1 mm x 0.5 mm computational cell. Figures 2 and 3 show the size history of the droplets where the ordinate is the square of the normalized drop diameter and the abscissa is the scaled time t/R_0^2 where R_0 is the initial droplet radius. Also shown on the figures are the results when the simplified vaporization model is employed. It may be seen that the results are within about 30%. In fact, the results from the simplified model show a lower drop life-time in all cases. A possible explanation is that in the case of the detailed model, there is a vapor and temperature boundary layer around the droplet inhibiting vaporization. This is not the case in the case of the droplet vaporizing in the computational volume where the large computational volume would lead to a condition where the droplet is vaporizing in an infinite medium. The estimation of properties at the reference states, in the case of the simplified model, may introduce inaccuracies. Also plotted on Fig. 2 is the result from a multidimensional model computation for the 600 K case when the resolution of the numerical grid is increased. There is an interesting trend. It may be seen that the life-time of the droplet increases. The resolution is increased by a factor of 10 in all directions. There is a limit to which grid resolution can be increased, but the trends in the results are as expected. As the resolution is increased, and the ratio of the mass of liquid to the mass of air in the computational cell decreases, the condition of the ambient air, which influence the vaporization, will change with time influencing the droplet vaporization process. Of course, in a Diesel spray the situation of an isolated droplet vaporizing in an infinite environment is rarely encountered. The picture would be that of droplets vaporizing in the presence of other droplets and the conditions of the environment are continually changing. These results then raise the question of how important individual droplet vaporization modeling is in the context of modeling overall Diesel sprays.

Recent experimental data of liquid penetration may be interpreted to imply that the vaporization process is mixing-limited and individual droplet vaporization times are not important when estimating liquid penetration [5, 6]. We have employed a Locally Homogeneous Flow (LHF) assumption model proposed by Faeth [7] to study this question. In the model, we define a mixture fraction, Z, where $Z=Y_t+Y_v$ where Y_t is the liquid mass fraction and Y_v is the vapor mass fraction. Given a value for Z and the fuel injection condition and the ambient air condition, an algebraic equation may be solved to determine what Y_t, Y_v and temperature are. In this way, a state relationship may be developed as shown in Fig. 4. This may then be employed in a multidimensional computation to compute the liquid penetration. Figures 5 and 6 show computed and measured results of liquid penetration when the parameter being changed is the injection pressure and ambient density respectively. The measured trends are reproduced in the case of the injection pressure, indicating that the process is mixing limited, but not in the case of the ambient density [8]. Separate work has identified the reason for this discrepancy to be the assumption of equal velocities for the two phases. When the differences in liquid-phase and gas-phase velocities are taken into account, the discrepancy appears to reduce. The conditions considered include both warm and cold-start operation. The Lagrangian-Drop-Eulerian-Fluid model was also employed to carry out these comparisons. Figure 7 shows the results. In this case, inadequate nu-

merical resolution appears to dominate the computed trends and results [9, 10]. Nevertheless, it is shown that if a modified droplet size dependency on ambient density is employed, the measured trend may be reproduced 11]. But, altogether the conclusion of our work is that it is not important to reproduce individual droplet vaporization in order to compute the liquid penetration in Diesel sprays under cold-start condition. The process appears to be mixing-limited. This also implies that droplet sizes are sufficiently small such that droplet vaporization times are short compared to mixing times of air and fuel.
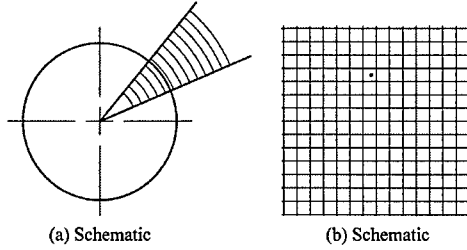
Fig. 1: Computational domain and grid for (a) detailed single droplet and (b) single droplet employing multidimensional model.
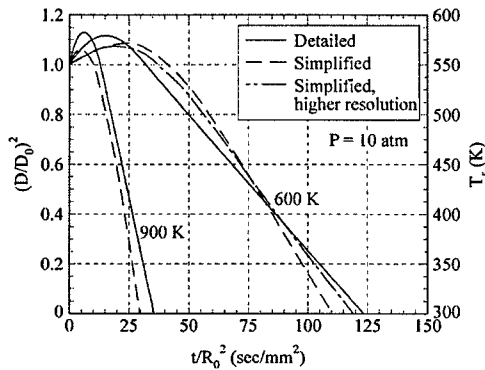
Fig. 2: Size and surface temperatures of n-hexadecane droplets vaporizing in nitrogen.
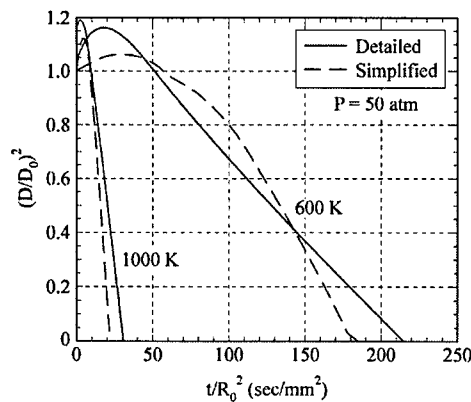
Fig. 3: Size histories of n-hexadecane droplets vaporizing in nitrogen at 50 atm.
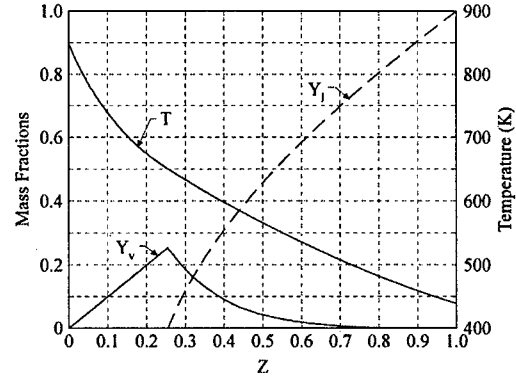
Fig. 4: Vaporization state relationship: T_a=850 K, ρ_a=60 kg/m^3. T_f=438 K: liquid and vapor mass fractions and temperature.
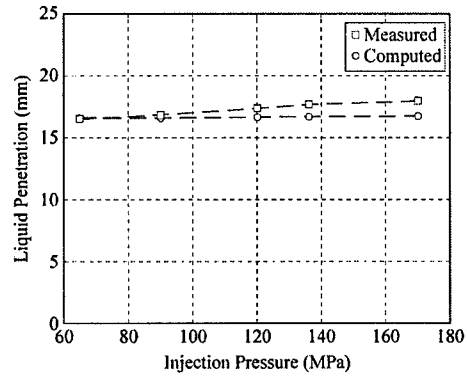
Fig. 5: Liquid penetration vs. injection pressure: ρ_a=30.2 kg/m^3, T_a=1000 K.
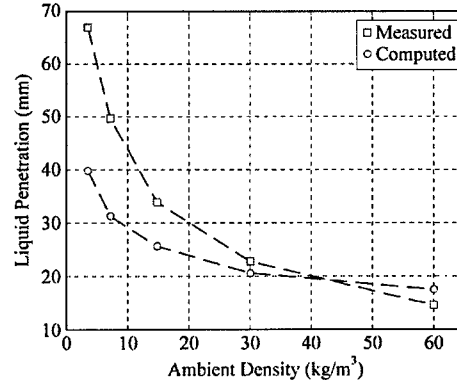
Fig. 6: Liquid penetration vs. ambient density: T_a=850 K, P_{inj}=136 MPa.

19
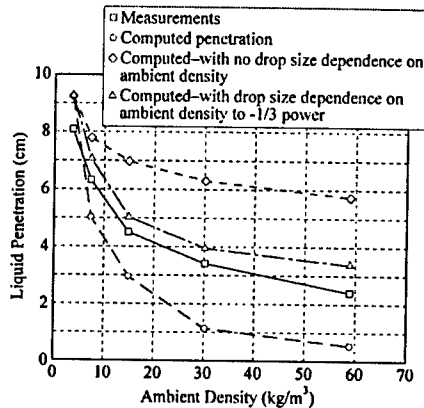
Fig. 7: Effect of ambient density on liquid penetration. d_0=0.246 mm, T_a=700 K, T_f=438 K, U_0=463 m/s.

REFERENCES

1. Abraham, J. and Givler, S.D., "Conditions in which Vaporizing Fuel Drops Reach a Critical State in a Diesel Engine," SAE Paper 1999-01-0511, 1999.

2. Faeth, G.M., "Current Status of Droplet and Liquid Combustion," Prog. Energy Combust. Sci., 3:191-224, 1997.

3. Law, C.K., "Recent Advances in Droplet Vaporization and Combustion," Prog. Energy Combust. Sci., 8:171-201, 1982

4. Sirignano, W.A., "Fuel Droplet Vaporization and Spray Combustion Theory," Prog. Energy Combust. Sci., 9:291-322, 1983

5. Siebers, D.L., "Liquid Phase Fuel Penetration in Diesel Sprays," SAE Paper 980809, 1998.

6. Siebers, D.L., "Scaling Liquid-Phase Fuel Penetration in Diesel Sprays Based on Mixing-Limited Vaporization," SAE Paper 1999-01-0528, 1999.

7. Faeth, G.M., "Mixing, Transport and Combustion in Sprays," Prog. Energy Combust. Sci., 13:293-345, 1987.

8. V. Iyer, S. Post, and J. Abraham, "Is the Liquid Penetration in Diesel Sprays Mixing-Controlled?" accepted for publication at the 28th Symposium (Int'l) on Combustion, August, 2000.

9. Abraham, J., "What is Adequate Resolution in the Numerical Computations of Transient Jets?" SAE Trans., 106:141-155, 1997.

10. Aneja, R. and Abraham, J., "How Far does the Liquid Penetrate in a Diesel Engine: Computed Results vs. Measurements?" Combust. Sci. Tech., 138:233-255, 1998.

11. Post, S. and Abraham, J., "A Computational Study of the Processes that Affect the Steady Liquid Penetration in Full-Cone Diesel Sprays," Combust. Sci. Tech., under review.

MODELING DIESEL ENGINE INJECTOR FLOWS

ARO Contract Number DAAG55-98-1-0318

Stephen D. Heister and Gregory A. Blaisdell

Purdue University School of Aeronautics and Astronautics

1282 Grissom Hall, W. Lafayette, IN 47907

SUMMARY/OVERVIEW:

This project is focused on the study of flows inside diesel injector flow passages with emphasis on resolution of time-dependent cavitation regions within the device. At present, both 2-D and 3-D laminar models exist and have been subject to substantial validation against experimental results. These models have been used to study the injector performance under both cavitating and noncavitating conditions. Effects of cavitation on the orifice exit plane conditions has been characterized for a wide range of inflow conditions.

TECHNICAL DISSCUSSION

We assume an incompressible flow and solve the Navier-Stokes equations on a fixed structured mesh using the Marker and Cell algorithm. Liquid density (ρ_l), the "Bernoulli" velocity in the orifice $v = \sqrt{2(P_1 - P_2)/\rho_l}$, and the orifice diameter (D) are chosen as dimensions. In this case, the two dimensionless parameters which characterize the flow are the Reynolds number (Re) and cavitation number (K):

$$\text{Re} = \frac{\rho_l v D}{\mu_l} \cdots\cdots\cdots K = \frac{P_1 - P_v}{P_1 - P_2}$$

where P_v is the fluid vapor pressure and μ_l is the liquid viscosity. The viscosity in the two-phase mixture is computed as $\mu = \rho\mu_l$ where ρ is the nondimensional mixture density. The mesh employed 140 grid points in the axial direction and 60 points in the radial direction. Recent grid convergence studies have verified that this mesh is adequate to resolve salient flowfield structures[5] for non-cavitating or cavitating flows. Constant pressure boundary conditions are imposed on inflow and outflow boundaries; no-slip conditions are imposed along walls, and symmetry conditions are imposed along the centerline. The two-phase treatment requires a constitutive relation for the pseudo-density, ρ, in order to obtain closure for the governing equations. The current treatment[1] is based on the dynamic response of a monodisperse bubble field to changes in pressure and inertial forces per the Rayleigh-Plesset equation.

The model has had extensive validation on a variety of cavitating flows. Comparisons have been made on experiments conducted in a high aspect ratio cavitating slot flow using a 2-D

approximation for the flowfield. In this case, cavitation lengths[5] and cavitation oscillation frequencies compare well with measurements from Dr. Collicott's research group at Purdue. Figures 1 and 2 provide comparisons of cavitation length and overall extent for measurements made by Henry and Collicott[3]
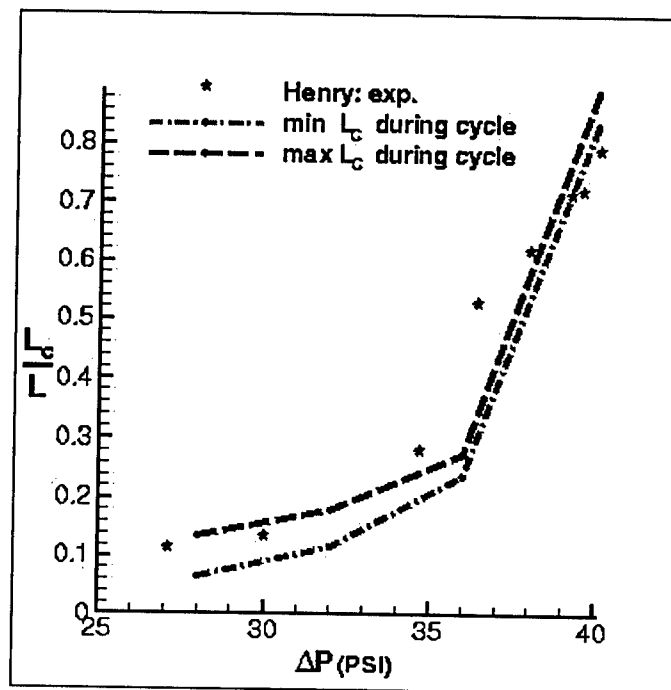
Figure 1 *Comparison of measured and computed cavitation lengths for flow in a high aspect ratio slot. Due to the oscillatory nature of the flow, both maximum and minimum lengths are plotted for the computational results.*

Three-dimensional simulations have also been conducted within the past year. In this case, the crossflow at the entrance to the orifice passage figures prominently in the results. A typical simulation is shown in Figure 3 for a large degree of cavitation (K=1.2). The presence of the crossflow leads to vortices which are shed from the upstream lip of the orifice and interact strongly with the cavitation field. These unsteady vortices also are shown to have profound influence on the exit velocity and presumably on subsequent spray formation processes outside the passage.

Substantial efforts have been made to quantify the unsteady effects inside plain orifice atomizers such as those used in diesel injectors and numerous other applications. The oscillatory collapse/growth/reformation process observed in cavitating flows leads to unsteadiness in the orifice massflow as well. Figure 4 illustrates this issue for a typical cavitating orifice. There are generally two fundamental frequencies obtained by the model; these two modes are apparent in the cavitation length oscillations in Fig. 4. Orifice discharge coefficients also exhibit unsteadiness.

In fact, simulations show unsteady behavior even under noncavitated conditions due to instabilities in the vena-contracta just downstream of the inlet lip. These results point to new fundamental atomization mechanisms which have not been identified previously. Figure 4 provides sample results from these axisymmetric studies. The length of the cavity, Lc, and orifice massflow discharge coefficient, C_D, both oscillate in a quasi-periodic fashion due to

22
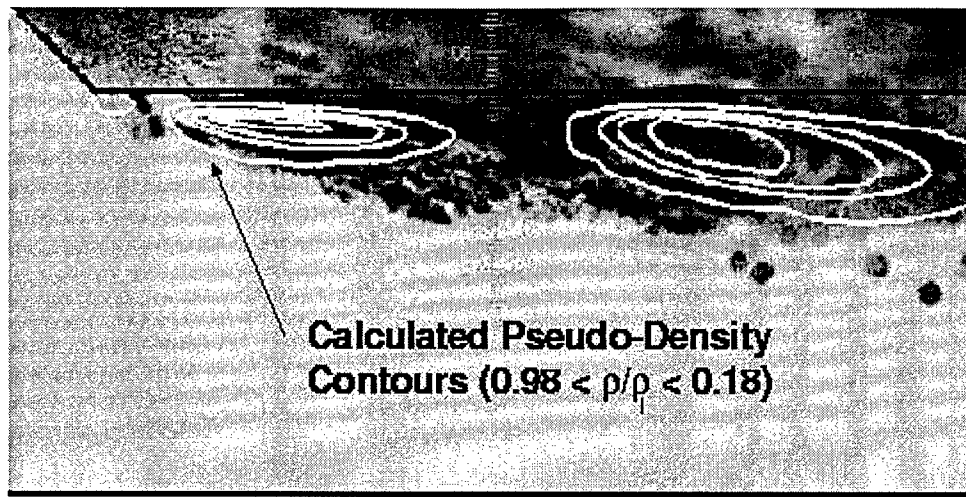
Figure 2 *Side-View overlay of cavitation field and predicted pseudo-density contours. The outermost pseudo-density contour reflects the overall size of the cavitation region as predicted by the model. While the process is inherently unsteady, similar comparisons are obtained at other instants in the quasi-periodic process.*
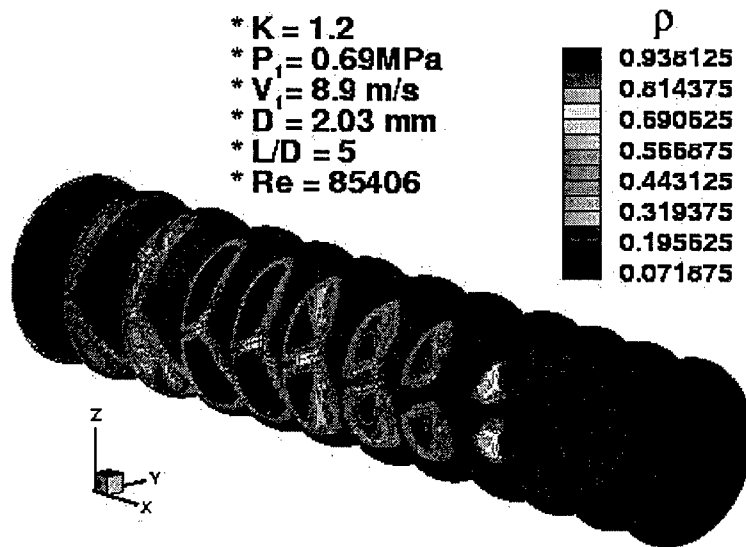
Figure 3 *Pseudo-density contours for an injector with a crossflow at the inlet – a flowfield consistent with diesel and rocket injector flows. Horseshoe vortices are shown to traverse the length of the passage and interact with the cavitation zone.*

instabilities of the vena contracta and the cavitation zone itself. The dimensionless frequencies of oscillation of these parameters are shown on the right-side plot as a function of cavitation number. Here, an f value of unity would correspond to the frequency at which fluid particles traverse the orifice passage at the ideal Bernoulli velocity. Note that the frequencies are nearly identical, indicating massflow oscillations are attributable to instabilities in the vena-contracta. Also, note that even under non-cavitated conditions ($K > 1.58$ in figure) oscillations are still present.
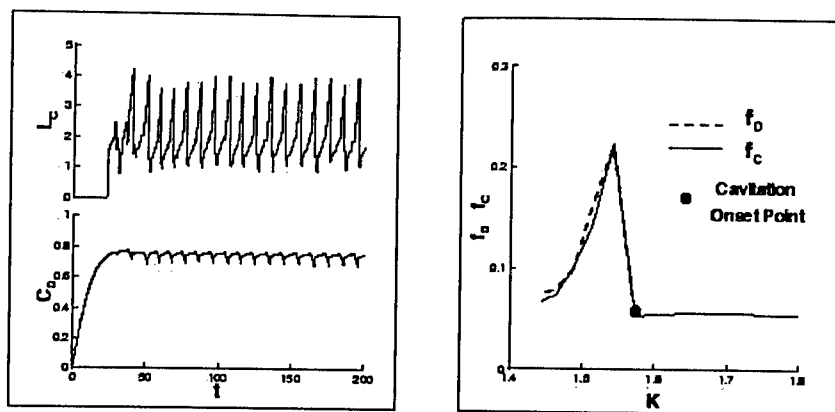
Figure 4 Unsteady behavior in a plain-orifice atomizer with length/diameter ratio of 8. The left-side curves show cavitation length and discharge coefficients as a function of time, while the right-side curves depict oscillation frequency (Strouhal number) for both cavitation and discharge as a function of cavitation number, K.

CURRENT EFFORTS

Current efforts are aimed at adding a turbulence model to existing 2-D and axisymmetric codes in order to assess the influence of turbulence on the injection processes. To this end, a k-omega formulation is being implemented. At the present stage, the model has been validated against single phase flows involving an aft-facing step. At present, validation against cavitation measurements made in Professor Collicott's group is underway. Since turbulence models for single fluid treatments of two-phase flows are largely non-existent, this validation is crucial to the successful implementation of the model. Results should be available for discussion in the contractors meeting in June.

REFERENCES

1. Xu, C., Bunnell, R.A., and Heister, S.D., "On the Influence of Internal Flow Structure on Performance of Plain-Orifice Atomizers," In Press, *Atomization and Sprays*.

2. Bunnell, R.A. and Heister, S.D., "Three-Dimensional Unsteady Simulation of Cavitating Flows in Injector Passages," In Review, *J. Fluids Engineering*.

3. Henry, M. and Collicott, S.H., "Visualization of Cavitating Slot Flow", To Appear, *Atomization and Sprays*.

4. Chen, Y. and Heister, S.D., "Modeling Hydrodynamic Non-Equilibrium in Bubbly and Cavitating Flows", J. Fluids Engineering, V118, 172-178, 1995.

5. Bunnell, R.A., Heister, S.D., Yen, C., and Collicott, S.H., "Cavitating Injector Flows: Validation of Numerical Models and Simulations of High-Pressure Injectors", To Appear, Atomization and Sprays, 2000.

Internally Mixed Fuel Injectors and Two-Phase Flow Modeling

Grant Number DAAH04-96-1-0008

Principal Investigators: J. Seitzman, M. Allen, M. Brooke, A. Glezer, W. Haddad, J. Jagoda, S. Menon, Y. Neumeier, J. Prasad, L. Sankar, B. Zinn

Georgia Institute of Technology
Schools of Aerospace, Electrical and Computer, and Mechanical Engineering
Atlanta, GA 30332-0150

SUMMARY/OVERVIEW:

This program focuses on the fundamental and practical issues that hinder development of intelligent control systems for improving the performance of turbine engines, such as rotorcraft turboshaft engines. Our approach to the development of an intelligent control system hinges on advances in the basic understanding of engine processes through experiments and advanced computational models, refinement of appropriate sensor and actuator technologies, and development of practical control strategies for control of steady-state and transient performance. Here, we report on recent theoretical and experimental advances in the development of a low air flow rate, internally mixed liquid fuel injector capable of producing controllable droplet sizes under a wide range of operating conditions. In addition, we report on recent advances in the development of efficient large eddy simulations (LES) tools for accurate two-phase, turbulent flow simulations. The improved LES tools include two-phase subgrid models and bidirectional turbulent coupling between the gas and the liquid droplets.

TECHNICAL DISCUSSION:

Internally Mixed Fuel Injector (PI: Neumeier/Zinn)

An internally mixed atomizer involves a two-phase flow of liquid and atomizing air through the injector's flow passage. The liquid flow interacts with the atomizing air inside the injector, resulting in the formation of liquid droplets. Two processes are primarily responsible for inducing atomization in these injectors. First, as both the liquid and the air share the same flow passage inside the injector, the liquid is restricted to a smaller available area. This reduction in flow area accelerates the liquid and, thus, increases its kinetic energy, which induces fine atomization. Second, the relative motion between gaseous and liquid phases produces a shear force at their interface. This force strips liquid droplets from the liquid filaments, resulting in the formation of a mixture consisting of liquid, air and liquid droplets inside the injector. This mixture produces a fine spray when it emerges from the injector. There are two parameters that control the flow rate of the liquid emerging from the injector and the size of the droplets produced by the injector: 1) the flow rate of the atomizing air, and 2) the supply pressure of the liquid. It has been shown in our previous reports that the liquid flow rate and the size of the droplets can be varied independently by changing the air flow rate and liquid supply pressure simultaneously.

A theoretical model has been developed to model the two-phase flow of liquid and air through the injector's flow passage and the atomization of the liquid into droplets. The developed model assumes one-dimensional (uniform) and steady flow of both phases, and neglects wall friction. The liquid flow is assumed to be isothermal and incompressible, while the air is assumed to behave as a perfect gas. The liquid column entering the injector is assumed to break up into droplets when its Weber number reaches a critical value of 10. These droplets continue to break up into smaller droplets as they are accelerated inside the injector by the expanding air. The

model consists of the basic conservation equations, e.g., liquid mass conservation, gas mass conservation, a combined momentum conservation for air and liquid, a combined energy conservation, and a separate conservation of energy for the liquid phase. This choice of equations ensures that the interactive term between the phases, which is modeled as a drag force acting on the liquid due to the relative velocity between liquid and air, is isolated and appears in only the energy equation for the liquid. The governing equations are solved along with the appropriate boundary conditions, which ensure that the pressure at the injector's exit matches the back pressure or the air flow is continuous at the exit.
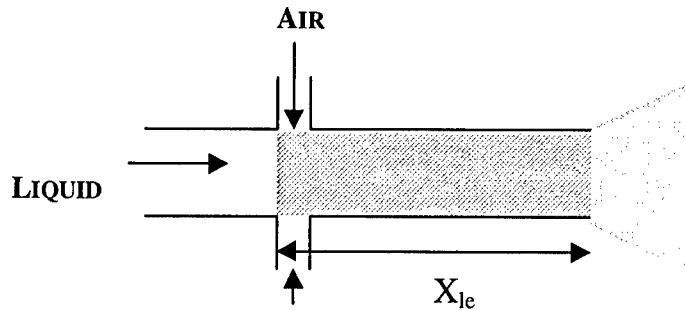
Figure 1. Schematic of the internally mixed atomizer.

In order to further understand the operation of an internally mixed atomizer, the effect of injector geometry on the performance of the injector was investigated experimentally and the results were compared with the results predicted by the theory to validate the developed model. A schematic of the injectors tested in this study is shown in Fig. 1. Liquid passes through the central tube that is 1.19 mm in diameter. Air is radially injected into the liquid flow through four, 0.35 mm diameter, holes upstream of the injector's exit. The two injectors (designated 1 and 2) investigated in this study differed only in their length (X_{le}=0.015 and 0.005 mm, respectively). The droplet sizes were measured 2.5 in. downstream from the injector exit using a PDPA. The liquid and air flow rates and supply pressures were measured just before their introduction into the injector. The liquid supply was maintained at a pressure of 20 psi.

Figure 2 shows the dependence of liquid flow rate on ALR for the two injectors. For both, the liquid flow rate decreases with an increase in ALR, This results from an increase in pressure inside the injector due to the higher air flow rate. The liquid flow rate increases with a decrease in the injector's length, which can be attributed to reduced forces compared to a longer injector. The theory also predicts the same trend in liquid flow rate. Furthermore, the theoretical predictions match quite well with the measured values. The droplet size decreases with increase in ALR due to a reduction in wetted area inside the injector and increased shear, as shown in Fig. 3. Furthermore, a decrease in injector's length causes an increase in the mean droplet diameter (SMD) beyond a certain ALR and the same trend is visible in theoretical predictions. Since the droplets were measured at a distance downstream from the injector's exit (PDPA cannot measure dense sprays) and the theoretical predictions were made at the exit of the injector, there are discrepancies between the magnitudes of measured values and the predictions. Also, the assumption of uniform liquid flow imposes a condition of mono-sized droplets, which is not true in reality.
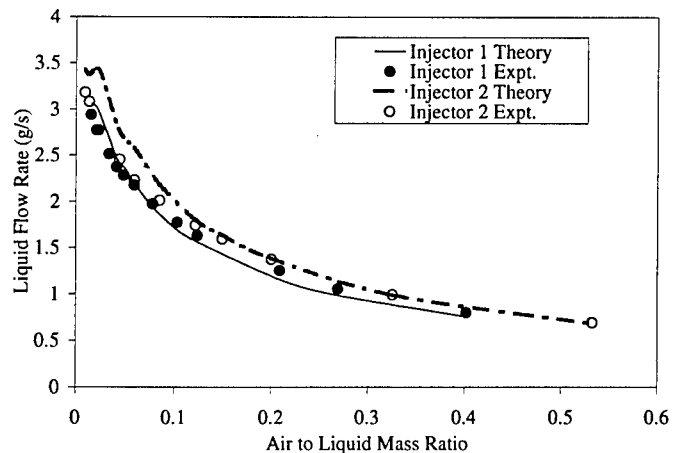
Figure 2. Dependence of liquid flow rate on mass air-liquid ratio (ALR) for the injectors of different length.

26

The model does not take into account the effect of turbulence in atomization, which is another potential source of error. But, this model, which is based on first principals, is reasonably accurate and can be used for first order engineering approximation of the performance of an internally mixed atomizer.

Two-Phase LES (PI: Menon)

A large-eddy simulation (LES) model for two-phase, turbulent reacting flows has been developed using a new subgrid-based scalar mixing and combustion model. The

Figure 3. Dependence of droplet SMD on ALR for the different length injectors.

unique feature of the model is that scalar mixing and the reaction-diffusion processes in the sub-grid domain are simulated inside every LES cell. Earlier studies under this MURI validated and demonstrated the method's ability to accurately capture Le, Sc, Re, Ka and Da number effects without requiring any explicit or *ad hoc* adjustments to the model. More recently, this LES model has been used to simulate liquid-gas flows, with the gas phase simulated using the Eulerian method while the droplets are tracked using a Lagrangian model. Only droplets up to a pre-specified cutoff size are tracked; droplets below the cutoff are included in a new Eulerian two-phase subgrid model. This approach captures the final stages of mixing more accurately than conventional models, where droplets below the cutoff are assumed to instantaneously vaporize and mix.

Additional validation of the two-phase LES model has been carried out by simulating stochastically forced, high-Re isotropic turbulence and spatial mixing layers. LES and DNS studies were carried out. DNS is carried out using a 128^3 grid for a stationary $Re_\Box$ of 62. The number of particles used are 32^3. LES is carried out using the same conditions but using a resolution of 64^3. Comparison with and without coupling between the two phases showed that the presence of droplets results in turbulence modulation and increases both the kinetic energy and its dissipation. Good agreement between LES and DNS was obtained in these studies and is shown in Fig. 4.

The effect of vaporization was also studied. Initially, there is a rapid accumulation of energy in the small scales, and a corresponding increase in dissipation. This state is followed by intermediate states tending to the baseline case of isotropic turbulence with momentum-coupled droplets. This suggests that droplets vaporize at a faster rate, when the temperature of the droplets is higher and there is constant heat transfer from the gas-phase. With time, the gas-phase loses energy and has more concentration of the fuel in the gas-phase. These two factors reduce the heat and mass transfer rates. This equilibration might not occur in flows with inflow/outflow conditions and where there is high mass and heat transfer between the phases.
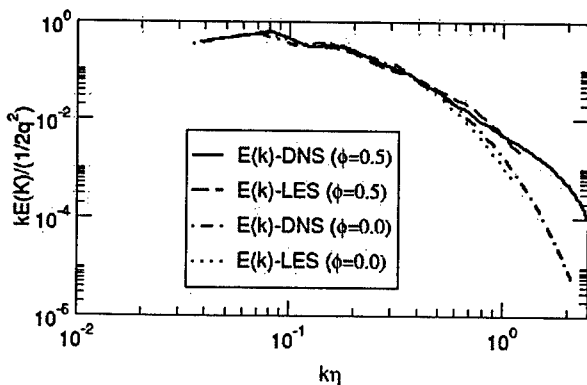
Figure 4. Isotropic turbulence spectra showing LES/DNS comparison with and without particles; note the increase in the energy at the small scales.
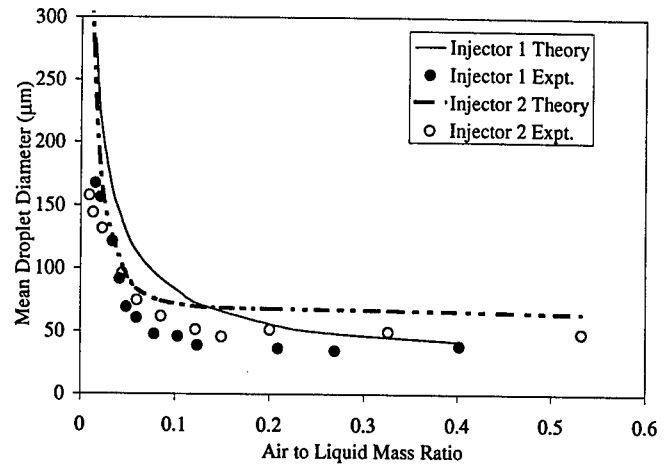
27
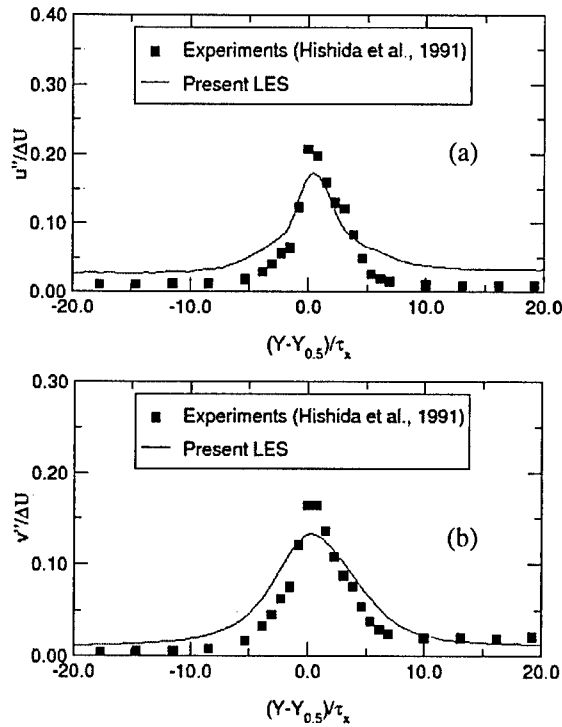
Figure 5. Gas-phase fluctuating velocity profiles at x=100 mm: (a) u_{rms}, (b) v_{rms}.
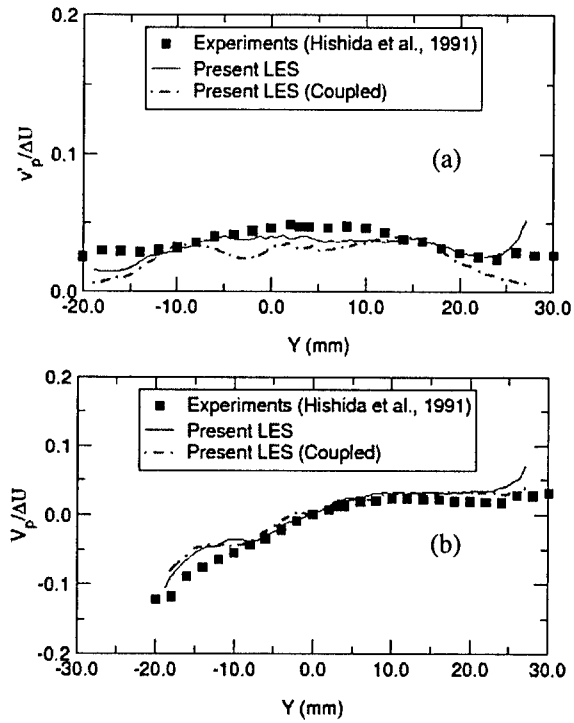
Figure 6. Particle phase velocity profiles at x=200mm for 42 μm droplets: (a) v_{rms}, (b) v_{mean}.

To validate the LES model, comparison with experiments by Hishida *et al.* (1991) for non-vaporizing droplet dispersion in a spatially evolving mixing layer was performed. Here, the spatial mixing layer was simulated using an incompressible code with a resolution of 197×197×5. Three different particle sizes used in the experiments (42, 72, and 135□m) were tracked. The boundary layer on the 1.17 mm thick splitter plate was resolved, and the entire 600mm long flow field was captured. In the experiments, the particles were injected at the end of the splitter plate. Since the present implementation currently works only for dilute sprays, the particles in the simulation were injected 100 mm downstream, where the evolution of the simulated mixing layer is very close to that of the experiments. This can be seen from the u_{rms} and v_{rms} gas velocities (Fig. 5). The particle velocities were based on the mean and fluctuating quantities, assuming that the fluctuations are Gaussian. On average, 15,000-20,000 particle groups were simulated after steady-state was achieved. Figure 6 shows mean and rms particle v-velocities for both uncoupled and coupled cases at x=200mm for the 42μm particles. Reasonable agreement between the experiments is obtained, and as expected, the coupled case gives slightly better agreement.

Finally, Fig. 7 illustrates the droplet distribution in the mixing layer. As observed in the temporal mixing layer simulations, the particles with Stokes Number (St) near 1 disperse the most. This can be clearly seen in Fig. 7, where the particles disperse throughout the mixing layer. The initial region downstream of the particle injection is reasonably void of large scale vortical structures. The instabilities become visible further downstream where the fundamental mode dominates resulting in formation of strong vortical structures. Further downstream the growth of the subharmonic mode results in pairing of adjacent vortices. The particles of St~1 respond to the centrifugal forces the most, leading to their concentration in the regions of low vorticity.
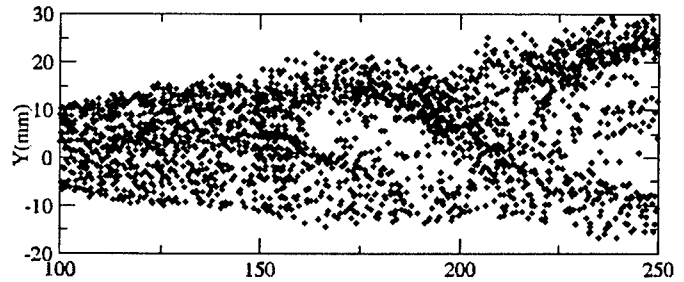
Figure 7. Shear layer droplet distribution (42 μm case).

28

FLUORESCENT DIAGNOSTICS AND FUNDAMENTAL APPROACHES TO DROPLET, SPRAY, ENGINE, AND AERODYNAMIC BEHAVIOR

ARO Contract DAAG55-97-1-0265

Principal Investigator(s):

Lynn A. Melton[a] and John Stufflebeam[b]

[a]Department of Chemistry
University of Texas at Dallas
Richardson, TX 75083-0688

[b]United Technologies Research Center
East Hartford, CT 06108

SUMMARY/OVERVIEW

Both UT-Dallas (UTD) and United Technologies Research Center (UTRC) have carried out experiments to investigate the shear field in liquid fuel sheets, ligaments and droplets by non-intrusive, optical techniques. The program at UTD emphasizes the development of fluorescent dopants whose fluorescence changes in response to shear within the liquid; these diagnostics should be appropriate for PLIF measurements. The program at UTRC utilizes birefringence, induced by liquid strain rate, on specially seeded fuels. Fringe patterns produced by interference of the light beams enable quantitative measures of the strain rate; these diagnostics should be appropriate for line-of-sight measurements. The data obtained with these shear diagnostics should provide information that is applicable to physics-based modeling efforts of primary atomization processes.

TECHNICAL DISCUSSION

AT UTD

The search for shear sensitive fluorescent molecules has focussed on polymers labeled with fluorescent tags, specifically polyacrylic acid (PAA) with covalently attached pyrene moities. PAA molecules of molecular weight greater than 500,000 are sufficiently large that the modest shear fields available with the shear apparatus (1-1000 sec^{-1}) can induce detectable changes in the polymer conformation. Modest shifts in the pyrene excimer to monomer emission ratio have been observed in pyrene labelled PAA at shear rates of approximately 1000 sec^{-1}.

PAA of sufficient molecular weight is known to show shear thinning behavior, i.e., the viscosity of PAA solutions decreases with increasing shear. The viscosity of PAA solutions is pH dependent. At low pH the carboxy groups are protonated, the molecule is electrically neutral and forms random coils, and the viscosity of PAA solutions are higher. At pH >5, the carboxy

groups are ionized, the molecule has numerous negative charges and, because of electrical repulsion, assumes more linear conformations, and the viscosity of the PAA solutions is lower. Thus, shear forces should drive random coil PAA molecules toward more nearly linear conformations. The pyrene moities should move apart and a reduction in pyrene excimer formation should be expected.

Professor F. Winnik (McMaster University) has synthesized pyrene labelled PAA and used the excimer/monomer fluorescence to characterize the pH dependent conformational changes. She has provided samples of labeled and unlabeled PAA, and the sensitivity of these samples to shear has been tested at UTD. Shear thinning is readily measured in PAA samples with molecular weight 500,000, but it was not detectable with the Winnik samples (molecular weight 150,000. Even so, in fluorescence tests of the Winnik samples, the excimer to monomer fluorescence ratio under shear of approximately 1000 sec^{-1} was approximately 5% higher than the ratio at zero shear. One potential conclusion is that the pyrene fluorescence is a more sensitive detector of shear than viscosity. However, tests with pyrene labeled PAA at a series of molecular weights would be required to confirm this or other hypotheses, and such samples were not available. Further work would also be required to understand why the excimer to monomer intensity ratio increases, rather than decreases, with increasing shear.

AT UTRC

Shear-induced birefringence is under investigation at a tool for study of the stress/strain rate in spray/break up ligaments.

A fluid (hexane) is seeded with optically-anisotropic polymer molecules (polyisobutylene), and when the fluid is subjected to flow, ambient stresses orient and/or distort the molecules. The resulting anisotropy of the molecules will impart a bulk birefringence to the fluid. This shear-induced birefringence creates a dependence of index-of-refraction on the polarization orientation of transmitted light, and the effect may be detected using standard polarimetry techiques. UTRC has developed a modified polarimetry apparatus which is based on a 2-D flow cell and which allows time resolved images to be obtained.

A useful approximation of flow-birefringent behavior is the linear *stress-optical rule*

$$n = n_0 I + C (t + p I)$$

t = stress tensor
n = index-of-refraction tensor
I = identity tensor
C = *stress-optical coefficient*

For light propagating in z direction, the local birefringence Δn is related to shear stress component τ_{xy} and normal stress components τ_{xx} and τ_{yy} by

$$\Delta n = C \sqrt{(\tau_{xx} - \tau_{yy})^2 + 4\tau_{xy}^2}$$

The shear stress τ_{xy} is related to strain rate by viscosity μ

Light propagating through a fixed thickness *d* of birefringence Δ*n* experiences a *retardation* Images are acquired under four different polarization states of probe beam

$$\delta = \text{retardation} = \frac{2\pi d \Delta n}{\lambda}$$

Polarization Orientation	Beam Helicity
0°	+
0°	-
45°	+
45°	-

These four plus four background images are combined to produce a complete image of retardation field.

Data was taken when the flow-cell was filled with fluid but the jet was not turned on. In this way, any birefringence in the glass can be distinguished from birefringence due to stresses in the jet flow. The data taken when the flow is off does indicate some birefringence in the glass, mostly near the nozzle exit.

The data taken when the flow is on indicates that birefringence is present in the region of the jet. The phase-retardation of the transmitted light ranges from 0 to 4 degrees. The thickness through which the probe beam passes is 12.7 mm, and the wavelength is 488 nm. The observed birefringence, or difference between indices of refraction for orthogonal polarizations, therefore ranges from 0 to 4.3 x 10-7.

The field of view included a region up to 2 nozzle-diameters on either side of the nozzle exit and up to 9 nozzle-diameters downstream. Birefringence wass evident throughout this region, following the direction of the jet and maintaining its intensity throughout this region. This data agrees qualitatively with observations made in earlier data-sets, when the jet was made to strike a wall placed several diameters downstream of the jet exit. This free jet should be more susceptible to comparison with analytical models. This comparison is underway and will lead to further understanding of how the observed birefringence corresponds to levels of stress in the flow.

Probe beam:
Collimated, expanded
laser beam
(Ar+ Laser,
488 nm)

Polarizer 1

Quarter Wave
Plate

Fluid Flow Cell
containing 2-dimensional
free jet

Polarizer 2 (rotated 90
deg. to Polarizer 1)

Screen

Fluid Pump

CCD Video
Camera

1.5 mm.

Jet Flow

3.9 mm.

Jet Exit 0.4 mm wide

Flow Off

Flow On
Avg Jet Speed 5 m/s

4
3.5
3
2.5
2
1.5
1
0.5
0

TITLE: AERATED-LIQUID INJECTION INTO A SUPERSONIC CROSS-FLOW

AFOSR TASK 2308BW

Principal Investigators: Thomas A. Jackson
                             Mark R. Gruber

Propulsion Sciences and Advanced Concepts Division
Propulsion Directorate
Air Force Research Laboratory
Wright-Patterson AFB OH 45433

SUMMARY/OVERVIEW

Injection of a heavy hydrocarbon fuel into the combustor of a high-speed propulsion engine such as a scramjet is complicated by the use of that same fuel in structural cooling. Variations in the fuel phase and composition are expected in managing the engine's thermal loads at flight Mach numbers above 4. Perhaps the most challenging of the injection problems is that of liquid fuel during the ignition of the scramjet. This follows the boost phase of flight in which a second propulsion cycle accelerates the system through the lower Mach numbers. Aerating the fuel during injection has been effective in penetrating the core flow from a flush-wall injector, and in accelerating the atomization of the liquid to support combustion in the high-speed cross-flow. More recent studies have focused on the effect of the boundary layer near the injector, and on the influence of a core flow shock system on the injector. These aspects are the focus of this discussion.

TECHNICAL DISCUSSION

At a sufficiently high gas-to-liquid mass ratio the mixed flow through a fuel injector is postulated to have characteristics depicted in Figure 1. Consistent with the modeling approach of Santangelo and Sojka[1], gas and liquid co-flow though the injector orifice with the liquid residing in the annulus formed between the gaseous central core and the walls of the injector passage. Injection of the mixture into a supersonic free stream induces a bow shock that may locally separate the boundary layer. Penetration height of the injectant into the free stream, the effectiveness of the atomization process, and the distribution of atomized fuel from the wall to the point of maximum penetration are parameters of interest.
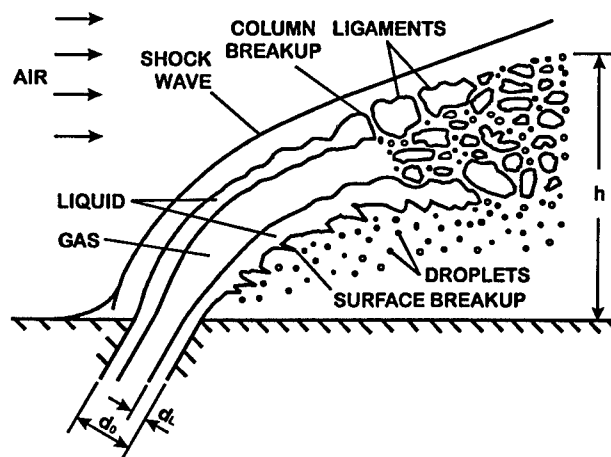
Figure 1. Angled aerated liquid jet in supersonic cross-flow

In initial studies we evaluated the behavior of the liquid or aerated-liquid injected normal to a high-speed cross-flow. For the simple liquid, the measured spray penetration height correlates with

$$h_0 / d_0 = 8.4 \, q_0^{0.44}$$

where d and q are the injector diameter and jet-to-freestream momentum flux ratio, respectively, and the subscript "o" denotes the liquid-only case.[2] The form of the expression is the same as that in Kush and Schetz;[3] the coefficient and exponent vary slightly from Kush and Schetz and from our earlier studies conducted in a different flow facility.[4] We believe the thickness of the local boundary layer relative to d_0 is an important factor in the jet's ability to penetrate the free stream. This is not a parameter in the existing correlations and must be the subject of further study.

The penetration height for the aerated liquid is given by a modification of the above expression, accounting for the liquid-gas co-flow and for the angle at which the injector is inclined from the direction of free stream flow.

$$\frac{h}{d_0 q_0^{0.44}} = 8.4 \left(1 + k^2 \, \frac{\rho_G}{\rho_L} \right)^{0.44} \left(\frac{\beta + k\,(1 - \beta\,)}{k\,(1 - \beta\,)} \right)^{0.38} \sin(\,\theta\,)$$

The coefficient k is the ratio of gas-to-liquid velocity within the injector tip and β is the void fraction in terms of the volumetric flow rates of gas and liquid:

$$\beta = Q_G / (Q_G + Q_L)$$

As the level of aeration increases from zero (pure liquid injection), the spray behavior is bi-modal, oscillating between slug-flow and aerated. Above a critical value of β the injectant transitions to steady, aerated flow. Further increases in the void fraction result in a monotonic increase in penetration height.

As noted above, our aerated-flow studies have taken place in two supersonic flow tunnels. Differences in the predicted behavior of the injectant in these environments suggest that the free stream momentum deficit within the boundary layer enables increased penetration of the jet within thicker boundary layers. The influence of the boundary layer on jet penetration is also evident in studies of angled aerated jets. Figure 2 depicts the measured penetration of a liquid into a Mach 1.9 cross-flow. The injector is inclined at 60 and then 30 degrees to the tunnel floor. The prediction of penetration height (dotted line) is made using the relationship deduced for 90° injection, modified by the injection angle. The flow approaching the injectors is the same for both cases. At 60° the prediction is very effective; at 30° the prediction substantially under predicts penetration of the jet.

A similar result is observed when the liquid is aerated. However, the analyses of these cases are complicated by design of the injector tip used in the angled injection studies. In our initial work on normal injection, the L/d_0 of the injector tip was small. In preparing the injectors for this more recent study, the L/d_0 was increased by a factor of 10. In formulating the model to predict penetration height for an aerated liquid, the gas and liquid velocities were assumed equal for the short L/d_0 tip. The prediction was effective for the early 90° injection studies. With a larger L/d_0 tip the assumption of equal gas and liquid velocities through the nozzle is not well founded. The flow within the nozzle tip has adequate length to become fully developed in the cases with the
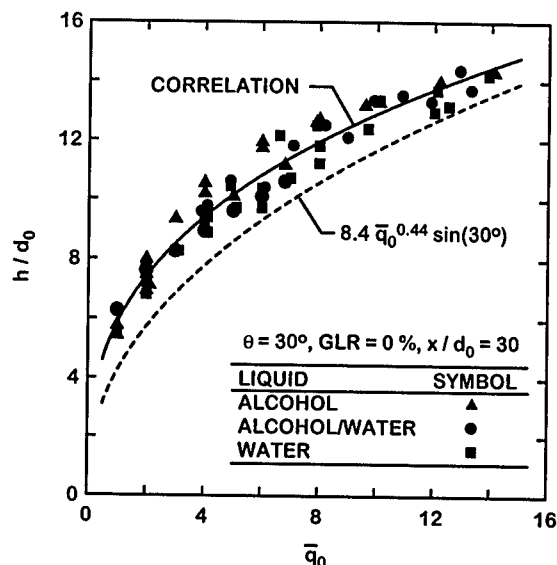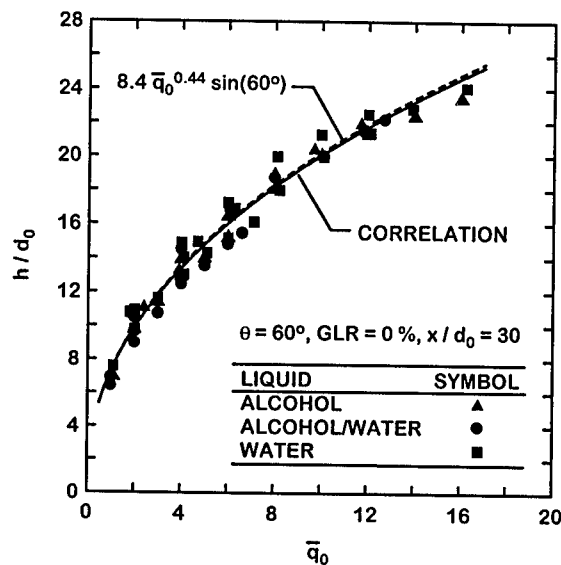
Figure 2 Spray penetration height for liquid jets: (a) 60° injector; (b) 30° injector.

larger L/d_0 tip. The slip velocity between the two phases can not be ignored. Figure 3 depicts the current data set for aerated, normal injection and overlays the prediction derived from the assumption of equal gas and liquid velocities. The off-set is significant. Additional analysis suggests the gas velocity through the injector tip is as high as ten times that of the liquid flow for the range of conditions studied.

Injection into a supersonic flow induces a bow shock in the vicinity of the injector. Heat release in the dual-mode scramjet combustor, however, back-pressures the flow and induces a much stronger shock system throughout the free stream. The influence of this shock system on the fuel penetration and fuel distribution in the near field behind the injector is critical to the stability of the scramjet. To evaluate this influence, a series of experiments was conducted in a Mach 1.94 tunnel.[5] In this facility the flow can be throttled with a valve to simulate the flow restriction induced by heat release. A single flush-wall injector, angled at 60° to the tunnel floor, was used to inject either simple liquids or aerated liquids. Initially the cross-flow is supersonic with only small disturbances in the flow apparent in the shadowgraphs. The back-pressure valve is gradually closed, establishing the free-stream shock system. Figure 4 shows a series of shadowgraph images during injection of an aerated liquid as the back-pressure is increased. The first image is of the flow with low back-pressure. The free stream is supersonic and the injection stream induces a weak bow shock. As the back-pressure increases a shock system begins to form (Figure 4b). At higher levels of back-pressure the leading edge of the shock system moves forward. The position of the free-stream shock system relative to the point of injection dramati-
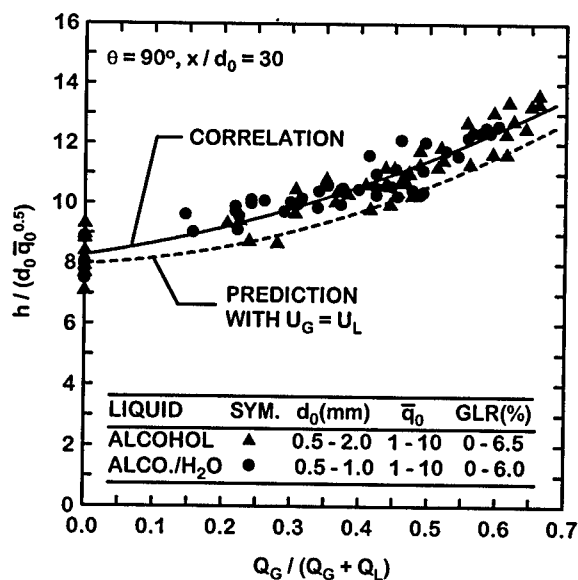
Figure 3 Normal injection; M = 1.94 cross-flow; injector L/d_0 =20.

cally affects the injector penetration and large-scale mixing.

Preliminary conclusions of the recent work on the behavior of an aerated-liquid jet in a high-speed cross-flow are:

(1) For a nozzle with a short L/d_0 tip, the gas and liquid velocities are essentially equal when the phases are stratified and co-flowing. In the fully developed flows of the high L/d_0 tips, the mean velocities of the two phases are very different.

(2) With the short L/d_0 there is a critical value for the gas-to-liquid mass ratio above which the flow is steady and aerated; below this value the flow is bi-modal, oscillating between slug flow and fully aerated. In a high L/d_0 nozzle this critical value is not evident.

(3) The local boundary layer affects the injectant penetration height. This is especially significant when the injector is at a low angle of inclination to the flow direction.

(4) The free-stream shock structure significantly affects the fuel penetration and near-field fuel distribution.

Quantitation of the influences of boundary layer thickness and the proximity and strength of the free-steam shock system on the injector behavior continues.

(a) No imposed back-pressure

References:

1. Santangelo, P.J. and Sojka, P.E., "A holographic investigation of the near-nozzle structure of an effervescent atomizer-produced spray," *Atomization and Sprays*, Vol 5, 1995, pp. 137-155.
2. Lin, K.-C., Kennedy, P.J., and Jackson, T.A., "Spray penetration heights of angle-injected aerated liquid jets in supersonic crossflows," AIAA Paper 00-0194, January 2000.
3. Kush, E.A. and Schetz, J.A., "Liquid jet injection into a supersonic flow," *AIAA Journal*, Vol. 11, No. 9, 1973, pp. 1223-1224.
4. Lin, K.-C., Kirkendall, K.A., Kennedy, P.J., and Jackson, T.A., "Spray structures of aerated liquid fuel jets in supersonic crossflows," AIAA Paper 99-2374, June 1999.
5. Lin, K.-C., Kennedy, P.J., and Jackson, T.A., "Structures of aerated liquid fuel jets interacting with a shock train in supersonic crossflows," Eighth International Conference on Liquid Atomization and Spray Systems, July 2000.

(b) Back-pressure of 100 kPa

(c) Back-pressure of 103 kPa

Figure 4 Shadowgraphs of an aerated-liquid jet interacting with a shock train. 2% by mass air in water as injectant, 60° to flow.

SUB- AND SUPER-CRITICAL EVAPORATION AND COMBUSTION OF A MOVING DROPLET

Principal Investigator: George Gogos

University of Nebraska-Lincoln
303 Canfield Administration Bldg
Lincoln, NE 68588-2618

SUMMARY/OVERVIEW:

A comprehensive computational study of fuel droplet evaporation and combustion in sub- and super-critical ambient conditions under forced convection is being conducted. The aim is to provide basic understanding and prediction of evaporation and combustion of moving droplets at elevated pressures. Results obtained are of great interest for major industrial applications (such as diesel engines, high-output combustors for aircraft jet engines and liquid-fueled rocket engines).

TECHNICAL DISCUSSION:

Two aspects of droplet evaporation/combustion have been studied during the past 12-month period. First, an experimentally validated model for a moving spherical droplet that undergoes evaporation has been developed. The model is used to predict evaporation constants and droplet lifetimes over a wide range of ambient pressures. Future work will allow for droplet deformation, which becomes important due to reduction in surface tension at elevated pressures. Second, a low pressure, experimentally validated model for a moving spherical droplet that undergoes combustion has been developed. This model employs a one-step overall reaction and is used to predict extinction velocities for different size droplets. In future work, semi-detailed chemical kinetics will be incorporated in the present model.

Results presented in Fig. 1 were calculated for a moving n-heptane droplet evaporating within a nitrogen environment. The initial diameter is 100 μm and the initial temperature is 300 K. Fig. 1a shows the droplet average evaporation constant as a function of ambient pressure for different initial droplet velocities. Here, the droplet average evaporation constant is defined as the average evaporation constant when the dimensionless droplet diameter squared is less than 0.5. The average evaporation constant increases almost linearly with ambient pressure. At an ambient pressure which is a few times the thermodynamic critical pressure of the fuel, the slope of the average evaporation constant changes sharply, leading to a weak linear variation with further increase in the ambient pressure. With increasing initial droplet velocity, the above change in slope occurs at higher ambient pressures. Simulations with initial velocities of 5.0 m/s were obtained for ambient pressures smaller than 4 MPa. For higher pressures the criterion for droplet sphericity is not valid and droplet deformation needs to be considered. The velocities considered in Fig. 1a are relatively small compared to actual velocities in a typical spray. It can then be concluded that in an actual spray, especially at elevated pressures, droplets experience significant deformation that can not be neglected. The decrease in surface tension with increasing ambient pressure leads to

significant droplet deformation. Fig. 1b shows the droplet lifetime as a function of ambient reduced pressure for four different initial droplet velocities. The droplet lifetime decreases with increasing ambient pressure or increasing initial droplet velocity.

Results are presented in Fig. 2 for extinction velocities for n-heptane droplets burning in air at room temperature and a pressure of 1 atm. Droplet diameter (d) is varied to determine its effect on extinction velocity $(U_{\infty,e})$. Spalding (1953) and Agoston et al. (1957) conducted porous sphere experiments employing kerosene and n-butyl alcohol, respectively. Both studies show that the extinction velocity varies linearly with diameter. The present numerical model (solid line) predicts this linear dependence for approximately d > 2 mm. Large activation temperature asymptotics by Wu et al. (1982) also predict this linear dependence. The magnitudes of the measured extinction velocities by Spalding and Agoston et al., however, differ from the present model predictions possibly because the fuels are different. Buoyancy effects are negligible for the size of porous spheres employed by Spalding and Agoston et al. due to the small Richardson number (~ 0.05). Gollahalli and Brzustowski (1975) employed the same fuel (n-heptane) as in the present simulations. The buoyancy-induced flow in their experiment aids the forced convection flow. Fig. 2 shows that the extinction velocity corrected for the presence of natural convection lies very close to the numerical prediction for the same fuel. In addition, Fig. 2 shows that for diameters in the range of 180 μm – 1000 μm, the present numerical model predicts that the extinction velocity exhibits a nonlinear dependence. Extrapolating the linear curve predicted for larger droplets may provide an erroneous value for extinction velocities of droplets of, say, 100 μm, which are encountered in a typical spray.
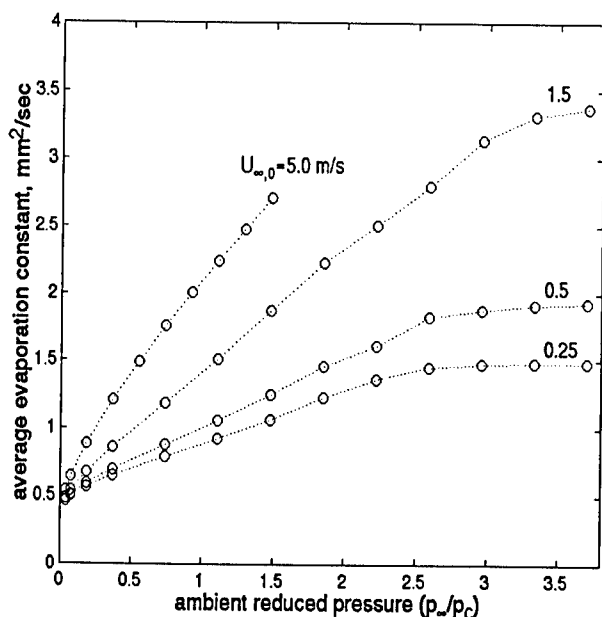
Fig. 1a. Average evaporation constant with ambient pressure for different initial droplet velocities (p_c =2.74 MPa).
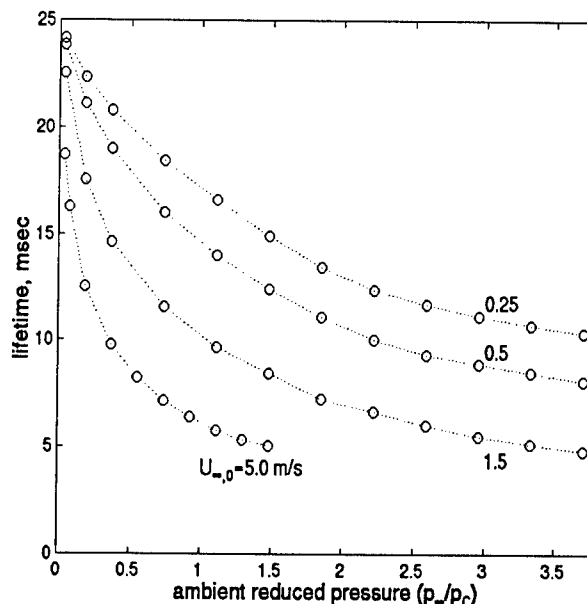
Fig. 1b. Droplet lifetime with ambient pressure for different initial droplet velocities (p_c =2.74 MPa).
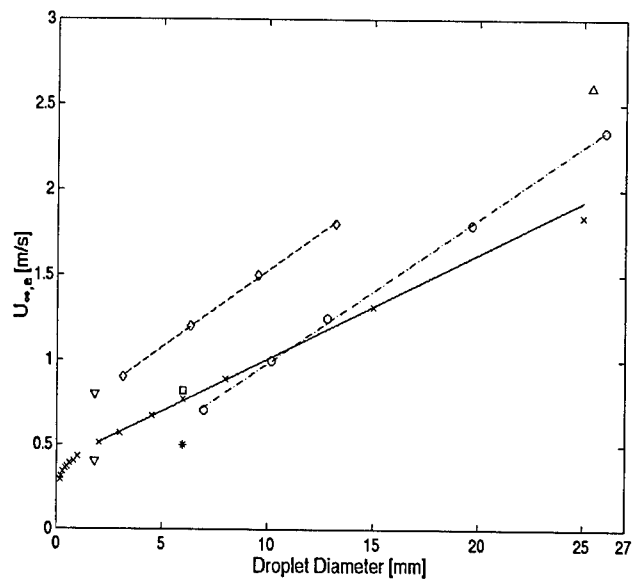
Fig. 2. Extinction velocity vs. droplet diameter: (x) - numerical predictions for n-heptane under zero-gravity (T_∞= 300 K and p_∞= 1 atm). Experimental data under normal-gravity for various fuels in air at "room" temperature and atmospheric pressure; (o) - kerosene (Spalding, 1953), (н) - n-butyl alcohol (Agoston et al., 1952), (*) - n-heptane (Gollahalli and Brzustowski, 1975), ( ) - previous point corrected for natural convection, (∇) - gasoline (Agafonova et al. 1960, lower: aiding natural convection, upper: opposing natural convection), (Δ) - n-heptane (Gore et al., 1990)

STUDY OF THE SUB- AND SUPERCRITICAL BEHAVIOR
OF FUEL DROPLETS AND JETS

Contract No. F49620-98-1-0373

Principal Investigator: Yaw D. Yeboah

Department of Engineering

Clark Atlanta University

223 J. P. Brawley Drive

Atlanta, GA 30314

SUMMARY

A study of the droplet gasification and combustion characteristics of several different hydrocarbon fuels from hexane (C_6) to tetradecane (C_{14}) was conducted under sub- and supercritical pressure and subcritical temperatures. This study is expected to provide new insights and data to advance the scientific understanding of the gasification and combustion of fuel droplets and jets that may contribute to the efficient, clean and safe utilization of liquid fuels. Results show that the system pressure, temperature, and the molecular weight of hydrocarbon fuels have significant effects on the characteristics of droplet gasification and combustion. The gasification rate of a suspended hydrocarbon droplet decreased with the increase of the hydrocarbon molecular weight under a fixed temperature and pressure condition, but it reached its maximum value at the critical pressure of each compound. The oscillatory deformation of a free-drop droplet, the buoyancy effects and flame propagation of a combusting free-drop droplet were found to be directly influenced by the system pressure. The effects of sub- and supercritical temperature on the gasification and combustion behavior of hexane and heptane are currently under investigation. Preliminary results indicate that the gasification rate increases with increase in temperature below the critical temperature of hexane.

EXPERIMENTAL

The droplet combustion experiment hardware primarily consists of a liquid-fuel supply system, a gas pressure-control system, a droplet formation and release system, a cylindrical high pressure and temperature chamber, an electrical ignition system, a heater, and a Kodak EktaPro high-speed CCD video system. Analytical grades of hexane, heptane, decane and tetradecane were used as the hydrocarbon fuels. The equipment and setup are capable of withstanding system pressures from 14.7 to 1200 psi, and temperatures ranging form 25 to ~600 °C, which cover sub- and supercritical pressures and temperatures of the hydrocarbons. Droplet gasification measurements, free falling non-combustion droplet and free falling droplet combustion tests were carried out at sub- and supercritical environmental conditions.

RESULTS AND DISCUSSION

Results of the droplet gasification tests, as shown in Figure 1, indicate that the n-hexane droplet closely exhibits classical d^2-law gasification behavior at subcritical temperatures, as the gasification rate is nearly constant over most parts of the gasification period. This linearity can be explained by surface effect. Because the gasification occurs on the surface of a droplet, at a constant temperature, the gasification rate is proportional to the surface area of a droplet. The surface area of a droplet, assumed as a sphere, is a function of the square of its diameter. The gasification rate increased with increasing temperature. This is to be expected since molecular motion increases with increasing temperature. At a diameter squared value of about 0.30 mm^2 (~0.6 mm in diameter) the hexane gasification rate doubled at 100 °C. This can be attributed to an increase in surface tension (energy) with decreasing droplet diameter which strengthens the
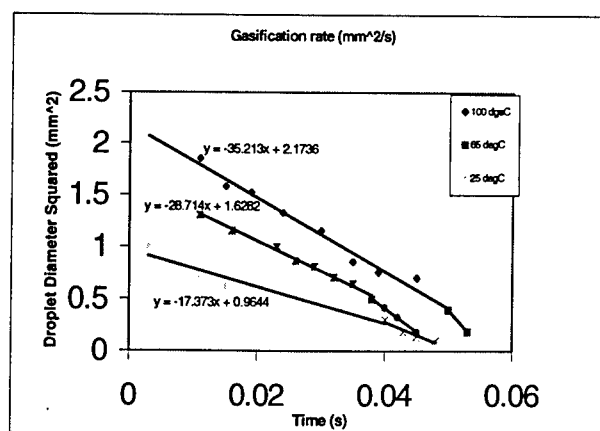
Figure 1. Variation of gasification rate (in mm^2/s) with time at different temperatures.

the escaping tendency of the molecules at the droplet surface, and also an increase in the deformation of the droplet as the droplet size decreased.

The gasification rate of a hydrocarbon droplet proportionally decreased with the molecular weight of the hydrocarbon under the system pressure around the critical pressure of the hydrocarbon as shown in Figure 2. This decrease occurs because as the molecular weight of a hydrocarbon increases, its size increases and its vapor pressure and activity decrease.
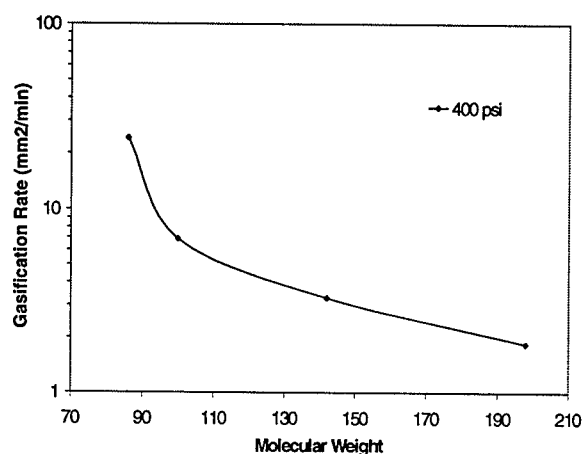
Figure 2. Variation of molecular weight of hydrocarbon fuels with gasification rate

Results of the free falling droplet indicate that the oscillatory deformation of a cold free-drop droplet is influenced directly by the system pressure at ambient temperature. The acceleration of a cold free-drop droplet proportionally decreased as the system pressure increased due to the increase of the falling resistance (Figure 3). The acceleration of a free falling droplet of hexane was found to vary proportionately with temperature as shown in Figure 4. The CCD image of the droplet showed an increase in molecular motion of the droplet as the system temperature was increased.

The effect of buoyancy was observed on a free falling combusting hexane droplet motion as the system pressure is increased from ambient to above the supercritical pressure. The combustion process of a free-drop droplet including ignition under different pressures and oxygen concentrations indicated that the supercritical pressure had a significant effect on the combustion rate, flame life, and flame movement of a free-drop droplet. At the critical pressure, the flame of the free-drop combusting droplet had the longest life.
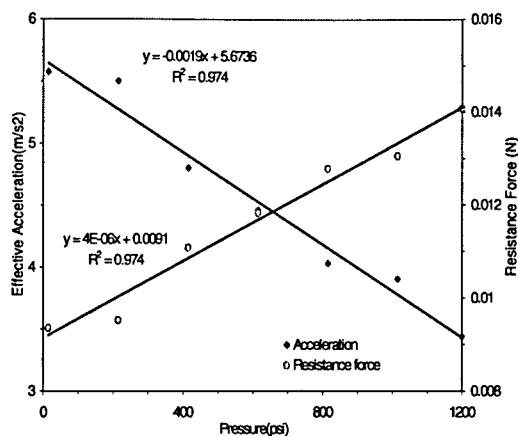
Figure 3. The effect of system pressure on the acceleration and resistance force of a free falling hexane droplet
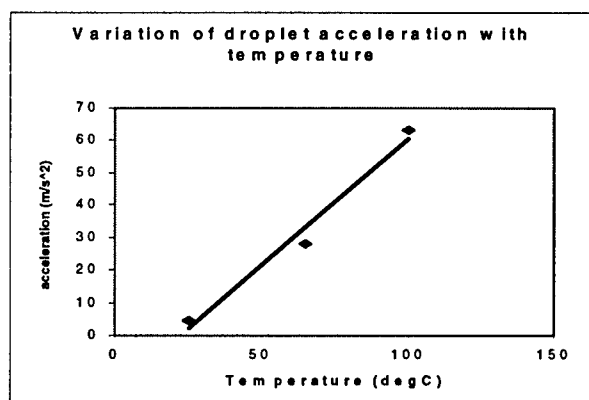
Figure 4. Variation of hexane droplet acceleration with temperature

CONCLUSIONS

The combustion and gasification behavior of hydrocarbon fuel droplets was studied under sub- and supercritical conditions. It was found that the system pressure and molecular weight of the hydrocarbons had a pronounced effect on the gasification behavior of the fuel droplets. At ambient temperature, the maximum gasification rate occurred when the system pressure was close to its critical pressure. Variation in the system temperature has a pronounced effect on the gasification behavior. The supercritical pressure had a significant effect on the combustion rate, flame life, and flame movement of a free-drop droplet. The oscillatory deformation of a non-combusting free droplet at ambient pressure was enhanced as the system temperature increased.

DROP/GAS INTERACTIONS IN DENSE SPRAYS

Principal Investigator: G. M. Faeth

Department of Aerospace Engineering
The University of Michigan
3000 François-Xavier Bagnoud Bldg.
Ann Arbor, Michigan 48109-2140, U.S.A.

SUMMARY/OVERVIEW:

Turbulence generation and secondary breakup of drops are being studied due to their relevance to dense combusting sprays. Turbulence generation is due to the dissipation of drop momentum and is the main source of turbulence in dense sprays; it consists of drop wake disturbances imbedded in a turbulent interwake region. The drop wakes are laminar-like turbulent wakes for intermediate Reynolds numbers in turbulent environments; the turbulent interwake region consists of isotropic turbulence in the final decay period. Present results have resolved the properties of the turbulent interwake region and the overall flow properties for monodisperse particles; current work is addressing these properties for more practical polydisperse particles.

Secondary drop breakup is important because drops formed by primary breakup are intrinsically unstable to secondary breakup. Past work has shown that secondary breakup should be treated as a rate process and has found the temporal properties of breakup in the bag, multimode and shear breakup regimes at large liquid/gas density ratios. Current work is considering drop deformation based on numerical simulations while emphasizing various liquid/gas density ratios, extending into the range of spray combustion processes typical of high-performance propulsion systems.

TECHNICAL DISCUSSION:

TURBULENCE GENERATION. Drop-generated turbulence differs from conventional turbulence because it is truly stationary while involving randomly-arriving velocity disturbances due to drops. Past stochastic analysis assuming that flow properties resulted entirely from wakes explained some properties of these flows but was still generally ineffective due to lack of information about particle wakes and measurement problems (Parthasarathy and Faeth 1990; Mizukami et al. 1992). Subsequently, Wu and Faeth (1994,1995) found the properties of particle wakes at turbulence generation conditions and assembly of a counterflow particle/air wind tunnel resolved experimental problems. Initial measurements for monodisperse particles showed that the particle wakes corresponded to the laminar-like turbulent wakes seen by Wu and Faeth

(1994,1995) and that the turbulent interwake region corresponded to isotropic turbulence in the final decay period (Chen et al. 2000; Chen and Faeth 2000a).

Current work is considering the properties of the turbulent interwake region and the flow as a whole. Wake-discriminating laser velocimetry (LV) has been developed to study the inter-wake region. Results for monodisperse particles show this flow generally corresponds to isotropic turbulence in the final decay period yielding turbulence intensities varying with a dissipation factor, D, defined by the dissipation rate, the particle wake momentum diameter and mean particle spacing, by analogy to grid-generated turbulence in the final decay period (Batchelor and Townsend 1948). The turbulence is sparse in the final decay period which modifies its properties from conventional turbulence. This is most readily seen from the plot of the dimensionless integral scale, A, as a function of the turbulence Reynolds number illustrated in Fig. 1. Conventional isotropic turbulence having large turbulence Reynolds numbers (greater than 10) yields values of A on the order of unity with some scatter due to the way the turbulence was generated (Hinze 1975). Present results at small turbulence Reynolds numbers (less than 10), however, yield much larger values of A which implies much greater rates of dissipation than conventional turbulence for similar values of integral scales. Thus, predicting the properties of these flows will require substantial corrections of existing turbulence models (or sub-grid scale models).

Conditional averaging of wake and interwake properties was considered to find overall flow properties (Chen and Faeth 2000b). Measurements and predictions of streamwise and crosstream relative turbulence intensities of flows resulting from turbulence generation due to monodisperse particles in both gases and liquids are illustrated in Fig. 2; the comparison between predictions and measurements is excellent. Typical measured and predicted streamwise and crosstream probability density functions (PDF) of velocities are illustrated in Fig. 3; these results are also in excellent agreement. The unusual form of the streamwise PDF results from mean streamwise velocities in particle wakes that are included in the turbulence because wake arrivals are random. Current work seeks to extend measurements of interwake and overall flow properties to more practical polydisperse turbulence generation processes.

SECONDARY BREAKUP. Past studies have established that secondary breakup should be treated as a rate process (Faeth 1996) and have determined the temporal properties of bag, multimode and shear breakup at large liquid/gas density ratios based on shock tube measurements (Chou et al. 1997; Chou and Faeth 1998; Dai and Faeth 2000). Current work is considering drop deformation using numerical simulations for various liquid/gas density ratios and effects of liquid viscosity more representative of practical spray combustion processes.

Results thus far have considered breakup of liquid columns in crossflow for comparison with recent measurements of deformation for this configuration due to Mazallon et al. (1999). Figure 4 is a typical result, involving normalized deformation as a function of normalized time for a liquid/gas density ratio of 2, an Ohnesorge number Oh = 0.1 and various Weber numbers, We. These results are remarkably similar to the deformation of drops and liquid columns at large liquid/gas density ratios, which also exhibit oscillatory behavior at smaller We and breakup for We in the range of 8-16. A typical breakup regime map for these conditions is illustrated in Fig. 5. These results also are similar to findings at large liquid/gas density ratios with increasing Oh

tending to stabilize the flow to deformation and breakup, see Faeth (1996) and Mazallon et al. (1999). Current work is addressing both liquid column and drop deformation and breakup properties.

REFERENCES

Batchelor, G.K. and Townsend, A.A. (1948) Proc. Roy Soc., London 193A, 539.
Chen, J.-H. and Faeth, G.M. (2000a) AIAA J., in press.
Chen, J.-H. and Faeth, G.M. (2000b) AIAA J., submitted.
Chen, J.-H. et al. (2000) AIAA J. 38, 636.
Chou, W.-H. and Faeth, G.M. (1998) Int. J. Mult. Flow 24, 889.
Chou, W.-H. et al. (1997) Int. J. Mult. Flow 23, 651.
Dai, Z. and Faeth, G. M. (2000) Int. J. Mult. Flow, in press.
Faeth, G.M. (1996) Proc. Comb. Inst. 26, 1593.
Hinze, J. (1975) Turbulence, 2nd ed., McGraw-Hill, New York, 539.
Mizukami, M. et al. (19) Int. J. Mult. Flow 18, 397.

Parthasarathy, R.N. and Faeth, G.M., J. Fluid Mech. 200, 485.
Wu, J.-S. and Faeth, G.M. (1994) AIAA J. 32, 535.
Wu, J.-S. and Faeth, G.M. (1995) AIAA J. 33, 171.
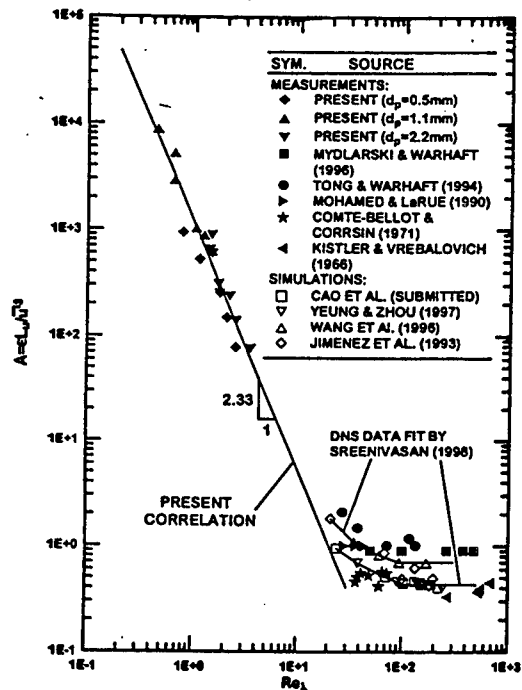
Fig. 1 Normalized integral length scales as a function of turbulence Reynolds number.
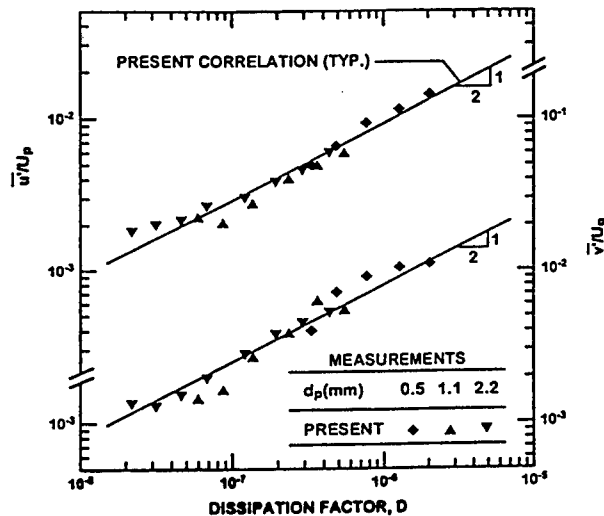
Fig. 2 Measurements and predictions of relative turbulence intensities as a function of dissipation factor.
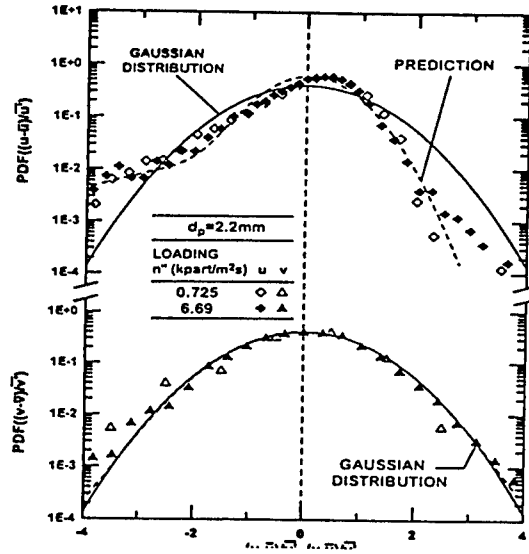
Figure 3. Streamwise and crosstream PDF's of velocities
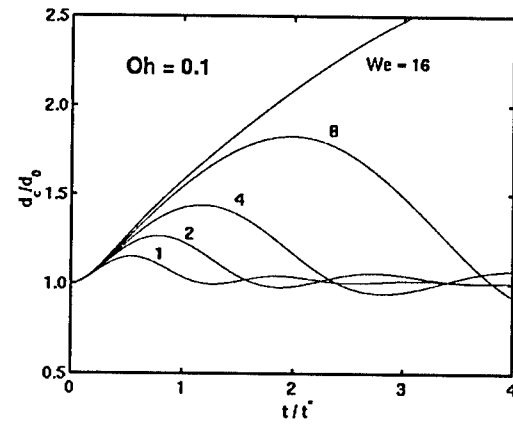
Fig. 4 Normalized liquid column deformation of nonuniform round liquid jets in uniform crossflows as a function of normalized time.
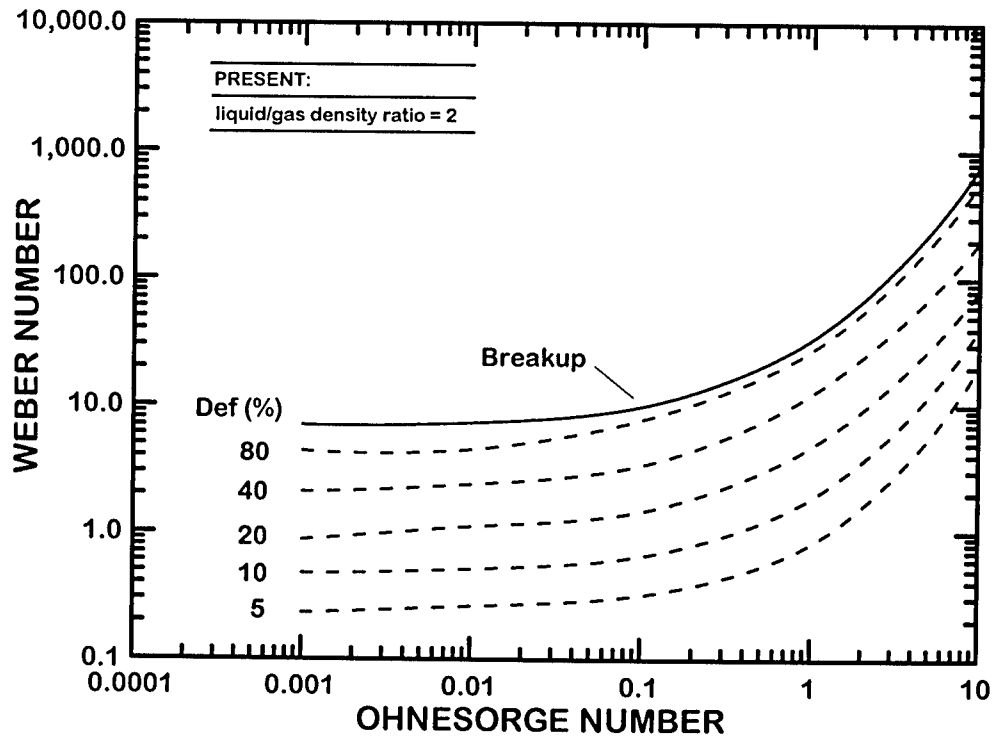
Figure 5. Deformation and breakup regime map for nonturbulent liquid columns in uniform crossflows.

NONLINEAR DISTORTION AND DISINTEGRATION
OF LIQUID SHEETS FOR PRESSURE ATOMIZATION SYSTEMS

PRINCIPAL INVESTIGATOR:

W.A. Sirignano

Department of Mechanical and Aerospace Engineering
University of California
Irvine, CA 92717

SUMMARY/OVERVIEW:

Following previous studies on the nonlinear motion and disintegration of thin planar and annular liquid sheets or films injected through slit nozzles, the three-dimensional distortion of thin swirling annular and conical sheets in a passive ambient gas have been analyzed. In addition, the nonlinear two-dimensional distortion and breakup of planar sheets with two coflowing gas streams have been analyzed. For the injected sheets, the long-wavelength approximation or lubrication assumption has been employed, leading to nonlinear unsteady one- or two-dimensional systems of equations for two- and three-dimensionally distorting thin sheets. For the surrounding gas flow a boundary-element method has been utilized. These methods have been successfully employed to predict spatial variations of velocity, pressure, sheet thickness, and sheet displacement for swirling conical sheets with three-dimensional modulating perturbations imposed at the nozzle exit, and for local two-dimensional disturbances on planar sheets subjected to two parallel gas flows. For the former case, a corkscrew-like sheet distortion has been identified. For the latter case, the dependence of sheet distortion on gas-to-liquid density ratio as well as gas Weber number has been analyzed.

AUTHORS

W.A. Sirignano   C. Mehring

TECHNICAL DISCUSSION

Previous analyses of planar and annular liquid sheets have been extended for the case of thin swirling conical liquid sheets subject to three-dimensional modulations at the nozzle exit. That approach is followed here. Liquid viscosity is neglected and the sheet is exiting into a void under negligible gravity. As for the analysis of thin planar and annular sheets, the dimensionality of the problem is reduced by integrating across the thickness of the sheet.

Semi-infinitely long, thin inviscid sheets of liquid are examined, with disturbance wavelengths in the streamwise (axial) and circumferential directions which are much larger than

the sheet thickness. General, three-dimensional disturbances are considered. The dynamics of the surrounding gas are neglected; i.e. a passive ambient gas is assumed and only capillary and inertia effects are included in the analysis of the discharging, swirling conical sheet subject to oscillatory modulations at the nozzle exit.

Following the reduced-dimension approach, three-dimensional motion is described by a two-dimensional unsteady problem. Similarly, a two-dimensional planar or axisymmetric motion is reduced to a one-dimensional unsteady problem. Details on the analytical method can be found in references [1]–[4].

For the three-dimensionally distorting annular and conical sheets exiting from a swirl atomizer, initial conditions for the simulations were obtained from the solution to the corresponding nonlinear steady-state problem without modulation imposed at the nozzle exit [4, 5]. The similar boundary conditions as previously employed for axisymmetric swirling conical sheets [4, 5] were utilized, with the exception that now modulations were imposed onto the sheet thickness and sheet centerline location rather than onto the axial and transverse sheet velocity. Also now, the modulations varied spatially in the circumferential direction at the nozzle exit.

Fig. 1 illustrates the evolution of the outer sheet interface with time τ, once the steady-state swirling conical sheet is being modulated for $\tau \geq 0$ at the nozzle exit. One observes the development of a corkscrew like-structure on the sheet, possibly leading to the formation of spiral ligaments once breakup occurs. Observation of the interface locations in planes perpendicular and parallel to the axial direction shows that the sheet curvature in the downstream or axial direction still dominates the distortion process, such that sheet break-up occurs more or less at constant values of the axial coordinate and simultaneously along the circumferential direction.

Figure 1: Location of the outer interface as function of time for the three-dimensional distortion of a thin inviscid swirling liquid sheet in a void, subject to harmonic modulations of the sheet-centerline location (in time and in the circumferential direction) at the nozzle exit, $x = 0$.

In a first effort to include the effects of a surrounding gas flow in the analysis of nonlinearly distorting and disintegrating/atomizing sheets or films, the analysis of two-dimensionally distorting planar sheets has been extended by including inertia effects of an ambient co-flowing gas stream. The liquid sheet/gas-phase model employs the reduced-dimension approach to describe the dilational and sinuous distortion of the thin planar liquid sheet, and a discrete boundary-element method in combination with a solution procedure for the unsteady Bernoulli equation in order to describe the surrounding flow field. For the inviscid case with similar gas-phase streams on both sides of the liquid sheet, i.e. same relative velocity U be-

tween the gas stream and the liquid sheet, two relevant nondimensional numbers have been identified, i.e., the gas phase Weber number $We_g = 2\rho_g U^2 h/\sigma$ and the gas-to-liquid density ratio ρ_g/ρ_l.

The boundary-element method (BEM) in combination with the unsteady Bernoulli equation determines the instantaneous gas pressure at the liquid-gas interfaces. The use of a discrete boundary-element method for the gas phase allows, in principle, the consideration of more practical applications where sheets of liquid are injected into a gaseous flowfield. This is of particular importance with regard to the complicated flowfields within and/or around fuel injection elements or atomizers used for spray combustion purposes, e.g. prefilming airblast atomizers. At present, such flowfields are not considered.

The current implementation assumes that the sheet is only disturbed locally and that the disturbance is prescribed by the initial conditions. There is no time-dependent forcing imposed onto the sheet and the sheet remains undisturbed at the boundaries of the computational domain. However, consideration of spatially developing semi-infinite sheets modulated at the nozzle exit and impacted by a surrounding gas flow is possible, if the liquid-phase algorithm is replaced by the one previously employed for (capillary waves on) modulated semi-infinite sheets [1, 3] and if appropriate boundary conditions are specified within the BEM procedure for the gas-phase flowfield.

For dilationally distorting sheets, symmetry allows the consideration of only one of the two co-flowing gas streams. For the sinuous mode, the flowfields within both gas streams have to be evaluated numerically. Due to symmetry in the dilational case, the corresponding solution can be viewed as that either for a dilationally distorting free stream or for the flow of a thin inviscid planar liquid sheet along a wall (with slip boundary conditions) and impacted by an inviscid co-flowing gas stream. This configuration is of potential interest in context with 'prefilming' airblast atomizers.

Within the current implementation, the computational boundaries for the solution of the thin sheet equations are placed far enough away from the initially imposed disturbance so that no disturbance reaches these boundaries within the considered time frames. Accordingly, the velocity in the gas along the left and right boundaries shown must be parallel to the undisturbed sheet interface at these boundaries. The gas-phase boundaries opposite to the the gas-liquid interface have been placed far enough away to presume axial freestream conditions here. Also, the liquid sheet is at rest, and the gas flow is to the right in Figs. 2,3.

Fig. 2 illustrates a typical result generated by the new model for the case of a dilationally distorting sheet. The gas streams flowing along the disturbed liquid-gas interface cause gas-pressure fluctuations which result in significant sheet distortion and eventually cause the liquid sheet to break. Without the influence of the coflowing gas, the initially imposed local dilational sheet disturbance would disperse symmetrically to both sides and its maximum amplitude would decrease continuously as the spreading continues. In the presence of an ambient gas, the maximum disturbance amplitude continuously increases (Kelvin-Helmholtz instability), sheet distortion is asymmetric around the original symmetric disturbance and sheet breakup finally occurs (for the case of an initially local sheet thickness increase) in the valley opposite to the direction from which the gas stream impacts the original local

disturbance. Observation of the velocity field within the gas-phase shows that the gas phase is significantly impacted by the sheet distortion, even at large distances from the nozzle.

Parametric studies on the effect of gas Weber number and gas-to-liquid density ratio on the distortion and breakup process have been performed for the dilational mode. They consistently show that, with increasing gas-phase influence due to increasing values of We_g and/or ρ_g/ρ_l, sheet breakup times continuously decrease. Also, with increasing gas Weber number and gas-to-liquid density ratio, capillary effects which are stabilizing and cause dispersion of dilational mode waves become less important. An initial dilational disturbance remains concentrated to an increasingly confined region of the sheet. Sinuous mode distortion of inviscid planar two-dimensional sheets subject to aerodynamic interaction with two coflowing gas streams is displayed in Fig. 3.

Figure 2: Dilationally distorting sheet in an ambient gas due to initial local sheet-thickness increase (− − −); symmetry axis at $y = 0$; $We_g = 2, \rho_g/\rho_l = 1.2 \cdot 10^{-3}$.
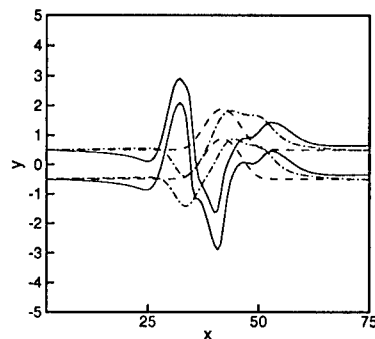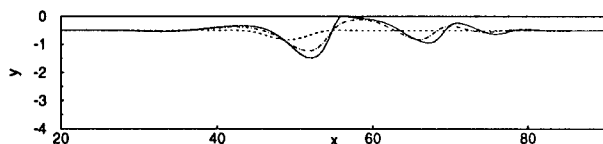
Figure 3: Sinusoidally distorting sheet in an ambient gas due to initial local sheet-centerline variation (− − −); $We_g = 1, \rho_g/\rho_l = 0.25$.

References

[1] C. Mehring and W. A. Sirignano, "Nonlinear capillary wave distortion and disintegration of thin planar liquid sheets," J. Fluid Mech., vol. 388, pp. 69–113 (1999).

[2] C. Mehring and W. A. Sirignano, "Axisymmetric capillary waves on thin annular liquid sheets. Part I: Temporal stability," Phys. Fluids, in press (2000).

[3] C. Mehring and W. A. Sirignano, "Axisymmetric capillary waves on thin annular liquid sheets. Part II: Spatial development," Phys. Fluids, in press (2000).

[4] C. Mehring, "Nonlinear distortion of thin liquid sheets," Ph.D. thesis, University of California, Irvine (1999).

[5] C. Mehring and W. A. Sirignano, Nonlinear capillary waves on swirling, axisymmetric liquid films, AIAA 2000-0432; presented at the 38th AIAA Aerospace Sciences Meeting, Reno, NV.

Principal Investigator: Dr. Josette Bellan

Jet Propulsion Laboratory
California Institute of Technology
4800 Oak Grove Drive
MS 125-109
Pasadena, Ca 91109-8099

SUMMARY/OVERVIEW:

The objective of this study is the fundamental understanding of fuel disintegration and mixing in a supercritical environment (relative to the fuel) in order to determine parameter regimes advantageous to mixing. The approach is based on developing a model of a supercritical, turbulent jet mixing with surrounding fluid. The method is one that combines the modeling of supercritical fluids with a systematic development based on the Large Eddy Simulation (LES) approach. This systematic development includes a consistent protocol based upon Direct Numerical Simulations (DNS) for developing a Subgrid Scale Model (SGS) appropriate to supercritical fluids, rather than choosing in an ad hoc manner an existing SGS model developed under assumptions inconsistent with supercritical fluid behavior. This SGS model will be used in the LES of a supercritical turbulent jet.

TECHNICAL DISCUSSION

The first step in this effort consists in the development of a DNS and associated code for a supercritical shear layer. The shear layer is chosen as the simplest configuration from which one may obtain results that will establish, through DNS, a framework for understanding mixing of supercritical fluids at small scales. Since the turbulent behavior at the Kolmogorov scales is universal (i.e. geometric-configuration independent), once this behavior is determined (e.g. in a shear layer geometric configuration), it can be utilized to model a variety of geometric configurations (for the same fluids) having the same physics. Since the interest of AFOSR is in hydrocarbons, the chosen shear layer is that of heptane (lower stream) in nitrogen.

Following previous modeling performed at JPL for isolated fluid drops (Harstad and Bellan, 1998, 2000), the model of supercritical behavior is based upon fluctuation theory (Keizer, 1987). The advantage of this theory is that it inherently accounts for nonequilibrium processes and naturally leads to the most general fluid equations by relating the partial molar fluxes and the heat flux to thermodynamic quantities. Thus, Soret and Dufour effects (which are potentially important at supercritical conditions) are taken into account from first principles through the transport matrix where they complement the traditional Fick's mass diffusion and Fourier thermal diffusion terms. Results from the recent supercritical simulations of Harstad and Bellan, 2000, using heptane drops in nitrogen have been validated with the microgravity data of Nomura, 1996,

within an average of 15%, thereby showing that the fluid model is correct. It is precisely this model that is here adapted to the shear layer configuration. However, there are specific issues that must be considered in the DNS of a three-dimensional (3D) shear layer that were not relevant to the drop model:

(a) In contrast to the drop study, the treatment of the transport coefficients cannot be exact in the context of DNS since the Reynolds number, Re, would be far too large to make the computations feasible. Since it is required that the Batchelor scales (the smallest scales associated with scalar mixing, $\eta_B \sim \eta_K/Sc$ where η_K is the Kolmogorov scale and Sc is the Schmidt number) be resolved, this dictates the maximum Sc which can be used in the particular calculation. For example, for heptane/nitrogen, Sc is too large for any domain size if heptane has a liquid-like density. The strategy is then to calculate these numbers based upon the observations that the viscosity is primarily a function of T, whereas Sc and Pr are primarily functions of the mass fractions, and to find approximate fits for these quantities in the range of parametric interest.

(b) It is here unpractical to use the very accurate and computationally efficient non ideal EOS's employed in Harstad and Bellan, 2000, because these might still be too computationally intensive when performing 3D simulations. Instead, we used the Peng-Robinson EOS based on pure species reference states accurate to better than 1% relative error (on pure reference states) through comparisons with highly accurate EOS's (Harstad et al., 1997) over the range of variables used in this study.

The shear layer equations were coded using a fourth order Runge-Kutta scheme for advancing in time, and an eight order compact method for spatial discretization. The implemented boundary conditions were those of Poinsot and Lele, 1992, for compressible flows. Since those boundary conditions were developed for perfect rather than real gases, they were adapted for the present real gas computations by calculating an 'equivalent gas constant' from the EOS; the accuracy of this simplistic substitution is discussed in more detail below. Also, the layer was perturbed in the mean velocity using the most unstable wavelength of Moser and Rogers, 1991, found in the context of atmospheric, incompressible gases.

Results were first obtained for a 2D shear layer in order to study an issue of general interest which is the identity [Irwing-Kirkwood (IK) or Bearman-Kirkwood (BK); see Sarman and Evans, 1992] and value of the thermal diffusion coefficient appearing in the Soret and Dufour contributions to the molar and heat flux. Although the recent modeling and validation of Harstad and Bellan, 2000, for a heptane fluid drop in nitrogen showed that it is possible to approximately evaluate these elusive parameters about which there is only scant information, generally the experimental data is not available and thus the issue of the model sensitivity to these properties is very pertinent. The results showed that indeed the model is sensitive to both the identity and value of the thermal diffusion factors. In fact, combined with the effect of the mass diffusion factor (a quantity calculated entirely from the EOS), constant positive large BK thermal diffusion factors retard diffusional mixing; whereas constant moderate IK factors tend to promote mixing. Constant positive BK thermal diffusion factors also tend to maintain density gradients, with resulting greater shear and vorticity. These conclusions about IK and BK thermal diffusion factors are species pair dependent, and therefore are not universal, pointing out to the difficulties associated with the lack of thermal diffusion factor values for most species.

Results from the 3D shear layer showed that the density stratification is stabilizing the layer and preventing it from achieving the transitional regime at a nondimensional time at which a transitional state had been reached by a layer whose lower stream was initially laden with drops. This lack of transition is due both to the initial strong density stratification and to the formation of regions of strong density gradient magnitude both in the braid and in between the braid plane. In fact, a density interface is very effective at damping turbulent eddies, being qualitatively

similar to a rigid flat plate. Hannoun et al., 1988, found that large eddies impinging on a density interface 'bounce' back without significant entertainment of unstirred fluid instead of overturning. Since the layer growth depends primarily on entertainment, and since it is this accelerated growth that promotes the appearance and evolution of the small turbulent scales, this damping mechanism may be enhancing the effect of density stratification in hindering transition.

The appearance and geometry of these regions of high density gradient magnitude is intriguing because it corresponds to the wispy threads of fluid emanating from a supercritical nitrogen jet in gaseous nitrogen as observed by Chehroudi et al., 1999. These features do not exist at subcritical conditions either in the experiment or in atmospheric air DNS simulations, indicating that they may be specific to the supercritical situation. These results were all documented in Miller, Harstad and Bellan, 2000.

Since the layer did not achieve transition in a physical time comparable to that, for example, of a drop laden mixing layer, the calculations were pursued with the goal of achieving transition at a later physical time. However, this did not occur for the chosen initial conditions, and moreover, the layer seemed to reach a culminating point in the averaged positive spanwise vorticity. The averaged positive spanwise vorticity is considered to be a good indicator of transition since the initial mean velocity profile is such that the spanwise vorticity is negative everywhere; transition is obtained when the positive spanwise vorticity exhibits and continues to display a large increasing rate. Our results are illustrated in Fig. 1 together with the momentum thickness, the product thickness and the enstrophy (another indicator of transition). To investigate the origin of the stability preventing transition in a physical time larger than

Figure 1. Momentum (------) and product (• • •) thickness, enstrophy (-- -- --) and averaged positive spanwise vorticity (--•--•--) as a function of time.

that, for example, of a drop laden mixing layer, the entropy equation has been derived for a supercritical fluid and the irreversible entropy production was examined. The irreversible entropy production is in fact the dissipation and it is inherently important in systems undergoing production of turbulent scales. For supercritical fluids, the dissipation was shown to contain three contributions: viscous, Fourier heat flux and molar flux contribution. The molar flux contribution contains both the effect of the mixture nonideality and that of the Soret term. The database from the long-time run was used to compute the budget of the small scale dissipation by calculating the difference between the DNS (i.e. unfiltered) and that of the filtered flow field. The results from plane averages and RMS of the three terms show that the dominant contribution to the small scale average dissipation is from the viscous term, but that the major RMS contribution is from the molar flux term at all times except at the culmination of the averaged positive spanwise vorticity. Since the molar flux contribution to the dissipation contains six terms, a budget of the molar flux dissipation was calculated to identify which of the terms is the principal contributor to the molar flux dissipation magnitude. As it turns out, the nonideality term is the major contributor in the heptane stream, whereas the nonideality and Soret terms tend to be of same order of magnitude in the nitrogen stream. These calculations as well

as contour plots show that the RMS of the molar flux dissipation correlates with the regions of maximum density gradient magnitude. Moreover, we also noticed that the DNS dissipation RMS, as well as each of its contributions is larger than the respective average value, indicating that there is considerable backscatter in the flow.

The calculation of the dissipation was valuable not only in elucidating the responsible mechanisms impacting the stability characteristics of the flow, but also in pointing out that at large simulation times the mass fractions and temperature displayed large gradients at the upper and lower boundaries of the computational domain; these are the only locations where non-periodic boundary conditions are applied. This prompted us to re-examine the implementation of the boundary conditions according to Poinsot and Lele, 1992, and Baum et al., 1994. Thus, we derived the 'characteristic' boundary conditions for a general fluid having a real gas equation of state. This derivation was consistent with the fact that for $Re \to \infty$ the conservation equations including the Soret and Dufour effects are an incomplete elliptic set. In fact the elliptic character is determined by the effective thermal conductivity which is always enhanced, while the effective diffusivity is always reduced (see Harstad and Bellan, 1999). Simulations of a one-dimensional propagation of acoustic waves in a two-dimensional domain using subsonic non-reflecting boundaries were conducted with the new, fundamental boundary conditions, and compared with the previous simulations based on the 'simplistic' effective gas constant (see above). The results revealed that whereas using the fundamental analysis results in the acoustic waves properly passing through the boundaries without reflections, the use of the simplistic approach yields significant reflections at the boundaries. Most discrepancies occurred when a source term was added to the mass fraction equations, where additional to the reflections at the boundaries, the solution within the entire domain was different in the simplistic and fundamental approaches. The fundamental boundary conditions are now being implemented in the code.

1. Baum, M., Poinsot, T. and Thevenin, D., Accurate boundary conditions for multicomponent reactive flows, *J. Comp. Phys.*, 116, 247-261, 1994
2. Chehroudi, B., Talley, D. and Coy, E., Initial growth rate and visual characteristics of a round jet into a sub- to supercritical environment of relevance to rocket, gas turbine, and Diesel engines, AIAA 99-0206, 37th Aerospace Sciences Meeting, Reno, NV, 1999
3. Hannoun, I. A., Fernando, H. J. S. and List, E. J., Turbulence structure near a sharp density interface, *J. Fluid Mech.*, 189, 189-209, 1988
4. Harstad, K. G. , Miller, R. S., and Bellan, J., Efficient high pressure state equations, *A. I. Ch. E*, 43(6), 1605-1610, 1997
5. Harstad, K. and Bellan, J., Isolated fluid oxygen drop behavior in fluid hydrogen at rocket chamber pressures, *Int. J. Heat Mass Transfer*, 41, 3537-3550, 1998
6. Harstad, K. and Bellan, J., The Lewis number under supercritical conditions, *Int. J. Heat Mass Transfer*, 42, 961- 970, 1999
7. Harstad, K. and Bellan, J., An all-pressure fluid drop model applied to a binary mixture: heptane in nitrogen, in print, *Int. J. of Multiphase Flow*, 26(9), 2000
8. Keizer, J., *Statistical thermodynamics of nonequilibrium processes*, Springler-Verlag, New York, 1987
9. Miller, R. S., Harstad, K. and J. Bellan, J., Direct numerical simulations of supercritical fluid mixing layers applied to heptane nitrogen, in review, *J. Fluid Mech.*, 2000
10. Moser, R. D. and Rogers, M. M., Mixing transition and the cascade to small scales in a plane mixing layer, *Phys. Fluids*, A3(5), 1128-1134, 1991
11. Poinsot, T. J. and Lele, S. K., Boundary conditions for direct simulations of compressible viscous flows, *J. Comp. Phys.*, 101, 104-129, 1992
12. Sarman, S. and Evans, D. J., Heat flux and mass diffusion in binary Lennard-Jones mixtures, *Phys. Rev.*, A45(4), 2370-2379, 1992

IN-CYLINDER TWO-DIMENSIONAL TWO-COLOR OPTICAL PYROMETRY AS AN INDICATOR OF ENGINE OUT EMISSIONS: EXPERIMENT AND SIMULATION

Principal Investigators: Mike Corradini, Pat Farrell, Dave Foster, Jaal Ghandhi, Jay Martin, John Moskwa, Rolf Reitz, Chris Rutland

Engine Research Center
1500 Engineering Drive
Madison, WI 53706

SUMMARY/OVERVIEW

This research was performed as part of an ongoing effort to gain further insight into the fundamental processes occurring during diesel engine combustion. Specifically, two-dimensional, two-color optical pyrometry was used to investigate the temporal and spatial evolution of the temperature and KL factor during combustion in a Cummins NH engine. Comparisons between the measurements from the individual combustion cycles, engine out emissions of NOx and soot, and the predictions of a phenomenological soot model indicated that single cycle observations could be related to engine out phenomena, and there was a good correlation between the measurements and the predicted in-cylinder phenomena. The data indicated important temperature and time regimes within the combustion process which were indicators of the particulate and NOx emissions.

TECHNICAL DISCUSSION

The application of two-dimensional two-color optical pyrometry to an engine is not new. The work presented here represents an iterative improvement to the method, followed by an investigation of the potential for using spatially resolved single cycle information to assess the averaged cylinder exit emission of soot and NOx. This was done by comparing the two-color signals from consecutive engine cycles to determine the cycle by cycle variation of the temperature and KL data, then identifying characteristics of the individual cycles which correlated with the engine out emissions of soot and NOx. Further insight into the combustion processes was gained by using the Engine Research Center's version of KIVA, into which a phenomenological soot model had been implemented [1,2], to compare measured and predicted radiant emissions resolved both spatially and temporally. Using the good agreement between the simulation and the in-cylinder measurements as an indication that the model includes the salient physics of the cylinder processes, the model was used to categorize the sequence of events occurring during combustion. The model predicted a "conceptual" model consistent with that proposed in the literature [3].

The experiments were conducted on a single cylinder Cummins NH research engines. Two operating conditions were investigated: an injection timing sweep (from -12^0 ATDC to -2^0 ATDC) at75% load, 1500 RPM, and a single injection timing at 25% load and 1200 RPM. The luminosity data were recorded on high speed nega-color film by imaging the combustion through a window installed in place of one of the exhaust valves. Five halogen

light bulbs were located around the window and were imaged simultaneously with the combustion on the film. Lenses were used to insure that the image plane for both the bulbs and the in-cylinder events were the same. The five halogen bulbs were each set to a different apparent temperature so they provided a reference on each film frame for determining the calibration curve for the film density versus apparent temperature. The individual film frames were digitized by imaging them through color filters (λ_1=500 nm and λ_2=640 nm) onto a CCD camera and then a pixel by pixel two-color analysis was performed. Compensation for the spectral transmissivity of the optics and windows was also made.

The 3-D computer simulation used was an Engine Research Center version of KIVA. The computational mesh represented a 45^0 (1/8) sector of the combustion chamber, with a maximum of 15,000 computational cells. The simulation was exercised from −140 to 120 crank angles ATDC. The fuel was taken as n-tetradecane with other sub-grid models being: RNG - k-ε turbulence, Kelvin − Helmholtz and Rayliegh − Taylor spray break-up, Shell multi-step ignition, characteristics time combustion, extended Zeldovich NOx and the phenomenological soot [2].
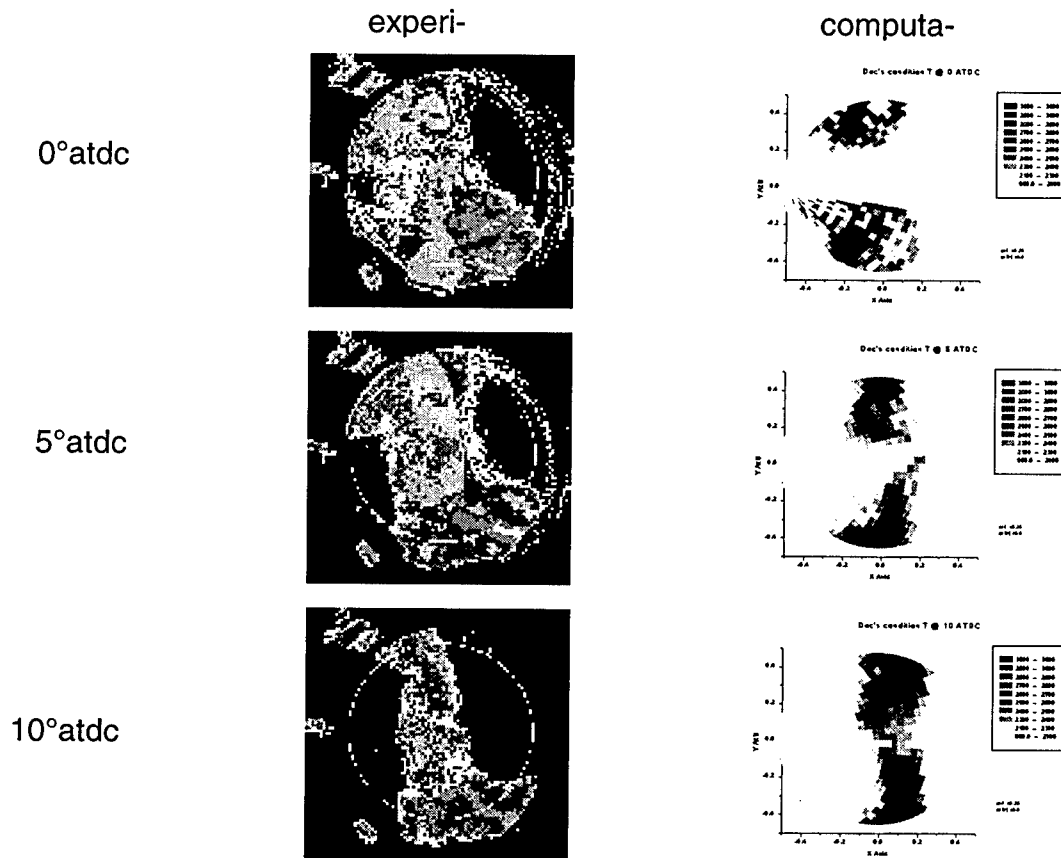
Figure 1 A comparison between the experimental two-dimensional two-color temperature and that calculated from the predicted radiant emission.

Figure 1 shows a comparison between the experimentally obtained two-dimensional two-color temperature distribution and the distribution obtained from the predicted radiant emission. Although it is difficult to compare the values of the temperatures in this figure, one can see the overall agreement of the spatial distribution and the changes in the distribution with time. Similar observations can be made when comparing the measured and predicted KL

factors. Figure 2 is a plot of the area averaged KL factors from the experiment and from the calculation.
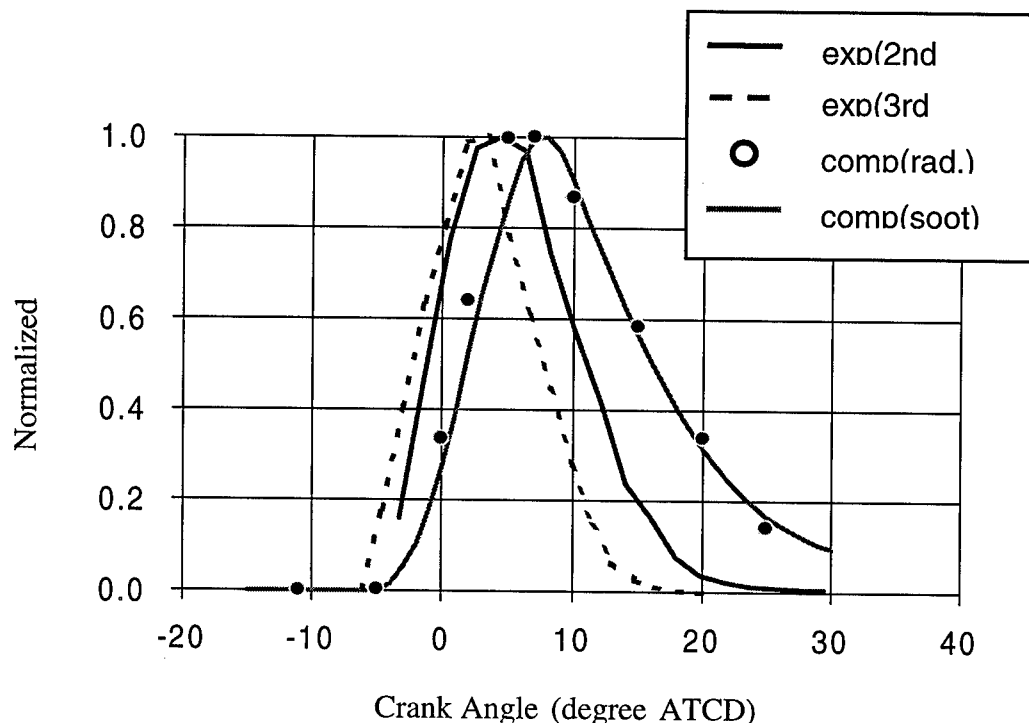
Figure 2, Normalized KL versus crank angle for both experimental results and simulation predictions

Shown in the figure are two consecutive engine cycles, the two left most curves, one dotted the other solid. From these data one can see that the cycle by cycle variation is very low. The single points which are plotted are the predicted KL from the simulation. The KL predictions were only selectively evaluated. The solid line approximately connecting the predicted KL is the total cylinder soot predicted by the simulation. As can be seen from these results, the KL measured through the window in the cylinder closely follows the trend of the total particulate load in the cylinder. Furthermore, the data from an individual cycle can be taken as representative of the integrated engine out emissions for the studied engine operating condition.

The data shown in Figure 2 as a comparison between experiment and simulation is indicative of what was observed experimentally. Namely, the individual cycle two-dimensional two-color optical pyrometry data could be used to compare in-cylinder phenomena with resultant engine out emissions. Figure 3 shows such a comparison. The left-hand column is the temperature data and the right-hand column is the KL factor. The different curves represent the percent of the observed image with temperatures, or KL factors, below the listed value. The data shown in the Figure is for a single engine operating condition with three different fuel/intake-charge compositions. The top row is a standard diesel fuel. The middle row is diesel fuel but with the intake air enriched to 23 percent oxygen by volume. The bottom row is diesel fuel with MTBE and normal air. The emission results for these three tests were what one might expect. The oxygen enriched air and the oxygenated fuel (MTBE) had lower soot than the regular diesel fuel operation. The diesel fuel and oxygenated diesel fuel (MTBE) had equivalent NOx emissions, which were lower than the NOx emission from the

oxygen enriched intake air. These trends could be deduced by looking at the temperature and KL curves for the individual cycles shown in the Figure.

Percent Area (%) — CA atdc (deg.)
(1a) Base temperature data

Percent Area (%) — CA atdc (deg.)
(1b) Base KL-factor data

Percent Area (%) — CA atdc (deg.)
(2a) 23% Oxygen enrichment temperature data

Percent Area (%) — CA atdc (deg.)
(2b) 23% Oxygen enrichment KL-factor data

Percent Area (%) — CA atdc (deg.)
(3a) 20% MTBE temperature data

Percent Area (%) — CA atdc (deg.)
(3b) 20% MTBE KL-factor data

Area with T>To:
——— To=2000K
- - - - - To=2300K
········ To=2500K
- · - · - To=2800K

Area with KL>KL$_o$:
——— KL$_o$=0.2
- - - - - KL$_o$=0.5
········ KL$_o$=1.0
- · - · - KL$_o$=2.0
···· · KL$_o$=3.0

FIGURE 3. TWO-COLOR TEMPERATURE, ON THE LEFT AND KL-FACTOR DATA, ON THE RIGHT, FOR BASE FUEL, 23% OXYGEN ENRICHMENT, AND 20% MTBE OXYGENATED FUEL RESPECTIVELY. LOAD = 75%

REFERENCES

1. Fusco, A., Knox-Kelecy, A. L., and Foster, D. E., "Application of a Phenomenological Soot Model for Diesel Engine Combustion", The Third International Symposium on Diagnostics and Modeling of Combustion in Internal Combustion Engines, Yokohama, Japan, 1994, p. 571-576.

2. Kazakov, A. and Foster, D.E. "Modeling of Soot Formation During DI Diesel Combustion Using A Multi-Step Phenomenological Model" SAE paper 982463 Transactions

3. Dec, John, "A Conceptual Model of DI Diesel Combustion Based on Laser-Sheet Imaging," SAE paper 970873, Transactions

ADVANCED DIAGNOSTICS FOR REACTING FLOWS

Principal Investigator: Ronald K. Hanson

High Temperature Gasdynamics Laboratory
Mechanical Engineering Department
Stanford University, Stanford, California 94305-3032

SUMMARY/OVERVIEW:

This research is aimed at establishing advanced laser-based techniques for non-intrusive measurements relevant to air-breathing combustion. Emphasis is placed on spectrally-resolved absorption using rapid-tuning laser sources, primarily in the near-infrared, and on planar laser-induced fluorescence, conducted using either near-infrared or ultraviolet laser sources. Significant progress was made in the exploration of IR PLIF as a diagnostic for imaging IR-active gases and in the development of frequency-modulation variations of laser absorption techniques for sensitive detection of CO using diode laser sources operating near 2.3 microns. New work is reported on the suitability of pentanone as an alternative flow tracer to acetone for PLIF imaging, while continuing work is reported on spectroscopy of high-pressure gases. Important refinements have been made in a diode laser absorption probe for veloc74ity measurements in hypersonic flows.

TECHNICAL DISCUSSION:

Infrared PLIF Imaging

Infrared (IR) PLIF shows the potential for visualization of important species such as CO, CO_2, CH_4 and H_2O that cannot be visualized using traditional PLIF techniques. In IR PLIF, a tunable IR laser source is used to excite vibrational transitions in molecules, and the resulting vibrational fluorescence is imaged onto an IR camera. Preliminary analytical and experimental results have been obtained which demonstrate the feasibility of IR PLIF for species imaging.

Fig. 1. (a) At left: single-shot visualization of the fuel region of a $CO/Ar/H_2$ laminar diffusion flame generated using IR PLIF of CO. (b) At right: single-shot visualization of mixing of a forced CO_2/Ar jet in air generated using IR PLIF of CO_2.

Excitation of CO (2.35 µm) and CO_2 (2.0 µm) followed by collection near 4.3-4.7 µm has been implemented using a high-pulse-energy tunable IR optical parametric oscillator and a gated InSb IR camera. Fig. 1 shows single-shot visualization of the fuel region of a CO diffusion flame (IR PLIF of CO) as well as visualization of mixing of forced CO_2-air jets (IR PLIF of CO_2).

We have also investigated techniques employing vibrational energy transfer to image multiple species using single laser excitation. Fig. 2 shows visualization of both CO (fuel) and CO_2 (fuel-product interface) of a CO-air laminar diffusion flame. Both images are generated using excitation of the R(12) line of the CO 2ν band; different collection filters are used to image the resulting fluorescence from either CO or CO_2.

Fig. 2. At left: CO fluorescence from fuel region of a $CO/Ar/H_2$ laminar diffusion flame after excitation of CO. At right: CO_2 fluorescence (indicating fuel-product interface) from the same flow using *identical laser excitation of CO*.

Ultra-Sensitive CO Detection

A diode-laser sensor system based on wavelength modulation spectroscopy (WMS) with $2f$ detection has been developed to measure 0.1 ppm-meter levels of carbon monoxide (CO) using a new room temperature diode laser operating near 2.3 microns. The primary feature of WMS techniques is their inherent robustness in hostile environments. Because the absorption signal is obtained from the variation of attenuation with optical frequency rather than the attenuation itself, the technique is immune to background emission noise (e.g., from hot particles) and is insensitive to laser attenuation noise (e.g., beam steering, scattering, and solid- or liquid-phase aerosol absorption). The result is a significant reduction in the noise component of the signal. The availability of 2.3 micron lasers (InGaAsSb) permits selection of strong CO transitions with minimal interference of H_2O absorption (<1%), which is prevalent in combustion environments.

A laboratory demonstration successfully yielded sensitive CO detection at a 50 Hz repetition rate. An atmospheric-pressure C_2H_4-air premixed flame was used to produce combustion products, and the diode laser beam was directed along the centerline of the horizontal exhaust duct (120-cm pathlength) and onto an InAs detector. The laser mean frequency was tuned over the CO R(15) transition by a 50-Hz ramp current modulation while a 33-kHz (f) injection dither current (sinusoidal) was superimposed to obtain wavelength modulation. Fig. 3 illustrates representative lineshapes (20-sweep average) recorded at equivalence ratios of 0.72 and 0.95. The signal-to-noise ratio of these lineshapes is approximately 100 which translates to a detection sensitivity of ~0.1 ppm-m for a repetition rate of 2.5 Hz.

Fig. 3. Representative $2f$ lineshapes (~1.46 modulation index, 20-sweep average) for CO measurements in the 120-cm exhaust duct of a laboratory combustor.

Ketone Photophysics for Quantitative PLIF Diagnostics

Our past studies of acetone (CH_3COCH_3, bp 56 °C) have led to new and useful strategies for instantaneous, 2-D temperature and mixture-fraction diagnostics for gaseous flowfields at atmospheric pressure. More recently, we have begun to extend these diagnostics to flows above atmospheric pressure, i.e. to conditions relevant to the mixing regions in high pressure combustors. In addition, we have continued to search for attractive alternatives to acetone in an effort to optimize current techniques and develop new ones based upon fluorescent and physical behavior. 3-pentanone ($C_2H_5COC_2H_5$, bp 102 °C) is a candidate with many of acetone's attractive photophysical attributes; furthermore its higher molecular weight makes it better suited for tracking

Fig. 4. Comparison of dual-wavelength fluorescence signal ratios from 3-pentanone and acetone – preliminary results. All data come from experiments at atmospheric pressure.

heavier compounds during mixing processes. Also, as shown in Fig. 4, initial experiments performed on 3-pentanone using 248 and 308 nm laser excitation indicate that it is a better temperature indicator than acetone up to 700 K; however, its complex behavior at higher temperatures may make quantitative imaging problematic. Further studies using other excitation wavelengths should lead to a better understanding of 3-pentanone as well as the potential for other ketones[*] as tracer candidates.

High-Pressure Diagnostics

Work has continued on two fronts: development of a new laboratory combustor well-suited for fundamental studies of absorption and fluorescence spectroscopy of gases at high pressures (to 50 atm) and temperatures (2000 K), and exploration of a diode-laser absorption diagnostic for H_2O and temperature in high-pressure environments. The new combustor duplicates a German design which has been utilized successfully at these conditions. Construction is complete and the combustor and associated control systems are now undergoing checkout. The associated pulsed dye laser system and associated spectroscopic recording devices are also nearly complete. The high-pressure diode laser absorption diagnostic has been applied to the transient flows in a shock tube, which has allowed convenient variation of pressure, temperature and composition over wide ranges. Experiments up to 65 atm and temperatures to 1800 K have been completed and submitted for publication. Data obtained in the shock tube experiments have provided an important complement to the current HITRAN spectral data base for water vapor.

TDLAS Probe Enhancement for Hypervelocity Flows

In previous years we reported on diagnostics strategies to measure temperature, velocity, and concentration in high-speed flows using tunable diode laser absorption spectroscopy (TDLAS) techniques. These measurements were performed using robust probes installed directly in high-enthalpy flowfields and fiber coupled to rapidly tunable laser sources operating at near-IR wavelengths. One system monitored water vapor which is both a contaminant and a combustion product in hydrogen-driven reflected shock tunnels, and the second monitored potassium, which was found to exist naturally in Calspan's 96" hypersonic shock tunnel and in Stanford's expansion tube facility.

Recent efforts have concentrated on abating potassium absorption in the boundary layer by introducing slot cooling capability to the probe. Fig. 5 shows a schematic of the diode-laser probe with slot injection capability. Additionally, the design

Fig. 5. A schematic of the diode laser probe with slot cooling capabilities and the counter propagating dual-pass optical train to enhance the velocity measurement.

---

[*] Ketone – an organic compound containing a carbonyl group (CO) attached to two carbon atoms.

incorporates removable optoelectronics enabling measurements of different species and parallel-counter-propagating beams for velocity measurement enhancement.

Recently the TDL probe was used to examine the velocity time history in the Stanford expansion tube with water vapor as the spectroscopic tracer; a sample set of results is shown in Fig. 6. The probe was situated at the exit plane of the expansion tube section and exposed to the following nominal free stream conditions: V = 2100 m/s, T = 340 K, and P = 140 torr. The laser was scanned rapidly at 30.3 kHz to obtain discrete velocity measurements every 33 μs. The initial velocity rise is attributed to the transition between helium acceleration gas and the water-seeded nitrogen test gas. The steady region possesses velocities which agree well with the contact surface velocity calculated by time-of-flight measurements. The fast time response of the TDL probe is used to reveal that the useful testing time in the facility, at these test conditions, is limited to about 100 μs.
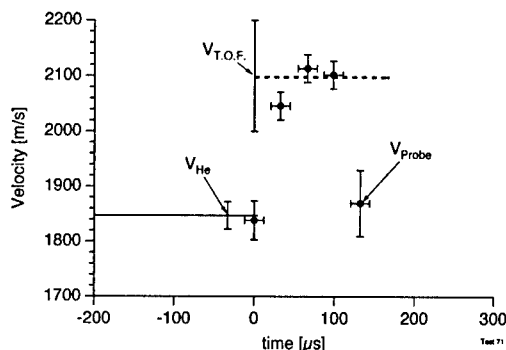
Fig. 6. Measurements of velocity recorded in the Stanford shock/expansion tunnel using the miniaturized probe. The helium flow velocity (V_{tof} = 1847 ± 25 m/s) is calculated from the secondary shock velocity. The time of flight velocity (V_{tof} = 2100 ± 100 m/s) is determined from the contact surface velocity.

PUBLICATIONS:

R.M. Mihalcea, D.S. Baer and R.K. Hanson, "Advanced Diode Laser Absorption Sensor for In-Situ Combustion Measurements of CO_2, H_2O and Temperature," 27th Symp. (International) on Combustion, The Combustion Institute, pp. 95-101 (1998).

A. Ben-Yakar and R.K. Hanson, "Experimental Investigation of Flame-Holding Capability of Hydrogen Transverse Jet in Supersonic Dross-Flow," 27th Symp. (International) on Combustion, The Combustion Institute, pp. 2173-2180 (1998).

S.D. Wehe, D.S. Baer and R.K. Hanson, "Diode-Laser Sensor for Velocity Measurements in Hypervelocity Flows," *AIAA J.* **37**, 1013-1015 (1999).

M.C. Thurber and R.K. Hanson, "Pressure and Composition Dependence of Acetone Laser Induced Fluorescence with Excitation at 248, 266 and 308 nm," *Appl. Physics B* **69**, 229-240 (1999).

V. Nagali, J.T. Herbon, D.C. Horning, D.F. Davidson and R.K. Hanson, "Shock Tube Study of High-Pressure H_2O Spectroscopy," *Appl. Optics* **38**, 6942-6950 (1999).

B.J. Kirby and R.K. Hanson, "Planar Laser-Induced Fluorescence Imaging of Carbon Monoxide using Vibrational (Infrared) Transitions," *Appl. Physics B* **69**, 505-507 (1999).

G. Totschnig, D.S. Baer, J. Wang, F. Winter, H. Hofbauer and R.K. Hanson, "Multiplexed Coupled-Wave Diode-Laser Cavity Ring-Down Measurements of Multiple Species," *Appl. Optics*, in press.

B.J. Kirby and R.K. Hanson, "Infrared PLIF Imaging of CO and CO_2," *28th Symp. (International) on Combustion*, Edinburgh, Scotland, July 2000, accepted.

J. Wang, M. Maiorov, D.S. Baer, D.Z. Garbuzov, J.C. Connolly and R. K. Hanson, "In Situ Measurements of CO using Diode Laser Absorption near 2.3 microns," *Appl Optics*, submitted February 2000.

High Temperature and Pressure Optical and MEMS Sensors

Grant Number DAAH04-96-1-0008

Principal Investigators: J. Seitzman, M. Allen, M. Brooke, A. Glezer, W. Haddad, J. Jagoda, S. Menon, Y. Neumeier, J. Prasad, L. Sankar, B. Zinn

Georgia Institute of Technology
Schools of Aerospace, Electrical and Computer, and Mechanical Engineering
Atlanta, GA 30332-0150

SUMMARY/OVERVIEW:

This program focuses on the fundamental and practical issues that hinder development of intelligent control systems for improving the performance of turbine engines, such as rotorcraft turboshaft engines. Our approach to the development of an intelligent control system hinges on advances in the basic understanding of engine processes through experiments and advanced computational models, refinement of appropriate sensor and actuator technologies, and development of practical control strategies for control of steady-state and transient performance. Here, we report on recent advances in the development of sensor technology and sensor strategies for monitoring high temperature and high pressure engine components. A MEMS pressure sensor capable of high temperature operation utilizes high temperature ceramic tape and a passive, wireless readout scheme. The non-intrusive optical sensors are based on spectroscopic methods and are capable of monitoring combustor conditions and temperature profile uniformity at the turbine inlet.

TECHNICAL DISCUSSION:

HIGH TEMPERATURE MEMS SENSOR (PI: ALLEN)

This research is based on the idea that micromachined mechanical structures can be fabricated from ceramic tape layers. The sensor (Fig. 1) consists of a sealed cavity, ideally a vacuum, on which two capacitor plates are formed. Either the top or the bottom (or both) bounding sides of the cavity can made of a flexible ceramic diaphragm. Thus the value of this capacitor changes with pressure. The ceramic tape is a high temperature material; to sinter and melt the glass matrix, the tape is processed at temperatures between 500 and 850 °C.

In order to measure the capacitance change, a resonant technique is employed, in which a planar spiral inductor coil fabricated using ceramic-based integral passive techniques is electrically connected to the capacitor. These components form a passive resonant LC circuit, in which the resonant frequency varies inversely with the square root of the capacitance. Thus, as the external pressure increases, the capacitance increases and the resonant frequency of the LC circuit decreases. To achieve passive wireless telemetry, the circuit is placed in proximity to an external loop antenna coil and the impedance and phase response of the antenna coil are monitored as a function of frequency by an impedance meter. At frequencies far from the sensor frequency (and below the self-resonant frequency of the antenna itself), the antenna appears as an inductance, with a rising impedance response with frequency and a phase shift of +90 degrees. At the sensor resonant frequency, the antenna impedance decreases and the phase response of the antenna
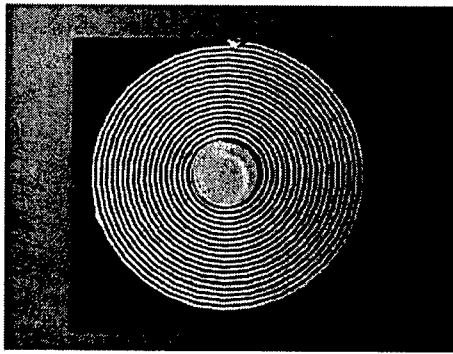
Figure 1. Fabricated micromachined ceramic pressure sensor using Ag screen-printed metallic elements.

drops from +90 degrees. Therefore, the resonant frequency occurs at the phase minimum, which shifts downward in frequency with increasing pressure.

Ceramic pressure sensors were designed, fabricated, and wirelessly tested at high temperatures and pressures. The performance of one of the sensors is shown in Fig. 2. The data show a temperature dependence of the resonant frequency. The quality factor is determined from the measured data using a standard bandwidth measurement. The quality factor as a function of temperature is shown in Fig. 3. It shows that the resonant frequency decreases with increasing temperature and that the quality factor decreases with increasing temperature. This is due to the effect of temperature on the dielectric constant of the capacitance and the series resistance. The pressure sensor array concept, that is more than one sensor read out simultaneously by a single antenna, has also been demonstrated. Each sensor is designed to have a different characteristic resonant frequency range The array, consisting of two pressure sensors, was tested at temperature (25-300°C) and pressure (0-7 bar).

The mechanical stability of the ceramic membranes was investigated using bulk pieces of laminate and exposing them to strain and temperature. The results showed that the ceramic laminate undergoes negligible additional strain at temperatures up to about 500°C. However, at temperatures greater than this, the ceramic laminate material will creep. To further assess the impact of creep of the ceramic membranes, a single pressure sensor was tested over a pressure range of 0-7 bar at room temperature (T=25°C). Next, the pressure vessel was heated to 500°C and pressurized to 7 bar. Once the pressure and temperature had stabilized, the sensor was left in place for 120 hours. After the sensor was cooled back to room temperature, the sensor was tested over the same pressure range.

The measured resonant frequency as a function of pressure before and after the creep test are plotted in Fig. 4. The criterion for this experiment is that the sensitivity of the sensor should not change. The results show that the while the value of the resonant frequency at each pressure is different, there was no change in the sensitivity of the sensor after the long-term exposure test.

Figure 2. Resonant frequency dependence on pressure (0-7 bar) and temperature (25°C-400°C) for sample sensor.

Figure 3. Quality factor for 0 bar and 25-400°C for the pressure sensor of Fig.2.

Figure 4. Ceramic sensor creep test results.

OPTICAL SENSORS (PI: SEITZMAN)

This research is based on the use of spectroscopic techniques to monitor combustor conditions. The goal is to design rugged sensor strategies to allow the detection of overall combustor performance and turbine inlet conditions. Both active and passive sensor approaches have been developed.

Much of our efforts have focused on a sensor approach for monitoring water mole fraction and temperature uniformity in the exit plane of a high pressure gas turbine combustor. The sensor is based on infrared line-of-sight absorption measurements of water. Unlike most absorption sensors previously proposed for engine applications, the current approach includes the possibility of employing a broadband IR source with a tunable bandpass filter. The sensor monitors the absorption due to water at least three wavelengths: one wavelength (λ_I) where the absorption (for a fixed pressure) is linearly proportional to the water mole fraction, but nearly independent of temperature; and two wavelengths where the absorption is monotonically increasing (λ_H) and decreasing (λ_C) with temperature. Thus, absorption measurements at λ_H are more sensitive to the presence of hot gases, while measurements at λ_C are biased towards cold gases.

Based on λ_I, wavelength that is nearly independent of temperature, we have shown previously through simulations that the sensor can determine the water content of a uniform, high pressure combustor exhaust and therefore be able to monitor overall combustor health. The uniformity of the temperature in the gases between the IR source and the detector can also be monitored by comparing the temperatures reduced by: 1) using the ratio of the absorption at λ_H to that at λ_I, and 2) the ratio of the absorption at λ_C to that at λ_I. Thus, we get two temperatures, which agree only when the flow is nearly uniform. The overall intent is to eventually create an active control system that would try to null the difference between these two inputs.

The meaningfulness of the difference between these two temperatures is illustrated
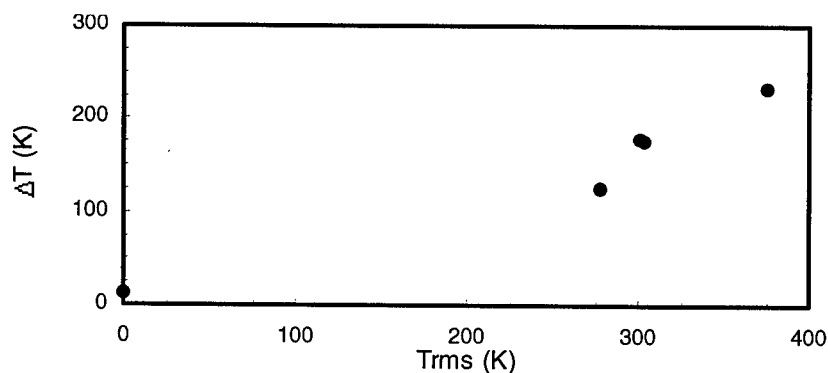
Figure 5. Relationship between the differential sensor output, $\Delta T = \overline{T}_{hot} - \overline{T}_{cold}$, and the rms temperature deviation, T_{rms}, for the five temperature profiles having the same average temperature.
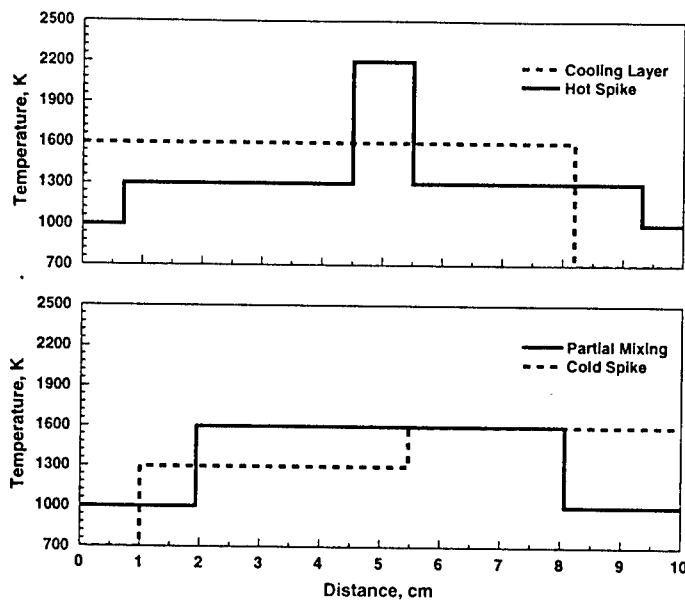
Figure 6. Test profiles of temperature across a 10 cm path through the exit plane of a combustor.

in Fig. 5. The difference signal (ΔT) is compared to the rms deviation of the temperature profile, for various profiles, see Fig. 6. The rms deviation was chosen since it scales with the square of the difference between the temperature at a given point and the mean temperature. Thus, it more heavily weights the large temperature fluctuations in the profile, and the largest temperature fluctuations will have a much more significant impact on turbine blade health than small deviations. As seen in Fig. 5, the sensor output (ΔT) scales roughly linearly with the rms deviation of the temperature profiles.

We have developed a prototype of such a sensor, and built a facility to test it. It is a constant volume combustion bomb, capable of operating up to 40 atm and temperatures up to ~2000 K.

For the proof-of-concept sensor, the source is the filtered ($\lambda_{pass}>1.7$ μm) output of a 1 kW (total power) tungsten halogen light. The output of the lamp is focused and directed through the facility and onto the entrance slit of an IR spectrometer by ZnSe lenses. The spectrometer is used to further refine the bandwidth of light received by the photodiode detector. The effective bandwidth of the transmitted light is indicated in Fig. 7, and corresponds more closely to a Gaussian profile than the Lorentzian presumed in the simulations. The 3.3 nm

Figure 7. Instrument function for proof-of-concept sensor, measured with a narrow bandwidth laser. Lorentzian and Gaussian curves with the same full-width at half-maximum (3.3 nm) are also

measured bandwidth of the device corresponds to a 7 cm^{-1} bandwidth at 2.2 μm, close to the 10 cm^{-1} bandwidth chosen for the simulations.

We have also recently examined the use of passive, emission sensors to monitor local combustor operating conditions, such as local equivalence ratio in nearly premixed, liquid-fueled combustors. Spectral emissions from a swirling, gas turbine model combustor have been characterized over a range of operating conditions (fuel flow rate, air flow rate, and inlet air temperature). The data show that the primary combustion emissions from CH, C_2 and OH, can be used to indicate the overall equivalence ratio and heat release from the flame, at least with sufficient accuracy to be useful in active control strategies. Results will be included in the presentation.

CROSSED-PLANE LASER IMAGING
OF
PREMIXED TURBULENT COMBUSTION PROCESSES

F. C. Gouldin

Mechanical and Aerospace Engineering
Cornell University, Ithaca, NY   14853

Overview

The objective of this research is to measure flamelet normal vectors in premixed turbulent flames. Normal vector data can be used to calculate important quantities such as the flamelet surface density, Σ, which is a measure of the wrinkling of the flamelet due to turbulence, and the rate of reactant consumption per unit volume in the flame, $<w>$, which appears as an unclosed term in premixed flame models and is related to the burning intensity. Instantaneous flamelet normals are measured in three dimensions using Crossed-Plane Imaging, a technique developed at Cornell with ARO support. In addition, Crossed-Plane Imaging provides data for flamelet crossing density and for the mean reaction progress variable field. The use of the technique and its extension to Crossed-Plane Rayleigh Imaging are expected to provide information about the form of flamelet normal PDFs, Σ, $<w>$, the overall burning intensity in the form of the burning rate integral, B_T, and instantaneous temperature gradients for as many different flames as possible. This work will provide new understanding of and expressions for Σ and I_o, the mean stretch factor, which appear in the equation for $<w>$.

I. Introduction

Premixed turbulent combustion has a broad range of practical applications, from powering many of the vehicles we drive to electrical power generation via stationary gas turbines. Many premixed turbulent flames fall within what is called the flamelet regime, in which reactions are confined to thin sheets, called flamelets, separating regions of reactants and regions of products. For flames in the flamelet regime, the burning intensity is related to the degree of wrinkling of the flame: the wrinkling serves to increase the mean flamelet surface area per unit volume (Σ) and hence the rate at which reactants are consumed. Σ can be written as a function of the distribution of the flamelet surface normal vector, $\underline{N}$, and the flamelet crossing density, n_c. Σ is an extremely important quantity in describing and modeling premixed turbulent flames because it is related to several other important quantities, such as the mean rate of creation of products per unit volume, $<w>$, which appears as an unclosed term in premixed turbulent combustion models, and B_T, which describes the overall burning intensity of a flame. Therefore, the ability to measure $\underline{N}$ and n_c is of vital importance to the modeling and description of premixed flames in the flamelet regime.

Crossed-Plane Imaging was developed in 1997 [1] at Cornell with ARO support to provide, for the first time, data of $\underline{N}$ in three dimensions. The first measurements made were performed to validate the technique and measure $\underline{N}$ in laboratory flames [1,2]. Repeated measurement of $\underline{N}$ allowed the PDF of $\underline{N}$ to be determined. It was found that, for laboratory V-flames, the PDF of $\underline{N}$ has a simple functional form depending on a single parameter, ξ. n_c data were used with the PDF

of $\underline{N}$ to determine Σ and B_T. More recently, the technique has been applied to a practical pre-mixed turbulent combustion system, an SI engine [3]. Also, a study was performed to examine the variation of the PDF of $\underline{N}$ for flames with different Markstein numbers, Ma [4]. Ma effects are of interest because it is expected that the PDF of $\underline{N}$ will be highly dependent on Ma.

II. Crossed-Plane Imaging

This technique is a significant extension of imaging techniques such as Laser Tomography or Planar Laser Induced Fluorescence (PLIF). In Laser Tomography, oil droplets are added to the reactants, which are consumed within the flamelet, so they are not present in the products. A pulsed laser sheet is propagated through the flame, and an image is recorded normal to the laser sheet. The image contains bright reactant regions, where light is scattered from the oil droplets, and dark product regions, where oil droplets are not present and hence no light is scattered. The flamelet is located by the interface of the bright and dark regions, and fitting this interface provides two dimensional information about $\underline{N}$. PLIF can be used in much the same way, except that the laser frequency must be chosen such that it excites to fluoresce a molecule in the reactants that is not present in the products. Crossed-Plane Imaging involves two simultaneous Laser Tomography or PLIF measurements. Two orthogonal, pulsed laser sheets intersect along a line, referred to as the measurement line. At points where the measurement line intersects the flamelet, tangent vectors to the flamelet surface in each illumination plane are determined, and used to calculate $\underline{N}$ in three dimensions. Crossed-Plane Imaging can also be used to measure n_c, by counting flamelet crossings along lines spanning the turbulent flame brush, and to construct the $<c>$ field, by making the recorded images binary and averaging.

The most significant discovery so far of Crossed-Plane Imaging measurements has been that the PDF of $\underline{N}$ appears to have a universal form. It was found that the surface weighted PDF of $\underline{N}$ takes the simple, single parameter form

$$P^s(\phi, \theta)\sin\phi d\phi d\theta = A \exp(-\phi^2/\xi^2) \sin\phi d\phi d\theta$$

when written in spherical coordinates with the polar axis aligned with the mean normal, $<\underline{N}>$, or equivalently with the normal to a mean progress variable constant ($<c>$) surface, $\underline{N}_{<c>}$ [2-4]. ϕ is the polar and θ is the azimuthal angle, and A is a normalization constant. Furthermore, for all of the flames studied to date, $<\underline{N}>$ and $\underline{N}_{<c>}$ are aligned [3, 4]. In surface weighted statistics, the

Figure 1. Marginal PDFs of ϕ and θ for an ethylene-air V-flame. Measured data are shown as points, and fits of the marginal PDFs based on the fit of the joint PDF of $\underline{N}$ are shown as solid
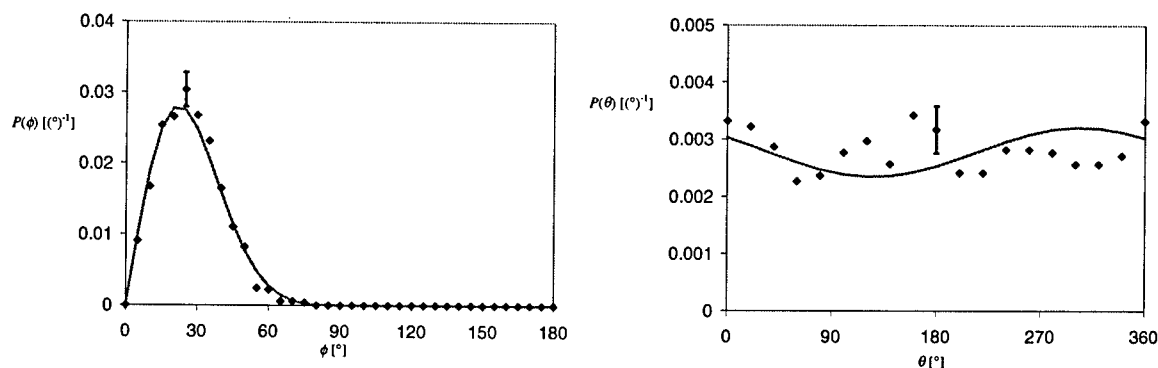
lines.

probability of $\underline{N}(\phi, \theta)$ in the range ϕ to $\phi+d\phi$ and θ to $\theta+d\theta$ is proportional to the fraction of the surface area of the flamelet with normal vectors in this range. The fact that the form of this fit has

applied to all the flames studied so far is promising because it indicates that the distribution of flamelet normals can be written in a simple form dependent on a single parameter, ξ.

III. SI Engine Study

To demonstrate the feasibility of applying the technique in a practical combustion system, measurements were performed on SI engine flames in a collaboration with workers at Sandia National Laboratory [3]. Crossed-plane acetone PLIF measurements were made at 600, 1200 and 1800 RPM using an experimental SI engine with appropriate optical access, providing data for ξ, n_c and Σ. It was found that for similar normalized turbulence intensity levels, $\underline{N}$ data are much more broadly distributed for engine flames than for previously studied V-flames, yet the functional form of the PDF is the same. $<c>$ constant contour images were also generated, Fig. 2, which describe the width and shape of the turbulent flame brush. $\underline{N}$ and n_c data were used to estimate the overall engine mass burning rate, and the results compared to the predictions of a thermodynamic model based on the cylinder pressure trace. It was found that the burning rate estimate based on $\underline{N}$ data significantly over-predicts the mass burning rate estimate from pressure trace data. Because no information about I_o was measured, we assumed $I_o = 1$ to estimate the mass burning rate from $\underline{N}$ data, which may be the cause of the discrepancy.
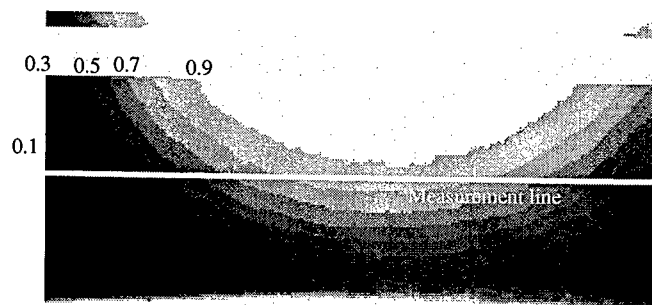
Figure 2. $<c>$ constant contours for an SI Engine Flame. The spark plug is located above the image and the piston is at the bottom. Also shown is the measurement line. The $<c>$ field is divided into tenths, each represented by a gray scale color. The boundary of two gray scale regions is a $<c>$ constant contour.

IV. Influence of *Ma*

The purpose of these measurements was to study how the distribution of $\underline{N}$ varies with Markstein number, *Ma*. There are a number of papers in the literature indicating that quantities describing the burning intensity of premixed flames are dependent on Lewis number, *Le*, and *Ma*, see [5,6] for example. *Ma* describes the response of a mixture's laminar flame speed to stretch. Measurement of positive *Ma* flames (ethylene-air) and negative *Ma* flames (methane-air) were made over a range of turbulence intensities, *u'*. It is expected that negative *Ma* flames will exhibit more wrinkling than positive *Ma* flames for the same value of *u'* normalized by the unstretched laminar flame speed, u'/S_L^o. The degree of wrinkling was quantified in two ways, first with values of ξ, and second by using measurements of n_c and the PDF of $\underline{N}$ to determine Σ. Because Σ varies across the flame brush, a spatial average across the flame brush is used to provide a single quantitative value describing the degree of wrinkling, $\overline{\Sigma}$. Values of ξ and $\overline{\Sigma}$ are plotted as a function of normalized turbulence intensity in Fig. 3. It can be seen that the values of ξ for the ethylene-air (positive *Ma*) flames are systematically larger than for the methane-air (negative *Ma*) flames, contrary to expectations. There is no observable difference between $\overline{\Sigma}$ values for positive and negative *Ma* flames at similar u'/S_L^o. These results are surprising, and warrant further investigation to determine if the results are general.

V. Future Work

The most exciting study we are currently planning is a novel experiment which is an extension of Crossed-Plane Imaging to Crossed-Plane
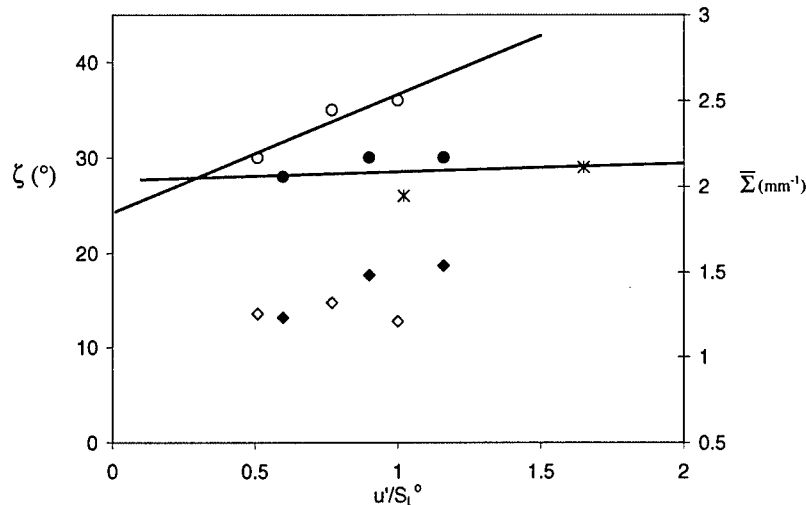
Figure 3. ξ (circles) and $\overline{\Sigma}$ (diamonds) as a function of u' for negative/unstable Ma (closed) and positive/stable Ma (open) flames. Also shown are ξ data from previous measurements of negative/unstable Ma flames (asterisks) [2].

Rayleigh Scattering, which will allow simultaneous measurement of $\underline{N}$ for isothermal surfaces and the magnitude of the temperature gradient. Number density information provided by Rayleigh scattering images can be used to calculate temperature directional derivatives across the flamelet in each measurement plane. By making simultaneous orthogonal measurements of temperature and directional derivatives, the magnitude of the temperature gradient in three dimensions and isothermal surface normals can be measured, providing additional information about the flamelet structure and reactant consumption rates.

Currently we are making additional measurements to study Ma effects, including higher turbulence intensity flames (and hence higher Karlovitz number flames), and a study of how ξ varies with axial distance from the V-flame stabilizing rod. We would also like to measure how ξ varies with $<c>$ for V-flames, and study the uncertainty in ξ. Additional measurements of SI engine flames are also under consideration, in order to build on the previous work by studying more precisely how the distribution of flamelet orientations evolves during a cycle and varies with engine speed, and to study the effects of cycle-to-cycle variation. Measurements in different burner configurations are also planned.

VI. Summary

Crossed-Plane Imaging was developed so that flamelet normals can be measured, expanding our physical description of premixed flames in the flamelet regime and providing data for important descriptive quantities of these flames. Most recently, the technique has been successfully applied to measurements in a practical device and has provided interesting results related to Ma effects in premixed flames. There is still a large amount of work to be done with Crossed-Plane Imaging. The development of Crossed-Plane Rayleigh Scattering, in particular, will add a powerful new dimension to the technique by allowing isothermal surface normals and temperature gradients to be measured, further expanding our knowledge of the chemical and physical processes in turbulent premixed flames.

References

1. Bingham, D. C., M. S. Thesis, Cornell University, Ithaca, NY (1998).
2. Bingham, D. C., Gouldin, F. C., Knaus, D. A., *Proc. Comb. Inst.* **27**: 77-84 (1998).
3. Knaus, D. A., Gouldin, F. C., Hinze, P. C., Miles, P. C., SAE Paper 1999-01-3543, 1999.
4. Knaus, D. A., Gouldin, F. C., to appear in *Proc. Comb. Inst.* **28** (2000).
5. Bradley, D., *Proc. Comb. Inst.* **24**: 247-262 (1992).
6. Wu, M. –S., Kwon, S., Driscoll, J. F., Faeth, G. M., *Comb. Sci. Tech.* **73**: 327-350 (1990).

PLANAR IMAGE PARTICLE ANALYZER FOR WHOLE FIELD SPRAY APPLICATIONS

Dr. Cecil F. Hess

MetroLaser 180010 Skypark Circle, Suite 100, Irvine, CA 92614

Summary/overview

The purpose of this work is to develop a whole-field measurement technique that is capable of simultaneously sizing multiple transparent droplets on a plane from scattered light features that are independent of laser beam intensity and obscuration. Light scattered by reflection and refraction from droplets immersed in a laser sheet will be recorded with digital holography and subsequently analyzed to produce the droplet size distribution as a function of position anywhere and everywhere on the sheet. One of the major challenges is transitioning from optical holography to digital holography. The small size of the CCD and large pixel size, limit the size of the measurement region and the smallest measurable particle.

technical discussion

The technique is called Planar Image Particle Analyzer (PIPA). The general configuration of PIPA is given in **Figure 1**. A laser sheet illuminates the particles and their scattered light (object beam) is collected by a receiver of finite f-number (f/#) and placed at a collection angle θ. A beamsplitter mixes the reference beam with the object beam on the hologram.
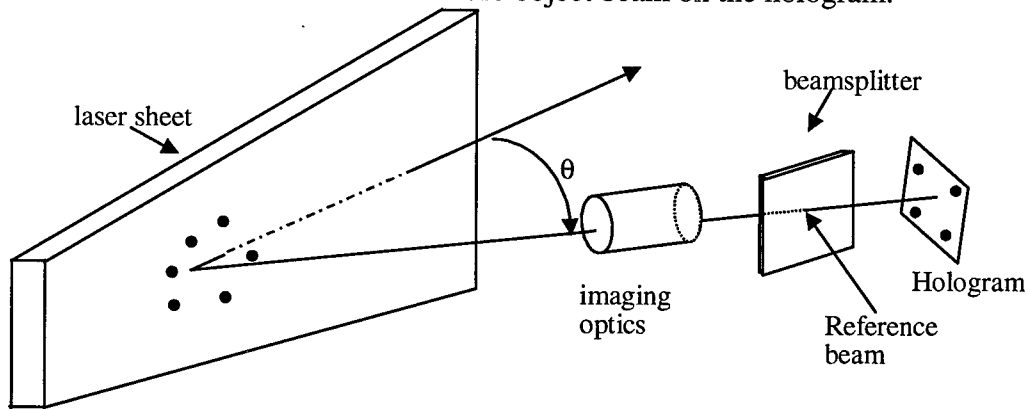
Figure 1. Schematic of PIPA.

Each particle will scatter a fringe pattern that results from the interference of the refracted and reflected light. The number of fringes corresponding to each particle is given by:

$$\#\text{fringes} = \frac{R_E L'}{f\# \lambda},$$

(1)

where $R_E L'$ represents the separation between the refraction and reflection spots of each droplet. This is related to the droplet diameter by simple trigonometric relationships. Note that the number of fringes anywhere in the reconstruction is only a function of the receiver f/# and the separation between the refraction and reflection spots from which the droplet size is obtained.

73

By way of example, for a collection angle $\theta = 68°$ and an index–of-refraction $n_2 = 1.33$, the refraction and reflection spots have nearly the same intensity.

For these conditions $R_E L' = 0.91$ d. Therefore, from Eqn. 1, we obtain

$$\# \text{ fringes } = \frac{R_E L'}{f \# \lambda} = \frac{0.91 d}{f \# \lambda}. \tag{2}$$

The minimum particle size that can be measured from the recorded fringes could be established if we require collecting at least one fringe for each particle image. Thus, from Eqn. 2 we obtain

$$d_{min} = \frac{f \# \lambda}{0.91} = 1.1 f \# \lambda. \tag{3}$$

Research Conducted

Phase I research at the time this abstract was written (three months into the program) has consisted of the following major elements:

1. Numerical analysis of PIPA using optical holography and digital holography.
2. Design and construction of optical holography breadboard.
3. Photographic and holographic spray droplet data acquisition and analysis.
4. Identification of digital holography strategies and their compatibility with the convolution theorem.

1. Numerical analysis

We have analyzed and concluded that the 3-D capability of holography makes global spray measurements in dense sprays possible with the PIPA technique. The holographic technique requires the ability to manipulate the recorded images one-by-one at any plane. Two forms of holography are being studied: 1) optical holography, and 2) digital holography. The former is the traditional form of holography that uses film, thermoplastic materials, or non-linear optical materials to record the hologram. Here, the reconstruction of the hologram is performed optically. In digital holography, the hologram is recorded directly onto a CCD and the reconstruction is performed mathematically. Each of the holographic strategies have pros and cons associated with them and we have opted to pursue both during the Phase I effort. The holographic film offers high resolution (5000 lines/mm) and is typically available in large formats (4" x 5" and larger). In contrast, the CCD has a resolution of 10 μm per pixel and it comes in smaller format sizes (0.5" to 1.5"). This limited size and resolution calls for strategies such as *Fourier Transform Holography* to take full advantage of the area of the CCD.

Unlike photography, holography permits recording signals in the far-field with subsequent reconstruction and analysis at any convenient plane. The recording of holograms requires the introduction of a reference beam. The angle between the object and reference beams is defined by the resolution of the recording media (in the case of a CCD, it is defined by the pixel pitch) according to the following relationship:

$$\text{Film resolution or pixel pitch } = \frac{\lambda}{2 \sin\left(\frac{\theta_{max}}{2}\right)}. \tag{4}$$

For $\lambda = 0.5$ μm and pixel pitch $= 10$ μm, $\theta_{max} = 0.05$ rad.

In PIPA, particle images appear as two point light sources that are separated by approximately 90% of the particle diameter. (See **Figure 2**). Thus, the off-axis image of the particle would appear as two bright points where the separation can be related to particle size. If the resolution of the recording medium is not adequate to record two closely spaced spots, the measurement strategy would have to shift to recording the scattered light away from the image plane where the light emmanating from the two spots interferes to produce a fringe pattern. Thus, at an out-of-

focus plane, the particles appear as a small area with fringes within. Size information can subsequently be obtained from the fringes. See **Figure 3**.
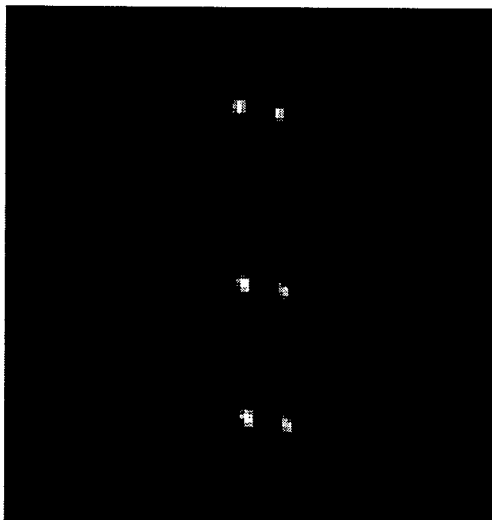
Figure 2. Refraction and reflection spots of monodisperse droplets of 145 µm diameter.
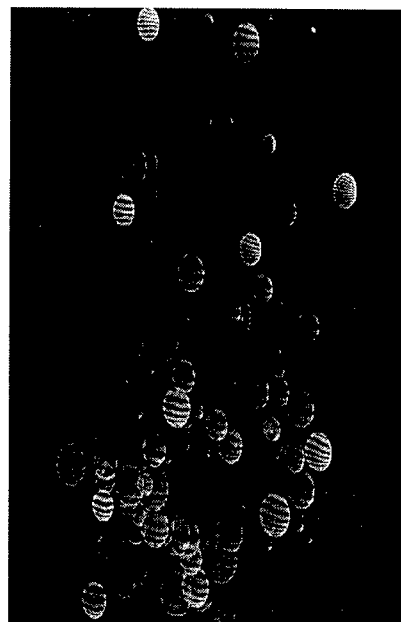
Figure 3. Images corresponding to small drops (2 to 12 µm) produced by ultrasonic humidifier.

With photography one can only record and examine one measurement plane. The problem of measuring the out-of-focus plane with photography is that for high particle concentration, the areas corresponding to individual particles overlap, making the fringe analysis difficult at best and impossible under some conditions. Glover and co-workers[†] used the out-of-focus strategy and they required fairly large areas to resolve the large number of fringes associated with large particles. Note for example how in the bottom left region of **Figure 3** the signals from adjacent particles overlap.

Holography enables the selection of the best measurement strategy for each particle. That is, the large particles could be measured from the separation between the two spots while the small particles could be measured from their fringe pattern. *One would need to be able to bring the particle image in and out–of-focus to choose the stragegy that best suits the measurement. Moreover, one would need to be able to bring clusters of adjacent particles in focus at the same time to be able to filter (block) some particles while analyzing others.* **Figure 4** illustrates the process of recording planes that are parallel to the laser sheet by placing the film at the Scheimpflug angle.

---

† A.R. Glover, S.M. Skippon, and R.D. and Boyle, "Interferometric laser imaging for droplet sizing: a method for droplet-size measurement in sparse spray systems", *Applied Optics*, Vol. 34, No. 36, pp. 8409-8421, 1995.
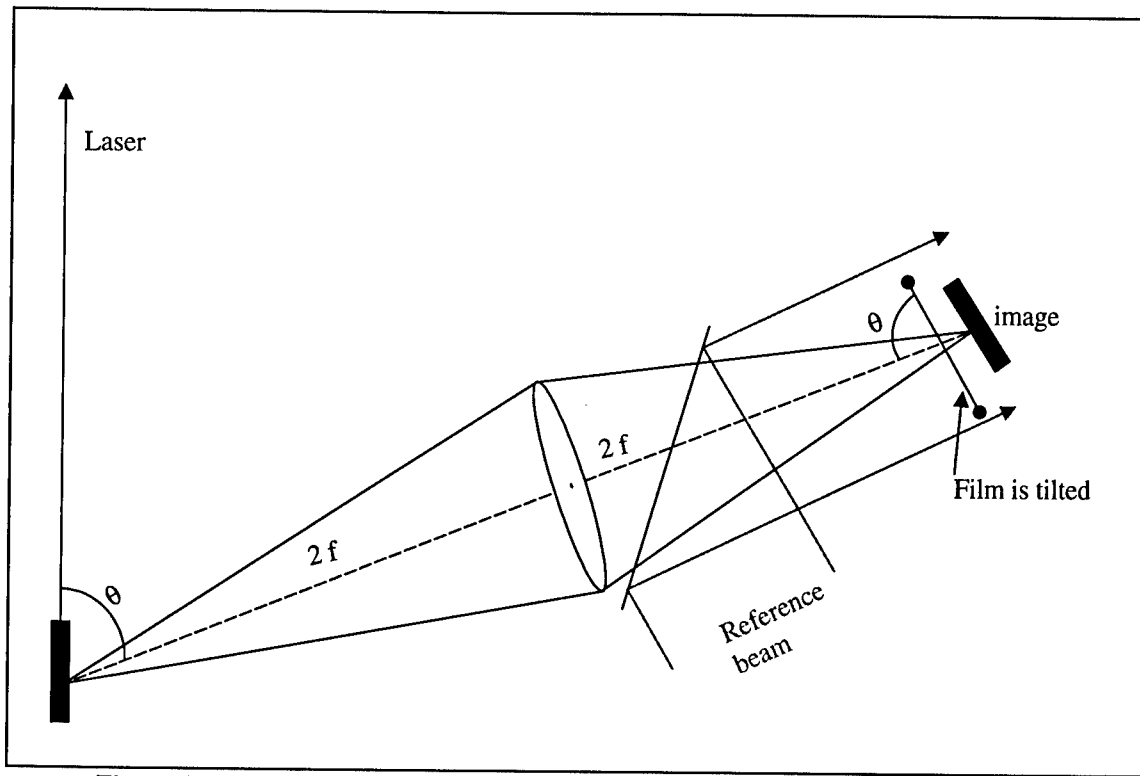
Figure 4. Schematic of imaging holography with film tilted at the Scheimpflug angle.

A controlled experiment with a single 250 ± 3-μm glass bead placed in the probe volume was run under the following conditions:

- Collection angle $\theta = 30°$.
- F# = 4.85.
- Magnification = 5.
- The film was perpendicular to the optical axis of the lens.
- The separation between spots at the image plane was measured with an eyepiece to be 1 mm.
- The number of fringes contained within the interference area was estimated to be 79.

The particle diameter of a glass bead can be estimated from either the spot separation or from the number of fringes according to the following relationships (see Eqn 2):

$$d = 1.24 \; x \; \#fringes \; x f\# \; x \; \lambda = 1.24 \; x \; 79 \; x \; 4.85 \; x \; 0.532 = 253 \; \mu m$$
$$d = 1.24 \; x \; spot \; separation/Magnification = 1.24 \; x \; 1 \; mm/5 = 250 \; \mu m$$

76

PLANAR THERMOMETRY IN SOOTING TRANSIENT DIFFUSION FLAMES

Principle Investigator: William Roberts

Dept. Of Mechanical and Aerospace Engineering
Box 7910
North Carolina State University
Raleigh, NC 27695-7910

SUMMARY/OVERVIEW:

It is well established that laminar counterflow diffusion flames under steady rates of strain exhibit many of the essential features of turbulent diffusion flamelets. However, all real turbulent flames are subjected to unsteady rates of strain due to the inherent unsteadiness of the flow field. Depending upon the frequency and amplitude of these oscillations, these unsteady strain rates may have a substantial impact on the fluid mechanic-chemical kinetic interaction and, therefore, effect the reaction zone temperature and the processes controlling the production of soot. The goal of this project is to quantify the effect of unsteady strain rates on the reaction zone by measuring the temperature field instantaneously throughout the oscillation period using optical diagnostic techniques.

TECHNICAL DISCUSSION:

Turbulent diffusion flames are of particular interest because of their presence in most practical combustion devices. Flamelet theory is a method that characterizes turbulent diffusion flames as a collection of strained, laminar, one-dimensional flamelets [1,2], which are solely dependent upon the mixture fraction and instantaneous scalar dissipation rate. The flamelets are assumed to respond quasi-steadily to the unsteady strain rates of the turbulent flow-field. Recent computational and experimental studies, however, have shown that conditions exist where this assumption is invalid [3-6]. If the turbulent Reynolds number is sufficiently large, there exists a range of eddy sizes where the characteristic turnover time of the smallest eddies is comparable to the diffusion time of the laminar flamelet [3]. The large-scale eddies establish the magnitude of the mean strain rate, while the fluctuations around this mean value are caused by the smaller eddies. These conditions can lead to a wide range of characteristic frequencies [4]. Thus, it is necessary to investigate the frequency response of flamelets in an attempt to extend the applicability of the flamelet theory.

Due to the stoichiometry in a counterflowing propane-air diffusion flame, the flame resides on the airside of the stagnation plane. The transport of fuel is a result of diffusion, while the transport of oxidizer to the flame is a result of both convection and diffusion. This convective-diffusive coupling on the airside effectively links the chemistry of the flame with the flow-field dynamics. A flame that is subject to a cyclical velocity field, with a characteristic cycle time much greater than that of any of the relevant transport times of the flame, should respond in a quasi-steady manner. As the characteristic cycle time of the velocity fluctuations decreases and approaches the relevant transport times of the flame, unsteady or transient characteristics in the flame behavior begin to appear.

Experimental Apparatus:

The unsteady counterflow diffusion flame burner is a modification of the design described in [7], and described in detail in [8]. Briefly, the oxidizer and fuel tubes are 25.4 mm in diameter and have a 12.7 mm separation distance, with many fine screens at the exits to assure uniform exit velocity profiles. Plenums located on the fuel and oxidizer sides are capped with loudspeakers which are driven by an amplified signal generator and impose the velocity fluctuations on the flame.

Velocity and relative [OH] measurements were made simultaneously as a function of initial steady strain rate (SSR) and frequency and amplitude of the imposed velocity oscillation. Measurements were made at four temporal locations within the sinusoidal voltage oscillation applied to the speakers: zero amplitude with positive slope (0+), maximum amplitude (Max), zero amplitude with negative slope (0-), and minimum amplitude (Min). Four forcing frequencies in investigated: 30, 50, 100, and 200 Hz.

To acquire simultaneous velocity and relative [OH], a dual PIV-OH PLIF measurement system was used. The PIV measurements were made using two frequency doubled Nd:YAG lasers (λ = 532 nm); in the probe region, the thickness of the two sheets were set to be 500 μm. Hollow zeospheres, having a mean diameter of 2.2 μm, were used to seed the airflow. PIV images were recorded using a Kodak interline-transfer digital camera (1008x1012 pixels) fitted with a 105 mm lens. An interference filter centered on 532 nm was used to eliminate background flame emission. Interrogation regions composed of 64 pixel squares (0.9 mm x 0.9 mm) with 75% overlapping were employed for the velocity measurements. Custom software including a cross correlation algorithm was used to derive the velocities.

The relative [OH] measurements were made using a Nd:YAG (which also served as one leg of the PIV system) pumped dye laser, which was flowing Rhodamine 590 dye, and the output of which was doubled down to ~282 nm, yielding a 10 ns pulse of approximately 10 mJ. The $R_1(8)$ transition of the $A^2\Sigma^+ \leftarrow X^2\Pi(1,0)$ band was excited and broadband fluorescence was detected using an ICCD camera. This transition was chosen because of its reduced sensitivity to temperature fluctuations. A 105 mm/f4.5 lens fitted with UG-11 and WG-295 filters was used to collect the OH fluorescence.

Temperature measurements were made by measuring, nearly simultaneously, the ground state population in two different rotational levels of OH. The ratio of these two different populations can be directly related to the temperature by assuming thermodynamic equilibrium between the rotational energy levels. If the fluorescence yield is J-state independent, then the ratio of these two PLIF images can be appropriately calibrated to yield a temperature image. The OH measurements were made using a pair of Nd:YAG pumped dye lasers, providing approximately 10 mJ at ~282 nm and 286 nm. The $Q_1(5)$ and $Q_1(14)$ transitions of the $A^2\Sigma^+ \leftarrow X^2\Pi(1,0)$ band were excited and broadband fluorescence was detected by a pair of ICCD cameras, with the same lenses and filters as above. A Henken burner with radiation corrected thermocouple measurements served as the calibration source.

Results and Discussion:

The measured strain rates and FWHM of the OH field for an initial SSR of 74 s^{-1} are plotted in Fig. 1 at the four temporal locations in the speaker oscillation for two of the four forcing frequencies investigated. At a forcing frequency of 50 Hz, the instantaneous strain rate continuously increases from the temporal locations of 0+ to 0-, as seen in Fig 1a. During this period, the OH field narrows continuously. Between the 0- and Min locations, the instantaneous strain rate decreases and the OH layer thickens. It was also found that when the instantaneous strain rate for the forced flame was above the steady strain rate, the OH field was thinner than the steady case. The converse of this was also found to be true. The strain rate and OH field behavior at a forcing frequency of 30 Hz mimicked the behavior found at 50 Hz. If the flame were responding quasi-steadily, increasing the strain rate would be accompanied by an increase in the convective velocities at the edge of the convective-diffusive zone of the flame. With this elevated supply of cool reactants, the flame would move closer to the stagnation plane and would also cool and become thinner. Thinning of the flame with increasing strain rate has been found previously in experimental and numerical studies [9]. Thus, from Fig 1a, the OH field, and hence the flame, is ob-

served to be responding to the instantaneous strain rate in a quasi-steady manner, at least at these lower forcing frequencies. Note that cyclic behavior of the OH concentration has been found previously in a N_2 diluted methane-air flame [6].

As the forcing frequency was increased to 200 Hz, the strain rate was found to decrease between the temporal locations of 0+ and Max and then increased continuously throughout the remainder of the period, as seen in Fig 1b. This is opposite to the behavior found for lower-frequency oscillations. The OH field width was found to increase sharply between the temporal location of 0+ and Max, increase very slightly between Max and 0-, and then decrease heading towards the Min location. Thus, for the 200 Hz case, between the Max and 0- locations, there is an increase in the instantaneous strain rate that is accompanied by an increase in the width of the OH layer. Similar results were seen at 100 Hz oscillation frequency, where between the 0- and Min locations, a decrease in the instantaneous strain rate was accompanied by a decreasing width of the OH layer. Thus, the OH field does not respond quasi-steadily to the instantaneous strain rate at forcing frequencies above 100 Hz.

A flame temperature marker was derived to help confirm the phase shifting behavior of the maximum temperature. Although no corrections for thermophoretic forces have been made to the velocities in the heat release zone, the difference between the maximum velocity in the reaction zone and the minimum velocity in the preheat zone can be used as an indicator of the flame temperature. The increasing velocities in the reaction zone are a result of density changes resulting from heat release, so the general behavior of the changes in velocity should follow the temperature trend. This velocity difference will be referred to as the dilatation velocity. Fig 2 shows the phase difference between the air velocity and the dilatation velocity as a function of frequency and initial steady strain rate. The magnitude of the phase difference was found to increase with increasing forcing frequency, which suggests there is a systematic increase in the phase difference between the velocity and the temperature. The time associated with the increasing phase difference is likely related to a diffusion time. As the forcing frequency is increased, the time rate of change of reactants delivered to the edge of the convective-diffusive zone increases; however, a finite amount of time is still necessary for the reactants to diffuse to the flame front. As the forcing frequency increases, this diffusion time becomes larger relative to the cycle time of the oscillation, which in turn shows up as an increasing phase difference. This "diffusion limited" response has been observed in previous numerical studies [3,4].

The two-color OH PLIF thermometry results are still being analyzed. To date, only a single steady strain rate has been analyzed for the two lower frequencies. This data is presented below in Fig 3. In Fig. 3a., the lower amplitude oscillation, the strain rate varies from a low of $41s^{-1}$ to a high of 46.5 s^{-1} throughout the oscillation. The temperature is observed to be in phase with the strain rate, i.e., when the strain rate is high, the maximum flame temperature is low. Thus, again we see that at 50 Hz, the heat releasing reactions are responding quasi-steadily to the instantaneous strain rate. In Fig 3b, the applied sine wave amplitude is increased while the frequency and initial steady strain rate remains the same. The oscillations in strain rate and temperature are seen to grow as well, but the chemistry dictating heat release continues to respond in a quasi-steady manor. It is expected that the temperature and strain rate will become de-coupled as the frequency is increased.

References:

1. Peters, N., Prog. Energy Comb. Sci., 10:319-339 (1984).
2. Bray, K.N.C., Peters, N., Turbulent Reacting Flows, Academic Press Ltd, (1994), p. 63.
3. Im, H.G., Law, C.K., Kim, J.S., Williams, F.A., Combust. Flame, 100:21-30 (1995).
4. Egolfopoulos, F.N., Campbell, C.S., J. Fluid Mech., 318:1-29 (1996).
5. Darabiha, N., Combust. Sci. and Tech., v86, pp. 163-181 (1992).
6. Brown, T.M., Pitz, R.W., Sung, C.J., Twenty-Seventh Symposium (International) on Combustion, The Combustion Institute, Pittsburgh, PA, 1998, pp. 703-710.
7. Puri, I.K., Seshadri, K., Combust. Flame, 65, 137-150 (1986).
8. DeCroix, M.E., Roberts, W.L., Comb. Sci. Tech v146, pp.57-84, (1999).
9. Sung, C.J., Liu, J.B., Law, C.K., Combust. Flame 102:481-492 (1995).
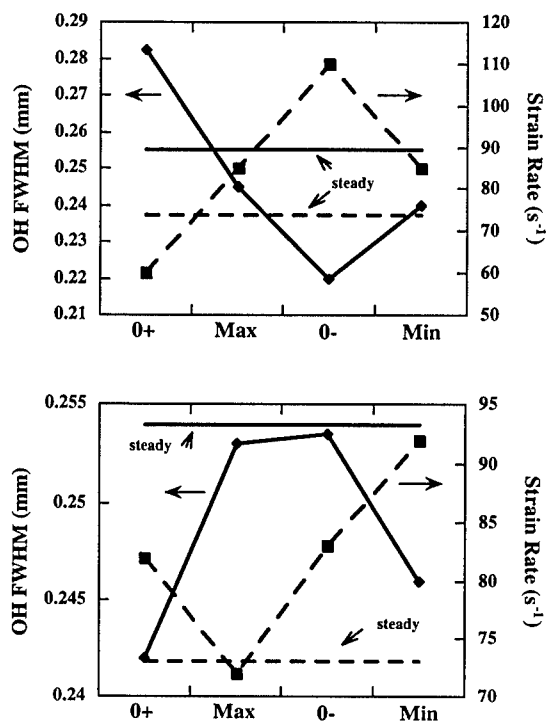
Figure 1 Strain rate and FWHM of the OH field results for SSR 74·s⁻¹ and all forcing frequencies. Top figure shows 50 Hz oscillation frequency and bottom shows 200 Hz.
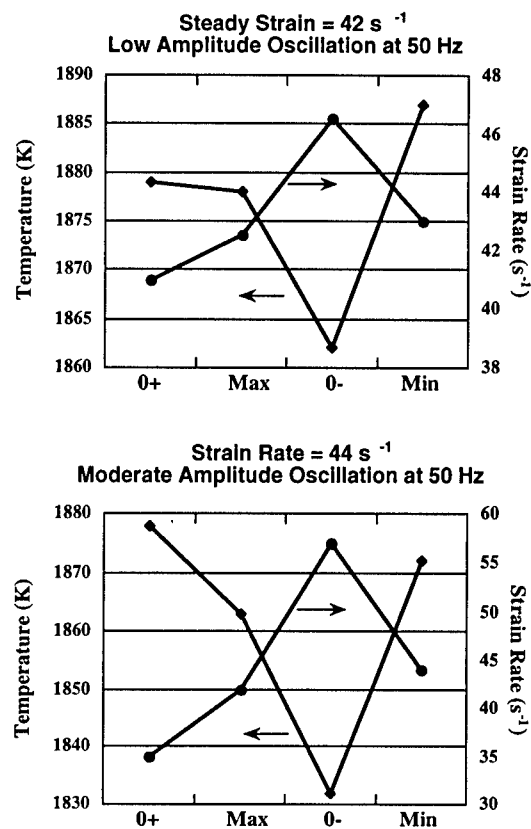
Figure 3. Top figure shows low amplitude oscillation and bottom figure shows moderate amplitude.
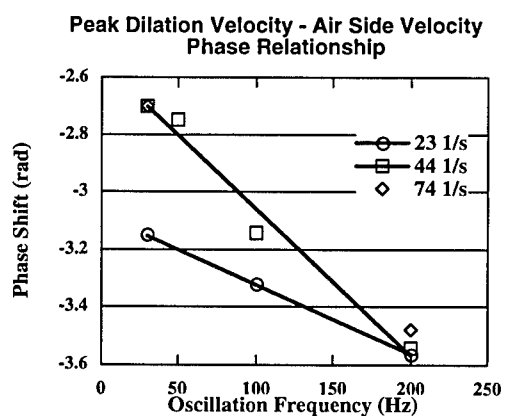
Figure 2. Phase difference relationships between the dilatation velocity and the air velocity.

SIMULTANEOUS MEASUREMENT OF SPECIES CONCENTRATION, TEMPERATURE, AND FLOW VELOCITY IN A FLAME

R. Gupta

Department of Physics
University of Arkansas
Fayetteville, AR 72701

SUMMARY/OVERVIEW

The goal of our experiments is to develop photothermal spectroscopy for a simultaneous measurement of the minority species concentration, temperature, and flow velocity in a flame. Preliminary experiments have been conducted in a cold-flow where all the parameters to be measured are precisely known. We have identified several effects, which, if not corrected for, can lead to large errors. Appropriate theoretical models have been developed to correct for these effects. Analysis of the cold flow data have yielded quite accurate values of the three parameters.

TECHNICAL DISCUSSION

The basic idea behind photothermal deflection spectroscopy (PTDS) is as follows: A laser beam (hereafter called the pump beam) passes through the flame. The laser is tuned to the absorption frequency of the molecules to be measured. The molecules absorb energy from the laser. Subsequently, most of the molecules decay by nonradiative means (i.e., they are collisionally de-excited). Thus, the optical energy eventually appears in the thermal modes of the flame gasses. In other words, the optically irradiated region gets slightly heated. The heating is accompanied by a change in the index of refraction. This refractive index change is probed by another, weaker laser beam which we shall refer to as the probe beam. The change in the refractive index has a spatial profile that mimics the spatial profile of the pump beam. The pump beam is assumed to have a Gaussian spatial profile. Thus, the probe beam experiences an inhomogeneous refractive index, and gets deflected by a small amount. We measure this deflection and the amplitude of the deflection is proportional to the concentration of the absorbing species. We use a pulsed laser for the pump beam. Thus, the absorption of the pump beam produces a pulse of heat. In a flowing medium, the heat pulse travels downstream with the flow. We set our probe beam slightly downstream from the pump beam. We measure the transit time of the heat pulse and from it deduce the flow velocity of the medium. The heat pulse broadens due to thermal diffusion as it travels downstream. From a measurement of this broadening we determine the thermal diffusion constant of the medium. Since the thermal diffusion constant is proportional to the temperature of the medium, we can measure the temperature of the medium. Thus, the measurement of the amplitude, transit time, and the broadening of the photothermal deflection signal can yield meas-

urements of the species concentration, flow velocity, and temperature, respectively, all simultaneously in a single laser pulse.

We have started our experiments in a cold flow (a room-temperature jet of N_2, seeded with 0.5% of NO_2). We chose NO_2 as the seed gas for experimental convenience. NO_2 is gaseous at room temperature, and has a quasi-continuous absorption throughout the visible range of the spectrum. A Q-switched (7ns pulse) frequency-doubled Nd:YAG laser at 532nm was used as the pump beam. A 0.5mW He-Ne laser was used for the probe beam. The deflection of the probe beam was measured by a position-sensitive detector. A long 1/4" O.D. stainless steel tube was used to form a jet of N_2. A laminar flow resulted. The measurements were made very close to the exit of the tube.

Photothermal signals were measured across the cross section of the jet and then analyzed. We found that the measured values of the flow velocity agreed quite well with our expectations. However, the measured value of NO_2 concentration was too low. Moreover, the measured value of the thermal diffusivity was too high. A particularly puzzling result was that the fitted value of the thermal diffusivity increased dramatically near the edge of the jet. After a considerable amount of experimentation, we have been able to determine the reasons for these anomalous results. The first of these is the effect of optical saturation, and the second is the effect of velocity gradient. These effects are described in detail below.

If the intensity of the pump beam is sufficiently high, then it decreases the absorption coefficient of the medium. This is due to the fact that the laser beam transfers some of the molecules from their ground state to their excited state, thus reducing the number of molecules that can participate in the absorption process. This is the usual process of optical saturation, and if not taken into account, would lead to an anomalously low value of the absorption coefficient, and consequently, an anomalously low value of the species concentration. Optical saturation has a surprisingly large influence on the measured values even at quite low intensities. Optical saturation not only reduces the size of the PTDS signal but it also broadens it, because the saturation is spatially dependent. Therefore, unless this effect is taken into account, one gets an anomalously large value of the thermal diffusivity, and consequently an anomalously large value of the temperature.

The second effect that influences the PTDS signal width is the existence of velocity gradient in the flow. In a laminar flow, which has a parabolic velocity distribution, the velocity gradient increases linearly from the center of the jet to the edge. Velocity gradient also causes a broadening of the PTDS signal. We have built an approximate theoretical model of the effect of velocity gradients, which works reasonably well within the constraints of a very narrow (tightly focused) pump beam.

Figure 1 shows the results for NO_2 concentration, flow velocity, and temperature obtained from the analysis of PTDS data and corrected for the effects of optical saturation and velocity gradient. Panel (a) shows the flow velocity (solid circles) and NO_2 concentration (open circles) as a function of position in the jet. Zero on the abscissa corresponds to the center of the jet. The solid line is a fit of experimental results to a parabolic velocity distribution expected for a lami-
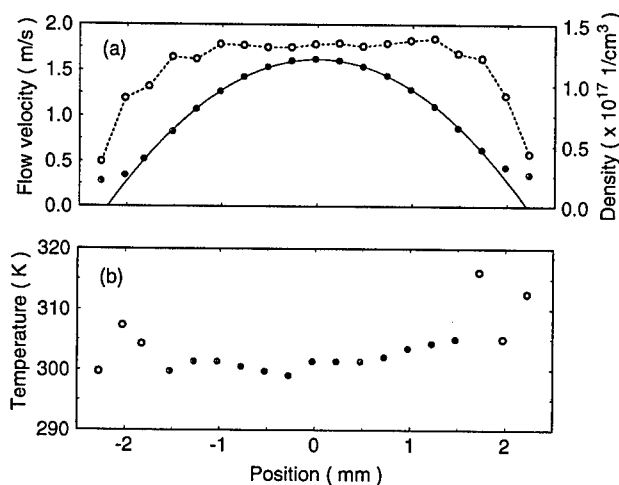
Figure 1
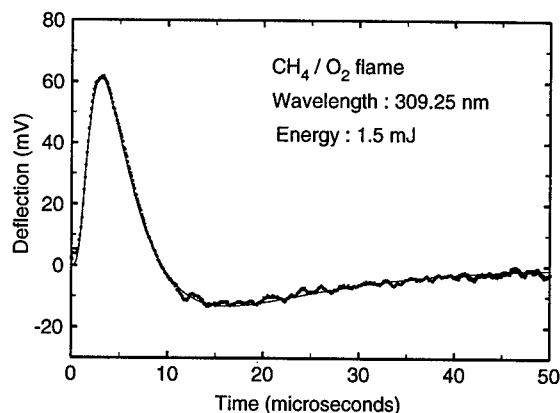
Figure 2

nar flow. The measured flow velocity at the center of the jet, 1.62 m/s, is in excellent agreement with that derived from the flowmeter reading, 1.66 m/s. The NO_2 concentration is approximately constant across the jet, as expected, and its value, ~ 1.4×10^{17} cm^{-3}, is in excellent agreement with the value given by the gas supplier, ~ 1.3×10^{17} cm^{-3}. Panel (b) shows the temperature. The measured temperature away from the edges (solid circles) is very close to the room temperature. The data points near the edges (open circles) have not been corrected for the effect of velocity gradients. The data near the edges is not reliable because of the drag of air by the flowing gas. Overall, the agreement between the measured values of the three parameters and the correct values is quite good.

Figure 2 shows the PTDS signal from OH in a methane-oxygen flame. We have not started analyzing the flame data yet.

STATISTICAL INTERPRETATION OF POWER SPECTRAL DENSITIES MEASURED BY PICOSECOND TIME-RESOLVED LASER-INDUCED FLUORESCENCE IN TURBULENT NONPREMIXED FLAMES

School of Mechanical Engineering, Purdue University, West Lafayette, IN 47907-1288

SUMMARY/OVERVIEW

This research is concerned with obtaining time-series measurements of minor-species concentrations so as to gain greater understanding of scalar fluctuation rates in turbulent nonpremixed flames. Measurements of OH and CH concentrations are reported for simple jet diffusion flames using a fuel mixture comprised of H_2, CH_4, and N_2. Power spectral densities and autocorrelation functions are computed from the time series and are used to calculate integral time scales for many axial and radial locations in seven jets. The OH autocorrelation functions are found to collapse when normalized by their integral time scales. CH autocorrelation functions are also found to be self-similar except at locations close to the jet centerline or for Reynolds numbers approaching blowoff.

TECHNICAL DISCUSSION

Measurements of minor-species concentrations in turbulent flames are of interest owing to their importance in pollutant chemistry and to their use as markers of instantaneous flame structure. Hydroxyl (OH) and methylidyne (CH) measurements have been reported by many researchers in a wide variety of flames; however, most of these studies have employed high-power, low-repetition-rate, pulsed lasers. With such instrumentation, two sequential measurements are further apart in time than most correlations arising from turbulent fluctuations. Thus, the measurements are temporally independent from one shot to the next and yield only single-time statistics, including the mean, variance, and probability density function (PDF).

Time-scale information can be provided by scalar time series when measurement repetition rates are sufficiently fast to resolve turbulent fluctuations. This approach has been demonstrated for many scalars including concentrations of CH[‡] and OH[§]. These time series of minor-species concentrations are recovered by use of picosecond time-resolved laser-induced fluorescence (PITLIF), which directly accounts for potential variations in both the electronic quenching rate coefficient and background flame emission.

Concentration measurements were made in seven jet diffusion flames with a fuel composition of 33.2% H_2, 22.1% CH_4, and 44.7% N_2 (by volume). The fuel issued from a circular nozzle into still air with cold-flow Reynolds numbers ranging from 2800 to 15,200. Two burners were examined with diameters of 3.4 and 7.8 mm. In both cases, the burners were sufficiently long to provide fully developed turbulent flow at the tube exit. The tubes were not contoured and no coflow or pilot flame was provided. The seven flames studied are designated A1-A5 and D1-

---

[‡] Renfro, M. W., Klassen, M. S., King, G. B., and Laurendeau, N. M., *Opt. Let.* 22:175 (1996).
[§] Renfro, M. W., King, G. B., and Laurendeau, N. M., *Appl. Opt.* 38:4596 (1999).

Figure 1.

D2, as shown in Table 1. Radial profiles of time-averaged [OH] were obtained at x/D=1, 2, 5, 10, 20, 40, and 60 in each 3.4-mm flame and at x/D=1, 2, 5, 10, and 20 in each 7.8-mm flame. Radial profiles of time-averaged [CH] were only obtained at x/D=1, 2, 5, and 10 in both the 3.4-mm and 7.8-mm burners owing to the reduced fluorescence signal. These profiles, including the OH and CH profile widths and peak concentrations, plus further experimental details are presented elsewhere[**,††]. At each height, time-series measurements were obtained with sampling rates as given in Table 1 for three radial locations displaying significant fluorescence signals. Fifty time series of 4096 points each were collected to obtain clean statistics at each measurement location. PDFs, PSDs, autocorrelation functions, and integral time scales were computed from these time series in the same manner as reported by Renfro *et al.*[‡‡], including a correction for the measured contribution of shot noise.

Sample OH time series for flames A1, A3, and A5 are shown in Fig. 1. These measurements represent the first 20 ms of data collected at the radial location of peak [OH] at x/D=20. A range of fluctuation time scales is present at each location in the flow, and the fluctuation rates depend strongly on Re. In each flame, the OH concentration often becomes zero as the OH layer fluctuates completely away from the fixed laser beam. These intermittent periods are typically longer in flame A1 than in flame A5. Likewise, periods for which measurable OH exists in the probe volume ([OH]>0) display a longer duration at lower Re.

These fluctuation rate variations are quantifiable in terms of the PSD and the autocorrelation function, ρ. Figure 2(a) shows autocorrelation functions for the radial location of peak [OH] at two heights in each of the seven flames. The autocorrelation functions for flames at higher Re are observed to decay much faster than for those at lower Re. This result is a manifestation of the faster fluctuations observed at greater Re in the time traces of Fig. 1.

Figure 2(b) shows the same autocorrelation functions normalized by the derived integral time scales. The normalized functions collapse to essentially a single curve. Since the PSD is a Fourier transform pair to the autocorrelation function, the collapse is observed equally in the frequency-domain statistics. This feature of OH fluctuation time scales was previously demon-

[**] Renfro, M. W., Guttenfelder, W. A., King, G. B., and Laurendeau, N. M., *Combust. Flame*, in review (2000).

[††] Renfro, M. W., King, G. B., and Laurendeau, N. M., *Combust. Flame*, in press (2000).

[‡‡] Renfro, M. W., Gore, J. P., King, G. B., and Laurendeau, N. M., *AIAA J.*, in press (2000).
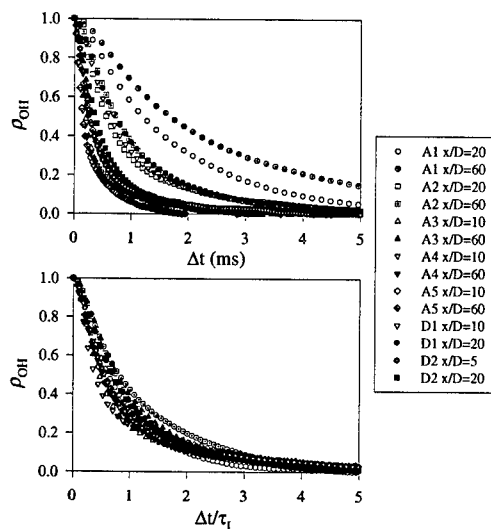
Fig. 2 Autocorrelation functions for the radial location of peak [OH] (a) measured and (b) normalized by the integral time scale.

strated for measurements in H_2/Ar flames[5]. The collapse of a two-time statistic implies that the distribution of fluctuation rates is independent of location within the flow. Thus, the integral time scale is a good representation of temporal variations in [OH].

CH autocorrelation functions measured on the air-side of the [CH] peak are also nearly exponential and depend strongly on Re. Normalization by τ_I successfully collapses the statistics. However, the shape of the CH fuel-side PSDs are notably different from those on the air side. Figure 3 shows CH autocorrelation functions about 0.1 mm to the fuel-side of the [CH] peak at x/D=5 for each of the flames from the 3.4-mm burner. Measurements at the [CH] peak essentially replicate these fuel-side measurements. For small time delays (high frequencies), the fuel-side CH autocorrelation functions are nearly exponential; however, a significant positive correlation exists for very large time delays (low frequencies). This difference in the autocorrelation functions for large time delays can be equivalently observed as a low-frequency difference in slope for the PSDs.

The CH autocorrelation functions on the fuel side are indicative of fluctuations with a second and longer time scale as compared to the air side. Since the CH time series are highly intermittent (much more than for OH), the corresponding autocorrelation function is quite sensitive to the rates of flame front fluctuations across the fixed laser beam. However, this observation also applies to the OH measurements, for which no such extended autocorrelation functions are observed. The difference may be related to the fact that the CH radical exists farther into the fuel stream than does $OH^{3,4}$ and thus lies closer to the shear layer and the associated region of intense mixture fraction fluctuations, as compared to the measurements made available by Meier[§§]. This additional fluctuation mechanism on the fuel side of the [CH] peak may arise from fluctuations in the scalar dissipation rate.

The self-similarity of the OH and CH PSDs and their autocorrelation functions is only valid sufficiently far downstream of the jet exit. Note that data for x/D=1 and x/D=2 (and larger heights for lower Re) is not included in Fig. 2. At x/D=2, the CH and OH fluctuations remain correlated for long periods of time (>50 ms), especially when compared to the downstream data which become uncorrelated by $\Delta t > 10$ ms even at the lowest Re. Hence, the fluctuations at x/D=2 are much slower (lower frequencies) than those incorporated into Fig. 2. This same trend is apparent in the CH measurement of Fig. 3 at Re=2800. These features are consistent with images of the reaction zone in the near field of jet diffusion flames which show a highly laminarized flame sheet[***].

Because of the statistical collapse of most of the PSDs, the task of describing fluctuations throughout the various jet flames is reduced to describing only the integral time scales. Simple eddy-turn-over time scaling predicts an integral time scale variation of[5,†††]

$$\tau_I \sim (1/Re)(x/D)^2[1+(0.644r/r_{1/2})^2]^2 \ . \qquad (1)$$

[§§] Meier, W, 1999, http://www.st.dlr.de/EN-CV/flamedat/intro.htm
[***] Clemens, N. T. and Paul, P. H., *Combust. Flame* 102:271 (1995).
[†††] Schlicting, H., *Boundary-Layer Theory*, McGraw-Hill, New York, 1979, pp. 747-750.

This scaling is qualitatively consistent with previous OH data for H_2/Ar flames over a limited range of conditions[5]. This relationship is now examined in more detail.

A series of OH measurements at r/x=0.075 and x/D=20 was obtained in eighteen flames at Re=2980-15,200. The resulting integral time scales are shown in Fig. 4, where $\tau_I \propto Re^{-1.41\pm0.15}$ at the 95% confidence interval. For other OH and CH data[3,4], the integral time scale also appears to decrease faster than Re^{-1}, although in many cases the uncertainty does not preclude the relationship of Eq. (1). This stronger dependence on Re may arise because the virtual origin (and its dependence on Re) has been neglected, as we observe an asymptotic approach toward Re^{-1} with increasing height.

If all of the OH data from flames A1-A5 are normalized to account for the observed dependence on Re, the results are found to be consistent with the radial scaling of Eq. (1). This implies that OH fluctuations are simply driven by velocity fluctuations and do not contain information about turbulence-chemistry interactions. However, only three radial measurements have been obtained at each axial height. As a more stringent test, a series of integral time scale measurements were made at 12 radial locations for axial heights of x/D=10, 20, 40, and 60 in Flame A3. These measurements show a much more complicated

Fig. 3 CH autocorrelation functions measured on the fuel side of the [CH] peak.
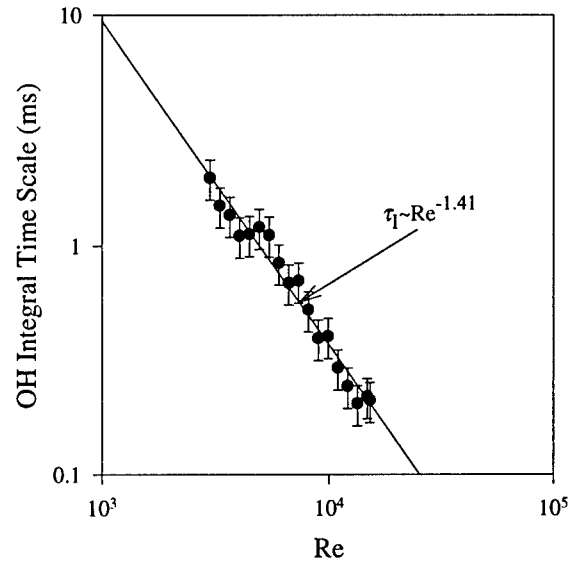
Fig. 4 Hydroxyl integral time scales as a function of Reynolds number.

profile shape than predicted by Eq. (1). Moreover, the axial scaling of the OH time scales is much closer to $x^{0.5}$ than x^2. Thus, simple eddy-turn-over-time scaling does not appear to be sufficient for time scales of reactive scalars.

In addition to the axial and radial dependence in Eq. (1), the integral time scale depends directly on the burner size as this impacts the integral length scale. The CH and OH integral time scales in flames D1 and D2 are found to be a factor of 1.5-3.0 larger than those in the smaller burner at the same x/D and r/x values. The ratio of burner diameters is 2.3 and thus the scaling may simply be $\tau_I \sim D$, but more extensive data is needed to resolve this relationship. In particular, it is not clear whether the appropriate length scale is related to the flow width or to the scalar width. The typical width of the OH and CH layers are small compared to the jet width, with CH typically a factor of two narrower than OH. Similarly, the CH and OH time scales are quantitatively different for similar locations in the same flame, with the CH fluctuation rates typically about   a   factor   of   two   faster   than   those   for   OH.

SUPERCRITICAL FUELS/COMBUSTION RESEARCH

AFOSR Task Nos. 93PR02COR and 92PR12COR

Principal Investigators: J. R. Gord, J. T. Edwards, W. M. Roquemore

Air Force Research Laboratory
Propulsion Directorate
Wright-Patterson Air Force Base OH

SUMMARY/OVERVIEW:

Detailed studies of supercritical aviation fuels and combustion processes demand the development and application of non-intrusive measurement techniques for quantifying species concentrations and fluid-dynamic parameters. Laser-based and other optical approaches are well-suited to these tasks. These approaches do little to disturb the reacting flows under study while providing the chemical and physical information required for computational modeling of the relevant chemistry and flowfields. This presentation summarizes recent developments associated with a number of continuing basic-research projects designed to provide the measurement technologies essential for fielding advanced propulsion systems.

TECHNICAL DISCUSSION:

Experimental and Computational Characterization of Spectral Shifts in Supercritical Fuel. Aviation fuels serve as the primary coolant for all aircraft on-board heat sources. As such, the thermal stability of these materials is an important issue. Through the continued development of JP-8+100, JP-8+225, and JP-900, the Propulsion Directorate's Fuels Branch has invested in the design of thermally stable fuels and fuel additives for current and next-generation aircraft. Basic research in this area has been focused on obtaining a detailed understanding of the chemical and physical processes at work in high-temperature fuels. Under extreme conditions of temperature and pressure, these fuels exist as supercritical fluids that exhibit unique properties. To study these properties at a molecular level, we have been investigating spectral shifts in the excitation and emission spectra of fluorophores doped into supercritical aviation fuels and fuel surrogates. Experiments accomplished with steady-state absorption and fluorescence instruments have been modeled recently through computations with *ab initio* quantum-mechanics calculations and Monte Carlo simulations.

Studying Fuels and Combustion with Terahertz Radiation. Novel sources of far-infrared radiation have been achieved through the marriage of ultrafast (femtosecond) lasers and semiconductor materials such as low-temperature-grown gallium arsenide (LT-GaAs). Ultrafast excitation and gated detection with these and other materials has enabled the development of millimeter-wave, terahertz-radiation systems for spectroscopic studies. Terahertz radiation features a number of ideal characteristics for diagnostic studies of aviation fuels and combustion. While kerosene-based fuels do not absorb radiation in this spectral regime, trace water dissolved in fuels interacts strongly with terahertz radiation. This situation permits the quantification of water in fuel while providing an opportunity for the study of water/fuel phase behavior and chemical dynamics. Similarly, soot particles are transparent to terahertz radiation while some key combustion species absorb in this spectral region. Furthermore, some ceramic materials pass terahertz radiation, suggesting the possibility of diagnostic studies in ceramic windowless combustors.

Optical Parametric Oscillator for Mid-Infrared Combustion Measurements. Much of the optical-diagnostics effort to date has involved laser sources and measurement schemes that operate in the ultraviolet, visible, and near-infrared spectral regimes. While a wealth of information could be obtained through measurements in the mid-infrared region where key combustion species exhibit strong spectroscopic transitions, suitable radiation sources for this region have been largely unavailable. To address this need in the mid-infrared, we have developed a continuous-wave optical parametric oscillator (OPO) based on periodically poled lithium niobate (PPLN) technology. This 2.3-μm OPO, which is the very first of its kind, has been used to record continuous frequency scans through absorption features of carbon monoxide, an important combustion product. These developments demonstrate the potential of such devices as room-temperature, low-cost, compact mid-infrared sources with numerous spectroscopic and species-detection applications.

Exhaust-Gas Analysis by Dual-Pump Coherent Anti-Stokes Raman Spectroscopy. Dual-pump coherent anti-Stokes Raman spectroscopy (DP-CARS) is being applied in our laboratories for characterizing exhaust gases from gas turbine combustors. The dual-pump CARS technique can be applied to measure temperature, pressure, and the concentration of two or more species with excellent temporal and spatial resolution. Dual-pump CARS measurements of CO_2 can be a powerful means for determining the efficiency of the combustion process and the extent to which combustion reactions have proceeded. Dual-pump CARS can be used to monitor equivalence-ratio distributions by quantifying fuel and oxidizer species simultaneously. Dual-pump CARS can also be used for very sensitive measurements of the relative concentrations of H_2 and one other species; the presence of significant quantities of H_2 in the post-flame gases indicates that a locally fuel-rich mixture has been burned. During the present measurements, an injection-seeded Nd:YAG laser system used in conjunction with a back-illuminated CCD spectroscopy system and a broadband dye laser produced excellent experimental results. To demonstrate the utility of our instrument, tests were performed in the exhaust of a swirl-stabilized combustor section fueled with JP-8+100.

Megahertz-Framing-Rate Images of a Gas Turbine Spark Igniter. Spark-ignition systems play a critical role in the performance of essentially all gas turbine engines. These devices are responsible for initiating the combustion process that sustains engine operation. Demanding applications such as cold start and high-altitude relight require continued enhancement of ignition systems. To characterize advanced ignition systems, we have developed a number of laser-based diagnostic techniques configured for ultrafast imaging of key spark parameters including emission, density, temperature, and species concentrations. These diagnostics have been designed to exploit an ultrafast-framing charge-coupled-device (CCD) camera and high-repetition-rate laser sources, including modelocked Ti:sapphire oscillators and associated regenerative amplifiers. Spontaneous emission measurements as well as laser-based schlieren and interferometry have been accomplished with this instrumentation and applied to the study of a novel Unison spark igniter. During past studies, we achieved 50-kHz framing rates that revealed shock structure in the spark-ignition event; however, these rates proved insufficient for full characterization of the spark. Through recent experiments, megahertz framing rates have been achieved, and laser-schlieren movies of a single spark event have been captured.

Vortex-Based Igniter for Advanced Propulsion Applications. A great deal of effort has been invested in developing novel ignition systems for advanced propulsion applications. Conventional gas turbines under cold-start or high-altitude relight conditions, scramjets, and pulsed-detonation engines represent just a few of the many challenging ignition scenarios facing both military and commercial aviation. In response to these challenges, ignition schemes based on sparks, plasmas, microwave discharges, and lasers have been explored. Recently, we initiated development of a vortex-based ignition system. During operation of this igniter, a toroidal vortex of combustible gases is injected into the propulsion system of interest. This injected vortex is ignited by a conventional spark-based system to produce a traveling ball of flame that ignites the gases in the combustor. This vortex-based igniter features a number of potential advantages over existing state-of-the-art technologies. Most notably, it delivers the ignition kernel well into the combustor. This penetration into the propulsion system and the extended duration of the vortex-based ignition event hold great promise for improved operation over some existing systems.

SELECTED REFERENCES:

(1) G. J. Fiechtner, C. D. Carter, J. R. Gord, P.-H. Renard, D. Thevenin, and J. C. Rolon, "Vortex-Flame Interactions: Experimental Observation of an Annular Local Extinction," submitted to Combustion and Flame, May, 2000.
(2) D. Thevenin, P.-H. Renard, G. J. Fiechtner, J. R. Gord, and J. C. Rolon, "Regimes of Nonpremixed Flame/Vortex Interaction," Proceedings of the Combustion Institute 28, in press.
(3) G. J. Fiechtner, P.-H. Renard, C. D. Carter, J. R. Gord, and J. C. Rolon, "Injection of Single and Multiple Vortices in an Opposed-Jet Burner," Journal of Visualization 2, 331-342 (2000).
(4) M. Linne, T. Setterson, J. Gord, and G. Fiechtner, "Density Matrix and Rate Equation Analyses for Picosecond Pump/Probe Combustion Diagnostics," AIAA Journal 37, 723-731 (1999).
(5) "Measurements of Temperature and CO_2 Concentration by Dual-Pump Coherent Anti-Stokes Raman Scattering," R. P. Lucht, V. V. Natarajan, G. J. Fiechtner, C. D. Carter, K. D. Grinstead, Jr., J. R. Gord, P. M. Danehy, and R. L. Farrow, to be presented at the 39th AIAA Aerospace Sciences Meeting and Exhibit, Reno, NV, January 8-11, 2001.
(6) "Physical and Structural Properties of Jet Fuels Studied at High- and Low-Temperature Extremes using Laser-Based Diagnostic Methods," C. E. Bunker and J. R. Gord to be presented at the 220th American Chemical Society Meeting, Washington, D.C., August 20, 2000.
(7) "New Spectral Sources for Studying Combustion and Fuels," J. R. Gord, G. J. Fiechtner, M. S. Brown., A. Henderson, P. Roper, R. Mead, J. V. Rudd, D. Zimdars, and M. Warmuth, to be presented at the 42nd Rocky Mountain Conference on Analytical Chemistry, Denver, CO, August, 2000.

(8) "Imaging Strategies for the Study of Gas Turbine Spark Ignition," J. R. Gord, C. Tyler, K. D. Grinstead, Jr., G. J. Fiechtner, M. J. Cochran, and J. R. Frus, International Symposium on Optical Diagnostics for Fluids/Heat/Combustion and Photomechanics for Solids, SPIE's 44th Annual Meeting, Denver, CO, July, 1999.

(9) "Continuing Development, Characterization, and Application of an Asynchronous Optical Sampler," K. D. Grinstead, Jr., G. J. Fiechtner, C. E. Bunker, D. K. Phelps, and J. R. Gord, 26th Annual Conference of the Federation of Analytical Chemistry and Spectroscopy Societies (FACSS), Vancouver, Canada, October, 1999.

(10) "Applying High-Repetition-Rate, Modelocked Lasers to the Study of Combustion," J. R. Gord, 10th Gordon Research Conference on Laser Diagnostics in Combustion, Lucca, Italy, June 20-25, 1999.

91
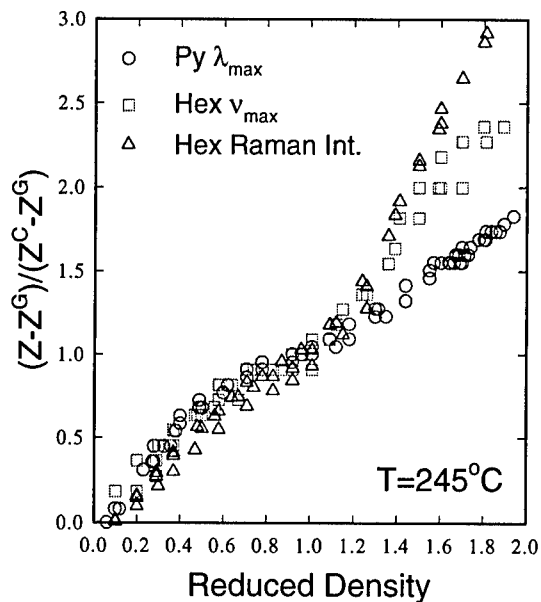
Figure 1. Fluid parameters plotted vs. reduced density in supercritical hexane. Y-axis values are cast in reduced terms based on behavior in the gas phase (G) and at the critical point (C). These data support the three-density-region model that describes supercritical solvation phenomena.
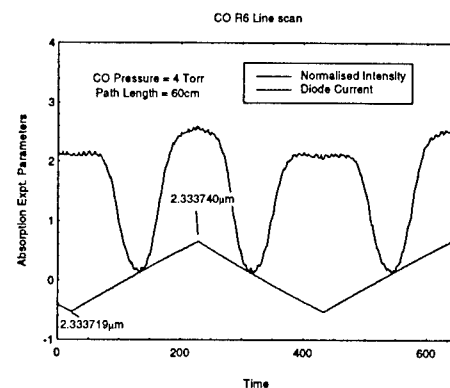
Figure 2. Carbon monoxide absorption line scans achieved with the 2.3-μm output of the Aculight ultranarrowband optical parametric oscillator.
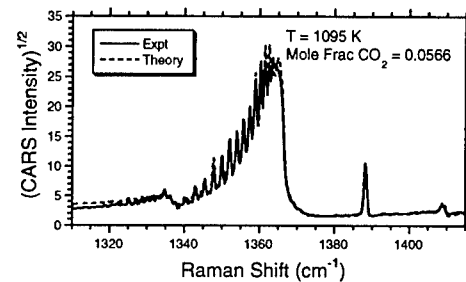
Figure 3. Spectrum obtained by DP-CARS in the exhaust of a single-cup CFM56 research combustor.

2 μs   6 μs   10 μs   14 μs

18 μs   22 μs   26 μs   30 μs
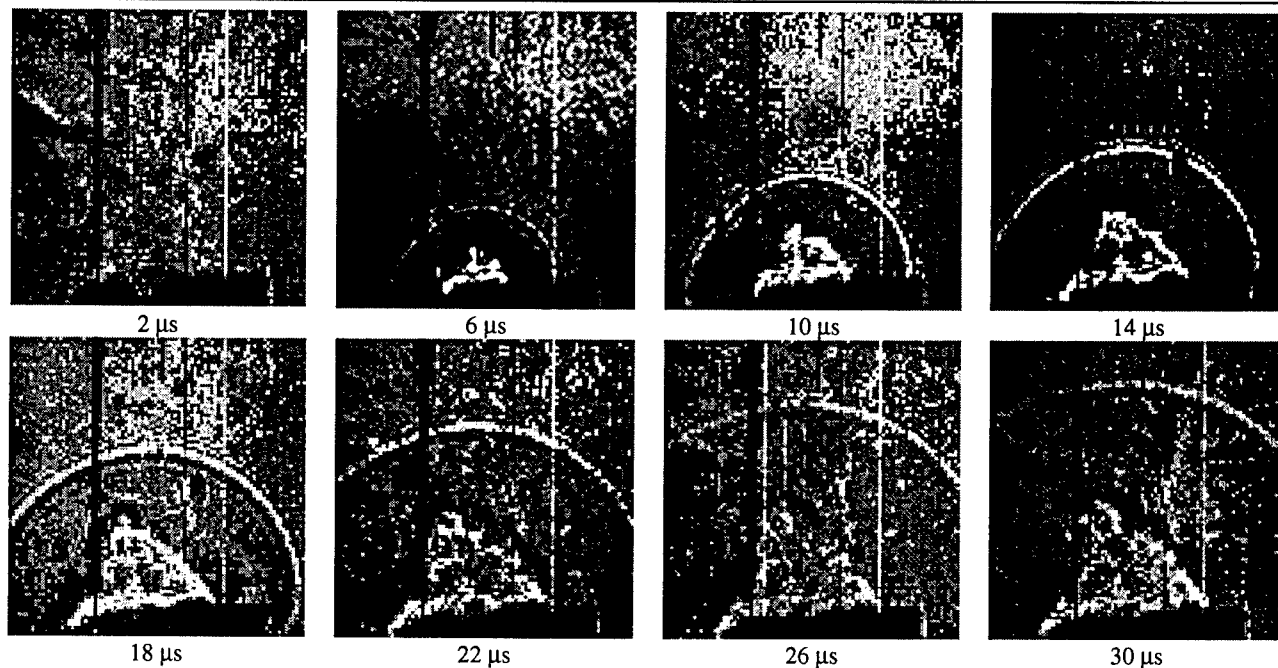
Figure 4. Selected images from a 32-μs laser-schlieren movie in which the shock produced during a single spark-ignition event is captured.

EFFECT OF NITRIC OXIDE AND OTHER DILUENTS ON COLD STARTING, COMBUSTION INSTABILITY, AND WHITE SMOKE EMISSIONS IN DIESEL ENGINES

Wayne State University
College of Engineering
Center for Automotive Research
Detroit, MI 48202
Tel.(313) 577-3887

SUMMARY/OVERVIEW:

The objective of this program is to reduce combustion instability and the emission of white smoke from military and commercial diesel engines during cold starting. The factors that contribute to combustion instability are investigated theoretically and experimentally. Misfiring occurs after engine acceleration to higher velocities due to an imbalance between engine dynamics and combustion kinetics. A new formulation for the ignition delay (ID) is developed to account for the piston motion in engines. The model is applied to predict the boundary of the stable combustion zone. Experimental results showed a good agreement with the model predictions. To improve the accuracy of the model predictions, the heterogeneity of the charge is considered in ID formulation. Based on the findings, controls will be developed for new engines, or for retrofitting in existing engines to reduce combustion instability and white smoke emissions.

TECHNICAL DISCUSSIONS

The causes of the cold starting problems in military and commercial diesel engines have been investigated in this program. The problems include hesitation, emission of large amounts of unburned hydrocarbons in the form of white smoke, or a complete failure of the engine to start. Two factors contribute to the cold start problems: a) the failure of the autoignition process, and b) combustion instability. The ignition delay (ID) is considered an indicator of the rate of the autoignition process. The rate of heat release is considered an indicator of the rate of combustion reactions. This presentation ideals with the results of the ID investigations.

A New ID Formulation Applied to Predict the Boundary of the Firing Zone

Many experimental investigations on diesel combustion are conducted in constant volume vessels, where the charge temperature, pressure and volume remain almost constant during the ID. This is not the case in engines because of the piston motion during the ID period. In this work, the ID in vessels will be identified as ID_v and the ID in engines will be identified as ID_e. A new formulation is developed for ID_e to account for the effect of piston motion on the global autoignition reaction rates. In the theoretical part of this work, ID_e is considered to end at the time the chain carriers reach a critical concentration. In the experimental part the ID will be considered to end when a rise in the cylinder pressure due to combustion is detected.

A 4-cylinder, direct injection, heavy-duty diesel engine was used in this investigation. The experiments were conducted in a cold room after the engine was soaked with its fuel tank and battery for more than eight hours before starting. The data was collected during the first few minutes of the starting process. The experiments covered a wide range of ambient temperatures, from 21° C to -10° C. The pressure history and injection events of all the four cylinders were measured during the starting transients. Figure 3 is an example of a typical trace of the instantaneous engine speed during the first 20 cycles (40 revolutions) of the cold start process. DF-2 fuel is used and the ambient temperature is 10° C. As can be seen from the figure, the engine fired after being motored, accelerated, misfired and decelerated and fired again for many cycles. This unstable combustion continued for a few minutes before the engine reached a steady idling speed. A detailed cycle-by-cycle and cylinder-by-cylinder analysis was made to determine the ID and the rate of heat release.

Figures 1 shows the effect of injection timing on ID_e, calculated by using the new formulation, at different speeds. Figure 2 shows the effect of injection timing on ID at different ambient
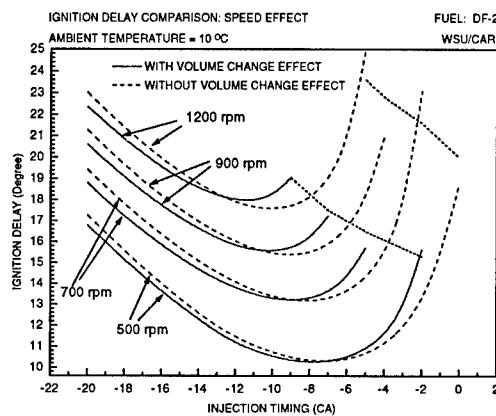
Fig. 1 Effect of injection timing on ID at different engine speeds.
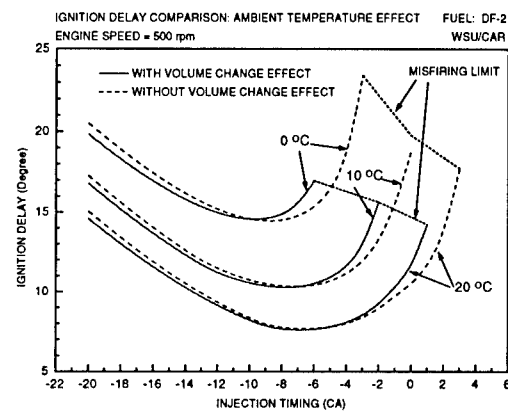
Fig.2 Effect of injection timing on ID at different ambient temperatures.

temperatures. The solid and dotted lines are for ID_e with and without piston motion respectively. The minimum ID occurs at an earlier crank angle degree with the increase in engine speed, or with the drop in ambient temperature. Similarly, the critical injection timing at the firing boundary occurs earlier with the increase in engine speed and with the drop in temperature.
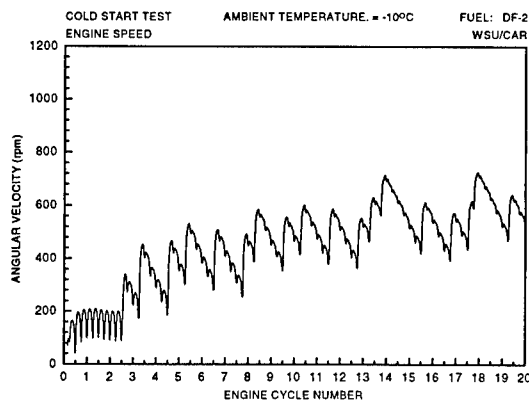
Fig. 3: Instantaneous angular velocity during the first 20 cycles of engine rotation.
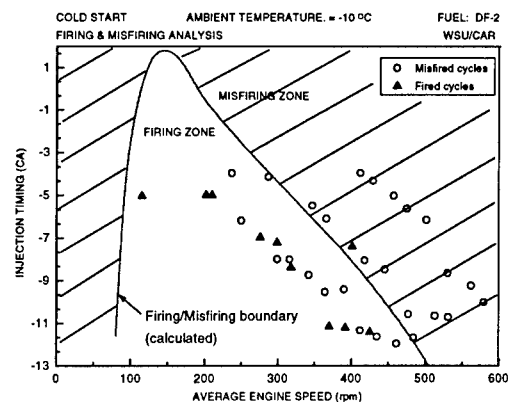
Fig. 4: Predicted boundary of the firing zone and experimental data.

94

The new ID_e formulation is applied to predict the misfiring cycles during the cold starting of a 4-cylinder, direct injection diesel engine at 10°C. The solid line in Fig. 4 shows the predicted firing zone boundary, based on the ID model. The experimental data is plotted on the same figure. It can be noticed that the majority of the misfiring cycles lie in the misfiring zone. Two issues need to be addressed here. The first is the firing zone boundary can be a strip rather than a line in order to account for the inaccuracies in the model assumptions. Second, the accuracy of the model can be improved if we consider the heterogeneity of the charge in diesel autoignition as will be explained later.

Development of maps for the firing zone boundary at different ambient temperatures and engine speeds can enhance the development of cold starting strategies to reduce combustion instability and the resulting white smoke emissions.

Effect of EGR on the Autoignition and Combustion Reactions

Figure 3 shows that, in most of the cases, misfiring occurred after engine acceleration in a firing cycle. Measurements of the cycle resolved emissions indicated the presence of high concentrations of NO in the exhaust of the firing cycles. The issue here is to find out if such high concentrations of NO and other diluents has an effect on the autoignition reactions. This is being investigated experimentally on a single-cylinder direct injection diesel engine. Calculations are made to determine the effect of charge dilution with different EGR ratios on the global activation energy of the autoignition reactions. EGR ratios up to 60% are applied.

A Model for ID Considering the Heterogeneity of the Charge

In previous ID models, autoignition has been considered to occur in a homogeneous mixture in the periphery of the spray. In the current investigation, autoignition is considered to start in a vortex in the periphery of the spray where the charge is heterogeneous. The vortex is divided into several elements that successively react to produce combustion chain carriers (radicals). Autoignition occurs when the concentration of the chain carriers reaches a critical value. All the elements contribute in the formation of the critical concentration.

Correlations have been developed for the ignition delay period, considering two types of reactions:
a) Global reaction rates determined from experiments conducted in constant volume vessels, and reported in the literature. The correlations are developed in a dimensionless form in order to be applied in different engines under different operating conditions.
b) Rates for 32 elementary reactions for dodecane, a heavy hydrocarbon suitable for diesel engines.
The results of both approaches agreed with the experimental results obtained on the single-cylinder diesel engine at different room temperatures.

Future Work

The effect of EGR on the global autoignition and combustion reactions will be determined on the single cylinder diesel engine. This will result in the development of correlations for the global activation energy as a function of EGR ratio. Three fuels will be used: DF2, JP-8 and AMCO premium. Meanwhile, the ID model, considering the heterogeneity of the charge, will be implemented to improve the accuracy of predicting the firing boundaries. Maps for the firing boundaries will then be developed for a heavy-duty, multi-cylinder diesel engine, based on the findings

on the single-cylinder engine. Tests will be conducted on the multi-cylinder, heavy-duty diesel engine to validate the model predictions. This will be followed by the development of new electronic control strategies for diesel engines. Tests will be conducted to verify the effectiveness of the new control strategies on reducing combustion instability and white smoke emissions in heavy duty military and commercial engines.

Investigation of Preflame Reactions and Flame Propagation
in Direct-injection Diesel Engines
(DAAG55-98-1-0494)

K. T. Rhee
Department of Mechanical and Aerospace Engineering
Rutgers, The State University of New Jersey
Piscataway, New Jersey 08855-0909

The study conducted during the present reporting period was directed to achieving several research goals, including:

(1) Visualization of in-cylinder preflame reaction (PFR) and combustion processes
(2) Improving spectral analysis methods for quantitative imaging
(3) Advancement of Rutgers high-speed spectral infrared imaging system
(4) Improvement of Rutgers Animation Program, and
(5) Design of speciation methods of in-cylinder reactions.

Visualization of PFR and Combustion Processes. Recall that fuel-air mixtures under compression in the engine cylinder undergo chemical reactions prior to being consumed via the propagation of flame fronts. For example, those in Diesel or compression ignition (CI) engines during the ignition delay period and mixtures in the end gas of spark ignition (SI) engines produce new intermediate species widely suggested as being the precursors of self-ignition. When such PFR are not properly controlled, engines undergo knock causing degraded behavior, which are affected by various engine design, operation and fuel factors.

Among questions in need for better understanding as to the PFR is to find where and what chemical species are produced in the PFR period. In addition, it would be highly desirable to find the relationship of the PFR to the onset of self-ignition at the end of the ignition delay period. In spite of such importance of understanding PFR in the cylinder, they have not been well studied perhaps partially due to the fact that PFR are invisible.

Thanks to some unique capabilities of our high-speed multi-spectra infrared (IR) imaging system (called Super Imaging System, SIS), visualization of PFR and combustion reactions in the cylinder became possible in recent years. Briefly, in the SIS or Rutgers System, four units of high-speed IR digital cameras are connected to a single optical train containing three spectral beam splitters so that four sets of images in respective spectral bands can be simultaneously captured at high rates. One of the spectral bands employed in the SIS is 3.42μm to exhibit images of progressively changing radiation produced by PFR species during the ignition delay period of a direct-injection (DI) CI engine.

While a new experimental approach of determining (radical and molecular) species during PFR and combustion periods is explored at present, in order to help understand the global picture of spatial and temporal process of PFR in CI-DI combustion, some extensive experiments were conducted for several engine-fuel combinations, including: (a) DI-CI using D-2 fuel; (b) DI-CI with fumigation by propane; (c) DI-CI self-ignition as fueled by homogeneous propane-air mixtures. Also the same was performed for reactions in a spark-ignition (SI) engine when operated by different fuels, e.g. gasoline and propane in order to compare their results with the findings from DI-CI combustion.

Some of the findings from this work are: (1) The fuel injected into the cylinder immediately starts to undergo chemical reactions in a CI-DI engine; (2) While the combustion reactions may not represent the real-world warmed engine if they are observed during the very first several cycles (as many do due to soot-deposit on the optical window), the PFR observed the early cycles, however, seem to mutually be comparable to those under the warm conditions; (3) It is discovered that multi-spectral images taken of an identical object (e.g. DI-CI reactions) differ from each other, even the direction of reaction propagation in some cases; (4) The PFR species were rapidly consumed as soon as high-temperature kinetics take over the in-cylinder reactions (i.e., after the onset of premixed combustion stage); (5) When the pilot injection was used to ignite the fumigated mixture (Case-c mentioned above), which indicated developing PFR as the piston ascended, the initiation of combustion seemed to be delayed compared to when the pilot injection is used alone (Case-a, as listed above); and more. (Some examples at the end)

Improving Spectral Analysis Methods for Quantitative Imaging. Since the conception of the SIS over ten (10) years ago, which was to achieve quantitative imaging (i.e., simultaneous determination of distributions of species and temperature distributions), improvement of the apparatus (as explained next) and spectral methods has continuously been pursued at Rutgers. Note that we have developed the following spectral methods in the past: (1) duel-band mapping method; (2) new band-ratio method and (3) three-band iteration method. The two former permit determination of distributions of temperature and water vapor concentration, and the latter method enables calculation of simultaneous distributions of temperature, water vapor and soot concentrations. (Note that a new four-band reference method is being developed at present.)

Among the key ingredients in those methods is the used of a massive amount of experimental data included in NASA IR Handbook. That is, there are nearly 100 pages of tables of absorption coefficients of various species in the handbook, which are employed in our spectral methods. It became clear in recent years that the numerical data included in those methods were either inaccurate or incomplete leading to inaccurate results.

Consequently, it was decided to construct a new accurate data file again being copied from the handbook. Instead of manually typing the individual numeric data, which was partially a source of error in our earlier endeavor, at this time we employed an optical scanner capable of character recognition for accurately copying the data into the file. (We would like to share this pleasant new experience of using a modern tool with research individuals who may be in need of using large volumes of numerical data for their research work.)

Advancement of Rutgers or SIS. The development of SIS started with designing a single unit high-speed IR digital imaging system, which evolved to a two-camera unit and next to a four-color system. The electronic control packages of the camera have been newly fabricated more than three times over in the past mainly for taking advantage of advancements in peripheral areas, including hardware and software. For example, our earliest electronic unit in the camera included a numerous amount of transistor-transistor-logic components (in late 1980s), which was later replaced by flexible programmable logic gate arrays.

Recently we came to recognize a possibility of greatly improving the SIS performance from what is today. Note that, in the present SIS, after simultaneously capturing four sets of 64 successive (spectral) images at rate of 2000 frames/sec/camera, it is necessary to transfer digital matrices (i.e. 4 cameras x 64 images/camera x (64x64) pixels/frame in 12-bit dynamic resolution) to a hard drive,

which takes about 30 seconds. That is, we can only investigate in-cylinder reactions in every 30-second period, for example, from the (cold) start. The new approach being implemented on the SIS is to achieve data acquisition in successive cycles, e.g. from the very first firing. Further more, this may be continued for over 150 cycles by capturing 128 frames/cycle by doubling the present amount per cycle.

Improvement of Rutgers Animation Program. It was obvious to recognize that even a simple review of vast amounts of experimental data captured by using the SIS far more than being handled by the conventional methods, e.g. multiple video devices loaded with the digital movies and played for analysis. It was urgent to find a new method to overcome the limitations. Finding that there was no such a method available in the field, about four (4) years ago we started to develop a new animation program in order to facilitate analysis of SIS results.

Rutgers Animation Program (RAP) is the recent form of this endeavor: It permits a simultaneous display of as many as twenty-eight (28) separate animation over a single PC screen in respective (adjustable) color maps. (A greater number of movies may be displayed but at the expense of image quality over the screen.) In addition, corresponding pressure-time histories can be simultaneously displayed for mutual comparison. While such animation is made by the RAP, various adjustment features can be utilized, e.g. control of display speed during the animation, and freezing of the animation for reversing or forwarding (frame by frame) of the animation. At the same time, an entirely new set of similar animation can be performed, placing it over the existing one. This step is taken to review the entire volume of experimental results, in order to select a most representative set from multiple trials. (Utilities of the RAP will be demonstrated in the oral presentation.) The RAP is recognized as one of the most critical ingredients of the present research, leading to more meaningful findings.

Design of Speciation Methods of In-cylinder Reactions. As explained in the oral presentation, it appears that the present SIS may be effectively employed not only for investigation of phenomenological aspects of in-cylinder reactions but also for determining individual species present in the cylinder.

Briefly, the present SIS will be incorporated with two additional units of the same IR cameras, that is, the system will become a 6-camera system. Briefly, one portion of the divided (50/50) radiation rays after the beam splitter would be imaged onto one of six cameras, say camera-5. The other radiation would be exposed to a grating device, by which the radiation would be spectrally distributed. This spectrally distributed radiation would be imaged onto camera-6, which would represent the spectra of the combustion radiation within the (replaceable) spectral band width of the same image recorded on camera-5. An attempt will be made to obtain spectra distributions in a resolution of 4 cm^{-1}, an adequate value for deducing the identity of an unknown compound.

Example of Results. Although various results will be shown in the actual presentation (in Santa Fe) by using RAP, a set of results obtained of the in-cylinder events in a propane-homogenous-charge self-ignition CI engine is shown in Fig. 1. In order to induce the self-ignition, the engine intake air temperature was increased to approximately 210°C.

The first image captured (-37 CA) already exhibits some significant PFR species (Fig. 1-A in 3.42 μm). The images were taken in 2-CA intervals. Looking at the flame images taken at the same time (Fig. 1-B in 2.47 μm), the first self-ignition zone incidentally occurred at almost the same zone near

the perimeter of the piston bowl. This initial occurrence instantly spread over the entire optical view. When the PFR images and those of flames are compared to each other, it is difficult to find any mutual relationship between them in terms of the spatial variation. On the other hand, the gradually increasing intensity of radiation revealing PFR as the piston moves up became insignificant as soon as the high-temperature flame reaction takes over the mixture. That is, the first heat-releasing reaction occurred when the highest intensity radiation from PFR was observed (Fig. 1-A).

This observation is consistent with those of similarly insignificant PFR images captured when the intake air temperature was high in DI-CI (D-2 fuel) engine combustion. That is, the decreased PFR radiation suggests a rapid consumption of intermediate species (e.g. formaldehyde and radicals) as the reaction environment attains high temperatures.

(A)   (B)
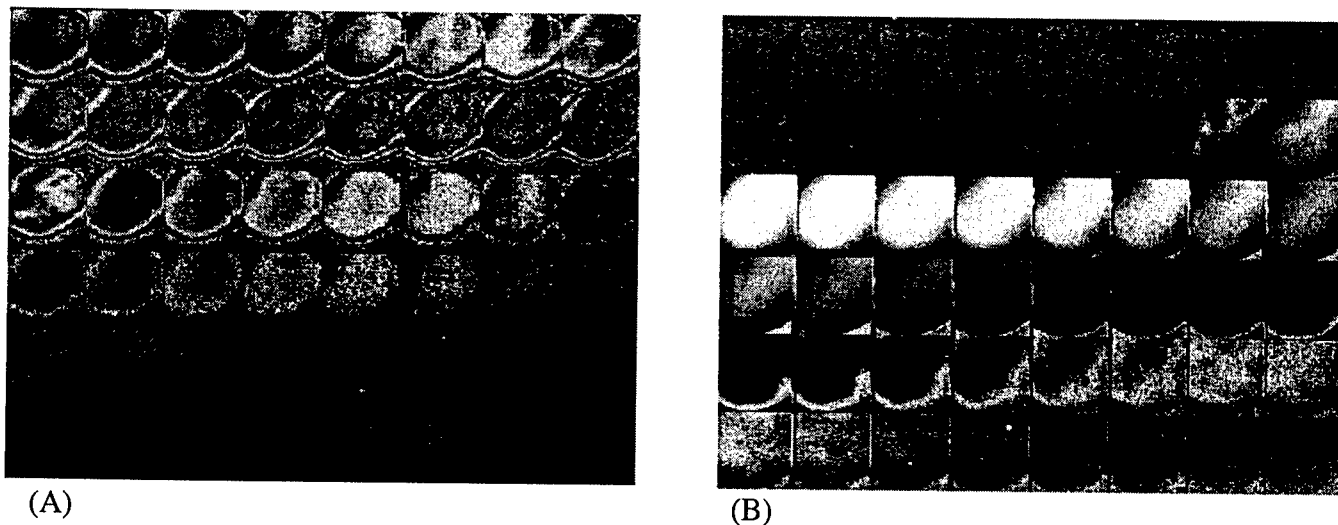
Fig. 1. High-speed Spectral IR Images Captured of Homogeneous Self-ignition
         DI-CI Combustion (Propane-air Mixture) in (A) 3.42μm and (B) 2.47μm.
         Successive Imaging in 2 CA intervals Starting at 37 bTDC.
         (The false gray-shade, manipulated for enhanced local variations)

CHEMICAL-KINETIC CHARACTERIZATION OF AUTOIGNITION AND COMBUSTION OF DIESEL AND JP-8

Grant/Contract Number DAAD19-99-1-0259

Principal Investigator: Dr. Kalyanasundaram Seshadri

Department of Mechanical and Aerospace Engineering
University of California at San Diego
La Jolla, California 92093

SUMMARY/OVERVIEW:

The principal objective of the research is to obtain a fundamental understanding of the mechanisms of autoignition and combustion of diesel and JP-8 in nonpremixed systems. Chemical-kinetic mechanisms describing autoignition and combustion of these fuels are not available. This research will address this deficiency by first developing simulated diesel and simulated JP-8 each preferably made up of three hydrocarbon compounds. Chemical-kinetic mechanisms will be developed for these hydrocarbon fuels. Experimental and numerical studies are in progress.

TECHNICAL DISCUSSION:

To compute the dynamics of the combustion process in engines, it is necessary to have knowledge of chemical-kinetic mechanisms of autoignition and combustion of diesel and JP-8. These fuels are made up of numerous different hydrocarbon compounds. Detailed chemical-kinetic mechanisms describing autoignition and combustion of a number of these hydrocarbon compounds are not available. Therefore, simulated diesel and simulated JP-8 each preferably made up of three hydrocarbon compounds will be developed. The hydrocarbon compounds in the simulated fuels will be chosen from n-heptane, n-dodecane, cyclohexane, methylcyclohexane, toluene, ethylbenzene and 1-methylnaphthalene. Experimental and numerical studies are in progress. The research is being conducted in collaboration with Dr. Charles Westbrook and Dr. William Pitz at Lawrence Livermore National Laboratory (LLNL), and Professor A. Liñán at the Universidad Politécnica de Madrid, Spain.

Experiments are conducted in the counterflow configuration. The burner is made up of two ducts – the fuel duct and the oxidizer duct. A fuel stream made up of prevaporized fuel and nitrogen is injected from the fuel duct and an oxidizer stream made up of oxygen and nitrogen is injected from the oxidizer duct. The temperatures of the streams at the exit of the ducts are measured using thermocouples. The gaseous flowrates are measured by mass flow controllers. The velocities of the reactants at the exits of the ducts are presumed to be equal to the ratio of their volumetric flowrates to the cross-section areas of the ducts. The velocities are used to calculate the strain rate on the oxidizer side of the stagnation plane, a_2. At autoignition the strain rate is denoted by $a_{2,I}$ and the temperature of the oxidizer stream by $T_{2,I}$.

Experiments are carried out at a pressure of 1.013 bar. Figure 1 shows experimental data on autoignition of n-heptane, n-decane, JP-10, and toluene, giving the temperature of the oxidizer stream, $T_{2,I}$ as a function of $a_{2,I}$. The points in Fig. 1 represent measurements. The lines are results of numerical calculations performed using one-step chemistry with overall chemical-kinetic rate parameters so chosen that they fit experimental data. For a given fuel and strain rate, autoignition will take place if the temperature of the oxidizer stream is greater than $T_{2,I}$. At a given value of the strain rate, the temperature of the oxidizer stream at autoignition, for toluene is the highest followed by JP-10, n-decane, and n-heptane. This indicates that among the fuels tested here, toluene is the most difficult to ignite followed by JP-10, n-decane, and n-heptane.
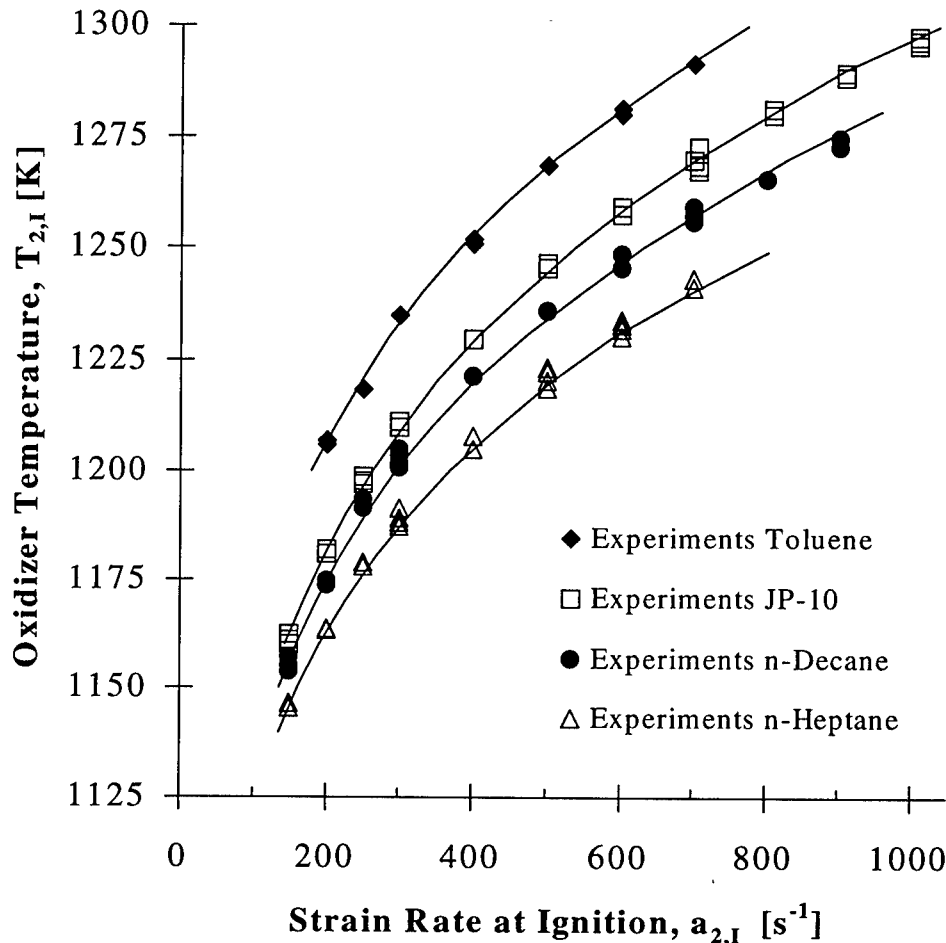
Figure 1: Experimental data showing the oxidizer temperature, $T_{2,I}$, as a function of the strain rate, $a_{2,I}$, at autoignition. The points represent measurements and the lines are results of numerical calculations obtained using one-step chemistry. The temperatures of the fuel stream are 378 K, 408 K, 408 K, and 378 K for n-heptane, n-decane, JP-10, and toluene respectively.

Overall chemical-kinetic rate parameters are deduced using the experimental data in Fig. 1. An asymptotic theory is developed for describing autoignition in nonpremixed systems. The chemical reaction that takes place between fuel and oxygen is described by a one-step overall process. In the asymptotic theory the activation energy of the reaction is presumed to be large in comparison to the thermal energy. The asymptotic theory developed here makes available explicit formulae for predicting autoignition. From these results a simple but reasonably accurate method is developed for deducing the activation energy, E, and frequency factor, B, of the rate of the one-step reaction between the fuel and oxygen. Values of E and B are shown in Table 1. To

test the accuracy of the asymptotic model, overall chemical-kinetic rate parameters

Table 1: Frequency factor B and activation energy E for one-step, irreversible reaction obtained from interpretation of experimental data using asymptotic analysis and from numerical calculations.

Rate Parameters		n-Heptane	n-Decane	JP-10	Toluene
Asymptotic Analysis	$B\left[cm^3/(mol \cdot s)\right]$	3.0×10^{17}	1.5×10^{17}	6.3×10^{16}	1.5×10^{17}
	$E\left[kJ/mol\right]$	200.7	195.0	186.9	199.2
Numerical Calculation	$B\left[cm^3/(mol \cdot s)\right]$	5.9×10^{17}	1.8×10^{17}	8.6×10^{16}	2.4×10^{17}
	$E\left[kJ/mol\right]$	218.0	208.5	202.5	217.0

are deduced from numerical calculations of the reactive flowfield. The values of B and E are so chosen that $a_{2,I}$ and $T_{2,I}$ calculated using these values agree with the experimental data. The numerically calculated values of B and E are given in Table 1. The lines in Fig. 1. represent results of numerical calculations performed using these rates. The asymptotic and numerical results agree well.

Detailed studies are performed to elucidate the mechanisms of extinction and autoignition of n-heptane. This part of the research is performed in collaboration with Dr. William Pitz at Lawrence Livermore Laboratories. A previously developed detailed mechanism made up of 2540 reversible elementary reactions among 556 species is the starting point for the study. An intermediate mechanism made up of 1282 reversible elementary reactions among 282 species and a short mechanism made up of 770 reversible elementary reactions among 159 species are assembled from this detailed mechanism. Ignition delay times in stoichiometric mixtures of n-heptane-vapor and air are calculated using these mechanisms for various values of pressure and initial temperature of the reactive mixture. The ignition delay times calculated using the intermediate and short mechanism are found to agree well with those calculated using the detailed mechanism.

Figure 2 shows the oxidizer temperature at autoignition, $T_{2,I}$, as a function of the strain rate, $a_{2,I}$. The symbols represent measurements. Figure 2 shows the results of numerical calculations performed using the short mechanism to agree well with those calculated using the intermediate mechanism. Numerical results agree well with experimental data at low values of the strain rate. The plus symbols in Fig. 2 indicate the conditions used in further numerical investigation.

Analysis is carried out to investigate the role of strain on autoignition. Numerical calculations are performed at three conditions, using the short mechanism, identified here as case A, case B, and case C. Case A refers to calculations at a value of strain rate, $a_2 = 200$ s^{-1} and oxidizer stream temperature, $T_2 = 1164$ K, case B at $a_2 = 500$ s^{-1} and $T_2 = 1252$ K, and case C at $a_2 = 500$ s^{-1} and $T_2 = 1164$ K. Case A and case B are close to the critical conditions of autoignition. At these conditions, sensitivity analysis was carried out to determine the influence of various elementary reaction on the concentration of OH, because this radical is considered to play a key role in autoignition. For all cases the top four reactions identified by the sensitivity analysis are $H + O_2 = OH + O$, $CH_3 + HO_2 = CH_3O + OH$, $HO_2 + OH = H_2 + O_2$, and $H + O_2 + M = HO_2 + M$. The chain breaking reaction $H + O_2 = OH + O$ is found to play a key role. This reaction plays a pivotal role in many applications where high temperature chemical processes are dominant. Thus the sensitivity analysis indicates that high temperature chemical processes control autoignition in the nonpremixed system investigated here.
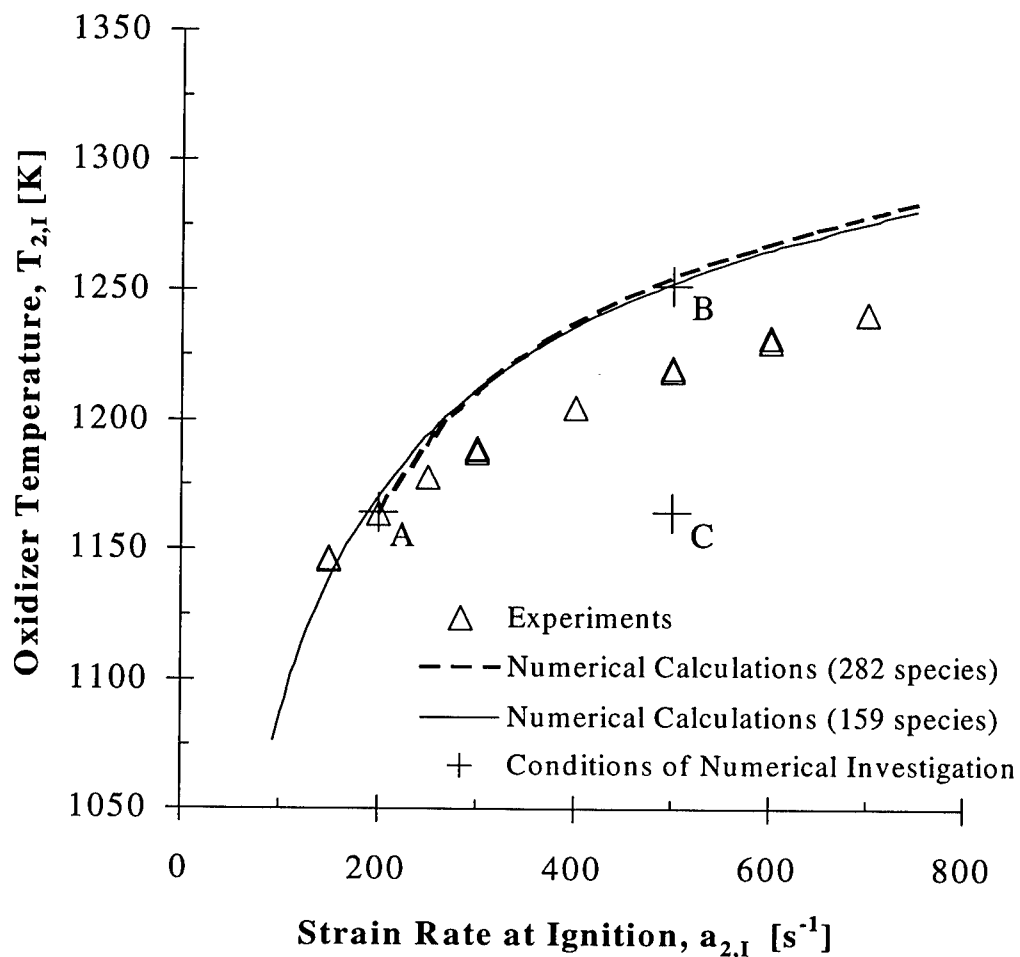
Figure 2: Oxidizer temperature at autoignition, $T_{2,I}$, as a function of the strain rate, $a_{2,I}$. The triangles represent measurements. The solid line represents results of numerical calculations performed using the short chemical-kinetic mechanism. The dashed line represents results of numerical calculations using the intermediate chemical-kinetic mechanism. The plus symbols indicate conditions used in numerical investigation.

It is of interest to focus on the differences among the three cases considered here. Sensitivity analysis shows that the influence of the reactions 2-$C_7H_{15}O_2$ = 2-$C_7H_{14}OOH$-4 and 3-$C_7H_{15}O_2$ = 3-$C_7H_{14}OOH$-5 on the concentration of OH, in case A to be much larger than those in cases B and C. These reactions represent the second generic step in the reaction sequence that leads to chain branching under low temperature conditions. The first generic step is heptyl radical addition to molecular oxygen to form $C_7H_{15}O_2$. This compound isomerizes to $C_7H_{14}OOH$, followed by reaction with O_2 that leads to the production of two OH radicals and chain branching. This is the classical low temperature branching sequence. Sensitivity analysis shows that the influence of reaction 2-$C_7H_{14}OOH$-4 + O_2 =2-$C_7H_{14}OOH$-4-O_2 on the concentration of OH, in case A to be much larger than those in cases B and C. This result clearly shows that low temperature chemistry is important at low strain rates. Sensitivity analysis shows that case C, which has the same value for T_2 as case A, does not exhibit low temperature chemistry. Thus, strain has a greater influence than oxidizer temperature on low temperature chemistry.

FUNDAMENTALS OF SOOT FORMATION IN GAS TURBINE COMBUSTORS

Principal Investigators: M. B. Colket, R. J. Hall, D. Liscinsky and M. Smooke

United Technologies Research Center   and   Yale University
Silver Lane, E. Hartford, CT 06108   New Haven CT

SUMMARY/OVERVIEW:

The overall objectives of this work are to obtain necessary fundamental data and to enhance and then validate modeling procedures in order to support modeling of soot production in practical gas turbine combustors. Several focused tasks of this effort include (1) extending measurements of surface growth rate constants to high temperatures; (2) modeling of steady, laminar diffusion flames to assist in validating the models; (3) advancing the modeling capabilities for describing known physical processes involved in soot production; (4) modeling of sooting, transient flames; and (5) soot particle measurements using a scanning mobility particle sizer (SMPS) and a condensation nuclei counter (CNC) to determine applicability to flame and combustor exhaust measurements.

Progress in several areas is summarized below and references provided for further detail. First, experimental measurements of soot surface growth are discussed. Next advancements to our PAH and soot models are discussed and applications of these models to modeling soot production in coflow diffusion flames are described.

Determination of Surface Growth Rates at High Temperatures

An important parameter for the prediction of soot production is the surface growth rate. Virtually all fundamental and reliable measurements of this parameter have been obtained over the temperature range of 1500-1950K. Yet for high performance gas turbine combustors the 'sooting' rich zone will be at temperatures well in excess of 2000K. A series of fuel-rich, laminar premixed flames are being examined, analogous to several previous studies [see for example, Ref. 1-2]. We've utilized four separate experimental techniques for gathering information on soot particle growth. These include thermocouple particle densitometry (TPD) [3]; laser extinction (LE); transmission electron microscopy (TEM); and differential mobility. The first two of these methods provide soot volume fraction, TEM provides primary particle size and agglomerate structure, and the last provides information related to particle (agglomerate) size distribution and particle number density. This latter system utilized a Scanning Mobility Particle Sizer (SMPS) for classification of particles based on 'aerodynamic' diameters (equivalent diameter of a charged spherical particle drifting through an E-field) and a Condensation Nuclei Counter (CNC) for particle counting, following extraction of particle-laden flame gases using a dilution probe. Using correlations for agglomerated particles [4-5] and definitions for the aerodynamic diameter [6], we have derived equations to convert data from the SMPS/CNC system into Feret's diameter for agglomerated particles and the soot volume fraction. Diameters of primary particles are needed and

available from the TEM results. A SMPS/CNC system with sample collection times of 90s is attractive for use in combustor/rig environments in which sampling time is at a premium.

Volume fractions determined as a function of height in an ethylene/O2/Ar flame with C/O=0.80 from the three techniques (TPD, LE and SMPS/CNC) compare within a factor of two to each other and to other results [7] for the same flame. The SMPS/CNC data is slightly low, due to loss of particles in the sampling process. The TPD method is preferred; it is a point measurement and provides information on temperature as well. The largest uncertainty is in the deposit 'void' fraction, which we determined experimentally. The value of this parameter is high (~0.1) near the flame front location, qualitatively consistent with results from [3], but decreases rapidly to a constant value near 0.023 in the post-flame region. Details of this work are provided in [8,9].

Measurements have been obtained in several flames, although the goals of collecting data at and above 2000K have not been achieved due to poor flame structure. High flow rates are required to minimize loss of energy via conduction to the burner due to high adiabatic flame speeds. The existing data has been analyzed to examine the cause of the known rapid decay of surface growth rates from the 'young' soots to the 'aged' soots. Primary mechanisms examined are (1) decay of superequilibrium H-atoms, (2) surface ageing, and (3) loss of PAH species (reservoir of surface growth species) produced near the flame front. Interpretations are incomplete, but we have been unable to explain our data based on (1) or (2). Hence recent efforts are focused towards a better description of the PAH production models.

Computed Inception Rates in CoFlow Flames

Recently [10-11], we compared new experimental data and model predictions of flame structure and soot formation in two-dimensional, coflow, diffusion flames. The two-dimensional model includes a detailed transport, finite rate (detailed) chemistry gas phase system coupled with aerosol dynamical equations in the sectional representation. The soot model had been developed for laminar flames [12] and used to model soot production in an opposed jet diffusion flame [13]. Detailed submodels for the inception, growth, oxidation, and dynamics of soot particulates, as well as effects of radiation, are included in the model. In this model, inception rates are computed using steady-state expressions for the formation of naphthalenyl radical and phenanthrene; the expressions are based on presently understood reaction mechanisms and local concentrations of gas-phase species, (i.e. H, H_2, C_2H_2, phenyl, etc.). To gain some insight on the computed values, a scatter plot of inception rates as a function of temperature is shown in Figure 1 for the diluted ethylene flame. The preponderance of points depicts a bell shaped curve peaking around 1600K. A second bell is apparent that peaks slightly higher in temperature, 1650K, at larger levels. An analysis of the points indicated that the higher temperature curve with fewer points characterize soot inception along the centerline while the other curve depicts processes occurring in the annular region, just inside the flame front (denoted as wing). These results suggest that the two environments for inception along the centerline and the wings of the flame may be slightly different; different reaction mechanisms may dominate for the two regions. This conclusion appears to be compatible with the observations in the work by Dobbins and coworkers [14] on particle evolution along the centerline of a coflow (pure) ethylene flame.

Predictions in CoFlow Flames at Variable Fuel Dilution

A noticeable discrepancy between our previous model predictions and the experimental data for both the coflow diluted, methane and ethylene flames [10-11] is the underprediction of soot mass along the centerline of the burner. As described in last year's abstract and in [15], we believe part

of this underprediction is an incomplete PAH formation mechanism. Other issues analyzed in [15] include the number of soot 'sections' in our aerosol equations, ageing, and trade-offs between surface growth and inception rates. Despite this identifiable weakness in the model, we have also investigated the applicability of our model to other flame parameters. In particular, we compared predictions from our model [16] to new data obtained under separate support for simulating the effects of variable fuel-dilution on the soot field and flame structure. The results of experimental (Fig. 2) and predicted (Fig. 3) soot volume fractions as a function of radial position and height are compared. The predictions utilize a slightly modified version of the soot model utilized in [10,11]. The figures depict flames in which the percent of fuel (ethylene) in the center fuel jet is varied (balance nitrogen). The inability of the model to simulate the soot production along the centerline is apparent. In addition, the increase in the peak volume fraction with increasing fuel levels is not quantitatively simulated.

Modifications to the soot model have been tested. The most effective were (1) termination of surface growth at a predetermined diameter (e.g. about 30nm), (2) reducing the activation energy for surface growth to zero, and (3) increasing the rate of oxidation by OH (x2 from literature values). Revised predictions for the 60% ethylene flame are shown in Fig. 4. Agreement with the experimental data set is much improved. We will also impose cessation of coalescence at a predetermined size as well, which will relax the requirement for the high OH oxidation rate. The low activation energy for surface growth is unusual, although it has been reported for an acetylene diffusion flame [17]. Other modifications to the coflow code, including incorporation of the aerosol dynamic equations with treatment of agglomeration [18], are in progress.

References

1. S. Harris, A. Weiner and R. Blint, Combust. Flame **72**, 91 (1988). And references contained therein.
2. P. B. Sunderland and G. M. Faeth, C&F **105**, 132 (1996).
3. C. S. McEnally, U. O. Koylu, L. D. Pfefferle, and D. E. Rosner, Combust. Flame, **109**, 701 (1997).
4. Ü. Ö. Köylü, C. S. McEnally, D. E. Rosner, and L. D. Pfefferle, Combust. Flame, **110**, 494 (1997).
5. C. M. Megaridis, and R. A. Dobbins, *Combust. Sci. and Tech.,* **7**, 95-109, (1990).
6. Aerosol Measurement, Willeke and Baron, eds, Van Nostrand Reinhold, NY, (1993).
7. S. J. Harris, and A. M. Weiner, Combust. Sci. Tech., **32**, 267 (1983).
8. D. Liscinsky, M. Colket, B. True, R. Hall, and A. Bhargava, "Growth of Soot Particulates in Laminar, Premixed flames," Chem. Phys. Proc. Comb., Rayleigh, NC, October 10-13, 1999.
9. D. Liscinsky, M. Colket, R. Hall, A. Bhargava, B. True, and S. Morford, "Comparison of Particulate Sizing Techniques in Sooting Premixed Flames," AIAA paper no. , Reno, NV, Jan. 2000.
10. M. Smooke, C. McEnally, L. Pfefferle, R. Hall, and M. Colket, Combust. Flame, **117**, 117 (1998)C. McEnally, A. Schaffer, M. Long, L. Pfefferle, M. Smooke, M. Colket, and R. Hall, Twenty-Seventh Symposium (International) on Combustion, The Combustion Institute, Pittsburgh, 1497 (1998).
11. M. B. Colket, and R. J. Hall, in Soot Formation in Combustion, Mechanisms and Models, H. Bockhorn, Ed., Springer Series in Chemical Physics 59, Springer-Verlag, (1994).
12. R.J.Hall, M.D.Smooke, and M.B.Colket, in *Physical and Chemical Aspects of Combustion, A Tribute to Irvin Glassman* (F.L.Dryer and R.F.Sawyer, Eds.), Gordon and Breach, Amsterdam, (1998).
13. R. A. Dobbins, W. Govatzidakis, Lu, A. F. Schwartzman, and R. A. Fletcher, Combust. Sci. Tech. **121**, p. 103 (1996).
14. M. D. Smooke, M. B. Colket, and R. J. Hall, "Toward Quantitative Modeling of Soot Formation in CoFlow Diffusion Flames," Chem. Phys. Proc. Comb., Rayleigh, NC, October 10-13, 1999.

15. M. D. Smooke, C. S. McEnally, J. Fielding, M. B. Long, L. D. Pfefferle, R. J. Hall, and M. B. Colket, "Investigation of the Transition from Non-Sooting Towards Sooting, CoFlow Diffusion Flames," in preparation, 2000.

16. P. B. Sunderland, Ü. Ö. Köylü, and G. M. Faeth, Combust. Flame, **105**, 132 (1995).

17. R. J. Hall and M. B. Colket, "Calculations of Soot Aggregate Growth and Oxidation Using a Sectional Size Representation," Chem. Phys. Proc. Comb., Rayleigh, NC, October 10-13, 1999.
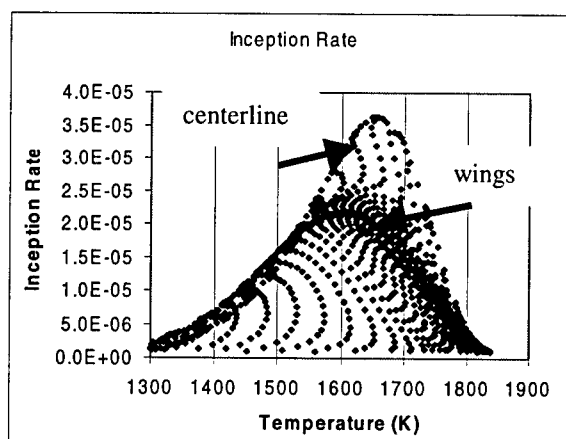
Figure 1. Inception Rate vs. Temperature at All Grid Points in the Ethylene Flame Simulation
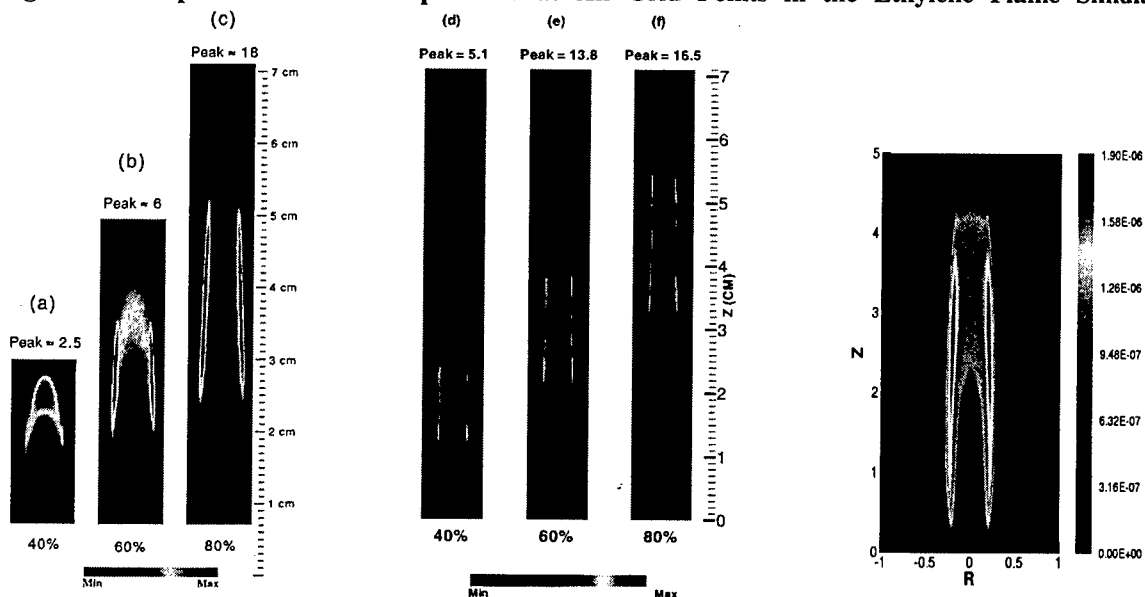
Fig. 2. Experimental soot contours for C2H4 coflow flames at 40, 60, 80% fuel.

Fig. 4. Predictions for 60% C2H4 coflow flame with revised model

Fig. 3. Predictions for C2H4 coflow flames at 40, 60, 80% fuel with original model.

CATALYTIC IGNITION AS A TOOL FOR CONVERTING SMALL ENGINES TO EFFICIENT JP-8 OPERATION

DAAD 19-00-1-0134 / P-40953-EG-DPS

Judi Steciak, Ph.D., P.E., Mechanical Engineering
Steve Beyerlein, Ph.D., Mechanical Engineering
Don Blackketter, Ph.D., Mechanical Engineering
David McIlroy, Ph.D., Physics

University of Idaho – Boise

800 Park Boulevard
Boise, Idaho 83712-7742

SUMMARY/OVERVIEW:

Recent innovations that partner catalytic igniters with conventional fuels promise technology that permits fuel flexibility in reciprocating engines. This research will support the development of a catalytic ignition system that permits more efficient operation of small, lightweight compression ignition engines operating with JP-8 or DF-2 diesel fuel. The scope of the research will include collecting data from flow reactor studies, performing engine durability testing, modeling in-cylinder catalytic ignition, characterizing catalyst surface degradation during long-term testing, developing new high-temperature materials, and integrating research with education through mentoring and cooperative learning. The results will improve commercialization of the system: a better understanding of the catalytic ignition mechanism, insights that improve igniter design and performance, demonstration of the technology robustness, and potential employees experienced in several aspects of combustion and engine research.

Applications include small generator sets, fire protection pumps, unmanned aerial vehicles, hybrid electric vehicle auxiliary power units, and miscellaneous lightweight 6 to 25 HP engines. Preliminary performance data show steady operation with some drops in NO_x and hydrocarbon emissions and improvements in thermal efficiency. The proposed research supports the DoD's strong need for engines that permit flexible fueling, use a single fuel type, exhibit improved performance, offer safer fuel storage, and generate fewer harmful emissions.

I. TECHNICAL DISCUSSION INTRODUCTION

Recent inventions [Cherry, et al., 1990; Cherry, 1992; Cherry, et al., 1992] permit the catalytic combustion of JP-8 in small, lightweight engines that operate efficiently. To overcome the difficulties related to burning heavy fuels in small engines, Cherry originally developed the Catalytic Plasma Torch (CPT) or SmartPlug [Cherry, 1992], referred to here as the catalytic igniter. Several advantages of the igniter's design were noted over conventional systems. These include increased power output, lower fuel consumption, extended lean-burn limits, reduced emissions, and simplified timing control [Cherry, et al., 1992].

The use of a catalytic igniter to oxidize a prechamber charge in an internal combustion engine is an example of a heterogeneous catalyst used to facilitate gas-phase combustion. The catalytic igniter is a self-contained ignition system that may be retrofitted to existing compression-ignition engines. Key design features are illustrated in Figure I.1. The igniter consists of a ceramic rod with an embedded heating element and a noble metal catalyst coating. Cold starting may require resistive pre-heating with up to 20 watts per igniter from an external power supply. The power supply is no longer necessary after a few minutes of operation at moderate loads. The ceramic rod is enclosed in a custom-machined shell, which forms a pre-chamber adjacent to the main combustion chamber. The shell fits into existing spark plug or fuel injector ports. Surface ignition begins as fresh mixture contacts the catalyst during the compression stroke. Because of the reduced activation energy associated with heterogeneous catalysis, this occurs at temperatures far below the normal gas-phase ignition temperature. Combustion products and intermediate species then accumulate in the pre-chamber surrounding the ceramic rod. After sufficient temperature is achieved because of compression, multi-point homogeneous ignition results [Cho, 1986]. The homogeneous reactions in the boundary layer over the catalyst surface rapidly propagate to the small volume of the igniter prechamber.
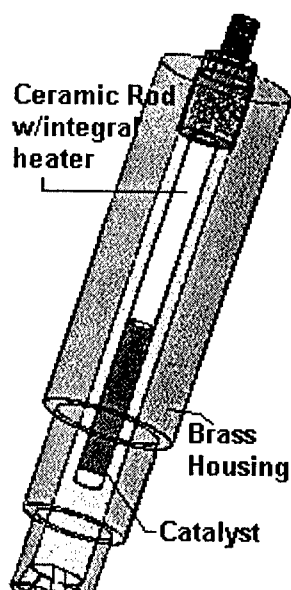
Figure I.1 Catalytic Igniter (U.S. Pat. # 5,109,817; Cherry, 1992) (Figure from Morton. et al.. 1999)

The mixture is then rapidly expelled through the nozzles at the bottom of the igniter. The nozzles cause the flame torch to swirl and ignite the main charge in an exceedingly short period of time. Adjusting the position of the catalyst section on the ceramic rod controls ignition timing. To cause an ignition delay, the catalyst must be moved away from the nozzles at the bottom of the igniter. To cause an ignition advance, the catalyst probe must be moved closer to the nozzles.

University of Idaho researchers have explored alternative fuel combustion in internal combustion (IC) engines. Ongoing research includes development of catalytic igniters and combustion of a variety of fuels. Current projects focus on practical applications of the technology, and additional work is needed to better understand the process in order to improve the technology. Fundamental research on catalytic engines systems is needed via flow reactor studies, materials properties work, and catalyst surface characterization. Modeling of in-cylinder heat release and fuel reforming/reaction kinetics is needed. The results of this program will help develop applications for integration onto test platforms and improve new igniter designs. The research will focus on include improved performance of lightweight heavy fuel engines operating with JP-8 or DF-2.

The research topics are divided into two broad areas - Catalyst Development, Optimized Ignition Timing, and In-system Operation - as described below.

A. Catalyst Development
1. Fabrication of temperature resistant substrate materials (McIlroy)
2. Manufacturability of practical igniters (Beyerlein, Steciak)
3. Catalyst surface characterization with scanning electron microscopy (SEM) and Auger electron spectroscopy (McIlroy)

B. Optimized Ignition Timing
1. Catalyst ignition studies with a plug flow reactor (Steciak and Beyerlein)
2. Catalytic ignition modeling (Beyerlein and Steciak)
3. Parametric studies with a single-cylinder CFR engine (Beyerlein)

C. In-system Operation
1. In-cylinder heat-release modeling (Beyerlein and Steciak)
2. Long-term engine durability testing (Blackketter)
3. Engine performance and emission testing (Steciak, Beyerlein, Blackketter)

Further discussion focuses on those tasks of special interest in combustion: B. Optimized Ignition Timing and C.1 In-cylinder modeling.

B.1 Catalytic Ignition Studies: In conventional combustion systems, control is maintained by manipulating gas temperature, equivalence ratio, and fluid mixing. Introducing catalytic surfaces into a combustible environment supplies an additional control parameter, namely the surface reaction rate. The objective of this project is to produce a model that accurately predicts heterogeneous and homogeneous ignition over a range of fuel types and initial thermal conditions. Data for this model will be generated from flow reactor studies and spectroscopic characterization of catalytic surfaces taken from different operating environments.

A plug flow, pressurizable reactor is being built that will permit fuel vaporization, gas mixing, near-adiabatic reaction, and emissions monitoring. The reactor will be capable of heating the fuel mixture before it reaches the catalyst to prevent condensation. Gas inlet temperature, initial catalyst temperature, and catalyst surface area will be variable. Reaction products will be examined. Species of interest will include alkanes, aromatics, carbon monoxide, and nitric oxides. The reactor will be used to obtain catalytic ignition temperatures at different partial pressures of fuel and oxygen. The transition temperature from kinetically controlled surface reaction to diffusion controlled surface reaction will be carefully documented. Special attention will be given to studying long-term changes in the flow reactor behavior under operating conditions similar to those experienced in catalytic engine tests.

B.2 and C.1 Catalytic Ignition and In-cylinder Heat-Release Modeling: Engine performance will be modeled in two ways: with a first generation model and with the KIVA program. The simple model uses heat release data derived from instantaneous pressure-crank-angle data. Of particular interest will be the role of excess water on compression and expansion characteristics. A first generation model indicates that maximum cylinder pressures with water/fuel mixtures can be increased over fuel-only operation, even though maximum cylinder temperatures are dramatically reduced. The goal of this analysis is to define the relationship between indicated mean effective pressure (IMEP) and water/fuel ratio over a range of throttle conditions. Engine operating conditions where catalytic ignition is not self-sustaining will be contrasted against these findings.

KIVA is a transient, three-dimensional, multiphase, multicomponent code for the analysis of chemically reacting flows with sprays. The program was designed for performing internal combustion engine calculations and it has been under development at the Los Alamos National Laboratory for the past several years. The code is valid from low speeds to supersonic flows for both laminar and turbulent regimes. Arbitrary numbers of species and chemical reactions are allowed.

B.3 Parametric Studies with a Single-cylinder CFR Engine: The single-cylinder CFR engine permits control of several key parameters for improving igniter modeling and design. Variation of the fuel-to-air ratio, the compression ratio, catalyst position in the prechamber, throttling (initial charge pressurization), and cold start amperage will provide a matrix for optimal igniter performance. The CFR engine will be modified to accommodate both main and pre-chamber pressure measurements.

II. Integration of Research and Education: The Mechanical Engineering Department at UI has developed a model for developing leadership skills among graduate mentors, senior design students, and faculty.

The increasing importance and complexity of projects in our capstone design curriculum motivated the model. Traditionally, leadership for capstone design classes comes from a senior faculty member responsible for the entire class. However, this does not equip students with the necessary human dynamics skills. The Idaho Engineering Works (IEWorks; Odom, et al. [1999]) model makes use of a continuous cycle of peer-to-peer training, customer communication, ongoing dialogue about personal/professional development, and commitment to excellence in the context of an engineering project. The result has been an increase in both the quality of the students' experience and in the products that have been developed.

The infrastructure for the development of graduate students within IEWorks is composed of one-on-one interaction with the major advisor, group meetings with all advisors and graduate students, and meetings with only the graduate students present. The meeting structure involves one 2 hour meeting per week as the entire group. Presently we have 10 graduate students and three advisors participating. As a group, the students are involved in leadership discussions and have a unifying project for the semester. For example, the IEWorks has developed hardware for custom research equipment and developed cost-effective electric and hybrid electric vehicle (HEV) technology that has won national competitions. The IEWorks provides a unique and powerful setting for graduate and undergraduate students to make valuable contributions to research, develop leadership skills, master life-long learning habits, and mentor peers.

IV. References

Cherry, M. A., Elmore, C. L., "Timing Chamber Ignition Method and Apparatus," *US Patent* 4,977,873, December 18, 1990.

Cherry, M. A., "Catalytic-Compression Timed Ignition," *US Patent* 5,109,817, May 5, 1992.

Cherry, M. A., Morrisset, R. J., Beck, N. J., "Extending Lean Limit with Mass-Timed Compression Ignition Using a Catalytic Plasma Torch," *Society of Automotive Engineers Paper 921556,* 1992.

Cho, P., and Law, C. K., "Catalytic ignition of fuel/oxygen/nitrogen mixtures over platinum," *Combustion and Flame*, Vol. 66, pp. 159-170, 1986.

Morton, A., Munoz-Torrez, G., Beyerlein, S., Steciak, J., McIlroy, D., and Cherry, M. "Aqueous Ethanol Fueled Catalytic Ignition Engine," *Society of Automotive Engineers Paper 99SETC-5*, September 1999.

Odom, E. M., Beyerlein, S. B., Tew, B.W., Smelser, R. E., and Blackketter, D. M., "Idaho Engineering Works: A Model for Leadership Development in Design Education," ASEE and IEEE Joint Conference, Frontiers in Education, November 1999.

Mixing, chemical reactions, and combustion
in subsonic and supersonic turbulent flows

P. E. Dimotakis and A. Leonard

Graduate Aeronautical Laboratories
California Institute of Technology, Pasadena, CA 91125

Summary/Overview

This research is focused on fundamental investigations of mixing, chemical-reaction, and combustion processes, in turbulent, subsonic, and supersonic flows. The program is comprised of an experimental effort; an analytical, modeling, and computational effort; and a diagnostics- and instrumentation-development effort. Computational studies have focused on fundamental issues pertaining to hydrocarbon-ignition/-combustion and the numerical simulation of compressible flows with strong fronts, in both chemically-reacting and non-reacting flows.

Technical discussion

Our work on hydrocarbon combustion in high-speed flows focused on the oxidative characteristics of ethylene (C_2H_4) because of its relevance to high Mach number, air-breathing propulsion concepts.[1] It was shown that for flight Mach numbers in the range, $4 < M\omega < 8$, C_2H_4 is a major product of the thermal cracking of the JP-type fuels, and that it largely affects the ignition characteristics of the resulting fuel mix? While C_2H_4 is a relatively simple molecule, its kinetics are not well understood, compared to the extensively studied methane (CH_4), for example. Furthermore, there are challenges in describing the kinetics of the destruction paths of the vinyl radical (C_2H_3) *[e.g., Refs. 3, 4]*.

A comparative numerical study of C^2H^4 kinetics was conducted in flames, by using six recent mechanisms: TAN94,[5] GRI21,[6] WF97,[7] MRN98,[4] GRI30,[8] and W99.[3] The simulations included laminar-flame speeds as well as the ignition/extinction curves at non-premixed conditions, of relevance to SCRAMJET operation. Relatively large discrepancies in predicting these fundamental flame properties were found among the six mechanisms. Differences by factors as high as 2.5 were found in the calculated laminar-flame speeds. The results for non-premixed systems (Fig. 1) also revealed large differences in predicted ignition and extinction strain rates, by factors between mechanisms as high as 300 and 3, respectively. Detailed analyses showed that uncertainties exist in fuel kinetics arid, most importantly, on the oxidation of C_2H_3 and the production of vinyoxy (CH_2CHO), whose kinetics are not well known and can crucially affect the production of the important H radicals. This part of the work is a collaboration with F. Egolfopoulos of USC. Experiments are under development to provide measurements for many of these important, but undocumented, hydrocarbon-flame properties.
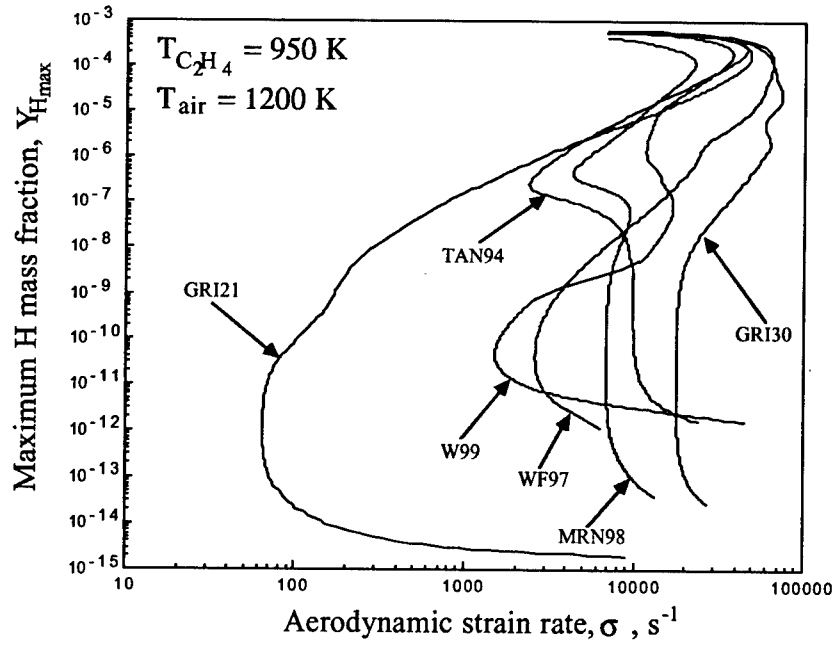
FIG. 1 Predicted Z-curve responses for non-premixed C_2H_4/air flames (see text for mechanism legend).

FIG. 2 3-D scalar structure of transverse jet at $Rc \simeq 1.0 \times 10^3$ and $x/d \simeq 100$. Highlighting intensity denotes jet-fluid-concentration values.

vantage of both the transverse jet configuration as well as recent progress in high-resolution, high-signal-to-noise digital imaging systems made as part of this effort. Quantitative measurements of the scalar field in the cross-section of the transverse jet were made using the Cassini digital-imaging system. Figure 2 depicts the 3-D structure of the scalar field of the transverse jet assembled from a sequence of LIF measurements. The figure shows the structure of two isosurfaces, 100 diameters downstream from the jet exit for a transverse jet at $Rej \sim 103$. Highlight intensity marks jet-fluid concentration values. A study of mixing in this flow has shed light on its dependence on Reynolds number.
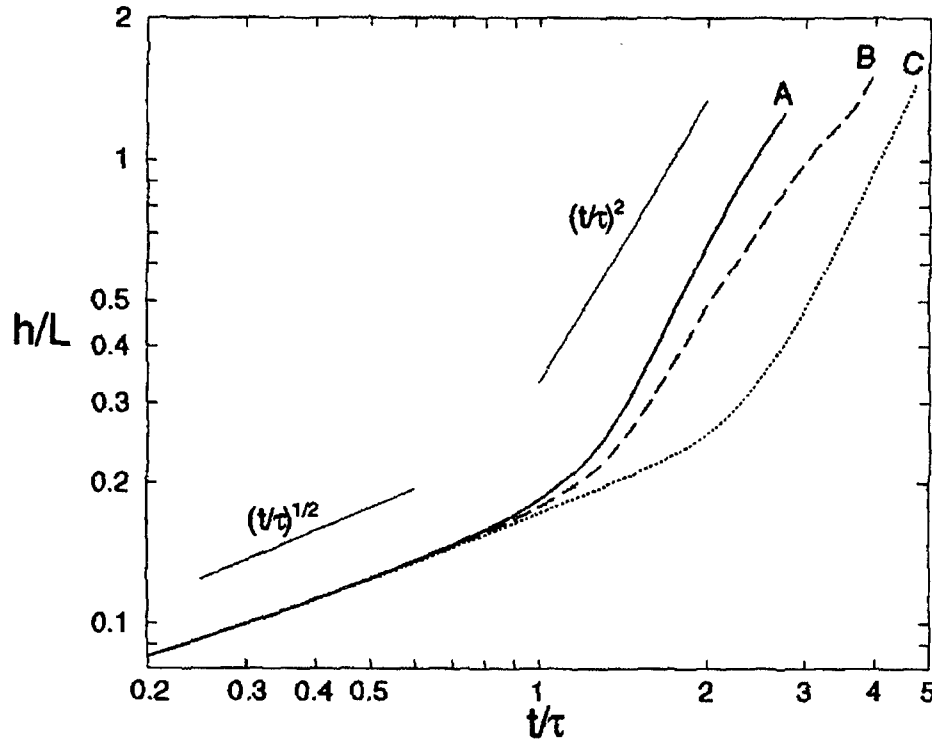
FIG. 3 Mixing-zone extent, h/L, vs. t/τ for three runs. L denotes the transverse extent of the simulation box and $\tau = (L/Ag)^{1/2}$), for A = 1/2, where A = $(\rho_2 - \rho_1)/(\rho_2 + \rho_1)$ is the Atwood number and g is the magnitude of the acceleration.

In our work on Rayleigh-Taylor instability (RTI), an important phenomenon in many nonuniform density flows exposed to accelerations of all kinds, we have extended previous direct numerical simulations (DNS) to outer-flow Reynolds numbers up to 3500. Figure 3 plots the growth rate for three runs with identical boundary conditions and small differences in their initial conditions. It indicates that the RTI mixing zone grows initially diffusively, with a late-time growth not too far from quadratic, even though it is difficult to say whether differences from quadratic growth are attributable to inadequate statistical convergence, or because asymptotic evolution does not correspond to $h \propto t^2$ growth, where h is the R-T mixing-zone height. If quadratic temporal growth is to be accepted, the effective growth coefficients must be regarded as sensitive functions of the initial conditions. Mixing is also found to reflect details of the initial conditions, at least for the timespan in these simulations. These results are in accord with documented behavior for high Reynolds number shear layers, for example, with which this flow bears some similarity.[9] The DNS-based investigations represent a collaboration with A. Cook of the Lawrence Livermore

National Laboratory. Experiments are also under development at Caltech, at low Atwood number, aimed at the effects of Reynolds number beyond those attainable by DNS.

In other work, progress has been made in investigations of internal flows downstream of expansion ramps, in Image Correlation Velocimetry,[10] as well as in high framing-rate digital imaging.

References

[1] Edwards, T., "Fuels and Fuel System Area: Air Force Perspective," AFOSR/NASA Workshop on Supersonic Scramjet Combustion. 13-16 May 1996, Newport News, VA (1996).

[2] Egolfopoulos, F. N., and Dimotakis, P. E., "Non-premixed hydrocarbon ignition at high strain rates," *Twenty-Seventh Symposium (International) on Combustion.* The Combustion Institute, Pittsburgh, 641-648 (1998).

[3] Wang, H., Laskin, A., Djurisic, Z. M., Law, C. K., Davis, S. G., and Zhu, D. L., "A Comprehensive Mechanism of C2Hx and C3Hx Fuel Combustion," *Chemical and Physical Processes of Combustion* (1999 Fall Technical Meeting of the Eastern States Section of the Combustion Institute, Raleigh, NC), 129-132 (1999).

[4] Marinov, N., "A Detailed Kinetic Model for High-Temperature Ethanol Oxidation," *Int. J. Chem. Kinet.* (in press) (1998).

[5] Tan, Y., Dagaut, P., Cathonnet, M., Boettner, J. C., Bachman, J. S., and Carlier, P., *Twenty-Fifth Symposium (International) on Combustion* The Combustion Institute, Pittsburgh, 1563-1569 (1999).

[6] Frenklach, M., Wang, H., Goldenberg, M., Smith, G. P., Golden, D. M., Bowman, C. T., Hanson, R. K., Gardiner, W. C., and Lissianski, V., "GRI-Mech -- An Optimized Detailed Chemical Reaction Mechanism for Methane Combustion," GRI Technical Report No. GRI-95/0058 (1995).

[7] Wang, H., and Frenklach, M., "A Detailed Kinetic Modeling Study of Aromatics Formation in Laminar Premixed Acetylene and Ethylene Flames," *Comb. and Flame* 110, 173-221 (1997).

[8] Bowman, C. T., Frenklach, M., Gardiner, W. R., and Smith, G., "The GRI 3.0 Chemical Kinetic Mechanism,"]attp://www. me. Berkeley.edu/gri_mech/ (1999).

[9] Slessor, M. D., Bond, C. L., and Dimotakis, P. E., "Turbulent shear-layer mixing at high Reynolds numbers: effects of inflow conditions," *J. Fluid Mech.* 376, 115-138 (1998).

[10] Pitz, R. W., Wehrmeyer, J. A., Ribarov, L. A., Oguss, D. A., Batliwala, F., DeBarber, P. A., Deusch, S., and Dimotakis, P. E., "Unseeded Molecular Flow Tagging in Cold and Hot Flows Using Ozone and Hydroxyl Tagging Velocimetry," *Meas. Sc. & Teeh.* (to appear) (2000).

CHEMICAL KINETICS AND AERODYNAMICS OF IGNITION

Principal Investigator: Chung K. Law

Princeton University
Princeton, NJ 08544

SUMMARY/OVERVIEW

This program investigates the coupled effects of convection, diffusion, chemical kinetics, and turbulence on ignition of a cold fuel jet by a counterflowing heated air jet, simulating the situation in Diesel engines. During the reporting period, the ignition temperatures of the reference fuels n-heptane and iso-octane were experimentally obtained and computationally modeled using semi-empirical mechanisms. The results were found to be similar to those for smaller hydrocarbons. Consequently, by comparing the ignition temperatures of a number of C_1 to C_8 alkanes under similar conditions, it was found that for larger hydrocarbons the ignition temperatures become fairly uniform with some fluctuations. In a second project, the first step in modeling turbulent ignition was taken by calculating the characteristics of non-reacting counterflows. It was found that a Reynolds stress turbulence model predicts the velocity profiles reasonably well. In a third project, an augmented reduced mechanism for methane oxidation and NO_x chemistry was developed and comprehensively validated.

TECHNICAL DISCUSSION

1. Ignition of n-heptane and iso-octane

N-heptane and iso-octane are used as reference fuels for engine knock because they have similar vaporization pressures while their fuel structures are representative of two important constituents of practical fuels, linear and branched alkanes. Considerable research has been conducted in homogenous systems, however in many practical devices, ignition occurs in strongly non-homogenous environments with large temperature and concentration gradients. To address this issue, nonpremixed ignition experiments were conducted for n-heptane and iso-octane in a counterflow of hot air against fuel diluted with nitrogen. The air temperature required to ignite the fuel mixture is indicated as a function of strain rate in Fig. 1 and pressure in Fig. 2. Since ignition in this configuration provides an additional test for the comprehensiveness of chemical models due to the highly non-uniform conditions experienced by the reactants as they are swept through the flow field, existing empirical models are compared with the experiments.

Ignition temperatures increased for both fuels as the strain rate increased due to reduced residence time. Increased pressure caused the ignition temperatures to decrease for both fuels because the limiting reactions are facilitated at higher pressures whereas the pressure-weighted diffusion rates are not affected much. N-heptane ignited at lower temperatures than iso-octane, consistent with the fact that its alkyl radical is much less reactive, resulting in a net consumption of hydrogen radicals from hydrogen abstraction. All of these results are consistent with the ignition of smaller hydrocarbon fuels.

The calculated ignition temperatures were about 100K higher than the experiments, similar to the discrepancy found when modeling methane and ethane ignition. Diffusive sensitivity analysis indicated that fuel diffusivity is very important, but even a 50% increase in diffu-

sivity does not bring the experiments and calculations into agreement. All reactions have lower sensitivities than fuel diffusion, and the highest reaction sensitivity coefficients are associated with C_3 species and smaller. Both heat release and chain branching are necessary to achieve ignition. These computational results are also similar to results for ethane.

The models do not include elements of low temperature chemistry, but this is not believed to be important under the conditions investigated. Indications of this include the good prediction of strain rate and pressure trends. In addition, the pressure dependence is like that of other hydrocarbons when they are not strongly influenced by low temperature chemistry. Finally, it was shown for ethane that low temperature chemistry does not qualitatively change the results and only has a small quantitative effect because of the dominance of high temperature pathways during ignition. The qualitative similarity between low temperature mechanisms of different hydrocarbons suggests that this conclusion should also apply to the fuels studied in the present work.

2. Ignition trends of C_1-C_8 hydrocarbons

The similarities noted between the ignition of n-heptane and iso-octane and other hydrocarbons invite a comparison of ignition temperatures under similar conditions. The results, shown in Fig. 3a for a 5% fuel concentration, indicate that the ignition temperature has a non-monotonic dependence on the fuel molecule size. Since ignition under these conditions is very sensitive to fuel concentration, the experiments were repeated holding the carbon atom content of the fuel constant and the results are shown in Fig. 3b.

Evidence is seen for three primary mechanisms that determine the ignition temperature. The first is the reactivity of the alkyl radical, which depends on the fuel structure. The second is the effect of fuel size on diffusivity. The third is the effect of finite rate kinetics and the complex coupling between reaction and transport for the many intermediate species. The effect of fuel structure is responsible for the high ignition temperatures of methane, iso-butane, and iso-octane. Decreasing fuel diffusivity as fuel size increases is responsible for a rise in ignition temperature from ethane through n-butane. It does not seem likely that this increase will continue indefinitely since this would imply that the large fuel molecules found in many practical fuels would have an extremely high ignition temperature. Indeed, unambiguous evidence for this increasing trend does not appear beyond n-butane, as the complexities of finite rate kinetics result in a somewhat uniform ignition temperature from n-butane through n-heptane. In both figures, the variation in ignition temperature for straight chain alkanes larger than propane is less than 20K, which is small relative to the uncertainties associated with determining the actual magnitude of the measured ignition temperatures. This indicates that even though the general finite rate kinetics of hydrocarbon combustion is important, the specific kinetic differences between these fuels, as long as they have similar structures, only have a small effect on ignition temperature.

3. Modeling of turbulent counterflows

Combustion usually occurs in flows that are highly turbulent. To understand these flows, it is important to consider the complex non-linear interactions between reaction, convection, diffusion, and turbulence. Fortunately, in some situations the problem can be simplified. Ignition is an important example since the amount of heat release *prior to* ignition is small enough that it does not significantly affect the flow or transport properties. As a result, the non-reacting turbulent flow field can be solved first and then the reactions can be solved within this known flow and the ignition process can be investigated. Therefore, the first step in a systematic investigation of turbulent ignition is to model the non-reacting turbulent counterflow

A quasi-one dimensional approach was selected for reasons of computational efficiency, and two different turbulence models were examined. The k-ε model is widely used due to its

computational efficiency since it only requires two new equations. However, this theory assumes near isotropy for the turbulence, which is not a good assumption in a counterflow. Many experiments are not isotropic at the boundaries, and even if they were, the stagnating flow would cause the turbulence to become quickly anisotropic. Figure 4 compares experimental values of turbulent kinetic energy with predictions using the k-ε model. The incorrectly calculated Reynolds stresses increase the turbulence production term leading to the significantly overpredicted turbulent kinetic energy.

A Reynolds stress model was used to explicitly calculate the Reynolds stresses to avoid this problem. The results, shown in Fig. 5, indicate that the agreement between the calculations and experiments is fairly good. Five additional equations were required, but the quasi-one dimensionality and the decoupling of chemistry kept the computational time low. The calculations did highlight several important points when trying to model experiments. It is important to accurately model mean velocity profile since the amount of turbulence production at a given location depends on the entire history of the fluid from when it left the boundary. In addition, the boundary value of turbulent dissipation is an important parameter that cannot be measured experimentally. To form an estimate, it is important to know the turbulent length scale at the boundary.

4. Development of Augmented Reduced Mechanisms

An augmented reduced mechanism (ARM) for methane oxidation, consisting of 16 species and 12 lumped reaction steps, was developed and showed excellent performance in reproducing the global responses of a wide range of combustion phenomena, including auto-ignition, laminar flame propagation, and counterflowing nonpremixed systems, under extensive thermodynamical parametric variations including those of temperature, pressure, and composition. The validation has now been extended to that of detailed thermal and concentration structure, and excellent performance is again observed. Augmented reduced mechanisms have also been derived from GRI-Mech 3.0, including the NO_x chemistry. This work is jointly supported by ARO and AFOSR.

MAJOR PUBLICATIONS

[1] "Ignition of Ethane, Propane, and Butane in Counterflow Jets of Cold Fuel versus Hot Air Under Variable Pressure," by C.G. Fotache, H. Wang and C.K. Law, *Combustion and Flame*, Vol. 117, pp. 777-794 (1999).

[2] "Effects of NO on the Ignition of Hydrogen and Hydrocarbons by Heated Counterflowing Air," by Y. Tan, C.G. Fotache, and C.K. Law, *Combustion and Flame*, Vol. 119, pp. 346-355 (1999).

[3] "Ignition of CO/H_2/N_2 versus Heated Air in Counterflow: Experimental and Modeling Results," by C.G. Fotache, Y. Tan, C.J. Sung and C.K. Law, *Combustion and Flame*, Vol. 120, pp. 417-426 (2000).

[4] "Non-Premixed Ignition of n-Heptane and iso-Octane in a Laminar Counterflow," by J.D. Blouch **and C.K. Law, *Proceedings of the Combustion Institute*, Vol. 28, in press.**

[5] "Further Validation of an Augmented Reduced Mechanism for Methane Oxidation: Comparison of Global Parameters and Detailed Structure," by C.J. Sung, C.K. Law, and J.Y. Chen, *Combustion Science and Technology*, in press.

[6] "Augmented Reduced Mechanisms for NO Emission in Methane Oxidation," by C. J. Sung, C.K. Law, and J.Y. Chen, submitted.
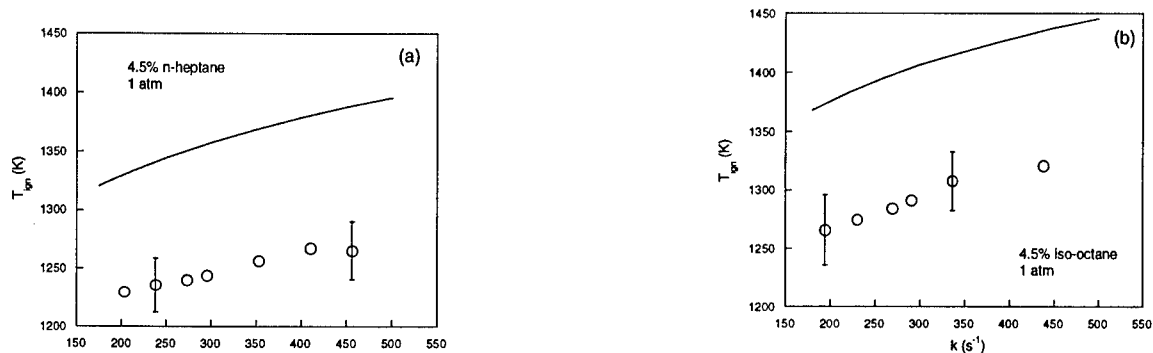
Figure 1: Effect of strain rate on ignition temperature. Experiments shown by symbols and calculations by solid line.

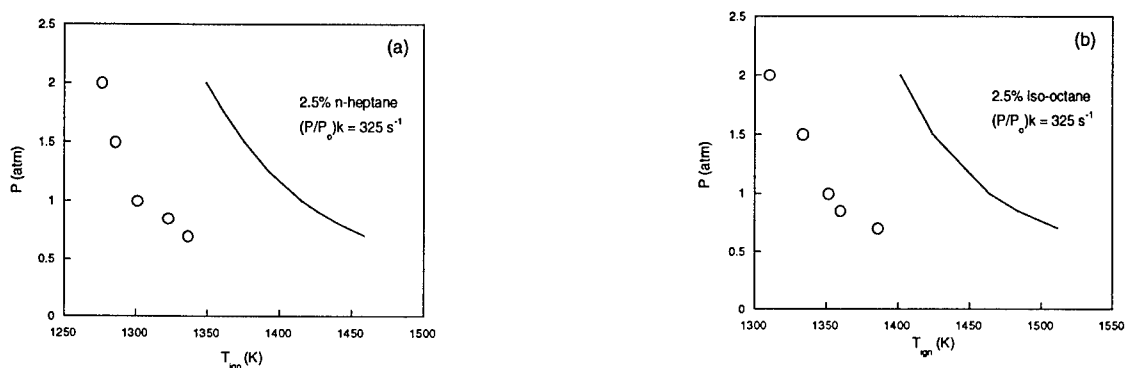

Figure 2: Effect of pressure on ignition temperature.
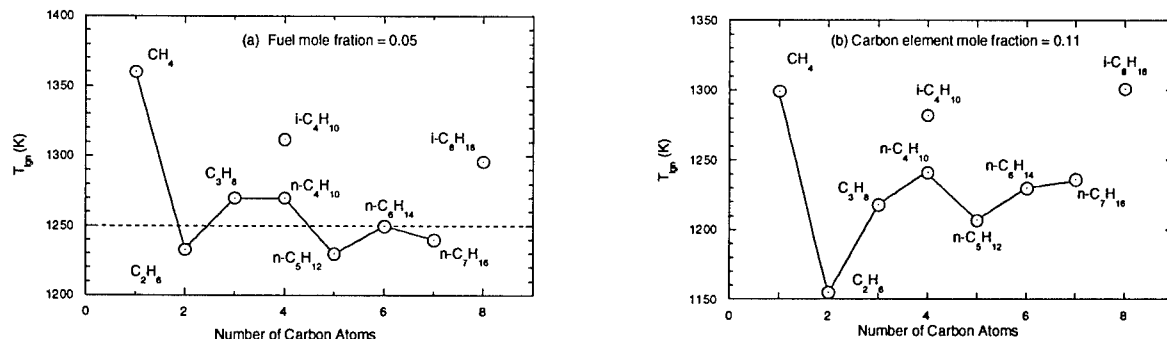

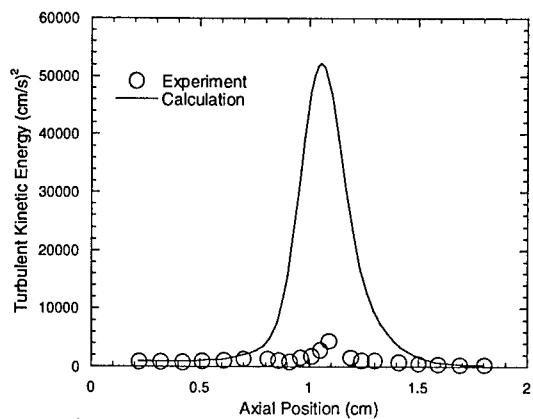Figure 3: Effect of fuel molecule size on ignition temperature at 1 atm. and a strain rate of 300s^{-1}.
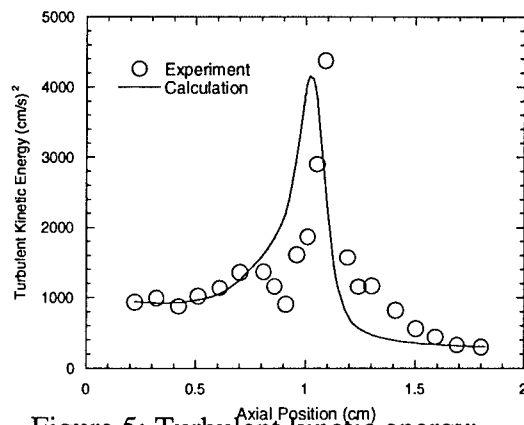

Figure 4: Turbulent kinetic energy: k-ε model.

Figure 5: Turbulent kinetic energy: Reynolds stress model.

PHYSICAL AND CHEMICAL PROCESSES IN FLAMES

Principal Investigators: Chung K. Law[*] and Hai Wang[&]

[*]Department of Mechanical and Aerospace Engineering
Princeton University
Princeton, NJ 08544

[&]Department of Mechanical Engineering
University of Delaware
Newark, DE 19716

SUMMARY/OVERVIEW

The objectives of the present program are to develop detailed and simplified chemical kinetics model for hydrocarbon-fuel combustion, and to understand and quantify the dynamics of flames. During the reporting period progress has been made in the following projects on reaction kinetics: (1) development of a detailed kinetic model for the oxidation of 1,3-butadiene, a key intermediate during the combustion of liquid-hydrocarbon fuels, (2) to address the fundamental question of model development in that whether a state-of-the-art model of C_1-C_2 combustion can be used as a kinetic subset for $C_{>3}$ combustion as is, without re-optimizing the kinetic parameters of this subset, and (3) to address the level of uncertainty associated with the diffusion coefficients of certain free-radical–molecule pairs. These projects represent the three key ingredients that are necessary to the success of the overall research program and goals. That is, (1) the formulation of physically justifiable kinetic model, (2) the methodology of model development, and (3) the physical-chemical properties of the flame that are relevant to kinetic model validation. Concerning flame dynamics, progress has been made on the following projects: (4) pulsation and flammability limits of lean heptane/air flames, (5) Effects of curvature on pulsating instability, and (6) radiation induced flamefront instability.

TECHNICAL DISCUSSION

1. Experiments and Detailed Kinetic Modeling of 1,3-Butadiene Oxidation at High Temperatures

The oxidation kinetics of 1,3-butadiene (1,3-C_4H_6) is of considerable importance to the hierarchical development of the kinetic mechanisms of long-chain aliphatics and aromatics combustion. Previously we developed a comprehensive kinetic model of acetylene, ethylene, allene, propyne, propene, and propane combustion. This model can predict a wide variety of combustion responses from ignition and laminar flame propagation to the overall and detailed structures of fuel oxidation and combustion. We have extended the previous model to include the kinetics of 1,3-butadiene pyrolysis and oxidation during the reporting period, a recent step in the direction towards a comprehensive and self-consistent kinetic model of liquid hydrocarbon-fuel combustion.

Specifically, the high-temperature kinetics of 1,3-butadiene oxidation was examined with detailed kinetic modeling. To facilitate model validation, flow reactor experiments were carried out for 1,3-butadiene pyrolysis and oxidation over the temperature range 1035-1185 K and at atmospheric pressure, extending similar experiments found in the literature to a wider range of equivalence ratio and temperature. The kinetic model was compiled on the basis of an extensive review of literature data. The reaction pathways and rate constants of several key reactions were examined closely by a detailed analysis of previous experimental results, by thermochemical considerations, and by Rice-Ramsperger-Kassel-Marcus (RRKM) calculations. Notably these

reactions include the attack of the H and O atoms on 1,3-butadiene. The accuracy of the rate constants associated with these reactions proves to be critical to the overall kinetics of 1,3-butadiene pyrolysis and oxidation.

The kinetic model was critically validated against a total of 15 sets of experimental data including species profiles during 1,3-butadiene pyrolysis and oxidation in flow reactors and shock tubes, and 1,3-butadiene flames. It is shown that the kinetic model compiled in this study is capable to closely predict a wide range of high-temperature oxidation and combustion responses.

The analysis of individual reactions and the reaction pathway based on the current kinetic model revealed a viewpoint of 1,3-butadiene kinetics significantly different from previous studies. We identified three parallel pathways to be relevant to 1,3-butadiene oxidation, with the chemically activated reaction of H and 1,3-butadiene to produce ethylene and the vinyl radical being the most important channel over all experimental conditions. Extensive sensitivity analyses were performed; and the remaining uncertainty of the butadiene chemistry is discussed.

The above results are reported in Publication No. 1.

2. Combustion Chemistry of Propane: A Case Study of Reaction Mechanism Optimization

Detailed reaction mechanisms describing hydrocarbon combustion have hierarchical structures with H_2 and CO chemistry at the base, supplemented by necessary reaction channels of larger chemical species. While this strategy provides rational organization of combustion chemistry, it is unknown whether parameter sets derived by optimizing smaller-hydrocarbon chemistry are secure foundations for extension to larger-hydrocarbon oxidation models. This question was addressed in the present work by combining the newly optimized GRI-Mech 3.0 for methane and ethane combustion with the C_3H_x chemistry developed by us previously. Model predictions were compared against methane, ethylene, ethane, propyne, allene, propene, propane laminar flame speed and shock tube ignition delay data. It was found from extensive sensitivity testing that the coupling between the C_3H_x chemistry and the C_1-C_2 kinetic subset was much stronger than anticipated. The C_3H_x combustion data could not be satisfactorily modeled using the C_1-C_2 kinetic subset without re-optimizing some of the $C_{<3}$ kinetic parameters. These parameters have stronger influences on C_3H_x combustion than the C_3 parameters. Parameter optimization analogous to the GRI-Mech 3.0 optimization was carried out using essentially the same methods as were used in the development of C_1-C_2 kinetic subset, including 21 optimization targets, of which 9 were ignition delays and 12 were atmospheric pressure laminar flame speeds. A reasonable match to the whole target set could be obtained, without deteriorating the agreement between experiment and calculation for the methane and ethane combustion data, by re-optimizing 9 parameters from the C_1-C_2 kinetic subset.

The implication of this study is significant, in that in a practical term any reaction mechanisms proposed previously and many more to come represent just individual points within the uncertainty space of a given kinetic set. Maximizing the likelihood that a kinetic model can predict a combustion property beyond the regime within which the model is validated can only be achieved by comprehensive optimization. In this way the size of the uncertainty space is reduced only to an extent as being inconsequential to the combustion of a given set of target fuels. The second implication of the study is that kinetic model optimization in a multi-parameter, -target, and -fuel space is entirely possible as will be pursued in our research program. Through this study, we also developed a tentatively optimized combustion model, which predicts very well a wide variety of C_1-C_3 fuel combustion.

The above results are reported in Publication No. 2.

3. Effect of Inelastic Collision on Binary Diffusion Coefficients of Free-Radical

Diffusion is a key factor in chemically reacting flow, notably combustion, where the propagation rate of a flame is determined by diffusion as well as chemical reaction and heat release. It is known that the sensitivity of flame propagation to the H-atom diffusion coefficient is as large as

that of the free-radical chain branching reaction H + O_2 → O + OH. Despite the recent progress in the description of H-atom diffusion coefficient, the molecular theory of H-atom diffusion remains to be that of Chapman-Enskog, in which elastic collision is assumed. On the other hand, it is known that collision of the H atom with notable combustion species including H_2, CO, CO_2, O_2, C_2H_2, and C_2H_4 is inelastic at combustion temperatures. At very high temperatures, say, 2500 K, nearly a quarter of collision encounter between the H atom and N_2 is inelastic. This inelastic collision can be best described by the formation of a transient chemical bond, whose binding energy is of the order of 10^3 times larger than the well depth of a typical Lennard-Jones potential.

In this work, we examine the influence of inelastic collision on diffusion coefficients. Our aim was to obtain an order-of-magnitude estimate for this influence, and compare it to the influence of reaction rate parameters. In this way the uncertainty resulting from the diffusion coefficients can be assessed.

Diffusion coefficient was examined using molecular dynamics simulation and the Green-Kubo formula, with pair interaction potential energies corresponding to collision with and without the elastic assumption. It was found that inelastic collision significantly increases the diffusion coefficients of free radical species at temperatures relevant to fuel combustion. Inelastic collision with a potential energy curve representative of molecule-radical interaction may cause the diffusion coefficient to increase by as much as 50% at 1500 K. This finding suggests that a molecular theory beyond the Chapman-Enskog equation is needed to describe accurately free-radical diffusion in laminar flames.

The above results are reported in Publication No. 3.

4. Pulsation and Flammability Limits of Lean Heptane/Air Flames

The unsteady propagation of lean heptane/air planar flames in the doubly-infinite domain was computationally simulated with detailed chemistry and transport, and with and without radiative heat loss. For the adiabatic situation, thermal-diffusive pulsating instability, promoted for large values of the Lewis and Zeldovich numbers, was observed to develop when the mixture becomes sufficiently lean. With subsequent progressive reduction in the equivalence ratio (ϕ), the mode of pulsation changes from that of monochromatic, to period doubling, and to hibernation characterized by bursts of high burning intensity separated by long period of dormancy. The flame nevertheless does not extinguish. This behavior is similar to that of the rich hydrogen/air flame studied previously. However, when heat loss is considered, the onset of pulsation is facilitated, although the regime in ϕ for sustained pulsating propagation is extremely narrow, and extinction occurs readily when the amplitude of the flame temperature oscillation becomes large enough to extinguish the flame during the negative phase of excursion. The abruptness of transition to extinction is quite different from that of the rich hydrogen/air flame. The pulsating extinction occurs at a larger ϕ (=0.5063) than steady extinction (ϕ=0.4762), again implying that the flame extinguishes in the pulsating instead of the steadily propagating mode, and that the flammability limit is accordingly narrowed. It is further demonstrated that the states for the onset of adiabatic and non-adiabatic pulsation can be accurately estimated by respectively using the criterion of Sivashinsky and of Joulin and Clavin, provided the Lewis number used is the global one, extracted from the response of stretched flames, demonstrating that it is a property of the flame instead of the unburned mixture alone. It is also suggested that the lean flammability limits of mixtures of large hydrocarbons and air can be estimated by using the criterion of Joulin and Clavin.

The above results are reported in Publication No. 4.

5. Effects of Curvature on Pulsating Instability

Effects of curvature on the pulsating instability of premixed flames were analytically and computationally investigated via the inwardly-propagating spherical flame. Analytically, linear stability analysis was conducted within the framework of the diffusion-thermal model and based on

the assumption that the flame is quasi-planar and quasi-stationary. Since the inwardly-propagating flame (IPF) is negatively-stretched, analytical results show that curvature promotes cellular instability but suppresses pulsating instability; the latter has not been explicitly shown in previous analytical studies. These analytical trends are further confirmed by computational results from fully transient simulations of rich hydrogen/air IPFs with detailed chemistry and transport properties. In particular, it is shown that for a given rich hydrogen/air mixture whose one-dimensional, freely-propagating flame is pulsatingly unstable, the IPF initially propagates at the laminar flame speed when the flame radius is large. Oscillation subsequently develops, and is then amplified, damped, and eventually suppressed when the flame is still sufficiently far away from the center. Thus negative stretch tends to suppress the occurrence of pulsating instability. This finding suggests that the flammable range of rich hydrogen/air IPFs is wider than that of their unstretched, planar counterpart.

The above results are reported in Publication No. 5.

6. Radiation Induced Flamefront Instability

Unsteady propagation and instability of radiative stretched premixed flames at Lewis numbers close to unity were numerically investigated using helium diluted counterflow methane flames, with the interest on understanding the stability of three near-limit and sub-limit multiple flame regimes, namely the near stagnation flame, the weak flame and the distant flame. It is shown that both the near-limit and sub-limit near-stagnation flames are stable close to the flammability limit, and that a new mode of oscillation instability exists at equivalence ratios sufficiently larger than the flammability limit. In addition, stability of the weak and the distant flames is demonstrated, while unsteady mutual transitions between the near-stagnation flame and the distant flame, and jump from the weak flame to the normal flame, are found. A comparison of the present prediction with the microgravity experimental observation shows qualitative agreement on the oscillation frequency and region for the occurrence of oscillation. Calculations for Lewis numbers larger and smaller than unity show that the radiation induced instability is a physically intrinsic phenomenon for radiative stretched premixed flame. The present study provides a satisfactory explanation for the microgravity observation.
The above results are reported in Publication No. 6.

MAJOR PUBLICATIONS (May 1999 – April 2000)

1. "Detailed kinetic modeling of 1,3-butadiene oxidation at high temperatures," by A. Laskin, H. Wang, and C. K. Law, *International Journal of Chemical Kinetics*, in press.
2. "Combustion chemistry of propane: A case study of detailed reaction mechanism optimization," Qin, Z., Lissianski, V., Yang, H., Gardiner, W. C., Jr., Davis, S. G., and Wang, H. *Proceedings of the Combustion Institute*, in press.
3. "Effect of reactive collision on binary diffusion coefficients of free-radical species," Wang, H. *Chemical Physics Letters*, in press.
4. "The role of pulsating instability and global Lewis number on the flammability limit of lean heptane/air flames," Christiansen, E. W., Law, C. K., and Sung, C. J. *Proceedings of the Combustion Institute*, in press.
5. "On curvature-affected pulsating instability in inwardly-propagating spherical flames," Sung, C. J., Sun, C. J., and Law, C. K., submitted.
6. "Radiation induced instability of stretched premixed flames," Ju, Y., Law, C. K., Maruta, K., and Niioka, T. *Proceedings of the Combustion Institute*, in press.
7. "Steady and pulsating propagation and extinction of rich hydrogen/air flames at elevated pressures," by Christiansen, E. W., Sung, C. J., and Law, C. K., submitted.
8. "Propene pyrolysis and oxidation kinetics in flow reactor and laminar flames," by Davis, S. G., Law, C. K., and Wang, H., *Combustion and Flame* vol. 119, pp. 375-399 (1999).
9. "Propyne pyrolysis in a flow reactor: an experimental, RRKM, and detailed kinetic modeling study," by Davis, S. G., Law, C. K., and Wang, H., *Journal of Physical Chemistry A* vol. 103, pp. 5889-5893 (1999).

THE CHEMISTRY CONTROLLING IGNITION OF HYDROCARBONS AND THEIR MIXTURES AT HIGH PRESSURES

David L. Miller and Nicholas P. Cernansky

Department of Mechanical Engineering and Mechanics
Drexel University, Philadelphia, PA 19104

SUMMARY/OVERVIEW:

This research program investigates the chemistry controlling ignition of hydrocarbons and their mixtures at elevated pressures. The objective of this program is the development of kinetic and mechanistic information in the low and intermediate temperature regime (600-1000 K) over a range of pressures (up to 20 atm). The methodology is to perform bench scale tests on single component pure fuels; on 2, 3, and 4 component mixtures of pure fuels; and on full boiling range fuels. The experiments are being carried out over a range of reaction conditions that are representative of actual engine conditions prior to and during the ignition process. Results from these studies will be used to provide kinetic and mechanistic information, to formulate hypotheses on autoignition mechanisms, to determine the relative effects of the various classes of components within multi-component fuel mixtures, and to provide combustion models that can be used in the design and evaluation of engine systems.

TECHNICAL DISCUSSION:

Recent efforts focused on several general research areas, the first is the experimental oxidation of low cetane number mixtures, single component fuels, and high cetane number mixtures. The second is the development and testing of statistical techniques, commonly referred to as chemometrics, for analyzing complex multi-component fourier transform infrared (FT-IR) spectra. The third as part of a related ASSERT program is a technique for the spectral separation of radical from non-radical species using Magneto-Optic Rotation (MOR) . The technique has been developed and tested successfully, and is now being applied to Cavity Ringdown Laser Absorption Spectroscopy (CRLAS).

Low Cetane Mixtures -- Seven fuels were oxidized in the Pressurized Flow Reactor (PFR), which included, 87 PRF (blend of iso-octane and n-heptane), 92 PRF (blend of iso-octane and n-heptane), RFA (Reference Fuel A, an ISF), RFB (Reference Fuel B, an ISF), a standard Ford test fuel, Indolene (an ISF), and a specially developed blend RON 92. RON 92 was developed by mixing the three major classes of hydrocarbons together, aromatics, olefins, and saturated hydrocarbons. The specific ratio of these classes was selected to correspond to the ratios of the ISF's.

The blend was created by mixing toluene and 1-pentene to 87 PRF. Using reactivity mapping of CO, NTC behavior was observed for all of the fuels. The temperature at which the reactivity peaks, referred to as the start of NTC, varied from fuel to fuel. For 87 PRF and 92 PRF the NTC region started at 688 K and 686 K, respectively. For the ISF's, RFA, RFB, Ford fuel, and Indolene, NTC behavior started at slightly higher temperatures of 699 K, 703 K, 700 K, and 702 K, respectively [Figure 1]. Furthermore, the ISF's also had a notable decrease in reactivity. This change can be related to the presence of olefins and aromatics in the fuel. This is the reason that the additional functional group was added to the RON 92 blend. As a result, the RON 92 blend also exhibited the decrease in reactivity and the shift of the NTC region 17°C higher than was observed in the 2-component blends, 87 PRF and 92 PRF. Using a semi-quantitative group analysis, CO and CO_2 were seen to coincide with the formation of aldehydes. The peak for olefin formation was observed at higher temperatures in ISF's than for PRF's. In the case of PRF's the olefin formation occurred at the start of the NTC region [Figure 2]. When the olefins and aromatics were added to the simple PRF blends, as in the case with RON 92, this peak of olefin formation shifted toward higher temperatures within the NTC region. In the oxidation of RFA, the shift of olefin peak was much larger than with the RON 92. This difference might be due to the large number of C4 and C5 alkanes and the formation of conjugate olefins, which occurs at higher temperatures within the NTC region. This experiment has shown that the surrogate fuel blends can be used to study the complex interaction of ISF's components.
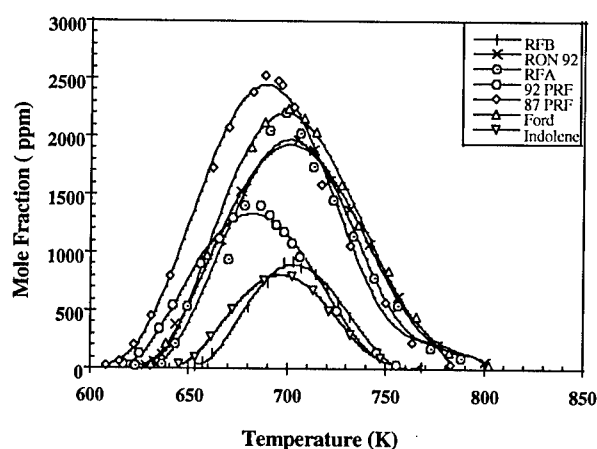
Figure 1: CO Reactivity mapping for multicomponent blends and ISF's
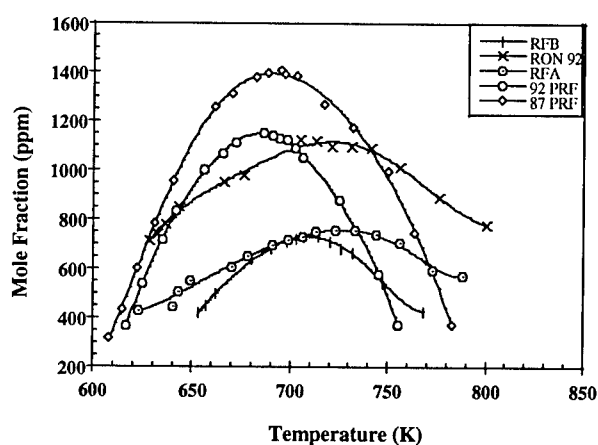
Figure 2: Olefin formation for multicomponent blends

Neopentane -- It is generally accepted that NTC behavior occurs due to a switch in the reaction mechanism dominance from alkylperoxies to conjugate alkenes in the NTC region. Neopentane has a molecular structure that does not form conjugate alkenes. Therefore, the traditional theory of NTC behavior does not apply and alternative explanations must be sought. Understanding of its NTC behavior may significantly improve our understanding of autoignition. Using our pressurized flow reactor system, we confirmed the negative temperature coefficient behavior for neopentane and determined its NTC temperature region for the first time. Detailed product distributions in low and intermediate temperature regimes were measured using Fourier Transform Infrared Spectroscopy and Non-Dispersive Infrared Analysis. These data provided new information for our kinetic modeling work. In conjunction with Drs. William Pitz and Charles Westbrook at Lawrence Livermore National Laboratory (LLNL), an existing detailed model for neopentane oxidation was expanded and refined. This model was first developed based on lim-

ited experimental results by Baker et al. (1976)[*]. After identifying some deficiencies in the existing model, several modifications were made to improve it: (1) upgrading the thermodynamic parameters of alkyl radical and alkylperoxy radical species; (2) adding an alternative isomerization reaction of hydroperoxy-neopentyl-peroxy; and (3) adding a multi-step reaction sequence for 2-methylpropan-2-yl radical with molecular oxygen. These changes improved the calculation of overall reactivity. The new model can reproduce all major species profiles measured in the experiment very well.

High Cetane Mixtures -- Continuing our work with industry standard fuels (ISF), JP-8 was oxidized in our Pressurized Flow Reactor to identify the existence of a Negative Temperature Coefficient (NTC) region. Utilizing the CO reactivity mapping technique, a clear NTC behavior was observed for JP-8 at two different experimental conditions. The JP-8 experiment was conducted at conditions similar to previous ISF work; pressure of 8 atm, equivalence ratio of 0.3, nitrogen dilution of 75%, and residence time of 180 ms. During the controlled cool down experiment, a clear NTC behavior was observed [Figure 3]. The temperature where the reactivity peaked, referred to as the start of NTC, occurred at 700 K.
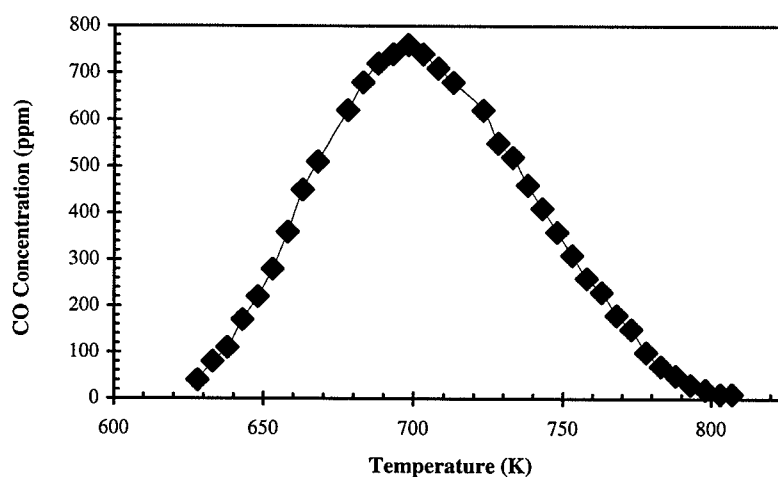
Figure 5: Controlled cool down PFR experiment for JP-8, showing a strong NTC behavior.

Chemometrics -- For larger hydrocarbons and multi-component blends, the number of intermediate species becomes sufficiently large that coelutions from a GC/FT-IR system are distinctly possible. As a result, direct analysis of the FT-IR spectra or GC peaks for qualitative or quantitative purposes may be unrealizable. Chemometrics offers a statistical approach to species identification and concentration measurements. Two chemometric techniques, factor analysis and target testing, have been applied to FI-IR spectra thus far. Factor analysis is a method by which the number of independent chemical species affecting the FT-IR absorption spectra of a multi-component mixture can be determined. Target testing is a method that tests whether a single chemical species has affected the measured multi-component spectra. Utilizing our factor analy-

[*] Baker, R. R., Baldwin, R. R., and Walker, R. W. (1976), "Addition of Neopentane to Slowly Reacting Mixtures of $H_2 + O_2$ at 480 C. Part II: The Addition of the Primary Products from Neopentane, and the Rate Constants for H and OH Attack on Neopentane", Combust. and Flame, 27, 147

sis and target testing algorithms, testing began into its capability to correctly determine the number and the identity of chemical species in a mixture. After extensive development, neopentane PFR data was analyzed with the algorithms. The results identified nine different chemical species, the same number of species identified during previous research. Furthermore, the method was able to identify all but one of the species identified previously. Additional development is being conducted into the inability of the chemometric technique to identify this one compound.

Laser Diagnostics -- In the related ASSERT program, we have been developing advanced laser diagnostics techniques for measuring radical and stable species in combustion environments. In order to optically detect species that are important to the combustion process, we are using the Cavity Ringdown Laser Absorption Spectroscopy (CRLAS) technique. Current work has focused around the detection of the HO_2 radical around 14300 Å. Preliminary measurements using CRLAS indicated that the 14300 Å region is much more congested than originally suspected. Therefore, finding lines due to the weakly absorbing HO_2 radicals will be difficult unless the radicals are "selected" from the stable species. This selection is possible optically using a technique involving Magneto-Optic Rotation (MOR). A MOR experiment was performed in an acetylene/air flame that was doped with Zn atoms (which are only weakly paramagnetic). A small nitrogen-pumped dye laser was used as the probe and scanned from 3050 to 3120 Å. The Zn line at 3075.9 Å overwhelmed the 25 to 30 much weaker lines due to OH radical. A 4 kilogauss external magnetic field was applied axially with respect to the laser propagation direction to produce the MOR effect. With MOR, the strongly absorbing Zn atoms show a very weak line at 3050 to 3120 Å and the OH absorption was predominant [Figure 4]. This technique will greatly improve our ability to detect the HO_2 radical at 14300 Å, which is a region congested with strong water, CO, and CO_2 lines. Since the exact lines and relative strength of these HO_2 lines have not been experimentally measured, only predicted, we have developed a system that can be used to create the HO_2 radical. The system generates Cl radicals which then react with H_2O_2 to produce the HO_2 radical.
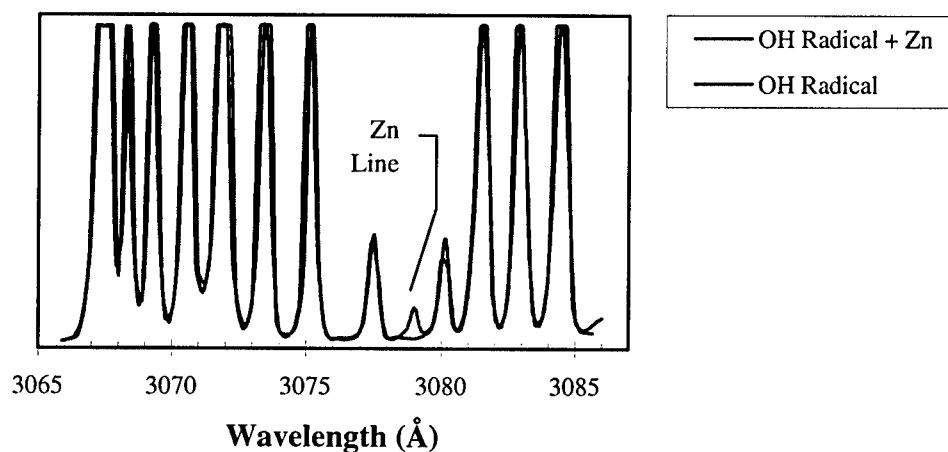

Figure 6: Effect of doping an acetylene/air flame with the strongly absorbing Zn atoms while using the Magneto-Optic Rotation technique.

ADVANCED SUPERCRITICAL FUELS

AFOSR Task # 93WL002

Principal Investigators: Tim Edwards, Jim Gord, Mel Roquemore
Air Force Research Laboratory
AFRL/PRSF Bldg 490
1790 Loop Rd N
Wright Patterson AFB, OH 45433-7103

SUMMARY/OVERVIEW:

Increases in aircraft and engine performance are increasing the heat load being transferred into an aircraft's primary coolant--the fuel. This research is aimed at understanding the limitations of operation of fuel heated to 480 °C (900 °F) and beyond. Important issues are expected to be thermal stability, heat transfer/flow instabilities, and injection/combustion properties.

TECHNICAL DISCUSSION

Thermal stability (resistance to deposit formation) is a key issue for high temperature fuels. At temperatures of 900 F and below, the major route to deposition is thermal-oxidative, as illustrated in Figure 1. Figure 1 is a combination of a fuel oxidation description developed under this program [1,2], with a deposition mechanism borrowed from work by Shell. A key feature of fuel oxidation is its complexity [3-9]. An important aspect of this research has been the separation of "anti-oxidant" species into several classes, based upon their mode of action in the mechanism. Mitigation or elimination of deposits can be achieved by interrupting this process at a number of points. AFRL work has examined chain-breaking peroxide decomposers, anti-oxidants, fuel deoxygenation, dispersants, and surface modification. To reduce deposition to levels found in highly refined fuels, such as JP-7, it has been found that several of these approaches together are necessary. As shown in Figure 2, the use of an effective dispersant, a chemically-inert surface treatment, and fuel deoxygenation, allows deposition to be reduced to levels approaching that of JP-7. The effectiveness of dispersants was field-demonstrated in the JP-8+100 program. Earlier AFOSR-sponsored research showed that the dispersant reduced fluid-borne particle size (by reducing agglomeration), which reduced surface deposition [10]. The understanding of the agglomeration/deposition steps is currently inadequate to accurately model these steps. The role of the surface is also not well understood. Research at AFRL and elsewhere has shown that the surface "finish" has a role in adhesion, to the extent that "rough surfaces are stickier". Beyond that, it was thought the chemical nature of the surface was not important in determining the level of thermal-oxidative deposition (but did have a small role in determining the fuel oxidation rate). However, recent work has identified a surface (as shown in Figure 2) that appears to resist deposition to a greater extent. Work is underway to understand the basis of this effect. Fuel deoxygenation has long been known to improve fuel stability. Recent advances in gas-permeable materials may make a flight-weight system a reality. AFRL has worked with groups looking at chemical deoxygenation (oxygen scavenging)[11], but the complexity of jet fuels has made this approach difficult.

The evolving AFRL model of thermal oxidative stability has been described [12]. Recently, the fuel oxidation chemistry part of the model was improved to more accurately simulate the behavior in Figure 1 [13]. Figure 3 shows the current model. The anti-oxidant (A) and peroxide decomposer (SH) chemistry is new. Another "upgrade" being considered is to separate out the fuel hydrocarbons ("RH") into appropriate chemical classes (such as paraffins, naphthenes, aromatics, as is done in some combustion models of these type of fuels [14,15]). The role of aromatics is being examined at AFRL. High thermal stability fuel like JP-7 have a much lower level of aromatics that JP-8/Jet A. Is this low level of aromatics a requirement for increased thermal stability? The deposition portion of the model needs to be improved to allow the action of dispersants to be captured. A difficulty that remains to be solved is the determination of appropriate parameters (such as "SH") to allow predictions for an "average" JP-8 or Jet A fuel. The thermal stability of these fuels can vary widely within their specifications in a non-Gaussian manner. For example, Figure 4 shows the distribution of fuel thermal stability (as characterized by a Hot Liquid Process Simulator" [16]) for a wide variety of fuels. This spread in thermal stability is not a surprise—fuels are refined by different methods (hydrotreatment, straight distillation, etc.) that result in products with differing amounts of sulfur compounds and other species which are key to determining the thermal stability. Currently, the model must be calibrated for a given fuel—what is needed by users is a set of parameters that are characteristic of a "typical" jet fuel. The determination of these parameters is not a simple task.

At temperatures above 900 F, fuel pyrolysis reactions dominate the deposition process. Current activity is focussed on determining the roles of molecular growth (aromatics formation) and conditions in pyrolytic deposition [17,18,23]. Various types of additives have been examined to mitigate this deposition, but the results have not been dramatic [19,20]. An interesting sidelight has been the use of the small scale reactor/GC-MS (used in the some of the molecular growth studies) to assess the thermal stability of several high-energy hydrocarbons being considered as rocket and air-breathing fuels as alternatives to RP-1 [21]. Some of the high-energy hydrocarbons were surprising stable, while quadricyclane was found to isomerize and form deposits at relatively low temperatures. This indicates the need to evaluate quadricyclane more thoroughly to determine its capability to be used in systems that employ regenerative cooling. The injection of supercritical fuels (not simulants) into a nominally supercritical environment has also been examined [22].

[1]. S. Zabarnick and M.S. Mick, "Studies of Hydroperoxide Decomposing Species for Inhibiting Oxidation in Jet Fuels," ACS Petroleum Chemistry Division Preprints, Vol. 43(3), pp. 349-352, 1998.
[2]. Grinstead, B., Zabarnick, S., "Studies of Jet Fuel Thermal Stability, Oxidation, and Additives Using an Isothermal Oxid. Apparatus Equipped with an Oxygen Sensor," Energy & Fuels, Vol 13(3), pp. 756-760, 1999.
[3]. Zabarnick, S., Mick. M. S., "Inhibition of Jet Fuel Oxidation by Addition of Hydroperoxide Decomposing Species," Industrial and Engineering Chemistry Research, Vol. 38, pp. 3557-3563, Sept. 1999.
[4]. Grinstead, B., Zabarnick, S., "Studies of Jet Fuel Thermal Stability, Oxidation, and Additives Using an Isothermal Oxidation Apparatus Equipped with an Oxygen Sensor," Energy and Fuels, Vol. 13, pp. 756-760, 1999.
[5]. Zabarnick, S., Mick, M. S., Striebich, R. C., Grinstead, R. R., "Model Studies of Silylation Agents as Thermal-Oxidative Jet Fuel Additives," Energy and Fuels, Vol. 13, pp. 154-159, 1999.
[6]. Balster, L. M., Balster, W. J., Jones, E. G., "Extended Liquid-Phase Oxidation of Aviation Fuels," ASME 99-GT-55, June 1999.
[7]. Jones, E. G., Balster, L. M., Balster, W. J., "Thermal Stability and Autoxidation of Jet Fuels Measured at 185 C," ACS Petroleum Chemistry Division Preprints, Vol. 44(3), pp. 382-385, 1999.
[8]. Jones, E. G., Balster, L. M., "Autoxidation of Dilute Jet Fuel Blends," Energy and Fuels, Vol. 13, pp. 796-802, 1999.
[9]. Binns, K. E., Dieterle, G. L., "High Temperature Thermal Stability of JP-8+100 and Other Fuels," ASME 99-GT-107, June 1999.
[12]. Katta, V. R., Jones, E. G., Roquemore, W. M., "Modeling of Deposition Process in Liquid Fuels," Combustion Science and Technology, Vol. 139, pp. 75-111, 1998.

[10]. Vilimpoc, V., Sarka, B, "Application of Photon Correlation Spectroscopy and Quartz-Crystal Microbalance to the Study of Thermally Stressed Jet Fuel," Industrial and Engineering Chemistry Research, Vol. 36(2), pp. 451-457, 1997.

[13]. Ervin, J. S., Zabarnick, S., Williams, T. F., "One-Dimensional Simulations of Jet Fuel Thermal-Oxidative Degradation and Deposit Formation Within Cylindrical Passages," submitted to ASME Journal of Energy Resources Technology, Feb 2000.

[14]. Khan, A. R., "Oxidation of Industry Standard Fuels and Blends of Primary Reference Fuels in the Low Temperature and Negative Temperature Coefficient Regions," M.S. thesis, July 1998, Drexel University (N.P. Cernansky, ARO DAAG55-98-1-0286).

[16]. Heneghan, S. P., Zabarnick, S., balla, D. R., "JP-8+100: The Development of High Thermal Stability Jet Fuel," AIAA 96-0403, 1996.

[15]. Edwards, T., Maurice, L. Q., "Surrogate Mixtures to Represent Complex Aviation and Rocket Fuels," AIAA Paper 99-2217, July 1999.

[17]. Beaver, B., Sharief, V., Teng, Y., DeMunshi, R., Guo, J. P., Katondo, E., "On the Development of Oxygen Scavenger Additives for Future Jet Fuels," ASME 99-GT-216, 1999.

[23]. Striebich, R. C., Maurice, L. Q., Edwards, T., "Formation of Cyclic Compounds in Cracking Reactions for Hydrocarbon-Fueled High Speed Vehicles," ASME 99-GT-136, June 1999.

[18]. Jones, E. G., Balster, L. M., Balster, W. J., Striebich, R. C., "Effect of Pressure on Supercritical Pyrolysis of n-Paraffins," ACS Petroleum Chemistry Division Preprints, Vol. 44(3), pp. 394-397, 1999.

[19]. Corporan, E., Minus, D. K., Williams, T. F., "Studies of Decalin as a Suppressor of Pyrolytic Deposits in JP-8+100," AIAA 99-2213, 35th AIAA/ASME/SAE/ASEE Joint Propulsion Conference, June 1999.

[20]. Corporan, E., Minus, D. K., "Hydrogen Donors: Thermal Stabilizers for JP-8+100 at High Temperatures," ASME 99-GT-056, June 1999.

[21]. Wohlwend, K., Maurice, L. Q., Edwards, T., Striebich, R. C., Vangness, M., "Thermal Stability of Energetic Hydrocarbon Fuels in Fuel Systems for Combined Cycle Engines," AIAA 99-2219, 1999.

[22]. Ervin, J. S., Williams, T. F., bento, J., Doungthip, T., "Studies of Jet Fuel Thermal Stability and Flow Characteristics within a Nozzle Under SupercriticalConditions," to appear in ACS Petroleum Chemistry Division Preprints, August 1999.
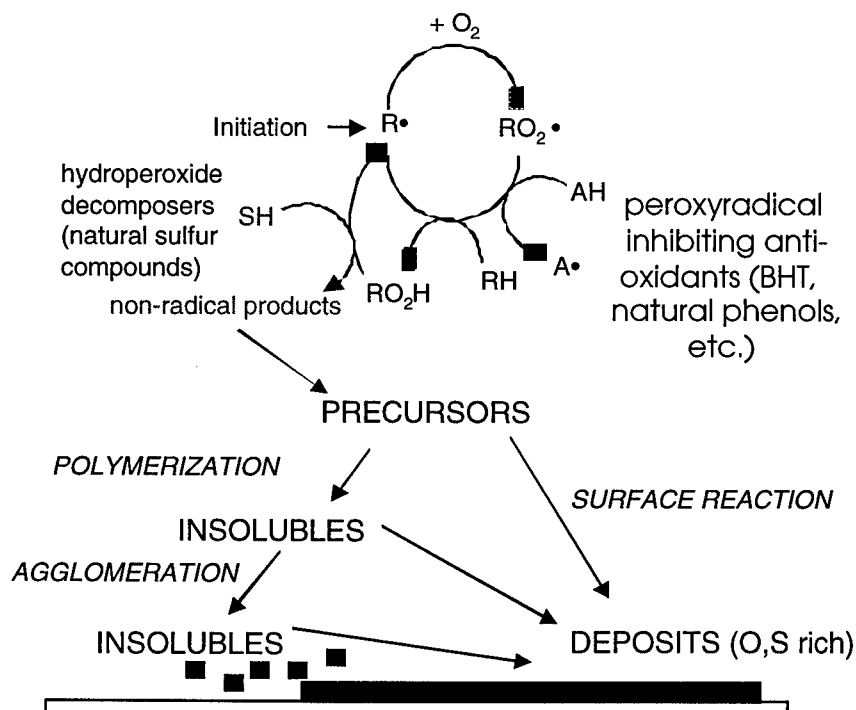
Figure 1 – Overall thermal-oxidative deposition mechanism [1,2].
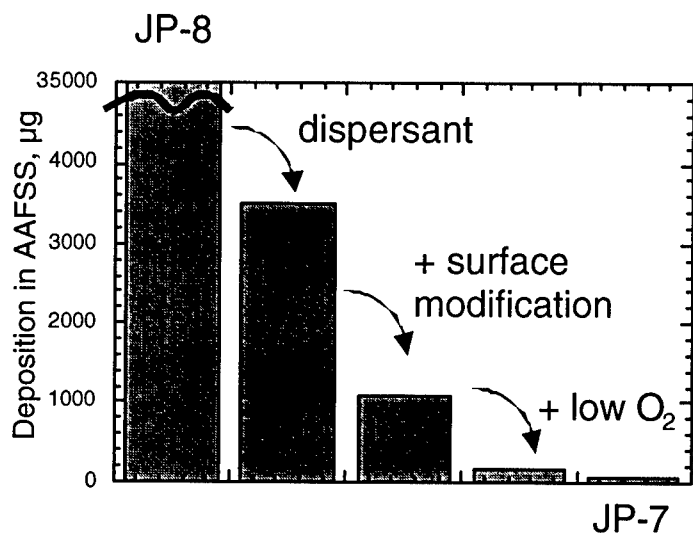
Figure 2 – Effect of various mitigation measures on thermal-oxidative deposition in a flowing test rig. Low O_2 corresponds to 3-5 ppm.

I → R• (initiation)

R• + O_2 → RO_2•
RO_2• + RH → RO_2H + R•
RO_2• + RO_2• → termination
RO_2• + AH → RO_2H + A•
AO_2• + RH → AO_2H + R•
A• + O_2 → AO_2•
AO_2• + AH → AO_2H + A•
AO_2• + AO_2• → products

R• + R• → R_2

RO_2H → RO• + •OH
RO• + RH → ROH + R•
RO• → R'• carbonyl
•OH + RH → H_2O + R•
RO• + RO• → termination
R'• + RH → alkane + R•
RO_2H + SH → products
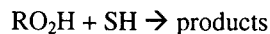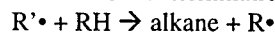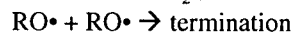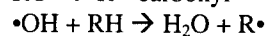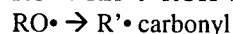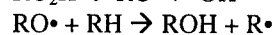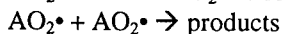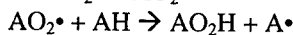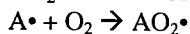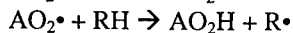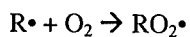
Figure 3 – Liquid phase fuel oxidation mechanism [13].
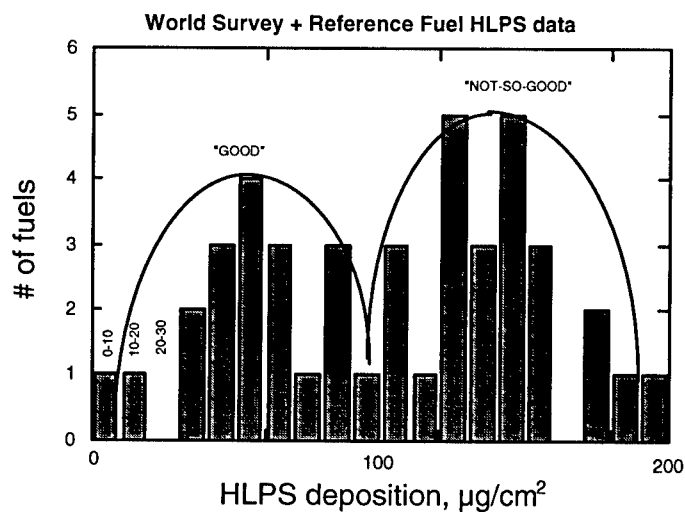
Figure 4 – Variations in thermal stability among specification JP-8 fuels.

132

FUELS COMBUSTION RESEARCH: SUPERCRITICAL FUEL PYROLYSIS

Princeton University
Department of Mechanical and Aerospace Engineering
Princeton, New Jersey 08544

SUMMARY/OVERVIEW

The fuels used in the next generation of hypersonic aircraft [1] will have to operate under very high pressures (beyond the critical pressures of most hydrocarbons) and will have to sustain very high heat loads in order to meet aircraft cooling requirements. Potential candidates for meeting these stringent cooling requirements are "endothermic" fuels, fuels that can undergo a controlled heat-absorbing chemical reaction (*e.g.*, dehydrogenation) prior to combustion. Critical to the development of the fuel systems in these aircraft is an understanding of the mechanisms of fuel decomposition under the range of conditions that the fuels will be operating. Under the direction of Professor Irvin Glassman at Princeton, recent studies [2-7] have uncovered important differences in the pyrolysis of model endothermic fuels under subcritical and supercritical conditions, which appear to be linked to solute/solvent interactions in the supercritical phase. Because solvent properties of supercritical fluids vary strongly with pressure, the degree of these solute/solvent interactions can vary greatly with pressure—having a marked effect on rates of reaction. In order to better elucidate the reaction mechanisms and kinetic rates of endothermic fuel pyrolysis under supercritical conditions, therefore, we are beginning a new study of the pyrolysis of model fuels over a range of supercritical pressures. The study includes the model endothermic fuels, methylcyclohexane and decalin, as well as toluene and heptane, hydrocarbons representative of the aromatic and aliphatic components of jet fuels. Because fuel-line fouling is a problem critically important to avoid in aircraft fuel systems, a key component of the experimental program is the analysis of the supercritical pyrolysis products for polycyclic aromatic hydrocarbons (PAH), which can serve as precursors to fuel-line deposits. It is anticipated that the results from this study will provide information of critical importance to the design and development of fuel systems for high-speed aircraft.

AUTHORS: M. J. Wornat, I. Glassman, J. F. Stewart, S. P. Zeppieri

TECHNICAL DISCUSSION

Under AFOSR Grant F49620-98-1-0134, subcritical [2,3] and supercritical [4-7] pyrolysis experiments have been conducted on three endothermic fuels: methylcyclohexane, decalin, and tetralin. Plotted in Figure 1 are the global kinetic rate data for the decomposition of the three endothermic fuels, determined from a first-order/pseudo-first-order analysis [6].
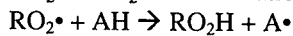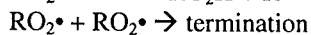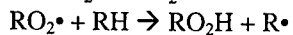
Table 1 summarizes the major results of the pyrolysis experiments conducted on the three endothermic fuels. Presented in the middle columns of Table 1 are the first-order global kinetic rate parameters derived for these fuels from the Arrhenius plot of Figure 1. These values show that the global activation energies for the supercritical pyrolysis experiments are each 65-66 kcal/mole—an equivalence that signifies similarity in the types of chemical reactions contributing to the pyrolysis of the fuels (the scission of aliphatic carbon-carbon and carbon-hydrogen

bonds, as well as various radical abstraction reactions [6]). The middle columns of Table 1 also reveal that the pre-exponential A factors derived from the supercritical pyrolysis experiments are at least two orders of magnitude greater than those determined for the subcritical pyrolysis of the same fuels.

In the last column of Table 1 are listed the major pyrolysis products from each experiment, determined by detailed gas chromatographic analyses. Of particular note from these lists of products is the observation that methylcyclohexane pyrolyzed under supercritical conditions yields significant quantities of the cyclic product dimethylcyclopentane; under subcritical pyrolysis conditions it does not. Similarly, decalin produces significant amounts of the cyclic product methylhexahydroindane under supercritical conditions; under subcritical conditions it does not. Supercritical pyrolysis of tetralin yields appreciable amounts of the cyclic product methylindane.

The fact that all three endothermic fuels, under supercritical conditions, produce cyclic structures that are not observed under subcritical conditions suggests that supercritical pressures permit the activation of certain reaction pathways that are not active at subcritical pressures. In the case of methylcyclohexane, the gas-phase and supercritical-phase decomposition pathways are illustrated in Figure 2. As proposed by Stewart [6], Figure 2 demonstrates that in the gas phase, methylcyclohexane decomposes to form the methylhexenyl radical (MHL), which undergoes a sequence of □-scission reactions to form the major products ethene and propene. This same decomposition pathway occurs during methylcyclohexane pyrolysis in the supercritical phase, but supercritical conditions afford methylcyclohexane an additional decomposition route that does not occur under subcritical gas-phase conditions. As shown in Figure 2, in the supercritical phase, MHL can undergo ring contraction to produce the cyclic product dimethylcyclopentane, a consequence of the caging effect [6].

The results for decalin pyrolysis are analogous to those for methylcyclohexane. As shown in Figure 3a, pyrolysis of decalin in either the gas phase or supercritical phase yields alkenes such as ethene and 1,3-butadiene. The caging effect, however, permits decalin pyrolysis in the supercritical phase to produce the methylhexahydroindanes, the cyclic products shown in Figure 3b.

To better understand the product distributions resulting from supercritical fuel pyrolysis, it is helpful to consider the alternate pathways of Figure 2, or those of Figure 3, as competitive routes. In order to form small alkene products such as ethene or propene, the products of the □ scission of a radical such as MHL must be able to diffuse away, in preference to colliding and bonding with other fuel fragments. In the low-density environment of the gas phase, such diffusion is not impeded, and □ scission products prevail. In the high-density environment of the supercritical phase, however, diffusion is impeded and collision processes are favored, enhancing carbon-carbon bond formation and thus the production of cyclic hydrocarbons such as dimethylcyclopentane and methylhexahydroindane. In any given practical fuel system, therefore, the pyrolysis product distribution will be determined by the relative contributions of these two competing "rate processes," one controlled by the diffusion of dissociated species (□ scission) and the other by a collision process that forms a new bond (caging).

The delineation of reaction pathways and pyrolysis products that are peculiar to supercritical conditions is of critical importance to the problem of fuel-line fouling in high-speed aircraft. The reason is that dimethylcyclopentane, methylhexahydroindane, and methylindane—the products specific to the supercritical pyrolysis of methylcyclohexane, decalin, and tetralin, respectively—are all hydrocarbons containing a methylated C_5 ring. Such cyclical C_5 species have been shown, under diffusion flame conditions, to have high propensities for soot formation [6 and references therein], due to their facile conversion to structures containing six-membered aromatic rings. Due to this same facile conversion, one would also expect the cyclical C_5 species to be prone to forming solid particulates under supercritical pyrolysis conditions, since the cyclical supercritical pyrolysis products would readily produce aromatic rings and serve as kernals for

pyrolysis products would readily produce aromatic rings and serve as kernals for further cyclic growth to PAH and ultimately solid deposits.

Confirmation that PAH are indeed formed during the supercritical pyrolysis of methylcyclo-hexane is found in Figure 4, which portrays the rising production, with residence time, of PAH from two to six fused aromatic rings. The results in Figure 4 come from exploratory analyses of the collected methylcyclohexane pyrolysis products by high-pressure liquid chromatography with diode-array ultraviolet-visible absorbance detection (HPLC/UV), a technique ideally suited for analysis of large PAH molecules, which are too involatile for analysis by gas chromatography. Because HPLC/UV provides isomer-specific PAH identification, this technique will be employed extensively in our future investigation of the formation chemistry of potential fuel-line deposits during supercritical pyrolysis.

REFERENCES

1. Edwards, T., "USAF Supercritical Hydrocarbon Fuels Interests," AIAA Paper 93-0807 (1993).
2. Zeppieri, S. P., Brezinsky, K., and Glassman, I., "Pyrolysis Studies of Methylcyclohexane and Oxidation Studies of Methylcyclohexane/Toluene Blends," *Combustion and Flame 108*: 266 (1997).
3. Zeppieri, S. P., "Pyrolysis and Oxidation of Endothermic Fuels," Princeton University, Department of Mechanical and Aerospace Engineering, Ph.D. Thesis, 1999.
4. Davis, G. D., "An Experimental Study of Supercritical Methylcyclohexane Pyrolysis," Princeton University, Department of Mechanical and Aerospace Engineering, M.S.E. Thesis, 1994.
5. Stewart, J. F., Brezinsky, K., and Glassman, I., "Supercritical Pyrolysis of Decalin, Tetralin, and N-Decane at 700-800 K. Product Distribution and Reaction Mechanisms," *Combustion Science and Technology 136*: 373 (1998).
6. Stewart, J. F., "Supercritical Pyrolysis of the Endothermic Fuels Methylcyclohexane, Decalin, and Tetralin," Princeton University, Department of Mechanical and Aerospace Engineering, Ph.D. Thesis, 1999.
7. Stewart, J. F., Glassman, I., and Brezinsky, K., "Supercritical Methylcyclohexane Pyrolysis. A Flow Reactor Study," ACS Symposium on Structure of Fuels V, ACS 216th National Meeting, Boston, MA, August, 1998.
8. Wornat, M. J., Vernaglia, B. A., and Marsh, N. D., "High-Temperature Reaction Pathways Leading to Large Polycyclic Aromatic Hydrocarbons from Aromatic Fuels," ACS Symposium on Structure of Fuels V, ACS 216th National Meeting, Boston, MA, August, 1998.

ABSTRACTS OF WORK UNITS NOT PRESENTED AT THE MEETING

FILTERED MASS DENSITY FUNCTION FOR SUBGRID SCALE MODELING OF TURBULENT DIFFUSION FLAMES

Principal Investigator(s): Peyman Givi and Farhad A. Jaberi

Department of Mechanical and Aerospace Engineering
State University of New York at Buffalo
Buffalo, NY 14260-4400

SUMMARY/OVERVIEW:

The objective of this work is to develop and implement a subgrid scale (SGS) closure methodology for reliable large eddy simulation (LES) of turbulent diffusion flames. The methodology is termed the "filtered mass density function" (FMDF) and has proven very effective for LES of turbulent combustion [1,2]. The novelty of the methodology is due to its inherent capability to account for the effects of SGS reaction rate in the FMDF transport equation in a closed form.

TECHNICAL DISCUSSION

A review of combustion literature identifies three general approaches for analytical description of turbulent reacting flows [3]: (1) Reynolds averaged simulations (RAS), (2) direct numerical simulation (DNS), and (3) large eddy simulation (LES). The first approach has been the most popular for prediction of engineering flows due to its relatively low computational cost [4]. The second approach has received significant attention within the past twenty years or so [5] but its use is limited to basic research problems due to its extensive computational requirements [6,7]. The third approach, regarded somewhere between the first two, is starting to gain attention in combustion [8,9].

We have recently developed a methodology, based on an idea first proposed by Pope [10], which has proven effective for LES of turbulent combustion. In this methodology, the effects of SGS fluctuations are represented in a "probabilistic" manner, and the large scale transport is simulated deterministically. The FDF (FMDF) is essentially the probability density function (PDF) of the SGS quantities. Thus, it has all the capabilities of PDF methods as widely recognized in RAS [11]. The primary advantage of the FDF, similar to PDFs in RAS, is that once the FDF is known then all of the SGS statistics are determined.

The use of PDF methods for LES of reacting flows had been previously suggested by several investigators. Recently we [1,2] have been able to derive a "transport equation" for the evolution of the FDF (FMDF) and to solve this equation in a mathematically-consistent and computationally-efficient manner. In this transport equation, the effects of chemical reactions on the SGS sta-

tistics appear in a closed form, allowing reliable LES of turbulent reacting flows. In Ref. [1], we solved the modeled transport equation for the FDF, and the results were compared with those obtained by direct numerical simulation (DNS), and by a "conventional" LES in which the effects of SGS scalar fluctuations are ignored (LES-FD). It was shown that in non-reacting flows, the first two SGS moments of the FDF are the same as those obtained by LES-FD. This demonstrate the consistency of the FDF and the convergence of its numerical solution. The advantage of the FDF was demonstrated in reacting flows in which its results were shown to deviate significantly from those obtained by LES-FD. Extensive comparisons with DNS data indicated clear advantage of FDF over LES-FD. The extension of the methodology for LES of variable density turbulent reacting flows is made by Jaberi et al. [2] who introduced the FMDF, which is essentially the density weighted FDF. Jaberi et al. [2] also observe excellent agreements between FMDF and DNS results. They assess the capabilities of FMDF further by comparison with experimental data.

The encouraging results obtained by FMDF warrant further improvements and implementations of this methodology for a wider class of reacting flows. The specific objectives of the present work are: (i) Further development of the SGS closures based on the FMDF, and (ii) implementation of the FMDF for LES of hydrocarbon diffusion flames. The efforts pertaining to (i) are concerned with: improvements of the closures of various terms in the "scalar FMDF" transport equation, developments of the joint "velocity-scalar" FMDF, and numerical solution of the joint velocity-scalar FMDF transport equation. The efforts pertaining to (ii) deal with implementations of the FMDF for actual LES of diffusion flames. The simulated results will be used for assessment of the spatial and the compositional structure of flames under non-equilibrium conditions.

Formulation: Large eddy simulation involves the spatial filtering operation [12]

$$\langle f(\underline{x},t)\rangle_\ell = \int_{-\infty}^{+\infty} f(\underline{x}',t)\mathcal{H}(\underline{x}',\underline{x})d\underline{x}' \tag{1}$$

where $\mathcal{H}$ denotes the filter function, $\langle f(\underline{x},t)\rangle_\ell$ represents the filtered value of the transport variable $f(\underline{x},t)$. In variable density flows it is convenient to consider the Favre filtered quantity, $\langle f(\underline{x},t)\rangle_L = \langle \rho f\rangle_\ell / \langle \rho\rangle_\ell$ For spatially & temporally invariant and localized filter functions, $\mathcal{H}(\underline{x}',\underline{x}) \equiv H(\underline{x}'-\underline{x})$ with the properties $H(\underline{x}) = H(-\underline{x})$, and $\int_{-\infty}^{\infty} H(\underline{x})d\underline{x} = 1$. Let $\Phi(\underline{x},t)$ denote the array of σ scalars and $U(\underline{x},t)$ denote the velocity field. The joint filtered mass density function (FMDF) of the velocity-scalars is formally defined as

$$\mathcal{F}_L(V,\varphi;\underline{x},t) \equiv \int_{-\infty}^{+\infty} \rho(\underline{x}',t)\xi[V,U(\underline{x}',t),\varphi,\Phi(\underline{x}',t)]H(\underline{x}'-\underline{x})d\underline{x}' \tag{2}$$

$$\xi[V,U(\underline{x},t),\varphi,\Phi(\underline{x},t)] = \prod_{k=1}^{3}\delta[V_k - U_k(\underline{x},t)]\prod_{\alpha=1}^{\sigma}\delta[\varphi_\alpha - \phi_\alpha(\underline{x},t)] \tag{3}$$

where $\rho(\underline{x},t)$ is the fluid density, δ denotes the delta function, φ denotes the composition domain of the scalar array, and V represents the composition domain of the velocity field. The term

$\xi[V, U(\underline{x}, t), \varphi, \Phi(\underline{x}, t)]$ is the "fine-grained" density [11], and Eq. (2) implies that the FMDF is the mass weighted spatially filtered value of the fine-grained density. The transport equation for the FMDF is obtained by following a procedure similar to that in PDF methods [11]

The most convenient means of solving the FMDF transport equation is via the "Lagrangian Monte Carlo" procedure. In this procedure, the FMDF is represented by an ensemble of computational "stochastic elements" (or "particles") which are transported in the "physical space" by the combined actions of large scale convection and diffusion (molecular and subgrid). In addition, transport in the "composition space" occurs due to chemical reaction and SGS mixing. The Lagrangian Monte Carlo procedure considers "notional particles" whose evolution can be computed from the known filtered field to yield a PDF transport equation which is identical to that of the FMDF transport. This is the basis for the concept of equivalent systems [11,13]. In this context, the notional particles evolve via a "stochastic process" to simulate motion in physical space by convection and diffusion. The compositional values on each particle are changed due to mixing and reaction.

When the FMDF is applied only to the scalar field, the filtered hydrodynamic field must be determined by the "conventional" LES procedure. In doing so, we have used a high-order accurate finite difference procedure. This discretization procedure is based on the "compact parameter" scheme which yields up to 6th order spatial accuracies. All the finite difference operations are performed on fixed grid points. Thus, the filtered values of the hydrodynamic variables are determined on these points. The transfer of information from the fixed finite difference points to the location of the Monte Carlo particles are conducted via interpolation. Based on our experience, 4th order interpolation provides more than sufficient accuracy.

When the FMDF is applied to both the scalar and the velocity fields, obviously additional SDEs must be considered. With this joint FMDF formulation, the effects of SGS convention appear in a closed form. In this regard, the FMDF scheme is expected to be more flexible and also more powerful than the conventional LES even for non-reacting flow simulations. The computational advantage is that the interpolation procedure as discussed above is not required since the Monte Carlo elements carry information pertaining to both the scalars and the velocity. Possible advantages or drawbacks of the joint velocity-composition FMDF formulation over the formulation which considers the composition FMDF alone are not fully established at the present time. We plan to start with the Langevin equations proposed by Pope [13]. This procedure is reasonably well developed in RAS and its relation to second order turbulence closures is well established [14].

Currently, we are in Year 1 of this project. It will take approximately three (3) years to achieve the goals of this research. We expect about 60% of our efforts will be devoted to development of the SGS closure exclusively for reacting flows. The other 40% of the efforts will be focused on conducting LES.

References:

[1] Colucci, P.J., Jaberi, F.A., Givi, P., and Pope, S.B., *Phys. Fluids*, 10(2):499--515 (1998).

[2] Jaberi, F.A., Colucci, P.J., James, S., Givi, P., and Pope, S.B., *J. Fluid Mech.*, 401:85--121 (1999).

[3] Libby, P.A. and Williams, F.A., Eds., *Turbulent Reacting Flows*, Academic Press, London, England, 1994.

[4] Jones, W.P., In Libby and Williams [3], chapter 6, pp. 309--374.

[5] Oran, E.S. and Boris, J.P., *Prog. Energy Combust. Sci.*, 7:1--72 (1981).

[6] Givi, P., *Prog. Energy Combust. Sci.*, 15:1--107 (1989).

[7] Poinsot, T., Candel, S., and Trouve, A., *Prog. Energy Combust. Sci.*, 21:531--576 (1996).

[8] Givi, P., In Libby and Williams [3], chapter 8, pp. 475--572.

[9] Riley, J.J., in *Recent Advances in DNS and LES*, (Knight, D. and Sakell, L., Eds.), volume 54 of *Fluid Mechanics and its Applications*, Kluwer Academic Publishers, The Netherlands, 1999.

[10] Pope, S.B., in *Proceedings of 23rd Symp. (Int.) on Combustion*, The Combustion Institute, Pittsburgh, PA, 1990, pp. 591--612.

[11] Pope, S.B., *Prog. Energy Combust. Sci.*, 11:119--192 (1985).

[12] Aldama, A.A., volume 49 of *Lecture Notes in Engineering*, Springer-Verlag, New York, NY, 1990.

[13] Pope, S.B., *Ann. Rev. Fluid Mech.*, 26:23--63 (1994).

[14] Pope, S.B., *Phys. Fluids*, 6(2):973--985 (1994).

SHOCK TUBE STUDIES OF RAM ACCELERATOR PHENOMENA

ARO DAAH55-97-1-0300

Principal Investigator: Ronald K. Hanson

High Temperature Gasdynamics Laboratory
Department of Mechanical Engineering
Stanford University, Stanford, CA

SUMMARY/OVERVIEW:

This research is aimed at developing an improved understanding of hypersonic exothermic flows through the application of modern experimental methods and finite-rate-chemistry flowfield modeling. The emphasis has been on providing fundamental data, of flowfield structure and combustion ignition times, which are relevant to the ongoing development of high-speed propulsion concepts. These data are critically needed to improve the accuracy of computational modeling of these flows.

TECHNICAL DISCUSSION:

Primary activities are highlighted below. Related publications are cited at the end.

Imaging and Modeling of Shock-Induced Combustion in High-Speed Wedge Flows

A key element of our program is a combined experimental and computational study of shock-induced combustion and oblique detonation wave formation in 2-D wedge and conical flows. Oblique detonations, which occur in the limit of fast ignition behind an oblique shock wave, are a phenomenon of significant importance to future high-speed propulsion systems, including ram accelerators and oblique detonation wave engines. Experimental work has primarily employed a 40° (half-angle) wedge body, with an embedded piezo-electric pressure transducer to record the pressure history at the wedge forebody surface throughout the experiment. An OH PLIF imaging system is used to provide an instantaneous map of the OH distribution (and consequently, the flame front) in the flowfield. Complementary information on the shock and expansion waves in the flow is provided by a schlieren image acquired within 2 μs of the PLIF result. Experiments have varied the gas mixture composition, pressure, and velocity to alter the ignition delay and energy release.

In parallel, an inviscid flow, finite-rate chemistry CFD code for wedge and conical flows has been developed and tested in our laboratory; see Fig. 1 for example results. Comparisons of numerical calculations with the experimental results have yielded good agreement. Current work is aimed at using the code to improve understanding of the transition from shock-induced com-

bustion to oblique detonation (Fig. 1), and identifying test scenarios which are good candidates for experiments which test different aspects of the code.
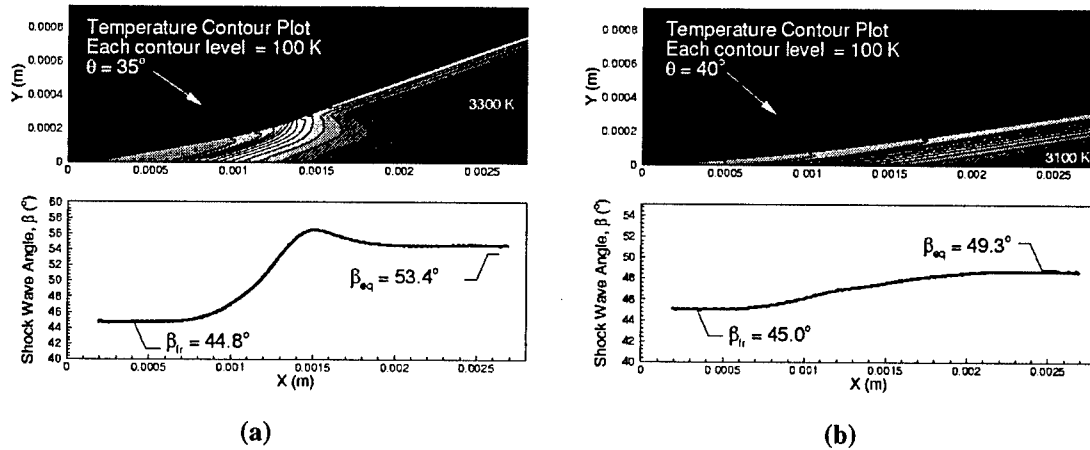
Figure 1: Temperature contour plot (upper panel), and corresponding plot of shock wave angle as a function of distance along the body surface (lower panel), demonstrate the transition from shock-induced combustion to oblique detonation. Mixture: $2H_2 + O_2 + 3.76N_2$, $V_\infty = 3160$ m/s, $T_\infty = 280$ K, $P_\infty = 0.5$ atm. (a) $\theta = 35°$ wedge flow (b) $\theta = 40°$ conical flow.

Experimental Study of Fuel Jets in Supersonic Combustion

A second element of our program is the experimental investigation of jet interactions with supersonic flows. Hydrogen and ethylene transverse jets injected into supersonic flow which simulates the burner entry conditions of an air-breathing propulsion system at flight Mach 10 are studied at several different conditions. Flow visualization using a unique, ultra-fast framing schlieren system revealed very different structural characteristics in the flow-field of these jets. Examples of schlieren images of hydrogen and ethylene jets, given in Fig. 2, show how the large eddies at the jet-free-stream interface develop differently for the two cases. Large-structures, formed periodically at the exit of the jet, are the primary mixing mechanism in the near-field of the jet, as they promote entrainment of the free-stream fluid into the jet. In the hydrogen case, these eddies stay coherent as they are convected downstream, but in the ethylene case, by contrast, they burst (cascade) into small eddies in the near-field of the jet. A systematic study has been pursued to understand the primary parameter leading to this phenomenon. More than 25 cases have been investigated using 5 gases injected into 10 different free-stream conditions.
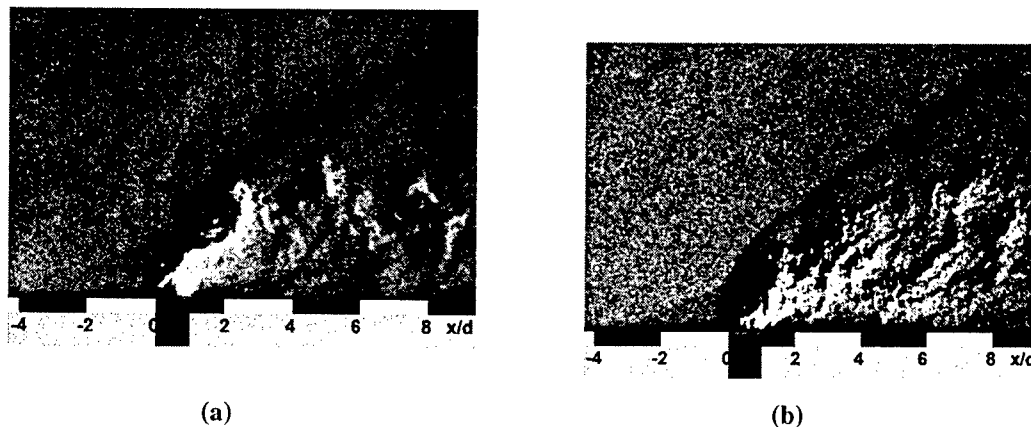
Figure 2: Instantaneous schlieren images of underexpanded (a) hydrogen and (b) ethylene injection into supersonic cross-flow obtained using the ultra-fast framing schlieren system. The injection total pressure and the free-stream conditions are similar in both cases. Velocity of the sonic jets at the exit of the injector are 1205m/s for hydrogen and 315m/s for ethylene jets.

144

Our experimental results reveal that this unsteady behavior of the jet depends directly on the velocity ratio between the jet and the free-stream. A critical value of the velocity ratio is found to exist above which the jet flow becomes unsteady resulting in improved mixing characteristics between the air and the jet.

Measurement and Modeling of Ignition Kinetics

This effort is a part of a larger program in our laboratory to investigate, through shock-tube experiments and chemical kinetics modeling, the ignition behavior of a wide variety of relevant military fuels. Initial work concentrated on high pressure (to 87 atm) H_2/O_2 and low pressure CH_4/O_2 ignition time measurements and modeling. More recently, we have extended measurements to larger, more complicated hydrocarbon fuels including n-heptane, n-decane, ethylene and JP-10. In this work were able to substantially improve on past measurements of ignition time by accurate *in situ* monitoring of the initial test gas mixture and by developing improved means of measuring the ignition time. Three complementary methods are now used to measure fuel concentration: manometric methods, IR laser absorption and gas chromatography. Ignition times are determined using either CH emission or pressure, or both. Substantially reduced scatter in ignition data has been possible with the implementation of these new methods. Representative data for several fuels is shown in Figure 3. Current work seeks to add measurements of transient species concentration time-histories that will be used as targets for validating detailed chemical kinetic mechanisms. Investigations are also in progress to measure the effects of selected ignition-enhancing additives on the ignition process of these candidate fuels.

Figure 3: Representative ignition delay time data: n-heptane, n-decane, JP-10 and ethylene in O_2/Ar.

PUBLICATIONS/PRESENTATIONS:

C. I. Morris, M. R. Kamel, A. Ben-Yakar, and R. K. Hanson, "Combined Schlieren and OH PLIF Imaging Study of Ram Accelerator Flowfields," Paper 98-0244 at the 36th AIAA Aerospace Sciences Meeting and Exhibit, Reno, NV, January 12-15, 1998.

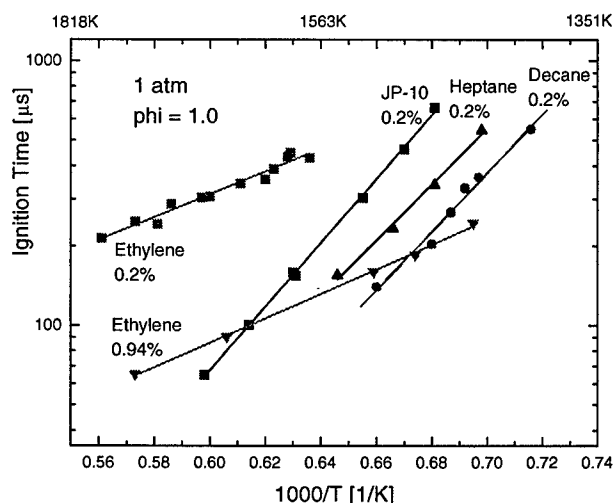A. Ben-Yakar, M. R. Kamel, C. I. Morris, and R. K. Hanson, "Hypersonic Combustion and Mixing Studies Using Simultaneous OH-PLIF and Schlieren Imaging," Paper 98-00940 at the 36th AIAA Aerospace Sciences Meeting and Exhibit, Reno, NV, January 12-15, 1998.

A. Ben-Yakar and R. K. Hanson, "Cavity Flameholders for Ignition and Flame Stabilization in Scramjets: Review and Experimental Study," Paper 98-3122 at the 34th Joint Propulsion Conference & Exhibit, Cleveland, OH, July 13-15, 1998.

C. I. Morris, M. R. Kamel, and R. K. Hanson, "Shock-Induced Combustion in High-Speed Wedge Flows," 27th *Symposium (International) on Combustion*, The Combustion Institute, pp. 2157-2164, 1998.

A. Ben-Yakar and R. K. Hanson, "Experimental Investigation of Flame-Holding Capability of Hydrogen Transverse Jet in Supersonic Cross-Flow," 27th *Symposium (International) on Combustion*, The Combustion Institute, pp. 2173-2180, 1998.

E. L. Petersen, D. F. Davidson, and R. K. Hanson, "Ignition Delay Times of Ram Accelerator CH_4/O_2/Diluent Mixtures," *Journal of Propulsion and Power*, Vol. 15, No. 1, pp. 82-91, 1999.

E. L. Petersen, D. F. Davidson, and R. K. Hanson, "Kinetics Modeling of Shock-Induced Ignition in Low-Dilution CH_4/O_2 Mixtures at High Pressures and Intermediate Temperatures," *Combustion and Flame*, Vol. 117, No. 1-2, pp. 272-290, 1999.

E. L. Petersen and R. K. Hanson, "Reduced Kinetics Mechanisms for Ram Accelerator Combustion," *Journal of Propulsion and Power*, Vol. 15, No. 1, pp. 82-91, 1999.

A. Ben-Yakar and R. K. Hanson, "Supersonic Combustion of Cross-Flow Jets and the Influence of Cavity Flame-Holders," Paper 99-0484 at the 37th AIAA Aerospace Sciences Meeting and Exhibit, Reno, NV, January 11-14, 1999.

A. Ben-Yakar and R. K. Hanson, "Cavity Flame-Holders For Ignition and Flame Stabilization in Scramjets: An Overview", submitted to J. of Propulsion and Power, September 1999.

A. Ben-Yakar and R. K. Hanson, "Characterization of Expansion Tube Flows for Hypervelocity Combustion Studies in the Flight Mach 8 – 13 Range", submitted to J. of Propulsion and Power, May 2000.

D. F. Davidson and R. K. Hanson, "Spectroscopic Diagnostics," chapter 4.2 in *Handbook of Shock Waves*, in press.

E. L. Petersen and R. K. Hanson, "Nonideal Effects Behind Reflected Shock Waves in a High-Pressure Shock Tube," submitted to Shock Waves, 1999.

D. C. Horning, D. F. Davidson, and R. K. Hanson, "Ignition Time Correlations for n-Heptane/O2/Ar Mixtures: A Parametric Study of Experimental Data and Kinetic Modeling," in preparation.

HIGH RESOLUTION MEASUREMENTS OF
SUPERSONIC SHEAR FLOW MIXING AND COMBUSTION

Werner J.A. Dahm and James F. Driscoll

Laboratory for Turbulence & Combustion (LTC)
Department of Aerospace Engineering
The University of Michigan
Ann Arbor, MI 48109-2140

Summary/Overview

Achieving supersonic mixing and combustion while maintaining flame stability and acceptable emissions of trace pollutant species are essential to the development of future airbreathing propulsion systems. This investigation contributes to this objective by making high-resolution imaging measurements of the physical structure of supersonic mixing and combustion in turbulent shear flows. The work consists of two major parts. The first is an investigation of the outer-scale properties of entrainment, mixing, and combustion in supersonic turbulent shear flows. Emphasis is on measuring changes in the large-scale structure and growth rate of a two-dimensional supersonic turbulent shear flow with increasing compressibility effects, and comparing with previous results on compressibility effects in supersonic mixing layers to identify the effects of compressibility that are generic to all supersonic turbulent shear flows. The second part of this work investigates the highly-resolved multi-dimensional structure of molecular mixing and chemical reaction in subsonic and supersonic turbulent shear flows. These measurements permit new insights to be gained into the fundamental issues that dominate the coupling between turbulent flow, molecular mixing, and nonequilibrium reaction chemistry in turbulent combustion systems.

Technical Discussion

During the past year we have extended our $M = 2$ PLMS imaging experiments and probe surveys to $M = 3$ (see Fig. 1), and from these have obtained new insights into the outer-scale properties and large-scale structure of supersonic turbulent shear flows. At both $M = 2$ and 3, as shown in Figs. 2 and 3, the growth rate and velocity decay under locally compressible flow conditions clearly follow the same power law scalings as in the corresponding incompressible turbulent wake flow.   Even the scaling constants agree with previous incompressible experiments for forced and unforced turbulent wakes. This is in stark contrast to results obtained in supersonic turbulent mixing layers, where dramatic reductions in growth rates occur with increasing compressibility, and suggests that at least some of the results previously obtained in mixing layers may be specific to that particular shear flow. Several archival papers have been written documenting these remarkable observations.

A PIV system has been developed for our supersonic combustion tunnel and used for a variety of experiments investigating compressibility effects on entrainment, mixing, and combustion. This system uses a novel seed particle that meets the Stokes number requirements even under these demanding high-speed flow conditions. Experiments to date have focused mainly on regions of high convective Mach number (see Fig. 4) to assess effects of compressibility on the large-scale structure of the turbulent wake. Additional experiments to investigate heat release effects in turbulent combustion have been done in collaboration with researchers at WFAPB. Several archival papers have been prepared that document these results.

147
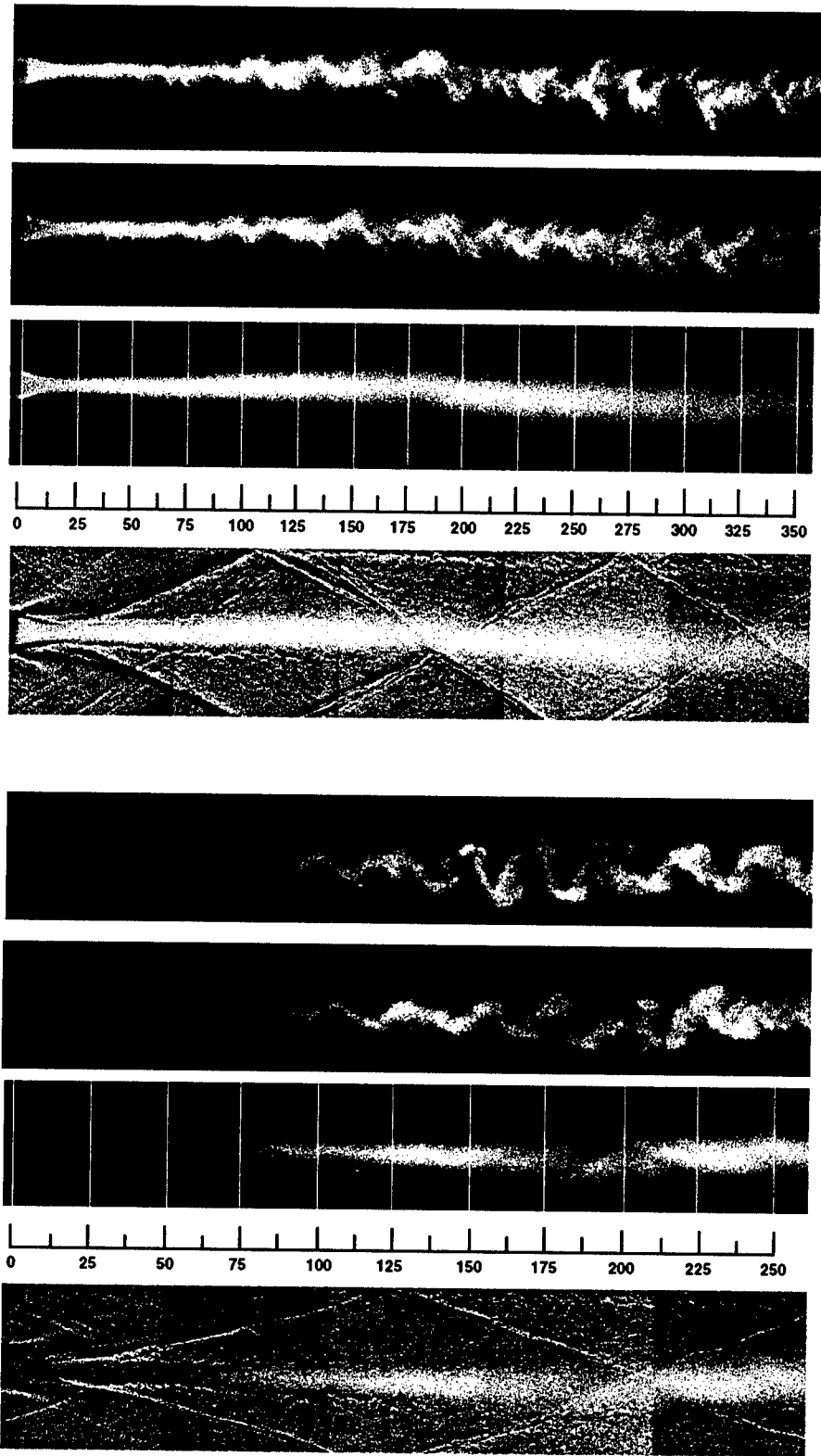
Figure 1. Instantaneous and mean planar laser Mie scattering (PLMS) images and instantaneous shadowgraph images of the supersonic planar turbulent wake at M = 2 *(top)* and M = 3 *(bottom)*. Scales give the downstream distance in (x/ϑ). Note effect of wave intersections on growth rate and large scale structure of the flow.
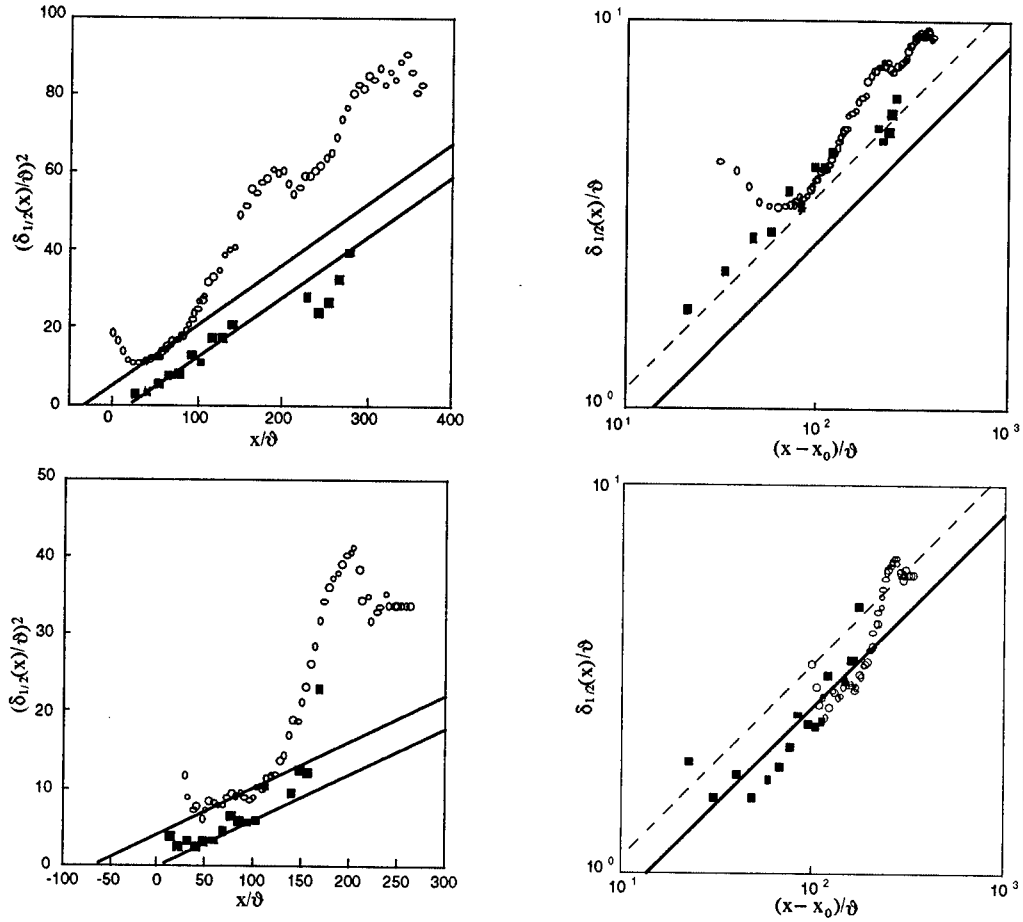
Figure 2. Flow width $\delta_{1/2}$ obtained from mean PLMS intensity profiles *(circles)* and mean velocity profiles *(squares)* for $M = 2$ *(top)* and $M = 3$ *(bottom)*. Straight lines show $(\delta/\vartheta) \sim (x/\vartheta)^{1/2}$ incompressible wake scaling. Increased growth rates coincide with recompression wave intersections. Log-log forms show lines indicating 1/2-power law scaling for values of the far-field scaling constant c_δ in forced incompressible wakes *(dashed line)* and unforced incompressible wakes *(solid line)*.
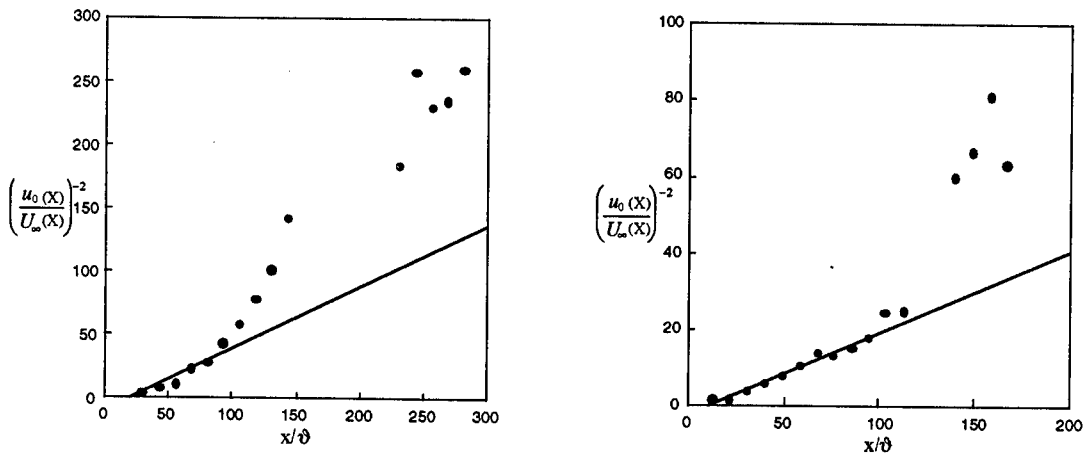
Figure 3. Comparison of velocity defect decay for $M = 2$ *(left)* and $M = 3$ *(right)* using the same ϑ. Straight lines show classical $(x/\vartheta)^{-1/2}$ incompressible wake scaling of the centerline velocity defect. Note that the compressible turbulent shear flow follows the same scaling as the corresponding incompressible flow, with the only apparent differences being due to reflected expansion and recompression wave intersections.
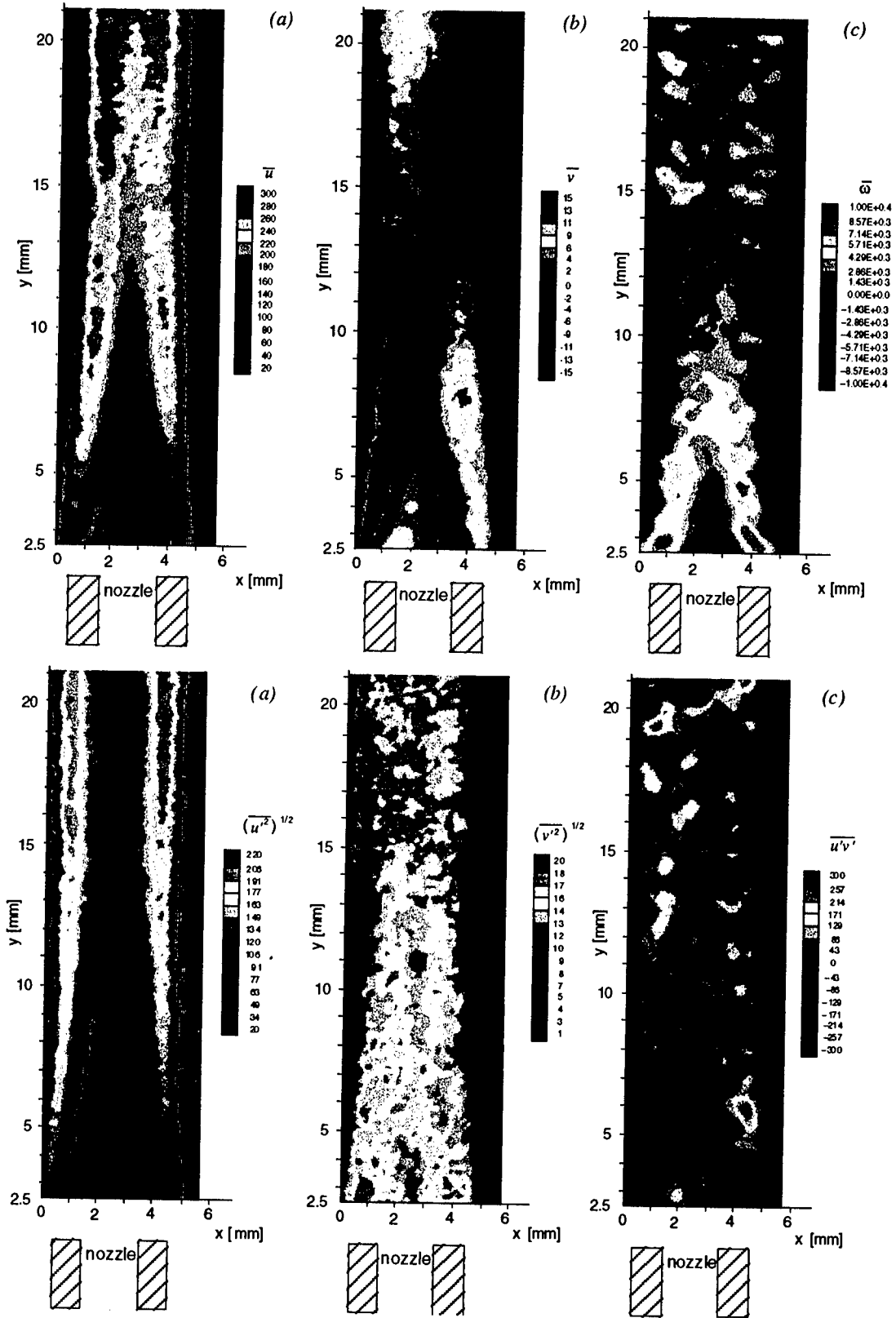
Figure 4. Typical supersonic PIV results obtained in the supersonic planar turbulent wake near field, showing at top
(a) mean streamwise velocity, (b) mean cross streamwise velocity, and (c) mean vorticity, and at bottom (a) rms
streamwise velocity fluctuation, (b) rms cross streamwise velocity fluctuation, and (c) Reynolds stress.

PDF MODELLING OF TURBULENT COMBUSTION

Principal Investigator: Stephen B. Pope

Mechanical & Aerospace Engineering

Cornell University

Ithaca, NY 14853

SUMMARY

Significant progress has been made in the application of PDF-based turbulent combustion models to the Sandia pilot-jet nonpremixed flames. These PDF calculations are described in two recent papers (Xu & Pope 2000 and Tang, Xu & Pope 2000) and they are summarized below. The first of these works shows that the PDF method is capable of describing, quantitatively, the phenomena of local extinction and reignition (as functions of jet velocity and axial distance) that are observed in these flames. The second paper extends the methodology to include radiative heat loss, and the calculation of NO_x.

PDF MODEL

The model is based on the transport equation for the joint probability density function of velocity, turbulence frequency and thermochemical composition. For the combustion of methane considered, the chemical kinetics are represented by the augmented reduced mechanism of Sung, Law & Chen (1998). Without NO_x chemistry (ARM1) there are 16 species; with NO_x there are 19. For computational tractability, the effects of reaction are implemented by the in situ adaptive tabulation (ISAT) algorithm (Pope 1997).

LOCAL EXTINCTION

The piloted jet nonpremixed flames measured by Barlow & Frank (1998) consist of a central jet of methane, a substantial annular pilot, and coflowing air. In the three flames considered, D, E and F, the jet velocities are $U_J = 50$, 74 and 99 m/s, respectively. The amount of local extinction increases with the jet velocity.

Figure 1 shows scatter plots of the CO_2 mass fraction against mixture fraction for Flame F at 30 jet radii downstream. In the measurements (left-hand figure), each point represents a laser shot: in the calculations (right-hand figure), each point represents a particle from the particle/mesh method used to solve the PDF equation. The upper curve is the composition of a mildly strained laminar flame. The fact that the bulk of the points lie beneath this line is an indication of local extinction. The lower curve is the conditional mean from the data. Good agreement between the calculations and the measurements may be observed.

Xu & Pope (2000) define a "burning index" (BI) as a measure of (the lack of) local extinction. To explain the definition of the burning index we again refer to Fig. 1. The

The vertical dashed line shows a mixture fraction range around strichiometric (defined by Barlow & Frank 1998). The lower solid circle is the mean of the data points that lie in this range; whereas the upper solid circle is the value from the laminar flame. The burning index is defined as the ratio of these two values. Consequently, a burning index of 1 corresponds (roughly) to complete combustion, and 0 corresponds to complete extinction.
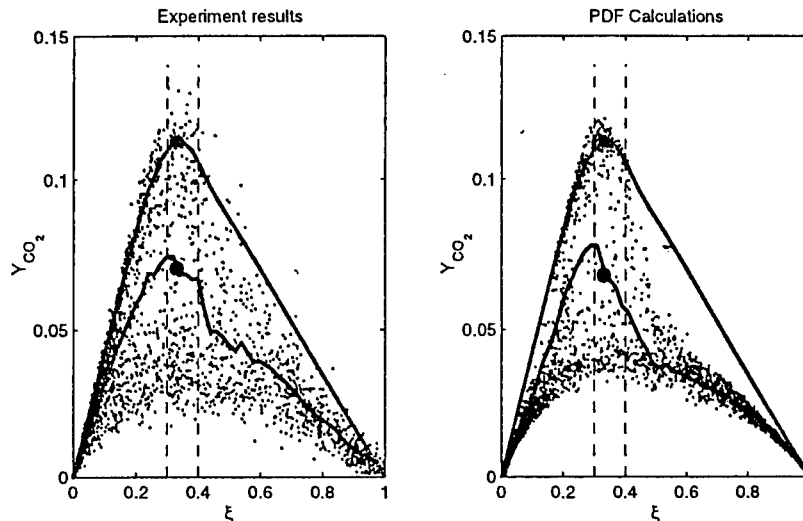
Figure 1: Scatter plots of CO_2 mass fraction against mixture fraction for flame F at an axial distance of 15 jet diameters. Left-hand plot, experimental data of Barlow & Frank (1998); right-hand plot, PDF calculations of Xu & Pope (2000).

Figure 2 compares the measured and calculated burning indexes of different species (and temperature) for all three flames as functions of axial distance. As may be seen, with few exceptions, the PDF calculations accurately describe the dependence of BI on both the jet velocity and on the axial distance. These results demonstrate a significant advance in our abilities to calculate substantial finite-rate chemistry-turbulence interactions.

MAJOR AND MINOR SPECIES

For flame D, Fig. 3 shows calculated radial profiles of the mean and r.m.s. of the NO mass fraction compared to the experimental data. Good agreement may be observed for both quantities, and the downstream evolution is well represented. It may be seen that radiative heat loss does not have a significant impact on NO (in this flame).

Figure 4 shows the conditional mean (conditioned on mixture fraction ξ) of various quantities. These conditional means provide a good indication of the accuracy of the chemistry calculations. As may be seen, the agreement between the calculations and the experiments is uniformly satisfactory. The trends of NO with jet velocity and downstream distance are accurately represented; and the accuracy of the CO calculations shows that ARM remedies previously observed discrepancies.
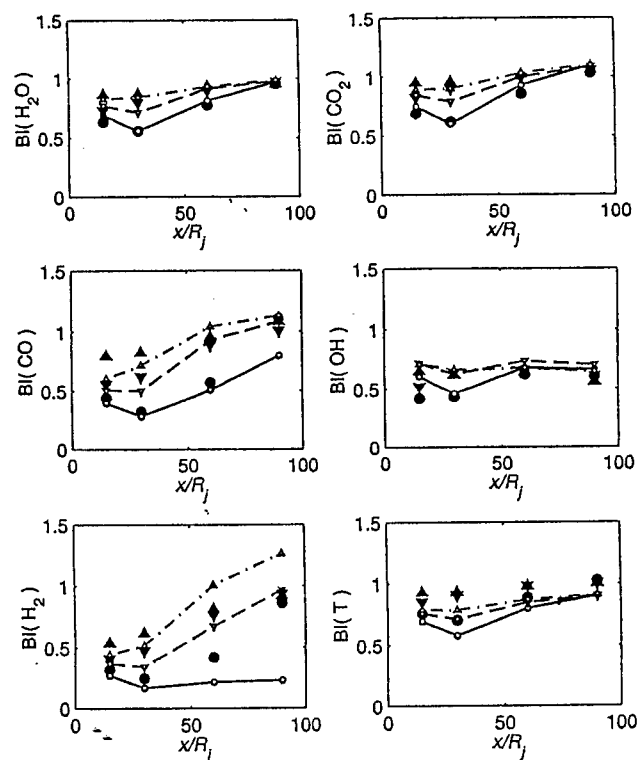
Figure 2: Burning indexes for flames D, E and F. Filled symbol: experiments; lines with empty symbols, PDF calculations. Circle and solid line, flame F; down-triangle and dashed line, flame E; up-triangle and dashed-dotted line, flame D. (From Xu & Pope 2000.)
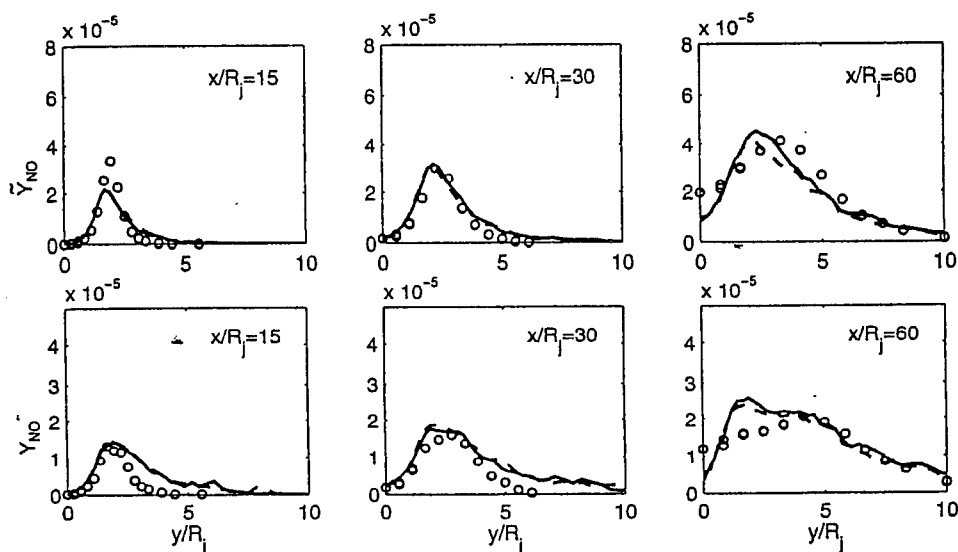
Figure 3: Radial profiles of the mean (upper plots) and r.m.s. (lower plots) of NO mass fraction in flame D. Symbols, experimental data (Barlow & Frank 1998); solid and dashed lines, PDF calculations without and with radiative heat loss. (From Tang, Xu & Pope 2000.)

REFERENCES

1. Barlow R.S. and Frank J.H. "Effects of turbulence on species mass fraction in methane/air jet flames," In *Twenty-seventh Symp. (Int'l) on Combust.*, page 1087, Pittsburgh, 1998. The Combustion Institute.

2. Pope S.B. (1997) "Computationally Efficient Implementation of Combustion Chemistry using In Situ Adaptive Tabulation," Combustion Theory and Modelling, **1**, 41–63.

3. Sung, C. J., Law C. K., and Chen J.-Y. (1998). "An augmented reduced mechanism for methane oxidation with comprehensive global parametric validation." In *Twenty-seventh Symp. (Int'l) on Combust.*, Pittsburgh, pp. 295–304. The Combustion Institute.

4. Tang Q., Xu J. and Pope S.B. (2000) "PDF calculations of local extinction and *NO* production in piloted-jet turbulent methane/air flames", Twenty-Eighth Symp. (Int'l) on Combust. (to be published).

5. Xu J. and Pope S.B. (2000) "PDF calculations of turbulent nonpremixed flames with local extinction," Combust. Flame (to be published).
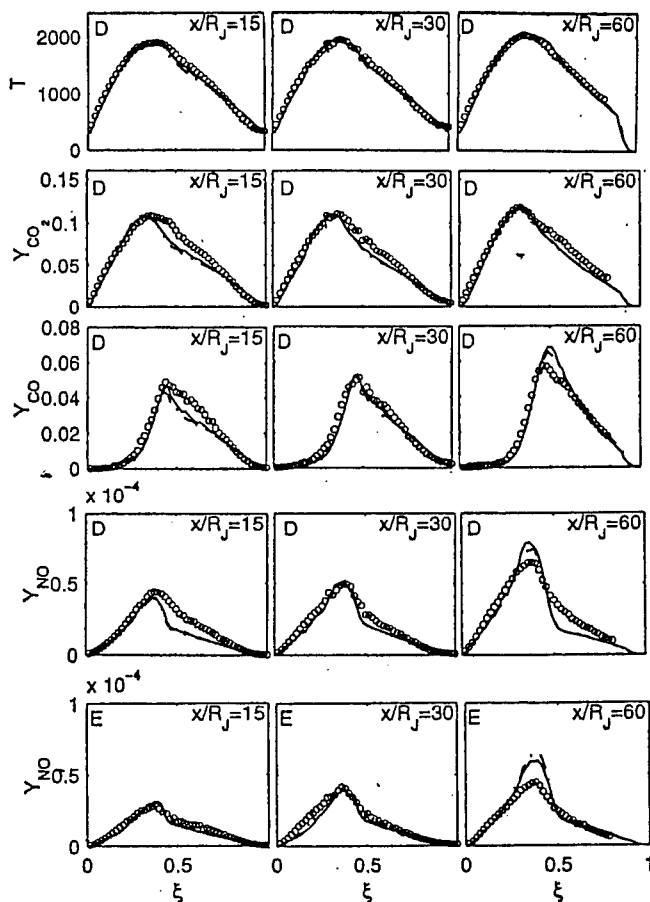
Figure 4: Conditional means in flames *D* and *F*. Lines and symbols as in Fig. 3.

INVITEES

Dr. John Abraham
Department of Mechanical Engineering
Purdue University
West Lafayette IN 47907
Phone: (765)494-1505
e-mail: jabraham@ecn.purdue.edu

Dr. Mukund Acharya
Allied Signal Engines, M/S 301-125
111 South 34th Street
PO Box 52181
Phoenix AZ 85072-2181
Phone: (602)231-2808
e-mail: Mukund.Acharya@alliedsignal.com

Dr. M. S. Anand
Allison Engine Company
P.O. Box 420
Speed Code T-14
Indianapolis IN 46206-0420
Phone: (317)230-2828
FAX:230-3691
e-mail: iemsa@agt.gmeds.com

Dr Griffin Anderson
NASA Langley Research Center
M/S 168
Hampton VA 23681
Phone: (804)864-6238
FAX:864-6243
e-mail: g.y.anderson@larc.nasa.gov

Dr. William Anderson
AMSRL-WT-PC
US Army Research Laboratory
Aberdeen Proving Ground MD 21005-5066
Phone: (410)278-9992
FAX: 278-7333
e-mail: willie@arl.army.mil

Dr Kurt Annen
Aerodyne Research, Inc.
45 Manning Road
Manning Park Research Center
Billerica MA 01821-3976
Phone: (978)663-9500
FAX:663-4918
e-mail: kannen@aerodyne.com

Dr Chris Atkinson
Dept of Mech. & Aerospace Eng.
West Virginia University
PO Box 6106
Morgantown WV 26506-6106
Phone: (304)293-4111
FAX:293-2582

Dr William Bachalo
Artium Technologies, Inc.
14660 Saltamontes Way
Los Altos Hills CA 94022-2036
Phone: (650)941-4233
e-mail: wbachalo@aol.com

Dr. Tiejun Bai
Engineering Department
Clark Atlanta University
223 James P Brawley Drive, SW
Atlanta GA 30314
Phone: (404)880-6983
FAX: 880-6853
e-mail: tbai@cau.edu

Mr. Lee Bain
AFRL/PRSS
Building 490
1790 Loop Road, North
Wright-Patterson AFB OH 45433-7103
Phone: (937)255-2175
FAX:656-4659
e-mail: Lee.Bain@wl.wpafb.af.mil

Dr S L Baughcum
Boeing Company
P O Box 3707, MS 6H-FC
Seattle WA 98124
Phone: (425)965-0426
FAX:234-4543
e-mail: baughcum@atc.boeing.com

Dr Howard Baum
National Institute of
Standards and Technology
Center for Fire Research
Gaithersburg MD 20899
Phone: (301)975-6668

Dr John Bdzil
Los Alamos National Laboratory
Los Alamos NM 87545

Dr. Bruce Beaver
Department of Chemistry
Duquesne University
Mellon Hall
Pittsburgh PA 15282-1503
Phone: (412)434-6340
FAX:434-5683

Mr. Steve Beckel
Pratt and Whitney
M/S 715-83
P.O. Box 109600
West Palm Beach FL 33410-9600

Dr Edward Beiting
Aerophysics Lab, Prop & Env Sc
The Aerospace Corporation
P O Box 92957, M5/754
Los Angeles CA 90009-2957
Phone: (310)336-7035

Dr Josette Bellan
Applied Technologies Section
Jet Propulsion Laboratory
4800 Oak Grove Drive
Pasadena CA 91109
Phone: (626)354-6959
FAX:393-1633
e-mail: josette.bellan@jpl.nasa.gov

Dr Michael Berman
AFOSR/NL
801 North Randolph Street, Room 732
Arlington VA 22203-1977
Phone: (703)696-7781
FAX:696-8449
e-mail: michael.berman@afosr.af.mil

Dr Thomas Beutner
AFOSR/NA
801 North Randolph Street, Room 732
Arlington VA 22203-1977
Phone: (703)696-6961
FAX:696-8451
e-mail: thomas.beutner@afosr.af.mil

Dr. Robert Bill
Propulsion Dir, Army Res. Lab.
NASA Glenn Res. Ctr., MS 77-12
21000 Brookpark Road
Cleveland OH 44135-3191
Phone: (216)433-3703
FAX:433-3000
e-mail: Robert.C.Bill@lerc.nasa.gov

Dr Mitat Birkan
AFOSR/NA
801 North Randolph Street, Room 732
Arlington VA 22203-1977
Phone: (703)696-7234
FAX:696-8451
e-mail: mitat.birkan@afosr.af.mil

Dr Kevin Bowcutt
North American Aircraft Div.
Rockwell International Corp.
P.O. Box 3644
Seal Beach CA 90740-7644

Dr C T Bowman
Department of Mechanical
Engineering
Stanford University
Stanford CA 94305-3032
Phone: (650)723-1745
FAX:723-1748
e-mail: bowman@navier.stanford.edu

Dr Iain Boyd
Department of Mechanical and Aerospace Engineering
246 Upson Hall
Cornell University
Ithaca NY 14853
Phone: (607)255-4563
FAX:255-1222
e-mail: boyd@scotch.mae.cornell.edu

Mr. Andy Brankovic
8432 East Garden Oaks Circle
Palm Beach Gardens FL 33410
Phone: (561)625-0029
e-mail: ABrankovic@aol.com

Dr K N C Bray
University of Cambridge
Department of Engineering
Trumpington Street
Cambridge CB2 1PZ, England UK
Phone: 0223 332744
FAX0223 332662

Dr Robert Breidenthal
Department of Aeronautics and
Astronautics
University of Washington, FS10
Seattle WA 98195
Phone: (206)685-1098

Dr Kenneth Brezinsky
Department of Chemical Engrg
University of Illinois-Chicago
810 S. Clinton St, Room 204
Chicago IL 60607-7000
Phone: (312)996-9430
FAX:996-0808
e-mail: kenbrez@uic.edu

Dr Garry Brown
Department of Mechanical and
Aerospace Engineering
Princeton University
Princeton NJ 08544-5263
Phone: (609)258-6083
e-mail: GLB@pucc.princeton.edu

Dr R C Brown
Aerodyne Research, Inc.
45 Manning Road
Manning Park Research Center
Billerica MA 01821-3976
Phone: (978)663-9500
FAX:663-4918

Dr. Adam Bruckner
Aerospace and Energ Rsrch Prog
University of Washington
120 Aero&Eng Rsrch Bldg FL-10
Seattle WA 98195
Phone: (206)543-6321
FAX:543-4719
e-mail: bruckner@aa.washington.edu

Dr. Walter Bryzik
Propulsion Systems Division
ATTN: AMSTA-TR-R, MS 121
USA Tank-Automotive Command
Warren MI 48397-5000
Phone: (810)574-6461
FAX: 574-5054
e-mail: bryzik@cc.tacom.army.mil

Dr John D Buckmaster
Department of Aerospace
Engineering
University of Illinois
Urbana IL 61801

Dr Dennis Bushnell
NASA Langley Research Center
Mail Stop 110
Hampton VA 23681
Phone: (804)864-4546
e-mail: d.m.bushnell@larc.nasa.gov

Dr Ron Butler
AFRL/PR
Building 490
1790 Loop Road, N
Wright-Patterson AFB OH 45433-7103

Dr T D Butler
MS B210 T-DO: THEORETICAL DIVISION
Los Alamos National Laboratory
Los Alamos NM 87545
Phone: (505)667-4401
FAX: 665-4055
e-mail: tdbutler@lanl.gov

Dr H F Calcote
Titan Corp, AeroChem Rsrch Lab
50 Washington Road
P. O. Box 2229
Princeton NJ 08543-2229
Phone: (609)716-1201
FAX:716-1204
e-mail: hcalcote@titan.com

Dr George Caledonia
Physical Sciences, Inc
20 New England Business Center
Andover MA 01810
Phone: (508)689-0003
FAX:689-3232

Mr. Donald Campbell
NASA Glenn Research Center
21000 Brookpark Road
Mail Stop 3-2
Cleveland OH 44135
Phone: (216)433-2929
(216)433-5266

Dr Graham V Candler
Department of Aerospace
Engineering & Mechanics
University of Minnesota
Minneapolis MN 55455

Dr Brian Cantwell
Department of
Mechanical Engineering
Stanford University
Stanford CA 94305-3032
Phone: (650)723-4825

Dr. Herb Carlson
AFOSR/CA
801 North Randolph Street, Room 732
Arlington VA 22203-1977
Phone: (703)696-7550
FAX:696-9556
e-mail: herb.carlson@afosr.af.mil

Dr. Len Caveny
13715 Piscataway Drive
Ft Washington MD 20744
Phone: (301)292-5319
FAX:292-3724
e-mail: Lcaveny@compuserve.com

Dr. Ismail Celik
Department of Mechanical and
Aerospace Engineering
West Virginia University
Morgantown WV 26506

Dr. Nicholas Cernansky
Mechanical Engineering Dept.
Drexel University
32nd and Chestnut Streets
Philadelphia PA 19104-2884

Dr. Chine I Chang
Director
US Army Research Office
PO Box 12211
Research Triangle Park NC 27709-2211
Phone: (919)549-4203
FAX:549-4348
e-mail: jchang@aro-emh1.army.mil

Dr Richard Chang
Applied Physics Department
P. O. Box 208284
Yale University
New Haven CT 06520-8284
Phone: (203)432-4272
FAX: 432-4274
e-mail: RK_CHANG@RAMAN.ENG.YALE.EDU

Dr Tryfon Charalampopoulos
Mechanical Engineering Dept.
Louisiana State University
Baton Rouge LA 70803
Phone: (504)388-5792
FAX:388-5894

Dr. Harsha Chelliah
Department of Mechanical, Aero
and Nuclear Engineering
University of Virginia
Charlottesville VA 22903-2442
Phone: (804)924-6037
FAX:982-2037
e-mail: harsha@virginia.edu

Dr. Jacqueline Chen
MS 9051
Sandia National Laboratories
P.O. Box 969
Livermore CA 94551-0969
Phone: (510)294-2586
FAX:294-1012
e-mail: jhchen@sandia.gov

Dr Lea D Chen
Mechanical Engineering Dept
University of Iowa
Iowa City IA 52242
Phone: (319)335-5674
FAX:335-5669
e-mail: ldchen@icaen.uiowa.edu

Dr Wai K Cheng
Department of Mechanical
Engineering
MIT
Cambridge MA 02139
Phone: (617)253-4531

Dr Robert Childs
Nielsen Engineering and
Research, Inc.
510 Clyde Avenue
Mountain View CA 94043-2287
Phone: (415)968-9457

Dr S Y Cho
Department of Mechanical and
Aerospace Engineering
Princeton University
Princeton NJ 08544-5263

Dr M-S Chou
Building R1, Room 1044
TRW Space and Technology Group
One Space Park
Redondo Beach CA 90278
Phone: (310)812-0469
FAX:812-7589

Mr. John M. Clarke
Caterpillar Inc.
Technical Center
P.O. Box 1875
Peoria IL 61656-1875
Phone: (309)578-3913
FAX:578-4232
e-mail: john.clarke@cat.com

Mr R.W. Claus
NASA Glenn Research Center
21000 Brookpark Road
Cleveland OH 44135-3127
Phone: (216)433-5869

Dr M B Colket
United Technologies Research
Center
411 Silver Lane
East Hartford CT 06108
Phone: (860)610-7481
FAX:610-2151
e-mail: colketmb@utrc.utc.com

Dr S M Correa
GE Corp. Research & Development
PO Box 8, K1ES112
Schenectady NY 12301
Phone: (518)387-5853
FAX:387-7258
e-mail: correa@crd.ge.com

Dr David Crosley
Molecular Physics Department
SRI International
333 Ravenswood Avenue
Menlo Park CA 94025-3696
Phone: (415)326-6200

Dr Clayton Crowe
Department of Mechanical
Engineering
Washington State University
Pullman WA 99164-2920
Phone: (509)335-3214

Dr F E C Culick
Engrg. and Appl. Sci. Dept.
California Institute of
Technology
Pasadena CA 91125
Phone: (626)395-4470

Dr Eli Dabora
Mechanical Engineering Dept
University of Connecticut
Box U-139 ME
Storrs CT 06268
Phone: (203)486-2415

Dr Werner Dahm
Department of Aerospace
Engineering
The University of Michigan
Ann Arbor MI 48109-2118
Phone: (734)764-4318
FAX:763-0578
e-mail: wdahm@engin.umich.edu

Dr John Daily
Center for Combustion Research
Mechanical Engineering Dept
University of Colorado
Boulder CO 80309
Phone: (303)492-7151

Mr. Eugene Danielson
US Army Tank-Automotive
and Armaments Command
ATTN: AMSTA-TR-R - MS 121
Warren MI 48397-5000

Dr Ron Davis
Chemical Science and Techn Lab
Building 221, Room B312
National Inst of Stds & Tech
Gaithersburg MD 20899

Dr. Peter A. DeBarber
MetroLaser
18006 Skypark Circle #108
Irvine CA 92714-6428

Dr Pablo G Debenedetti
Department of Chemical
Engineering
Princeton University
Princeton NJ 08544-5263
Phone: (609)258-5480
e-mail: PDEBENE@princeton.edu

Dr George Deiwert
NASA Ames Research Center
MS 230-2
Moffett Field CA 94035
Phone: (415)604-6198

Dr R W Dibble
Department of Mechanical Eng
6159 Etcheverry Hall
University of California
Berkeley CA 94720
Phone: (415)642-4901
FAX:642-6163
e-mail: rdibble@euler.vine.berkeley.edu

Dr Paul Dimotakis
California Institute of Tech
1201 East California Blvd.
MC 301-46
Pasadena CA 91125
Phone: (626)395-4456
(626)395-4447
e-mail: dimotakis@caltech.edu

Dr. Glenn Diskin
NASA Langley Research Center
Hampton VA 23681
Phone: (757)864-6268
FAX:864-7923
e-mail: g.s.diskin@larc.nasa.gov

Dr Richard Dobbins
Department of Engineering
Brown University
164 Angel Street
Providence RI 02912-9104
Phone: (401)863-2653
FAX:863-1157
e-mail: richard_dobbins@brown.edu

Dr Gregory Dobbs
United Technologies Research
Center - Mail Stop 90
Silver Lane
East Hartford CT 06108
Phone: (860)610-7145

Mr Lee Dodge
Southwest Research Institute
P O Drawer 28510
San Antonio TX 78284
Phone: (512)684-5111

Dr Michael Drake
Physical Chemistry Department
General Motors Research Labs
Twelve Mile and Mound Roads
Warren MI 48090-9055

Dr. James F. Driscoll
Department of Aerospace Engrg
3004 FXB Building
University of Michigan
Ann Arbor MI 49109-2118
Phone: (734)936-0101
FAX:763-0578
e-mail: jamesfd@engin.umich.edu

Dr. J. Philip Drummond
NASA Langley Research Center
Mail Stop 197
Hampton VA 23681-0001
Phone: (757)864-2298
FAX:864-7923
e-mail: j.p.drummond@larc.nasa.gov

Dr Frederick Dryer
Department of Mechanical and
Aerospace Engineering
Princeton University
Princeton NJ 08544-5263
Phone: (609)258-5206

Dr C Dutton
Department of Mechanical and
Industrial Engineering
University of Illinois
Urbana IL 61801

Dr Harry Dwyer
Department of Mechanical
Engineering
University of California
Davis CA 95616

Dr A C Eckbreth
United Technologies Research
Center
411 Silver Lane
East Hartford CT 06108
Phone: (860)610-7269

Dr. Charles A. Eckert
Department of Chemical Engrg
Georgia Institute of
Technology
Atlanta GA 30332-0100
Phone: (404)853-9344
FAX:894-6956

Dr Raymond Edelman
WC 70
Rocketdyne
6633 Canoga Avenue
Canoga Park CA 91304
Phone: (818)586-1247

Dr J T Edwards
AFRL/PRSF
Building 490
1790 Loop Road, N
Wright-Patterson AFB OH 45433-7103
Phone: (937)255-3524
FAX:255-1125
e-mail: edwardjt@pr.wpafb.af.mil

Dr. Fokion N. Egolfopoulos
Department of Mechanical Engrg
University of Southern Calif
Olin Hall 400B
Los Angeles CA 90089-1453
Phone: (213)740-0480
e-mail: egolfopo@alnitak.usc.edu

Ms Charlotte Eigel
AFRL/PR
Building 490
1790 Loop Road, N
Wright-Patterson AFB OH 45433-7103
Phone: (937)255-5106

Dr Said Elghobashi
Department of Mechanical
Engineering
University of California
Irvine CA 92717
Phone: (714)856-6002

Dr Phillip Emmerman
Harry Diamond Laboratories
Attn. SLCHD-ST-RD
2800 Powder Mill Road
Adelphi MD 20783-1197
Phone: (301)394-3000

Dr K C Ernst
Pratt and Whitney Aircraft
Group
Government Products Division
West Palm Beach FL 33402

Dr G M Faeth
Department of Aerospace
Engineering
University of Michigan
Ann Arbor MI 48109-2118
Phone: (734)764-7202
FAX:936-0106
e-mail: gmfaeth@umich.edu

Dr. Daniel Fant
South Carolina Energy Research
and Development Center
386-2 College Avenue
Clemson SC 29634-5180
Phone: (864)656-2267
FAX:656-1429

Dr Gregory W Faris
Molecular Physics Laboratory
SRI International
333 Ravenswood Avenue
Menlo Park CA 94025-3493
Phone: (650)859-4131
FAX:859-6196
e-mail: faris@mplvax.sri.com

Dr. Patrick Farrell
Engineering Research Center
University of Wisconsin-Madison
1500 Engineering Drive
Madison WI 53706
Phone: (608)263-1686
FAX:262-6707
e-mail: farrell@engr.wisc.edu

Mr Ted Fecke
WL/POTC
Building 18
1950 Fifth Street
Wright-Patterson AFB OH 45433-7251
Phone: (937)255-2351
e-mail: fecket@wl.wpafb.af.mil

Dr Francis Fendell
TRW Space and Technology Group
Building R1, Room 1022
One Space Park
Redondo Beach CA 90278
Phone: (213)812-0327

Dr Richard Field
U. S. Army Armament R&D Center
DRSMC-LCA-G(D)
Building 382-S
Dover NJ 07801
Phone: (201)724-5844

Dr Farley Fisher
National Science Foundation
Chemical and Thermal Syst Div
4201 Wilson Boulevard
Arlington VA 22230
Phone: (703)306-1371
FAX:306-0319
e-mail: ffisher@nsf.gov

Dr Arthur Fontijn
Department of Chemical and
Environmental Engineering
Rensselaer Polytechnic Inst.
Troy NY 12180-3590
Phone: (518)276-6508
FAX:276-4030
e-mail: fontijn@rpitsmts.edu

Dr. David E. Foster
Engine Research Center
University of Wisconsin
Madison WI 53706
Phone: (608)263-1617

Dr Michael Frenklach
Department of Mechanical
Engineering
University of California
Berkeley CA 94720-1740
Phone: (510)643-1676
FAX:642-6163
e-mail: myf@euler.berkeley.edu

Mr Jack Fultz
AFRL/PR
Wright-Patterson AFB OH 45433-6563
Phone: (937)255-2175

Dr Bish Ganguly
AFRL/PRPS
2645 Fifth Street, Suite 13
Wright-Patterson AFB OH 45433-7919
Phone: (937)255-2923
FAX:656-4095
e-mail: biswa.ganguly@pr.wpafb.af.mil

Dr. Richard G. Gann
Building and Fire Research Laboratory
National Inst. Of Stds. & Technology
100 Bureau Drive, Stop 8650
Gaithersburg MD 20899-8650
Phone: (301)975-6866
FAX:975-4052
e-mail: rggann@nist.gov

Dr Alon Gany
Faculty of Aerospace Engrg
Technion-Israel Institute of
Technology
32000 Haifa, ISRAEL
Phone: 972-4-8292554
FAX:972-4-8230956
e-mail: gany@aerodyne.technion.ac.il

Dr Alan Garscadden
AFRL/PR
1950 Fifth Street, Building 18A
Wright-Patterson AFB OH 45433-7251
Phone: (937)255-2246
FAX:986-4657
e-mail: alan.garscadden@pr.wpafb.af.mil

Dr. Kresimir Gebert
BKM, Inc.
5141 Santa Fe Street
San Diego CA 92109
Phone: (858)270-6760
e-mail: bkm-inc@worldnet.att.net

Dr Ahmed Ghoniem
Department of Mechanical
Engineering
MIT
Cambridge MA 02139
Phone: (617)253-2295
FAX:253-5981
e-mail: ghoniem@mit.edu

Mr R Giffen
General Electric Company
Aircraft Engine Group
Neumann Way
Cincinnati OH 45215

Dr P Givi
Department of Mechanical and
Aerospace Engineering
State University of New York
Buffalo NY 14260
Phone: (716)645-2593
FAX:645-3875
e-mail: givi@eng.buffalo.edu

Dr Irvin Glassman
Department of Mechanical and
Aerospace Engineering
Princeton University
Princeton NJ 08544-5263
Phone: (609)258-5199
FAX:258-5963
e-mail: glassman@princeton.edu

Dr. George Gogos
Mechanical Engineering Department
University of Nebraska
104 WSEC
Lincoln NE 68588-0656
Phone: (402)472-3006
e-mail: ggogos@unlserve.unl.edu

Dr Judah Goldwasser
Office of Naval Research
Mechanics Division, Code 333
800 North Quincy Street
Arlington VA 22217-5660
Phone: (703)696-2164
FAX:696-2558
e-mail: goldwaj@onr.navy.mil

Dr. James Gord
AFRL/PRSC
Building 490
1790 Loop Road N
Wright-Patterson AFB OH 45433-7103
Phone: (937)255-7431
FAX:656-4570
e-mail: james.gord@pr.wpafb.af.mil

Dr. Jay P. Gore
School of Mechanical Engrg
Purdue University
1003 Chaffee Hall
West Lafayette IN 47907-1003
Phone: (317)494-1500
FAX:494-0530

Dr. Sol Gorland
NASA Glenn Research Center
21000 Brookpark Road
Mail Stop 60-4
Cleveland OH 44135
Phone: (216)977-7561
FAX:977-7500
e-mail: sol.h.gorland@lerc.nasa.gov

Dr A D Gosman
Department of Mechanical Engrg
Imperial College of Science
and Technology
London WS7 2BX UK

Dr Larry Goss
Research Applications Division
Systems Research Labs, Inc.
2800 Indian Ripple Road
Dayton OH 45440-3696
Phone: (513)252-2706

Dr Richard Gould
Department of Mechanical and Aerospace Engineering
Box 7910
North Carolina State University
Raleigh NC 27695-7910
Phone: (919)515-5236
FAX:515-7968
e-mail: gould@eos.ncsu.edu

Dr Frederick Gouldin
Department of Mechanical and
Aerospace Engineering
Cornell University
Ithaca NY 14853-5692
Phone: (607)255-5280
e-mail: fcg2@cornell.edu

Dr F Grinstein
Laboratory for Computational
Physics & Fluid Dynamics
Naval Research Laboratory
Washington DC 20375-5344
Phone:
e-mail:

Dr. Mark Gruber
AFRL/PR
1950 Fifth Street, Suite 10
Wright-Patterson AFB OH 45433-7251
Phone: (937)255-4141
FAX:656-4659
e-mail: grubermr@possum.appl.wpafb.af.mil

Dr. Brian K. Gullett
U.S. Environmental Protection Agency
National Risk Management Research Laboratory
Air Pollution Technology Branch (MD-65)
Research Triangle Park NC 27711
Phone: (919)541-1534
FAX:541-0290
e-mail: gullett.brian@epa.gov

Dr. Rajendra Gupta
Department of Physics
University of Arkansas
120 Ozark Hall
Fayetteville AR 72701-1201
Phone: (501)575-5933
e-mail: rgupta@comp.uark.edu

Dr Ephraim Gutmark
Mechanical Engineering Dept
2508 CEBA
Louisiana State University
Baton Rouge LA 70803
Phone: (504)388-5899
FAX:388-5924
e-mail: gutmark@me.lsu.edu

Dr. Mark A. Hagenmaier
AFRL/PR
Building 18
1950 Fifth Street, Suite 10
Wright-Patterson AFB OH 45433-7251
Phone: (937)255-5210
FAX:476-4659
e-mail: hagenma@possum.appl.wpafb.af.mil

Dr. Nabil S. Hakim
Director, Advanced Engineering
Detroit Diesel Corporation
13400 W. Outer Drive, R03-B
Dteroit MI 48239-4001
Phone: (313)592-7455
FAX:592-5906

Dr. Robert B. Hall
SAF/AQRT
1060 Air Force Pentagon
Washington DC 20330-1060
Phone: (703)588-7802
(703)588-8388
e-mail: hall@aqpo.hq.af.mil

Dr Robert D. Hancock
AFRL/PR
Building 490
1790 Loop Road, N
Wright-Patterson AFB OH 45433-7103
Phone: (937)255-7487
FAX:255-1125
e-mail: hancockr@ward.appl.wpafb.af.mil

Dr Ronald Hanson
Mechanical Engineering Department
Stanford University
Building 530, Room 112
Stanford CA 94305-3030
Phone: (650)723-4023
FAX:725-4862
e-mail: hanson@cdr.stanford.edu

Dr Stephen Harris
Physical Chemistry Department
General Motors Research Labs
30500 Mound Road
Warren MI 48090-9055
Phone: (313)986-1305

Dr D L Hartley
Sandia National Laboratories
MS0735
Albuquerque NM 87185-5800

Dr. Stephen D. Heister
Department of Aeronautics
and Astronautics
Purdue University
West Lafayette IN 47907-1282
Phone: (765)494-5126
FAX:494-0307
e-mail: stephen.d.heister.1@purdue.edu

Dr Simon Henbest
Airframes & Engines Division
Aero & Maritime Research Lab
P O 4331
Melbourne, Victoria AUSTRALIA 3001
Phone: (03)647 7585
FAX:646 6771
e-mail: henbests@aedmel.arl.dsto.gov.au

Dr. Naeim Henein
Department of Mechanical Engrg
Wayne State University
2121 Engineering Building
Detroit MI 48201
Phone: (313)577-3887
FAX:577-8789
e-mail: henein@me1.eng.wayne.edu

Dr Cecil F. Hess
MetroLaser
18006 Skypark Circle
Suite 108
Irvine CA 92714-6428
Phone: (714)553-0688
FAX:553-0495

Dr L Hesselink
Department of Aeronautics and
Astronautics
Stanford University
Stanford CA 94305-3032
Phone: (650)723-3466

Dr E D Hirleman
Department of Mechanical and
Aerospace Engineering
Arizona State University
Tempe AZ 85287
Phone: (602)965-3895
FAX:965-1384

Mr Norman Hirsch
AFRL/PR
Wright-Patterson AFB OH 45433-6563
Phone: (937)255-2175

Dr David Hofeldt
125 Mechanical Engineering
111 Church Street, S E
University of Minnesota
Minneapolis MN 55455
Phone: (612)625-2045
e-mail:

Mr Robert Holland
United Technologies Chemical
Systems Division
P O Box 49028
San Jose CA 95161-9028
Phone: (408)224-7656
e-mail:

Dr Hans G Hornung
Graduate Aeronautical Labs
California Institute of
Technology
Pasadena CA 91125
Phone: (626)395-4551
e-mail: hans@galcit.caltech.edu

Dr David Huestis
Molecular Physics
SRI International
333 Ravenswood Avenue
Menlo Park CA 94025-3493
Phone: (650)859-3464
FAX:859-6196
e-mail: huestis@mp1vax.sri.com

Dr Lawrence Hunter
Applied Physics Laboratory
Johns Hopkins University
Johns Hopkins Road
Laurel MD 20707-6099
Phone: (301)953-5000

Dr. Frank Hurley
US Army Research Office
PO Box 12211
Research Triangle Park NC 27709-2211
Phone: (919)549-4432
FAX:549-4310
e-mail: hurley@aro-emh1.army.mil

Dr A K M F Hussain
Mechanical Engineering Dept
4800 Calhoun Road
University of Houston
Houston TX 77204-4792
Phone: (713)743-4545
FAX:743-4503
e-mail: mece1w@jetson.uh.edu

Dr Essam A Ibrahim
Department of Mechanical
Engineering
Tuskegee University
Tuskegee AL 36088
Phone: (205)727-8974
FAX:727-8090
e-mail: emeei@acd.tusk.edu

Dr Thomas Ishii
Department of Electrical
Engineering
Marquette University
Milwaukee WI 53233
Phone: (414)288-6998
FAX:288-7082

Dr. Farhad Jaberi
Department of Mechanical and
Aerospace Engineering
State University of New York
Buffalo NY 14260
Phone: (716)645-2593
FAX:645-3875
e-mail: jaberi@eng.buffalo.edu

Dr. Thomas Jackson
AFRL/PRSS
Building 490
1790 Loop Road North
Wright-Patterson AFB OH 45424-7251
Phone: (937)255-2175
FAX:656-4659
e-mail: Thomas.Jackson@pr.wpafb.af.mil

Dr. Joseph Janni
AFOSR/CC
801 North Randolph Street, Room 732
Arlington VA 22203-1977
Phone: (703)696-7553
FAX:696-9556
e-mail: janni@afosr.af.mil

Dr Jay Jeffries
Mechanical Engineering Department
Thermophysics Division, Building 520
Stanford University
Stanford CA 94305-3032
Phone: (650)736-0007
FAX:723-1748
e-mail: jeffries@Navier.Stanford.edu

Mr Gordon Jensen
United Technologies Chemical
Systems Division
P O Box 49028
San Jose CA 95161-9028
Phone: (408)365-5552

Mr. Jeff Jensen
Kaiser-Marquardt
16555 Staycoy Street
Van Nuys CA 91406

Dr. William Johnson
BKM, Inc.
5141 Santa Fe Street
San Diego CA 92109
Phone: (619)270-6760

Mr. Craig Johnston
Lockheed Advanced Dev. Company
Lockheed-Martin Corporation
1011 Lockheed Way
Palmdale CA 93599-7212

Dr Sheridan Johnston
Combustion Sciences
Sandia National Laboratories
Livermore CA 94551-0969
Phone: (510)294-2138

Dr K Kailasanath
Code 6410, LCP&FD
US Naval Research Laboratory
4555 Overlook Avenue, SW
Washington DC 20375-5344
Phone: (202)767-2402
FAX:767-4798
e-mail: KAILASANATH@lcp.nrl.navy.mil

Dr Ann Karagozian
Department of Mechanical and
Aerospace Engineering
University of California, LA
Los Angeles CA 90095-1597
Phone: (310)825-5653
FAX:206-4830
e-mail: ark@seas.ucla.edu

Dr Laurence R Keefe
Nielsen Engineering and
Research, Inc.
510 Clyde Avenue
Mountain View CA 94043-2287
Phone: (415)968-9457
FAX:968-1410

Dr Dennis Keefer
University of Tennessee
Space Institute
Gas Diagnostics Research Div.
Tullahoma TN 37388-8897
Phone: (615)455-0631

Dr Arnold Kelly
Department of Mechanical and
Aerospace Engineering
Princeton University
Princeton NJ 08544-5263
Phone: (609)258-5221

Dr John Kelly
Altex Technologies Corporation
650 Nuttman Road
Suite 114
Santa Clara CA 95054
Phone: (408)980-8610

Dr Ian Kennedy
Mechanical & Aero Engrg
University of California,
Davis
Davis CA 95616-5294
Phone: (530)752-2796
FAX:752-4158
e-mail: IMKENNEDY@ucdavis.edu

Dr Lawrence A Kennedy
Department of Mechanical
Engineering
The Ohio State University
Columbus OH 43210-1107
Phone: (614)292-5782

Dr James Kezerle
Gas Research Institute
8600 West Bryn Mawr Avenue
Chicago IL 60631
Phone: (312)399-8331

Dr G B King
Department of Mechanical
Engineering
Purdue University
West Lafayette IN 47907-1288
Phone: (765)494-6518
e-mail: kinggb@ecn.purdue.edu

Dr Merrill K King
NASA Headquarters
Code UG
300 E Street, SW
Washington DC 20546
Phone: (202)358-0817
FAX:358-3091
e-mail: mking1@mail.hq.nasa.gov

Dr William H Kirchhoff
Office of Energy Research
U.S. Department of Energy
19901 Germantown Road
Germantown MD 20874
Phone: (301)903-5820
e-mail: william.kirchhoff@oer.doe.gov

Dr. David E. Klett
Mechanical Engineering Dept
North Carolina Agricultural
and Technical State Univ
Greensboro IG 27401-3209

Dr Charles Kolb
Aerodyne Research, Inc.
45 Manning Road
Manning Park Research Center
Billerica MA 01821-3976
Phone: (978)663-9500
FAX:663-4918

Dr Wolfgang Kollmann
Mechanical & Aerospace Engrg
University of California,
Davis
Davis CA 95616-5295
Phone: (530)752-4152
FAX:752-4158
e-mail: wkollmann@ucdavis.edu

Dr George Kosaly
Mechanical Engineering Dept
University of Washington
Box 352600
Seattle WA 98195-2600
Phone: (206)543-6933
FAX:685-8047
e-mail: kosaly@u.washington.edu

Mr David Kruczynski
Attn SLCBR-IBA
Interior Ballistics Division
Army Research Laboratory
Aberdeen Proving Gnd MD 21005-5066
Phone: (410)278-6202

Dr Kenneth Kuo
Department of Mechanical
Engineering
Pennsylvania State University
University Park PA 16802
Phone: (814)865-6741
FAX:863-3203

Dr. Ming-Chia Lai
Department of Mechanical Engrg
Wayne State University
Detroit MI 48202

Dr Marshall Lapp
High Temperature Interfaces
Division
Sandia National Laboratories
Livermore CA 94551-0969
Phone: (510)294-2435

Dr John Larue
Department of Mechanical
Engineering
University of California
Irvine CA 92717

Dr Allan Laufer
Office of Energy Research
U. S. Department of Energy
19901 Germantown Road
Germantown MD 20874
Phone: (202)903-5820
e-mail: Allan.Laufer@oer.doe.gov

Dr Normand Laurendeau
Department of Mechanical
Engineering
Purdue University
West Lafayette IN 47907-1288
Phone: (765)494-2713
FAX:494-0539
e-mail: Laurende@ecn.purdue.edu

Dr Moshe Lavid
ML Energia, Inc.
P. O. Box 1468
Princeton NJ 08540
Phone: (609)799-7970

Dr C K Law
Department of Mechanical and
Aerospace Engineering
Princeton University
Princeton NJ 08544-5263
Phone: (609)258-5271
FAX:258-6233
e-mail: cklaw@princeton.edu

Dr C C Lee
Environmental Protection
Agency
Cincinnati OH 45268
Phone: (513)569-7520

Dr Spiro Lekoudis
Office of Naval Research
Mechanics Division, Code 432
800 North Quincy Street
Arlington VA 22217-5660
Phone: (703)696-4403

Dr Anthony Leonard
Graduate Aeronautical Labs
California Institute of
Technology
Pasadena CA 91125
Phone: (626)395-4465

Dr Deborah Levin
Department of Chemistry
George Washington University
725 21st Street, NW
Washington DC 20013
Phone: (202)994-5637
FAX:994-5873
e-mail: dalevin@gwu.edu

Dr Jay Levine
AFRL/PR
10 East Saturn Boulevard
Edwards AFB CA 93524-7600
Phone: (805)275-6179
FAX:275-6233
e-mail: levine@plablink.ple.af.mil

Dr. Arthur Lewis
University of Dayton Research Inst.
Aerospace Mechanics Division
300 College Park
Dayton OH 45469-0110
Phone: (937)229-4235
FAX:229-4251

Dr Chiping Li
Naval Research Laboratory
Code 6910, CCP&FD
Washington DC 20375-5344
Phone: (202)767-3254
FAX:767-4078
e-mail: LI@lcp.nrl.navy.mil

Dr Goang Liaw
Department of Civil Engineering
Alabama A&M University
PO Box 367
Normal AL 35762
Phone: (205)851-5565
e-mail:

Dr Paul Libby
Department of AMES 0310
9500 Gilman Drive
University of California
La Jolla CA 92093-0310
Phone: (858)534-3168
FAX:534-4543
e-mail: libby@ames.ucsd.edu

Dr Wilbert Lick
Department of Mechanical and
Environmental Engineering
University of California
Santa Barbara CA 93106

Dr Hans Liepmann
Graduate Aeronautical Labs
California Institute of
Technology
Pasadena CA 91125
Phone: (626)395-4535

Dr. Charles L. Liotta
Department of Chemical Engrg
Georgia Institute of
Technology
Atlanta GA 30332-0100
Phone: (404)853-9344
FAX:894-6956

Dr Lyle N Long
Department of Aerospace Engrg
233 Hammond Building
Pennsylvania State University
University Park PA 16802
Phone: (814)865-1172
FAX:865-7092
e-mail: lnl@psu.edu

Dr Marshall Long
Mechanical Engineering Department
Yale University
PO Box 208284
New Haven CT 06520
Phone: (203)432-4229
FAX:432-6775
e-mail: long-marshall@yale.edu

Dr F E Lytle
Department of Chemistry
Purdue University
West Lafayette IN 47907
Phone: (765)494-5261

Dr Bruce MacDonald
Research Applications Division
Systems Research Labs, Inc.
2800 Indian Ripple Road
Dayton OH 45440-3696
Phone: (513)252-2706

Dr. John Magill
Physical Sciences, Inc.
20 New England Business Center
Andover MA 01810
Phone: (508)689-0003
FAX:689-3232

Dr Edward Mahefkey
AFRL/PR
Wright-Patterson AFB OH 45433-6563
Phone: (937)255-6241
e-mail:

Mr Nick Makris
SA-ALC/SFT
Kelly AFB TX 78241-5000
Phone: AV945-8212
FAX:945-9964
e-mail:

Dr David Mann
U. S. Army Research Office
P. O. Box 12211
4300 South Miami Boulevard
Research Triangle Pk NC 27709-2211
Phone: (919)549-4249
FAX:549-4310
e-mail: dmann@aro-emh1.army.mil

Dr Nagi Mansour
Computational Fluid Mechanics
Branch, RFT 202A-1
NASA Ames Research Center
Moffett Field CA 94035
Phone: (415)604-6420

Dr Frank Marble
Engrg. and Appl. Sci. Dept.
California Institute of
Technology
Pasadena CA 91125
Phone: (626)395-4784
e-mail: marble@cco.caltech.edu

Dr John Marek
NASA Glenn Research Center
Mail Stop 5-11
21000 Brookpark Road
Cleveland OH 44135-3127
Phone: (216)433-3584
FAX:433-3000
e-mail: cecil.j.marek@lerc.nasa.gov

Dr. Jay Martin
University of Wisconsin-Madison
Engine Research Center
1500 Engineering Drive
Madison WI 53706
Phone: (608)263-9460
FAX:262-6707
e-mail: martin@engr.wisc.edu

Dr James McDonald
Code 6110
Naval Research Laboratory
Chemistry Division
Washington DC 20375-5342
Phone: (202)767-3340

Dr D K McLaughlin
233 Hammond Building
Pennsylvania State University
University Park PA 16802
Phone: (814)865-2569

Dr Keith McManus
Physical Sciences, Inc
20 New England Business Center
Andover MA 01810
Phone: (508)689-0003
FAX:689-3232

Dr Constantine M Megaridis
University of Illinois-Chicago
Mechanical Engineering Dept
842 West Taylor Street
Chicago IL 60607-7022
Phone: (312)996-3436
FAX: 413-0447
e-mail: cmm@dino.me.uic.edu

Dr Mehran Mehregany
Department of Electrical Engineering
Case Western Reserve University
10900 Euclid Avenue
Cleveland OH 44106-7221

Dr A M Mellor
Mech & Matls Engrg Dept
512 Kirkland Hall
Vanderbilt University
Nashville TN 37240
Phone: (615)343-6214
FAX:343-6687

Dr Lynn Melton
Programs in Chemistry
University of Texas, Dallas
P. O. Box 830688
Richardson TX 75080-0688
Phone: (972)883-2913
FAX:883-2925
e-mail: melton@utdallas.edu

Dr. Suresh Menon
Department of Aerospace Engineering
Georgia Institute of Technology
Atlanta GA 30332-0150
Phone: (404)894-9126
e-mail: suresh.menon@aerospace.gatech.edu

Dr R Metcalfe
Department of Mechanical
Engineering
University of Houston
Houston TX 77004
Phone: (713)749-2439

Dr Michael M Micci
Department of Aerospace Engrg
233 Hammond Building
Pennsylvania State University
University Park PA 16802
Phone: (814)863-0043
FAX:865-7092
e-mail: micci@henry2.aero.psu.edu

Dr Richard Miller
Office of Naval Research
Mechanics Division, Code 432
800 North Quincy Street
Arlington VA 22217-5660
Phone: (703)696-4404
FAX:696-0934
e-mail: millerr@onr.navy.mil

Dr Andrzej Miziolek
Ignition and Combustion Branch
Interior Ballistics Division
Army Research Laboratory
Aberdeen Proving Gnd MD 21005-5066
Phone: (410)278-6157
FAX:278-6094

Dr Parviz Moin
Center for Turbulence Research
Stanford University
Stanford CA 94305-3032
Phone: (650)725-2081

Dr. H. C. Mongia
Manager, Combustion Technology
GE Aircraft Engines
One Neumann Way, M/D A404
Cincinnati OH 45215-6301
Phone: (513)243-2552
FAX:243-2538

Dr P J Morris
233-L Hammond Building
Pennsylvania State University
University Park PA 16802
Phone: (814)863-0157

Dr Edward Mularz
Attn: AMSRL-VP-C
NASA Glenn Res. Ctr., MS 77-12
21000 Brookpark Road
Cleveland OH 44135-3191
Phone: (216)433-5850
FAX:433-3720
e-mail: Edward.Mularz@lerc.nasa.gov

Dr M G Mungal
Department of Mechanical
Engineering
Stanford University
Stanford CA 94305-3032
Phone: (650)725-2019
FAX:723-1748
e-mail: mungal@leland.stanford.edu

Dr Phillip E Muntz
Department of Aerospace Engrg
Univ of Southern California
854 West 36th Place, RRB 101
Los Angeles CA 90089-1191
Phone: (213)740-5366

Dr Arje Nachman
AFOSR/NM
801 North Randolph Street, Room 732
Arlington VA 22203-1977
Phone: (703)696-8427
FAX: 696-8450
e-mail: arje.nachman@afosr.af.mil

Dr Herbert Nelson
Code 6110, Chemistry Division
Naval Research Laboratory
4555 Overlook Avenue, SW
Washington DC 20375-5342
Phone: (202)767-3686

Dr David Nixon
NWING, Inc.
883 North Shoreline Boulevard
Suite B200
Mountain View CA 94043
Phone: (415)254-0202
FAX: 961-9286

Dr G B Northam
NASA Langley Research Center
MS 188B
Hampton VA 23681
Phone: (804)864-6248
e-mail: g.b.northam@larc.nasa.gov

Dr. Michael Nusca
AMSRL-WT-PC
US Army Research Laboratory
Aberdeen Proving Ground MD 21005-5066
Phone: (410)278-6108
FAX: 278-7333
e-mail: nusca@arl.army.mil

Dr A K Oppenheim
Department of Mechanical
Engineering
University of California
Berkeley CA 94720
Phone: (415)642-0211

Dr Elaine Oran
LCP&FD, Code 6404
US Naval Research Laboratory
4555 Overlook Avenue, SW
Washington DC 20375-5344
Phone: (202)767-2960
FAX:767-4798
e-mail: ORAN@lcp.nrl.navy.mil

Dr T E Parker
Engineering Division
Colorado School of Mines
Golden CO 80401-1887
Phone: (303)273-3657
FAX:273-3602
e-mail: tparker@mines.colorado.edu

Dr Timothy Parr
Naval Air Warfare Center
Weapons Division
C02392
China Lake CA 93555-6001
Phone: (760)939-3367
FAX:939-6569
e-mail: t.parr@genie.geis.com

Lt. John S. Paschkewitz
AFRL/VAVE
Building 45 Annex
2130 Eighth Street, Suite 1
Wright-Patterson AFB OH 45433-7542
Phone: (937)255-4640
FAX:656-7915
e-mail: paschkjs@wl.wpafb.af.mil

Dr. Phillip H. Paul
MS 9051
Sandia National Laboratories
P. O. Box 969
Livermore CA 94551-9051
Phone: (510)294-1465
FAX: 294-1012
e-mail: phpaul@sandia.gov

Dr Alex Pechenik
AFOSR/NA
801 North Randolph Street, Room 732
Arlington VA 22203-1977
Phone: (703)696-7236
FAX:696-8451
e-mail: alex.pechenik@afosr.af.mil

Dr S S Penner
Center for Energy and
Combustion Research, 0411
University of California
La Jolla CA 92093-0411
Phone: (858)534-4284

Dr Richard Peterson
Department of Mechanical
Engineering
Oregon State University
Corvallis OR 97331-6001
Phone: (503)754-2567

Dr Lisa Pfefferle
Department of Chemical
Engineering
Yale University
New Haven CT 06520-8286
Phone: (203)432-2222
FAX:432-7232
e-mail: pfefferle@htcre.eng.yale.edu

Dr Emil Pfender
Department of Mechanical Engrg
125 Mechanical Engineering
The University of Minnesota
Minneapolis MN 55455

Dr W M Pitts
National Institute of
Standards and Technology
Center for Fire Research
Gaithersburg MD 20899
Phone: (301)975-6486

Dr Robert Pitz
Department of Mechanical and
Materials Engineering
Vanderbilt University
Nashville TN 37235
Phone: (615)322-0209
FAX:343-8730
e-mail: pitzrw@ctrvan.vanderbilt.edu

Dr S B Pope
Department of Mechanical and
Aerospace Engineering
Cornell University
Ithaca NY 14853-7501
Phone: (607)255-4314
FAX;255-1222
e-mail: pope@mae.cornell.edu

Dr. David Pratt
AFRL/VAVE
Building 45 Annex
2130 Eighth Street, Suite 1
Wright-Patterson AFB OH 45433-7542
Phone: (937)255-4640
FAX:656-7915
e-mail: prattdm@wl.wpafb.af.mil

Dr C L Proctor II
Department of Mechanical
Engineering
University of Florida
Gainesville FL 32611
Phone: (904)392-7555

Dr. Martin J. Rabinowitz
Mail Stop 5/10
NASA Glenn Research Center
21000 Brookpark Road
Cleveland OH 44135-3191
Phone: (216)433-5847
FAX:433-5588
e-mail: marty@lerc.nasa.gov

Dr Herschel Rabitz
Department of Chemistry
Princeton University
Princeton NJ 08544-1009
Phone: (609)258-3917
FAX:258-6746

Dr. Larry Rahn
Sandia National Laboratories
7011 East Avenue
Mail Stop 9056
Livermore CA 94551-0969
Phone: (510)294-2091
FAX: 294-2276
e-mail: rahn@sandia.gov

Dr S R Ray
National Institute of
Standards and Technology
Center for Chemical Engrg
Gaithersburg MD 20899

Dr. Mohan K. Razdan
Allison Engine Company
P.O. Box 420
Speed Code T-14
Indianapolis IN 46206-0420
Phone: (317)230-6404
FAX:230-3691
e-mail: iemkr@agt.gmeds.com

Mr. Robert Reed
Sverdrup Technology, Inc.
AEDC
1099 Avenue C
Arnold AFB TN 37389-9013
Phone: (615)454-4648
(615)454-6317

Dr R G Rehm
National Institute of
Standards and Technology
Center for Fire Research
Gaithersburg MD 20899
Phone: (301)975-2704

Dr Rolf D Reitz
Mechanical Engineering Dept
University of Wisconsin
1500 Johnson Drive
Madison WI 53706
Phone: (608)262-0145
FAX:262-6717

Dr M Renksizbulut
Department of Mechanical
Engineering
University of Waterloo
Waterloo, Ontario CN N2L 3G1
Phone: (519)885-1211

Dr Eli Reshotko
Case Western Reserve Univ
Department of Mechanical and
Aerospace Engineering
Cleveland OH 44106
Phone: (216)368-6447
FAX:368-6445
e-mail: exr3@po.cwru.edu

Dr David Reuss
Fluid Mechanics Department
General Motors Research Labs
30500 Mound Road
Warren MI 48090-9055
Phone: (313)986-0029

Dr William Reynolds
Department of Mechanical
Engineering
Stanford University
Stanford CA 94305-3032
Phone: (650)723-3840

Col. Steven Reznick
AFOSR/CD
801 North Randolph Street, Room 732
Arlington VA 22203-1977
Phone: (703)696-7555
FAX:696-9556
e-mail: steven.reznick@afosr.af.mil

Dr. Kyung T. Rhee
Department of Mechanical and
Aerospace Engineering
Rutgers, The State Univ of NJ
Piscataway NJ 08854-0909
Phone: (732)445-3651
e-mail: KTRhee@jove.rutgers.edu

Dr James Riley
Mechanical Engineering Dept
University of Washington
Seattle WA 98195
Phone: (206)543-5347
e-mail: 73671.737@Compuserve.com

Dr William Roberts
Department of Mechanical and Aerospace Engineering
Box 7910
North Carolina State University
Raleigh NC 27695-7910
Phone: (919)515-5294
FAX:515-7968
e-mail: wrobert@eos.ncsu.edu

Dr Michael Roco
National Science Foundation
Chemical and Thermal Syst Div
4201 Wilson Boulevard
Arlington VA 22230
e-mail: mroco@nsf.gov

Mr Wayne Roe
AFRL/PR
5 Pollux Drive
Edwards AFB CA 93523-5000
Phone: (805)275-5206
FAX:275-5852

Mr. Gerald A. Roffe
GASL
77 Raynor Avenue
Ronkonkoma NY 11779

Dr Won B Roh
Department of Engrg Physics
Air Force Institute of
Technology
Wright-Patterson AFB OH 45433-6583

Dr U S Rohatgi
Department of Nuclear Energy
Brookhaven National Laboratory
Upton NY 11973
Phone: (516)282-2475

Dr Glenn Rolader
Science Applications
International Corporation
1247-B N Eglin Parkway
Shalimar FL 32579
Phone: DSN 872-0391

Dr W M Roquemore
AFRL/PRSC
Building 490
1790 Loop Road, N
Wright-Patterson AFB OH 45433-7103
Phone: (937)255-6813
FAX:255-1125
e-mail: melr@ward.appl.wpafb.af.mil

Dr Anatol Roshko
Graduate Aeronautical Labs
California Institute of
Technology
Pasadena CA 91125
Phone: (626)395-4484

Dr Daniel Rosner
Department of Chemical
Engineering
Yale University
New Haven CT 06520-8286
Phone: (203)432-4391
FAX:432-7232
e-mail: daniel.rosner@yale.edu

Dr John Ross
Department of Chemistry
Stanford University
Stanford CA 94305-3032
Phone: (650)723-9203

Dr Gabriel Roy
Office of Naval Research
Mechanics Division, Code 1132
800 North Quincy Street
Arlington VA 22217-5660
Phone: (703)696-4406
FAX:696-0934
e-mail: roy@ocnr-hq.navy.mil

Dr. Robert C. Ryder
Flow Parametrics, LLC
15 Debra Drive
Bear DE 19701
Phone: (302)838-7368
FAX:838-7369
e-mail: RRyder@FlowParametrics.com

Mr Kurt Sacksteder
NASA Glenn Research Center
MS 500-217
21000 Brookpark Road
Cleveland OH 44135
Phone: (216)433-2857

Dr Michael Salkind
President
Ohio Aerospace Institute
22800 Cedar Point Road
Cleveland OH 44142
Phone: (440)962-3001
FAX:962-3120
e-mail: MichaelSalkind@oai.org

Dr Mohammad Samimy
Ohio State University
Mechanical Engineering Dept
206 West 18th Street
Columbus OH 43210-1107
Phone: (614)422-6988
FAX:292-3163
e-mail: msamimy@magnus.acs.ohio-state.edu

Dr G S Samuelsen
Department of Mechanical and
Aerospace Engineering
University of California
Irvine CA 92697-3975
Phone: (949)824-5468

Dr Billy Sanders
University of California
Davis CA 95616

Dr Joseph Sangiovanni
United Technologies Research
Center
Silver Lane
East Hartford CT 06108
Phone: (860)610-7328

Dr Lakshmi Sankar
School of Aerospace Engrg
Georgia Institute of
Technology
Atlanta GA 30332
Phone: (404)894-3014

Dr Domenic Santavicca
Propulsion Engineering Research Center
Pennsylvania State University
106 Research Building East - Bigler Road
University Park PA 16802-2320
Phone: (814)863-1863

Dr R J Santoro
Department of Mechanical
Engineering
Pennsylvania State University
University Park PA 16802-2320
Phone: (814)863-1285
FAX:865-3389
e-mail: rjs2@email.psu.edu

Dr Sutanu Sarkar
Department of Applied Mech
and Engr Science, MC 0411
University of California
La Jolla CA 92093-0411
Phone: (858)534-8243
FAX: 534-7599
e-mail: sarkar@ames.ucsd.edu

Mr William Scallion
NASA Langley Research Center
Mail Stop 408
Hampton VA 23665
Phone: (804)864-5235

Dr Klaus Schadow
Naval Air Warfare Center
Code 3892
China Lake CA 93555-6001
Phone: (760)939-6532
FAX:939-6569
e-mail: klaus_schadow@imdgw.chinalake.navy.mil

Dr John Schaefer
Energy and Environmental Div.
Acurex Corporation
555 Clyde Ave., P. O. Box 7555
Mountain View CA 94039

Dr. Peter Schihl
U.S. Army TACOM RD&E Center
Propulsion Research Group
Warren MI 48397-5000
Phone:
FAX:574-5054
e-mail: schihlp@tacom.army.mil

Dr W H Schofield
Aeronautical Research Labs
506 Lorimer St, Fishermen's Bn
Box 4331, P O
Melbourne, Victoria AUSTRALIA 3001

Dr. Lyle Schwartz
AFOSR/NA
801 North Randolph Street, Room 732
Arlington VA 22203-1977
Phone: (703)696-8457
FAX:696-8451
e-mail: lyle.schwartz@afosr.af.mil

Dr. Ernest Schwarz
Propulsion Systems Division
ATTN: DRSTA-RGD
USA Tank-Automotive Command
Warren MI 48397-5000
Phone: (810)574-5656
FAX:574-5054
e-mail: schwarze@cc.tacom.army.mil

Mr. Lee Scuderi
McDonnell Douglas Aerospace
P.O. Box 516
St. Louis MO 63166-0516

Dr D J Seery
United Technologies Research
Center
Silver Lane
East Hartford CT 06108

Dr. Corin Segal
AeMES Department
University of Florida
P.O. Box 116250
Gainesville FL 32611-6250
Phone: (352)392-6132
FAX:392-7303
e-mail: cor@AeMES.aero.ufl.edu

Dr Jerry Seitzman
School of Aerospace Engineering
Georgia Institute of Technology
Atlanta GA 30332-0150
Phone: (404)894-0013
e-mail: jerry.seitzman@ae.gatech.edu

Dr Balu Sekar
AFRL/PRSC
Building 490
1790 Loop Road North
Wright-Patterson AFB OH 45433-7103
Phone: (937)255-5974
FAX: 255-2660
e-mail: sekarb@possum.appl.wpafb.af.mil

Dr Hratch Semerjian
National Institute of
Standards and Technology
Chem Sci & Tech Laboratory
Gaithersburg MD 20899
Phone: (301)975-3145
FAX:975-3845
e-mail: HRATCH@micf.nist.gov

Dr Robert V. Serauskas
Gas Research Institute
8600 West Bryn Mawr Avenue
Chicago IL 60631
Phone: (312)399-8208
FAX:864-2774
e-mail: rserausk@gri.org

Dr Kalyanasundaram Seshadri
Center for Energy and
Combustion Research, 0407
University of California
La Jolla CA 92093-0407
Phone: (858)534-4876
e-mail: seshadri@ames.ucsd.edu

Dr G S Settles
309 Mechanical Engrg Building
Pennsylvania State University
University Park PA 16802
Phone: (814)863-1504

Dr Robert Shaw
Division of Chemical and
Biological Sciences
U S Army Research Office
Research Triangle Park NC 27709-2211
Phone: (919)549-0641

Dr. Adam Siebenhaar
Aerojet Propulsion Division
P.O. Box 13222
Sacramento CA 95813-6000

Mr David Siegel
Chief of Naval Research,
804 BCT1
800 North Quincy Street
Arlington VA 22217-5660
Phone: (703)696-4771
FAX:696-4274

Dr. Gupreet Singh
U.S. Department of Energy
1000 Independence Avenue, S.W.
Washington DC 20585
Phone: (202)586-2333
FAX:586-4166
e-mail: GUPREET.SINGH@hq.doe.gov

Dr. Robert Singleton
Director, Eng. & Env. Sciences Div.
US Army Research Office
PO Box 12211
Research Triangle Park NC 27709-2211
Phone: (919)549-4250
FAX:549-4310
e-mail: singleton@aro-emh1.army.mil

Dr William Sirignano
Department of Mechanical and
Aerospace Engineering
University of California
Irvine CA 92697-3975
Phone: (949)824-3700
FAX:824-3773
e-mail: sirignan@uci.edu

Mr. Davey Smith
Northrop Grumman Corporation
B-2 Division Dayton Office
2850 Presidential Dr., Ste 100
Fairborn OH 45324

Dr Gregory Smith
Department of Chem Kinetics
SRI International
333 Ravenswood Avenue
Menlo Park CA 94025-3493
Phone: (415)859-3496

Dr. Kenneth A. Smith
Department of Chemical Engrg.
Room 66-540
Massachusetts Inst. Of Technology
Cambridge MA 02139
Phone: (617)253-1973
FAX:253-2701
e-mail: kas@mit.edu

Dr Alan Stanton
Southwest Sciences, Inc.
1570 Pacheco Street
Suite E-11
Santa Fe NM 87501
Phone: (505)984-1322

Dr. Judi Steciak
University of Idaho-Boise
800 Park Boulevard
Boise ID 83712-7742
Phone: (208)364-4080
e-mail: jsteciak@uidaho.edu

Dr F Dee Stevenson
Office of Basic Energy Science
U. S. Department of Energy
1000 Independence Avenue, N W
Washington DC 20585

Dr David Stewart
Department of Theoretical and
Applied Mechanics
University of Illinois
Urbana IL 61801

Dr Anthony Strawa
NASA Ames Research Center
MS 230-2
Moffett Field CA 94035
Phone: (415)604-3437

Dr Robert M. Stubbs
Mail Stop 5-11
NASA Glenn Research Center
21000 Brookpark Road
Cleveland OH 44135-3127
Phone: (216)433-6303
FAX:433-5802
e-mail: rstubbs@lerc.nasa.gov

Dr Geoffrey J Sturgess
Innovative Scientific Solutions
2786 Indian Ripple Road
Dayton OH 45440-3638
Phone: (513)252-2706
FAX:056-4652
e-mail: gsturgess@aol.com

Dr B Sturtevant
Engrg and Appl Sci Dept
California Institute of
Technology
Pasadena CA 91125

Dr G Sullins
Applied Physics Laboratory
Johns Hopkins University
Johns Hopkins Road
Laurel MD 20707-6099
Phone: (301)953-5000

Dr. Rodney Tabacyznski
Director, Power Train Research Lab
Ford Motor Research Laboratory
3623 Scientific Research Lab, PO Box 2053
Dearborn MI 48121-2053
Phone: (313)322-8930

Dr Larry Talbot
Department of Mechanical
Engineering
University of California
Berkeley CA 94720
Phone: (415)642-6780

Dr. Douglas Talley
AFRL/PR
9 Antares Road
Edwards AFB CA 93524-7660
Phone: (805)275-6174

Dr. Richard Tankin
Mechanical Engineering Dept
Northwestern University
Evanston IL 60208-3111
Phone: (847)491-3532
FAX:491-3915

Dr. Jefferson W. Tester
M.I.T. Energy Laboratory
Room E40-455
Massachusetts Inst. Of Technology
Cambridge MA 02139
Phone: (617)253-3401
FAX:253-8013
e-mail: testerel@mit.edu

Dr Julian Tishkoff
AFOSR/NA
801 North Randolph Street, Room 732
Arlington VA 22203-1977
Phone: (703)696-8478
FAX:696-8451
e-mail: julian.tishkoff@afosr.af.mil

Dr T Y Toong
Department of Mechanical
Engineering
MIT
Cambridge MA 02139
Phone: (617)253-3358

Dr Michael Trenary
Department of Chemistry
The University of Illinois
Chicago IL 60680

Dr Robert J Trew
Director for Research
Defense Research & Engineering
3040 Defense Pentagon
Washington DC 20301-3040

Dr James Trolinger
MetroLaser
18006 Skypark Circle
Suite 108
Irvine CA 92714-6428
Phone: (714)553-0688
FAX:553-0495
e-mail: jtrolinger@vmsa.oac.uci.edu

Dr Timothy Troutt
Department of Mechanical
Engineering
Washington State University
Pullman WA 99164-2920

Dr. Gretar Tryggvason
Dept of Mech Engrg & Appl Mech
2350 Hayward, Room 2250
The University of Michigan
Ann Arbor MI 48109-2125
Phone: (734)763-1049
FAX:764-4256
e-mail: gretar@umich.edu

Dr Allen Twarowski
Rockwell International Sci Ctr
1049 Camino dos Rios
P O Box 1085
Thousand Oaks CA 91360
Phone: (805)373-4576
FAX:373-4775
e-mail: ajtwarow@scimail.remnet.rockwell.com

Dr C J Ultee
United Technologies Research
Center
Silver Lane
East Hartford CT 06108

Dr A D Vakili
University of Tennessee
Space Institute
Tullahoma TN 37388

Dr. Mark Valco
Propulsion Directorate
Army Research Laboratory, MS 49-1
NASA Glenn Research Center
Cleveland OH 44135-3127
Phone: (216)433-3717
FAX:433-2182
e-mail: aamark@lims01.lerc.nasa.gov

Dr. David Van Wie
The Johns Hopkins University
Applied Physics Laboratory
11100 Johns Hopkins Road
Laurel MD 20723-6099
Phone: (240)228-5194
e-mail: David.VanWie@jhuapl.edu

Dr John Vanderhoff
Ballistic Research Laboratory
DRSMC-BLI(A)
Aberdeen Proving Ground MD 21005
Phone: (410)278-6642

Dr S P Vanka
Department of Mechanical
and Industrial Engrg
University of Illinois
Urbana IL 61801

Dr James Verdieck
Rockwell International
Rocketdyne Div, M/S FA26
6633 Canoga Avenue
Canoga Park CA 91303
Phone: (818)700-4709

Dr Juan A. Vitali
AFRL/VA (Stop 37)
139 Barnes Drive, Suite 2
Tyndall AFB FL 32403-5323
Phone: (904)283-9708
FAX:283-9707
e-mail: 75023.56@compuserve.com

Dr Robert Vondra
PO Box 596
Wrightwood CA 92397
Phone: (619)249-3451

Dr. Paul Waltrup
The Johns Hopkins University
Applied Physics Laboratory
11100 Johns Hopkins Road
Laurel MD 20723-6099
Phone: (240)228-5626
e-mail: Paul.Waltrup@jhuapl.edu

Dr Joe Wanders
AFRL/MLQ
139 Barnes Drive
Tyndall AFB FL 32403-5319
Phone: (904)283-6026

Dr Charles Westbrook
Lawrence Livermore National
Laboratories
P. O. Box 808
Livermore CA 94551
Phone: (925)422-4108
FAX:422-2644
e-mail: westbrook1@llnl.gov

Dr. Phillip R. Westmoreland
Department of Chemical
Engineering
University of Massachusetts
Amherst MA 01003
Phone: (413)545-1750
(413)545-1647
e-mail: westm@ecs.umass.edu

Dr James Whitelaw
Department of Mechanical Engrg
Imperial College of Science
and Technology
London SW7 2BX UK

Dr Forman Williams
Center for Energy and
Combustion Research, 0310
University of California
La Jolla CA 92093-0310
Phone: (858)534-5492
FAX: 534-5354
e-mail: faw@ames.ucsd.edu

Dr. Skip Williams
AFRL/VSBP
29 Randolph Street
Hanscom AFB MA 01731
Phone: (781)377-2076
FAX: 377-7091
e-mail: skipw@plh.af.mil

Dr Michael Winter
United Technologies Research
Center
411 Silver Lane, MS/90
East Hartford CT 06108
Phone: (860)610-7805
FAX:610-7911
e-mail: mw@utrc.utc.com

Mr Steve Wirick
WL/AAWW-3
Wright-Patterson AFB OH 45433-6543
Phone: (937)255-4174
FAX:476-4642

Dr Bernard T Wolfson
Wolfson Associates
International
4797 Lake Valencia Blvd West
Palm Harbor FL 33563
Phone: (813)786-3007

Dr Joda Wormhoudt
Aerodyne Research, Inc.
45 Manning Road
Manning Park Research Center
Billerica MA 01821-3976
Phone: (978)663-9500
FAX:663-4918

Dr. Mary J. Wornat
Department of Mechanical and
Aerospace Engineering
D239 Engineering Quadrangle
Princeton NJ 08544-5263
Phone: (609)258-5278
FAX: 258-5963
e-mail: mjwornat@princeton.edu

Dr J M Wu
University of Tennessee
Space Institute
Tullahoma TN 37388

Dr. Vigor Yang
Propulsion Engrg Rsrch Ctr
The Pennsylvania State Univ
111 Research Building East
University Park PA 16802-2320
Phone: (814)863-1502
FAX: 865-4784
e-mail: vigor@arthur.psu.edu

Dr. Yaw Yeboah
Engineering Department
Clark Atlanta University
223 James P Brawley Drive, SW
Atlanta GA 30314
Phone: (404)880-6619
FAX: 880-6615
e-mail: yyeboah@cau.edu

Dr Richard Yetter
Department of Mechanical and
Aerospace Engineering
Princeton University
Princeton NJ 08544-5263
Phone: (609)258-2947
FAX:258-1939
e-mail: rich@dante.princeton.edu

Dr Pui-kuen Yeung
School of Aerospace Engrg
Georgia Institute of
Technology
Atlanta GA 30332-0150
Phone: (404)894-9341
FAX:894-2760
e-mail: yeung@peach.gatech.edu

Dr Shaye Yungster
Institute for Computational
Mechanics in Propulsion
NASA Glenn Research Ctr
Cleveland OH 44135
Phone: (216)433-6680

Dr Michael Zachariah
National Institute of
Standards and Technology
Center for Chemical Engrg
Gaithersburg MD 20899
Phone: (301)975-2063

Mr Fred Zarlingo
Code 3246
Naval Air Warfare Center
China Lake CA 93555-6001
Phone: (760)939-7395

Dr Ben Zinn
School of Aerospace Engineering
Georgia Institute of Technology
Atlanta GA 30332-0150
Phone: (404)894-3033
FAX:894-2760
e-mail: ben.zinn@aerospace.gatech.edu